RICARDO PATRICIO ÁLVAREZ BRICEÑO

Avaliação experimental de força equivalente e parâmetros dinâmicos na vibração induzida por escoamento bifásico externo em banco de tubos

São Carlos
2018

RICARDO PATRICIO ÁLVAREZ BRICEÑO

Avaliação experimental de força equivalente e parâmetros dinâmicos na vibração induzida por escoamento bifásico externo em banco de tubos

Tese apresentada para obtenção do título de Doutor em Engenharia Mecânica pela Escola de Engenharia de São Carlos da Universidade de São Paulo.

Área de concentração: Dinâmica de Máquinas e Sistemas.

ESTE EXEMPLAR TRATA-SE DA VERSÃO CORRIGIDA.
A VERSÃO ORIGINAL ENCONTRA-SE DISPONÍVEL JUNTO AO DEPARTAMENTO DE ENGENHARIA MECÂNICA DA EESC-USP.

Orientador:
Prof. Dr. Leopoldo P. R. de Oliveira

São Carlos
2018

Ficha catalográfica elaborada pela Biblioteca Prof. Dr. Sérgio Rodrigues
Fontes da EESC/USP

Álvarez Briceño, Ricardo Patricio
A473a Avaliação experimental de força equivalente e parâmetros dinâmicos na vibração induzida por escoamento bifásico externo em banco de tubos / Ricardo Patricio Álvarez Briceño ; orientador Leopoldo P.R.de Oliveira. -- São Carlos, 2018.

Tese (Doutorado)- Programa de Pós-Graduação em Engenharia Mecânica e Área de Concentração em Dinâmica de Máquinas e Sistemas -- Escola de Engenharia de São Carlos da Universidade de São Paulo, 2018.

1. Escoamento bifásico. 2. Viga em balanço. 3. Vibração induzida por escoamento. 4. Vibração induzida por turbulência. 5. Filtro de Kalman. I. Titulo.

Elaborado por Elena Luzia Palloni – CRB 4464

RICARDO PATRICIO ÁLVAREZ BRICEÑO

Experimental assessment of equivalent loads and dynamic parameters on vibration induced by two-phase crossflow in tube bundles

São Carlos
2018

RICARDO PATRICIO ÁLVAREZ BRICEÑO

Experimental assessment of equivalent loads and dynamic parameters on vibration induced by two-phase crossflow in tube bundles

PhD Thesis presented to the Graduate Program in Mechanical Engineering of the São Carlos School of Engineering of the University of São Paulo, Brazil, in partial fulfillment of the requirements for the degree of Doctor in Mechanical Engineering (USP).

Concentration area: Machine and System Dynamics

Supervisor:
Prof. Dr. Leopoldo P. R. de Oliveira

São Carlos
2018

FOLHA DE JULGAMENTO

Candidato: Engenheiro **RICARDO PATRICIO ALVAREZ BRICEÑO.**

Título da tese: "Avaliação experimental de força equivalente e parâmetros dinâmicos na vibração induzida por escoamento bifásico externo em banco de tubos"

Data da defesa: 03/08/2018

Comissão Julgadora:	**Resultado:**
Prof. Dr. **Leopoldo Pisanelli Rodrigues de Oliveira (Orientador)** (Escola de Engenharia de São Carlos/EESC)	APROVADO
Prof. Associado **Gherhardt Ribatski** (Escola de Engenharia de São Carlos/EESC)	APROVADO
Prof. Titular **Celso Pupo Pesce** (Escola Politécnica/EP-USP)	Aprovado
Prof. Dr. **Aldemir Aparecido Cavallini Junior** (Universidade Federal de Uberlândia/UFU)	APROVADO
Prof. Dr. **Adriano Todorovic Fabro** (Universidade de Brasília/UnB)	APROVADO

Coordenador do Programa de Pós-Graduação em Engenharia Mecânica:
Prof. Associado **Gherhardt Ribatski**

Presidente da Comissão de Pós-Graduação:
Prof. Associado **Luís Fernando Costa Alberto**

This thesis is dedicated to my parents Ricardo and Anita, to whom I owe everything.

Acknowledgements

This project has been funded by the Brazilian National Council for Scientific and Technological Development - CNPq (grant numbers 481044/2010-8 and 307369/2013-7) and the doctorate scholarship from CAPES Foundation, for which I am grateful.

I would like to thank the São Carlos School of Engineering, University of São Paulo, USP - Brazil, which welcomed me and has been my home during these six years of study and work.

My big and sincere thank goes to my promoter, Prof. Leopoldo de Oliveira, who supported me in several ways since the very first time we got in touch via e-mail. Thank you, Leopoldo, for always be in a good mood and available for answering my questions, for your respect to my time and your consideration. Thank you for sharing your knowledge about experimental structural dynamics and, specially, for making feasible the ideas I proposed for our tests. I use to make a joke: if I would necessitate enriched uranium, Leopoldo would provide. Thanks for the freedom you gave me to make the decisions in the present project.

My sincere thanks go to Prof. Gherhardt Ribatski, who let me be part of the project. Also, I would like to thank your "encouraging phrases", they were used to challenge me in the subject that you imparted to me, as well as, to take me out from my comfort zone in many times. Moreover, I would like to thank you for considering myself to write the chapter for the Encyclopedia of Two-Phase Heat Transfer and Flow, it was an invaluable experience.

I would like to express my thanks to Prof. Fabio Kanizawa, who designed and mounted the test bench in which I performed the experimental campaign. Thank you for your patience and to be willing to help. Actually, this paragraph should be longer, however, I already gave a speech when you left São Carlos.

I would like to offer my thanks to everyone I met during my stay at our "Labdin": Tatiane Godoy, Jaime Mosquera, Guido Gómez, Kleber Rodrigues, Willians Godoy, Rafael Avanco, Jelder Quiñonez, Paulo Martins, Augusto Shigueoka, Hélio Cruz, Heitor Silva, Luiz Nascimento, Natália de Paula, Marcela Demarzo, Gabriel Rodrigues, David Díaz, Jorge Pablo Galdames and Andrés Gomez. Thank you for the interesting discussions on several topics, and to make our days funnier. Special thanks to Augusto, who always saved me when codes were not compiling or latex templates were not running.

I wish to thank the secretarial services offered by Cristina Márcia Pessa, Ana Paula Bueno, and Iara Alice de Oliveira. Furthermore, I would like to thank the technicians Leandro Pedrassolli, Sérgio Ferreira, José Francisco de Morães (Xina) and, especially, to Jair Diego Antonietti, who constructed the structural devices that were used in the experimental campaign.

Although I mentioned them above, I would like to thank again to Kleber Rodrigues and Willians Godoy, who helped me with everything they could and adopted me on many weekends and holidays. Being far away from home is easier when you have something similar to a family. Thank you for every *churrasco* we organized, every beer we drank and every football game we watched. Words are insufficient to express my gratitude to you guys. I also owe some gratitude words to Kleber's family: Madalena, Margareth, Mario, Vivi, Ronaldo, Silmara, and Odila. Furthermore, I would like to thank Fernanda Picon, thanks for your sincere friendship and receiving me at home in many times.

I would like to thank Thiago Caspão and Wagner Filho for those moments listening MPB and drinking some beers. Thank you, Thiago Caspão, for teaching me the suitable proportions of food for a successful *churrasco*. This is not related to the Ph.D. program but it is learning for life. In addition, I would like to thank Thiago Soares for receiving me at home during the time I was studying for the admission test of the Ph.D. program.

I wish to thank Nicoly Almeida, for your patience and sincere friendship, and for planning the activities on the weekends. My biggest thanks go to the "Illustrious Community of Ecuadorians in São Carlos", whose members are: Juan Chambers, Esteban Cueva, David Aveiga, Jhosua Almeida, Felipe Alvear, Cristian Morante, Víctor Sánchez, Andrés Delgado, Caren Castillo and Michelle Moreno. You constitute a piece of Ecuador in Brazil, it was awesome to have met you! Moreover, I would like to thank Diego Calero, one of the former members of the Community, for the trips, conversations and given tips.

The day I took the flight from Quito to São Paulo I left many friends in Ecuador, who, during these six years, have always been supporting me via messages and calls. Among them, I would like to thank Pablo Vizcaíno, Vladimir Vizcaíno, Carlos Peña, Carolina Tapia, Daniel Vergara, Alexandra Vaca, María del Pilar Arévalo, Andrea Arias, Rossana Barba, Patricia Pontón, José Antonio Rodríguez, David Montenegro and Daniel Soria. Thank you for all your good vibes, my dear friends!

I am especially grateful to Prof. Víctor Guerrero, who was the promoter of my undergraduate thesis project and friend. Thank you, Prof. Guerrero, for sowing the seeds of curiosity on post-graduate courses and research.

I would like to thank my father Ricardo, my mother Anita and my sister Heysel, for their love. They are the most important I have in my life. This would not have been possible without their support. Despite the 7000 Km between us, their words and

prayers accompanied me all the time.

Finally, I thank God, whoever he is, for all.

"Only the most naive of questions are truly serious."
(Milan Kundera)

Abstract

ÁLVAREZ-BRICEÑO, R. P. **Experimental assessment of equivalent loads and dynamic parameters on vibration induced by two-phase crossflow in tube bundles**. 2018. 150 p. Thesis (Doctor in Mechanical Engineering) - São Carlos School of Engineering, University of São Paulo, São Carlos, 2018.

Flow-induced vibration (FIV) is probably the most critical dynamic issue in the design of tube bundles in shell-and-tubes heat exchangers. This fluid-structure phenomenon may generate high amplitude vibration of tubes or structural parts, which leads to fretting wear between the tubes and supports, noise or even fatigue failure of internal components. Several test sections have been constructed in order to study FIV problems, however, the vibration properties of tubes in the tube bundle, principally those related with two-phase flow, have not been totally understood yet. In order to enhance the current understanding on these phenomena, the present research proposes an extensive review on the behavior of the dynamic parameters of tube vibration in tube bundles. Furthermore, the characteristics of turbulence-induced vibration mechanism, including the design guidelines to predict its severity, are analyzed. Such a study is complemented by an experimental campaign in which the databases of dynamic parameters and turbulence-induced vibration design guidelines found in literature are validated. For this, a 19 mm O.D. and 381 mm long tube was mounted in cantilever in a tube bundle with normal triangular configuration ($\tau = 1.26$), which is subjected to upward air-water crossflow with void fractions from 30% to 95%. The dynamic response of this tube was measured by using piezoelectric microaccelerometers. The obtained results show good agreement with the database of dynamic parameters and turbulence-induced vibration design guidelines. Further, the results allowed the redefinition of a design guideline, which led to understand fluid-structure interaction as a function of flow patterns and mass velocities. In addition, Kalman filtering techniques were used to estimate flow-induced forces based on output only. The results suggests the presence of forces with a periodic component of quasi-constant frequency, in transverse direction, for void fractions up to 50%. Furthermore, it was noticed that flow-induced forces are generally higher in parallel direction.

Keywords: two-phase flow; cantilever-beam; flow-induced vibration; turbulence-induced vibration; Kalman Filter.

Resumo

ÁLVAREZ-BRICEÑO, R. P. **Avaliação experimental de força equivalente e parâmetros dinâmicos na vibração induzida por escoamento bifásico externo em banco de tubos**. 2018. 150 f. Tese (Doutorado em Engenharia Mecânica) - Escola de Engenharia de São Carlos, Universidade de São Paulo, São Carlos, 2018.

A vibração induzida por escoamentos é provavelmente o problema dinâmico mais importante no projeto da tubulação de um trocador de calor de casco e tubos. Esse fenômeno fluido-estrutural pode gerar vibração de grande amplitude de tubos ou partes estruturais, o qual pode conduzir a situações de desgaste por atrito entre tubos e suportes, ruído ou até falhas por fadiga dos componentes internos. Várias seções de testes vêm sendo construídas visando o estudo da vibração induzida por escoamentos, porém, as características da vibração dos tubos na tubulação, principalmente aquelas relacionadas com escoamento bifásico, não são totalmente compreendidas. Com a finalidade de melhorar o conhecimento atual sobre esse fenômeno, essa pesquisa apresenta uma revisão sobre o comportamento dos parâmetros dinâmicos da vibração dos tubos no trocador. Além disso, as características do mecanismo de vibração induzida por turbulência, incluindo as diretrizes de projeto que estimam sua severidade, são analisadas. Esse estudo é complementado por uma campanha experimental na qual as bases de dados dos parâmetros dinâmicos e as guias de projeto para vibração induzida por turbulência são validadas. Para tanto, um tubo de 19 mm de diâmetro externo e 381 mm de comprimento é montado em balanço num banco de tubos com configuração triangular normal ($\tau = 1.26$), a qual é sujeita a um escoamento vertical ascendente água - ar com frações de vazio desde 30% até 95%. A resposta dinâmica do tubo foi medida usando microacelerômetros piezoelétricos. Os resultados obtidos mostram concordância com as bases de dados, tanto dos parâmetros dinâmicos como das diretrizes de projeto, para vibração induzida por turbulência. Baseado nos presentes resultados, uma das diretrizes de projeto foi reformulada, a qual permitiu entender a interação fluido-estrutura como uma função dos padrões de escoamento e velocidades mássicas. Além disso, técnicas relacionadas ao filtro de Kalman foram usadas para estimar a força induzida pelo escoamento baseado unicamente nas medidas de aceleração. Os resultados dessa análise sugerem a presença de uma componente periódica de

frequência quase-constante na direção transversal para frações de vazio menores do que 50%. Ademais, notou-se que as forças estudadas são geralmente maiores na direção paralela à direção da velocidade principal do escoamento.

Palavras-chave: Escoamento bifásico; viga em balanço; vibração induzida por escoamento; vibração induzida por turbulência; filtro de Kalman.

List of Figures

List of Tables

Contents

List of Symbols

Letters

A Reference transverse area (ch. 2), overall coefficient for damping (ch.3)

$\mathbf{A}$ State matrix

A_y Oscillation amplitude

$\mathbf{B}$ Input matrix

$\mathbf{b}$ Force selection matrix

$\mathbf{b_d}$ Disturbance selection matrix

$\mathbf{B_1}$ Input disturbance matrix

C Lumped damping coefficient

$\mathbf{C}$ Damping matrix

C_I Coefficient of interaction

$C\,(De/d)$ Confinement effect

c Damping coefficient

C_0 Phases parameter distribution

C_D Drag coefficient

C_R^* Effective random excitation coefficient

(D_e/d) Confinement parameter

d Tube diameter

d_0 Reference diameter

d_h Hydraulic diameter

F_D Force due to parallel (drag) flow

F_d Damping force

f Tube resonance frequency

$\mathbf{f}$ Force vector

$\mathbf{f_d}$ Force disturbance vector

f_g Tube resonance frequency in air

f_n Natural frequency

f_w Frequency of wake shedding

f_{tb} Turbulent buffeting frequency

f_{L0} Darcy friction factor

G Mass velocity

$\mathbf{G}$ Covariance matrix of state estimates before measurement update

g Gravitational acceleration

$\mathbf{H}$ Measurement matrix

$\mathbf{H_{dm}}$ Dummy measurements matrix

J Joint acceptance

j Superficial velocity

j^* Non-dimensional superficial velocity

K Lumped stiffness

$\mathbf{K}$ Stiffness matrix

K_{TP} Correlation factor

(K_l/K_g) Moment coefficient ratio

L Tube length

L_0 Reference length

M Lumped mass

$\mathbf{M}$ Mass matrix

MF_{L0} Moment flux

m Mass per unit length

m_h Hydrodynamic mass per unit length

m_t Tube mass per unit length

m_0 Total mass of the tube per unit length

$\dot{m}$ Mass flow rate

P Pressure

$\mathbf{P}$ Covariance matrix of state estimates

p_0 Pressure scaling factor

Q Volumetric flux (ch. 2), amplification factor (ch. 3)

$\mathbf{R_v}$ Measurement noise covariance matrix

$\mathbf{R_w}$ Process noise covariance matrix

$\mathbf{R_z}$ Input noise covariance matrix

S Slip ratio

S_F Power spectral density function

$\tilde{S_F}(f)$ Dimensionless force power spectral density function

$\tilde{S_F}(f)_e$ Equivalent dimensionless force power spectral density function

$\tilde{S_F}(f)_e^0$ Reference equivalent dimensionless force power spectral density function

S_p Power spectral density of excitation force per unit length

s_1 Transverse pitch

s_2 Longitudinal pitch

T Temperature

U Bulk flow velocity

$\mathbf{u}$ Input vector in state state formulation

u flow velocity

$\bar{u}$ Homogeneous flow velocity

u_{rel} Relative velocity between flow and structure

u_{mb} Average velocity of two-phase flow

u_{gl} Relative velocity between the liquid and gas phases

u_{gj} Phases slip parameter

u_{pc} Critical pitch velocity

V Amplitude of the velocity oscillation

$\bar{v}$ Mixture specific volume

$\mathbf{v}$ Measurement noise vector

$\mathbf{w}$ Process noise vector

x Mass quality

$\mathbf{x_s}$ System state vector

$\hat{\mathbf{x}}_\mathbf{s}$ State estimation after measurement update

$\bar{\mathbf{x}}_\mathbf{s}$ State estimation after time update

y_{rms} Root mean square amplitude of vibration

$\mathbf{y}(t)$ Measurements vector

$\mathbf{y_{dm}}(t)$ Dummy measurements vector

$\mathbf{z}$ Input noise vector

Greek letters

α Superficial void fraction

α_3 Volumetric void fraction

β Volumetric quality

$\mathbf{\Gamma}$ Discrete input matrix

$\mathbf{\Gamma_1}$ Discrete disturbance matrix

δ Logarithmic decrement

ζ_f Damping ratio due to friction

ζ_f Damping ratio due to squeeze film

ζ_{nNs} Damping ratio normalized by the number of spans

ζ_{nsw} Damping ratio normalized by effect of support thickness

ζ_S Structural damping ratio

ζ_{SFcyl} Damping of a cylinder in a viscous and quiescent fluid

ζ_T Total damping ratio

ζ_V Viscous damping ratio

ζ_{VTP} Viscous two-phase fluid damping ratio

ζ_x Damping ratio in transverse direction

ζ_y Damping ratio in parallel direction

η Loss factor

η Modal coordinates vector

θ Angle parameter in tube bank

λ_c Correlation length

μ Fluid dynamic viscosity

$\bar{\mu}$ Mixture viscosity

ν Fluid kinematic viscosity

ξ Physical coordinate vector

ρ Fluid density

$\bar{\rho}$ Mixture density

σ Surface tension

τ Transverse pitch-to-diameter ratio

$\mathbf{\Phi}$ Discrete state matrix

Φ_{L0}^2 Two-phase friction multiplier

χ Longitudinal pitch-to-diameter ratio

Ψ Modal matrix

ψ Mode shape deflection

ω Circular frequency

ω_n Natural circular frequency

Operators

$\langle\rangle$ Spatial average

Subscripts

GO Corresponding to the mixture flow flowing as a gas

g Relative to gas phase

H Based on the homogeneous void fraction model

LO Corresponding to the mixture flow flowing as a liquid

l Relative to liquid phase

Dimensionless numbers

Cap Capillary number

Eu Euler number

Fr Froude number

f_R Reduced frequency

Re Reynolds number

Ri Richardson number

St Strouhal number

We Weber number

X_{tt} Lockhart - Martinelli parameter

Acronyms

EMA Experimental Modal Analysis

FEI Fluid-elastic Instability

FIV Flow-induced Vibration

FRF Frequency Response Function

KF Kalman filter

AKF Augmented Kalman filter

AKF-DM Augmnted Kalman filter implemented with dummy measurements

OMA Operational Modal Analysis

Chapter 1

Introduction

Shell-and-tube heat exchangers are the most common type of heat exchanger found in industrial processes (KANIZAWA; RIBATSKI, 2016a). These devices are also used in more complex systems, for example, as steam generators in pressurized water reactors of nuclear power plants, which correspond to a critical operational condition since a mechanical failure implies significant economical losses, unexpected shut downs, not to mention critical radioactive accidents. According to Weaver et al. (2000), traditionally, the shell-and-tube heat exchangers presented thick tubes and support walls, and the flow velocity was kept low. Conversely, efficient designs often require high flow velocities on the shell side and reduction of the pipes wall thickness, while an optimum design would necessitate as much as possible reduction in the structural support (NOGHREHKAR et al., 1999). However, these requirements for efficient designs are limited by the vibration mechanisms that could take place in the tube bundle. In this way, the Flow-Induced Vibration (FIV) problem arises as the most relevant dynamic issue at the design stage of a heat exchanger

According to the TEMA Standards (TEMA Standards, 1999), tube failures due to FIV have been reported along all regions of shell-and-tube heat exchangers; nonetheless, regions with flexible tube spans and/or high flow velocities are regions of primary concern. Actually, Pettigrew & Taylor (2003a) indicated that for such heat exchangers, the forces generated by the axial component of the flow velocity are negligible, while the transverse component is critical for FIV. In this context, it is accepted that the most important FIV mechanisms during single-phase flow are: (i) fluidelastic instability, (ii) vortex shedding, (iii) random excitation and (iv) acoustic resonance (TAYLOR; PETTIGREW, 2001). In addition, Green & Hetsroni (1995) and Noghrehkar et al. (1999) estimate that half of shell-and-tube heat exchangers in the industry operate under two-phase flow conditions in the shell side, which correspond to a more critical condition for FIV. During these operation conditions, the phases can present distinct geometrical distributions, which are referred to as flow patterns, and its occurrence depends on flow velocity, phases properties, void fraction and geometrical configuration of the tube bundle.

Furthermore, the identification of the flow pattern is important since, as suggested in the literature (PETTIGREW; TAYLOR, 2004), non-continuous flow patterns, such as intermittent and churn, should be avoided because they can generate high amplitude vibration, and therefore, fretting-wear between tubes and fatigue of structural components. Moreover, besides the loading on the tubes, void fraction and flow pattern do affect the dynamic parameters of a vibrating tube in a tube bundle, specifically hydrodynamic mass and damping ratio (PETTIGREW et al., 1991; PETTIGREW; TAYLOR, 2004), which in turn modify the vibration response of the tube.

Regarding the vibration mechanisms, Khushnood et al. (2012) pointed out that the same vibration mechanisms of single-phase flow are present during two-phase flow, and that the occurrence of a specific vibration mechanism depends on the operational conditions. According to Pettigrew et al. (1991), fluidelastic instability and turbulence excitation are the most important mechanisms in tube bundles during two-phase cross-flow, while periodic shedding and acoustic resonance are unlikely to occur. However, based on results reported by Feenstra et al. (2000), an exception can be opened for very low void fractions since the characteristics of these conditions are similar to single-phase flow and periodic shedding is still possible. Among the most relevant vibration mechanisms in two-phase flow, the fluidelastic instability have been extensively studied since it is the most dangerous excitation mechanism (PETTIGREW; TAYLOR, 2003a), and it may lead to a bundle collapse within reduced working hours. Conversely, only few experimental data for turbulence-induced vibration mechanism under conditions two-phase flow are available, which is somehow surprising since this vibration mechanism is unavoidable, and is always present in heat exchanger tube bundles. Actually, more recent experimental studies (ZHANG et al., 2007; PERROT et al., 2011) have shown that there is a lack of knowledge in this mechanism since they found out that it consists of turbulence and periodic components, which have not been reported in literature before.

Certainly, further experimental data are necessary to understand and characterize the turbulence-induced vibration mechanism. However, an appropriate instrumentation is hard to be accomplished, mainly due to reduced spaces in tube bundles and because typical instruments are hardly liquid resistant. Despite the difficulties, several methodologies to measure flow - induced forces in tube bundles have been proposed. For example, Zhang et al. (2007) measured dynamic forces on both directions, transverse and parallel to flow main velocity, via strain gauge instrumented cylinders. In order to do that, the instrumented tubes were designed so that the fundamental natural frequency was higher than 150 Hz, which is considerably higher than both the expected force frequencies to be analyzed and the range of tube resonance frequencies in real heat exchangers. In this manner, the cantilever cylinder functioned basically as a dynamic force transducer, whose frequency response function (FRF) is flat in the frequency bandwidth of interest. Therefore, strain measurements can only be associated with the first

vibration mode shape and, based on some hypothesis, an equivalent concentrated force can be estimated.

Several other studies report the use of strain gauges to assess force in FIV (TAYLOR et al., 1988; TAYLOR et al., 1989; AXISA et al., 1990; PETTIGREW et al., 1995; PETTIGREW et al., 2002; PETTIGREW et al., 2005; PERROT et al., 2011). In strain gauge applications, in which a secondary quantity (other than strain) is needed, a preliminary calibration step is required, in which a known loading condition is used to relate the measurement output to that desired quantity. Despite this being a common practice, it is not a robust approach (NAETS et al., 2015a), as system changes and varying operating conditions can considerably affect this calibration. Moreover, the very nature of the operational load may differ from that used in the calibration step as, usually, concentrated forces are used in the latter, whereas the distributed loads may have an important role during system operation. As it can be seen, there is a need for alternative methods capable of estimating flow-induced forces, whose results can increase database in turbulence-induced vibration mechanism and can be compared with those obtained via strain gauges measurements.

In recent years, researchers have explored techniques for using incomplete measurement data to estimate the response at unmeasured locations in structural or mechanical systems (PETERSEN et al., 2018), which are referred to as virtual sensing techniques. In this context, Kalman filtering based techniques have been proposed by some references (BERG; Keith Miller, 2010; LOURENS et al., 2012; NAETS et al., 2015a; NAETS et al., 2015b; CROES, 2017) as a solution for coupled input and state estimation, which is of particular interest in the present work since it seems to be an alternative to study forces based on outputs only. Regarding the implementation of Kalman filtering techniques in fluid-structure interaction, very few references can be cited. For instance, Berg & Keith Miller (2010) implemented this type of technique to estimate typical wind forces on a wind turbine blade model. The authors mentioned that the estimate is not perfect, but it does track the shape of the force profile. Despite this, in most cases flow-induced forces imply distributed forces and the instrumentation up-to-date can hardly estimate its characteristics directly (say frequency components and amplitude), unless a set of hypotheses is adopted. For this reason, and for the sake of easiness, some authors (ZHANG et al., 2007; PERROT et al., 2011) prefer the estimation of an equivalent force that is capable of representing a set of forces under some hypotheses.

In order to improve the understanding of the effect of vibration of tubes in tube bundles under two-phase flow, the present manuscript proposes an experimental assessment on the behavior of dynamic parameters (*e.g.* hydrodynamic mass and damping ratio), turbulence-induced vibration and the flow-induced forces involved under upward crossflow air-water mixtures with homogeneous void fractions from 30% to 95%. In addition, an extensive review of literature related to dynamic parameters and

turbulence-induced vibration design guidelines is presented. The experimental campaign consists of two stages; the first one is devoted to the analysis of the tube response aiming to study its dynamic parameters via conventional techniques (*e.g.* peak picking, half-power bandwidth method) and validate turbulence-induced vibration guidelines. In a second stage, the flow-induced forces on an instrumented cylinder are estimated via Kalman filtering techniques, from which an equivalent force is defined for each condition. Most of the results obtained in this work are discussed in terms of mass velocity, void fraction and flow patterns, which are parameters that characterize distinct operational conditions of heat exchangers.

1.1 Methods and objectives

The main objective of this doctorate work is to develop an experimental study on flow-induced vibration of tubes in a normal triangular tube bundle, which is subjected to air-water upward crossflow. This study aims at establishing links between flow parameters and the tube dynamic response, as well as, the nature of the induced forces. In view of that, a number of specific objectives can be highlighted:

- To conceive, design and construct a device whose vibration response can be used to study flow-induced vibration phenomena in tube bundles under two-phase flow;
- To analyze the system dynamics response via traditional techniques (peak-picking and half-power frequency bandwidth) in order to evaluate its dynamic parameters and vibration amplitude for validating the database in open literature and revisit classical design guidelines;
- To estimate the flow-induced loads and analyze their features by discussing results in terms of two-phase flow parameters.

In order to achieve these objectives, this work presents:

- A review of the literature regarding two-phase flow fundamentals that includes definitions on void fraction and flow patterns;
- A review of the literature regarding flow-induced vibration due to external crossflow in tube bundles with emphasis on dynamic parameters (*e.g.*: hydrodynamic mass and damping ratio) and turbulence-induced vibration mechanism;
- The theoretical background for virtual sensing, particularly Kalman filtering techniques, used for force identification, and its feasible use on flow-induced loads;

- A complete description of the experimental apparatus, including the identification of the system dynamics via Experimental Modal Analysis (EMA).

1.2 Text organization

This manuscript is organized in the following chapters:

- **Chapter 2:** introduction of the geometrical parameters of a tube bundle, parameters and fundamentals of two-phase flow, description of flow patterns and kinematic modeling of two-phase flows.
- **Chapter 3:** description of dynamic parameters that characterize a structure immersed in two-phase flow, review of the vibration mechanisms in two-phase flow focused on practical approaches for turbulence-induced vibration mechanism
- **Chapter 4:** concepts of virtual sensing, Kalman filtering equations based on results obtained from EMA procedures
- **Chapter 5:** detailed description of the test bench used in the experimental campaign.
- **Chapter 6:** results on dynamic parameters, validation of turbulence-induced vibration design guidelines, results on flow-induced forces via Kalman filtering.
- **Chapter 7:** conclusions and recommendations for future works.

Chapter 2

Parameters of two-phase flows across tube bundles

This chapter presents definitions on two-phase flow characterization parameters as well as geometrical parameters necessary for tube bundle description. The information in the sections below is based on the review presented in Kanizawa (2014), which is the doctoral thesis in which the design and construction of the experimental facility used in the present study is detailed. Based on the defined parameters, a review on the two-phase flow kinematic models is presented and a method for estimating the flow velocity across the test section is derived, which will be used as a reference to discuss results on FIV phenomena.

2.1 Geometrical parameters in tube bundles

This section describes the geometrical parameters that characterize the tube bundles in shell-and-tube heat exchangers. Figure 2.1 roughly depicts the distribution of the most important parts in a straight-tube heat exchanger with a single pass in the tube-side. In this equipment, the tubes conduct the internal fluid that will exchange heat with the shell-side fluid and, depending on the requirements, its external surface may be plain or finned. The baffles are intended to guide the external flow across the tube bundle, support the tubes along their total span and maintain the tubes spatial distribution. In this way, the fluid that flows externally to the tubes and between two baffles can be assumed as crossflow.

Tube banks or tube bundles can be installed according to two distinct configurations: staggered or parallel, which are depicted in Fig. 2.2.

The geometrical parameters in a tube bundle are defined as a function of the distance between the centers of neighboring tubes. The transverse pitch, s_1, is defined as the distance measured between two adjacent tubes along the direction perpendicular to

Figure 2.1: *Shell-and-tube heat exchanger (ÁLVAREZ-BRICEÑO et al., 2018).*

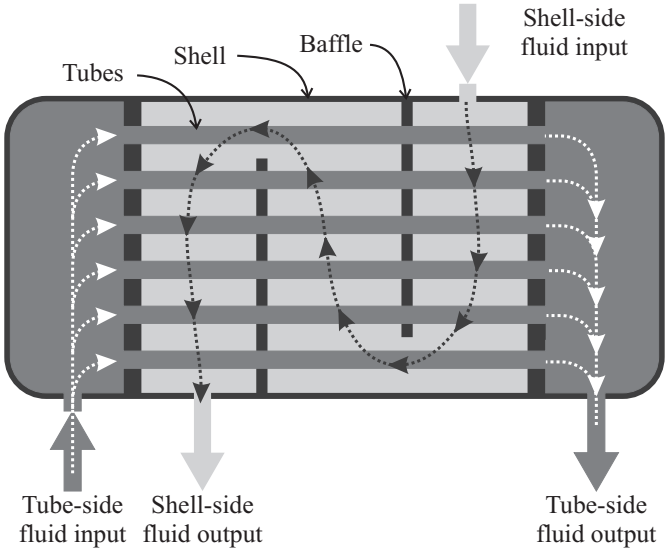

Figure 2.2: *Configurations of tubes in a bundle.*

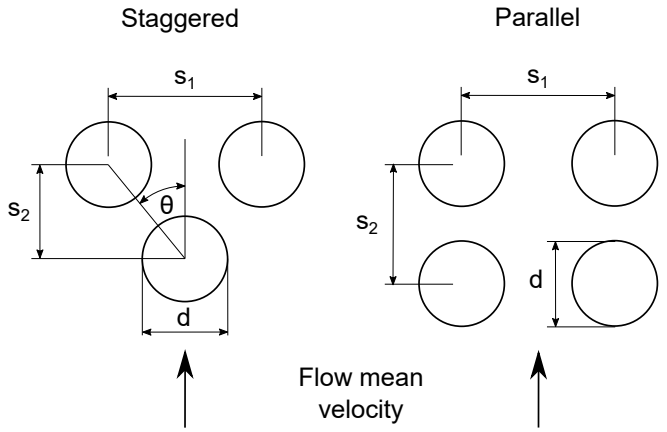

the flow main velocity direction. The longitudinal pitch, s_2, is defined as the distance measured between two adjacent tubes along the direction parallel to the flow main velocity direction. For staggered tube banks, the angle parameter θ is generally equal to 30, 45 and 60°. Based on these common configurations, Païdoussis et al. (2011) present the following definitions for common tube banks found in industry, which are depicted in Fig. 2.3:

- Rotated triangular (or parallel triangular): staggered configuration with $\theta = 60°$;
- Normal triangular: staggered configuration with $\theta = 30°$;
- Normal square: in-line configuration with $s_1 = s_2$;
- Rotated square: staggered configuration with $\theta = 45°$

In this manner, the distribution of the tubes in the bank and the space between the tubes to the fluid flow through can be expressed as a function of transverse and

Figure 2.3: *Common configurations of tube banks (PAïDOUSSIS et al., 2011).*

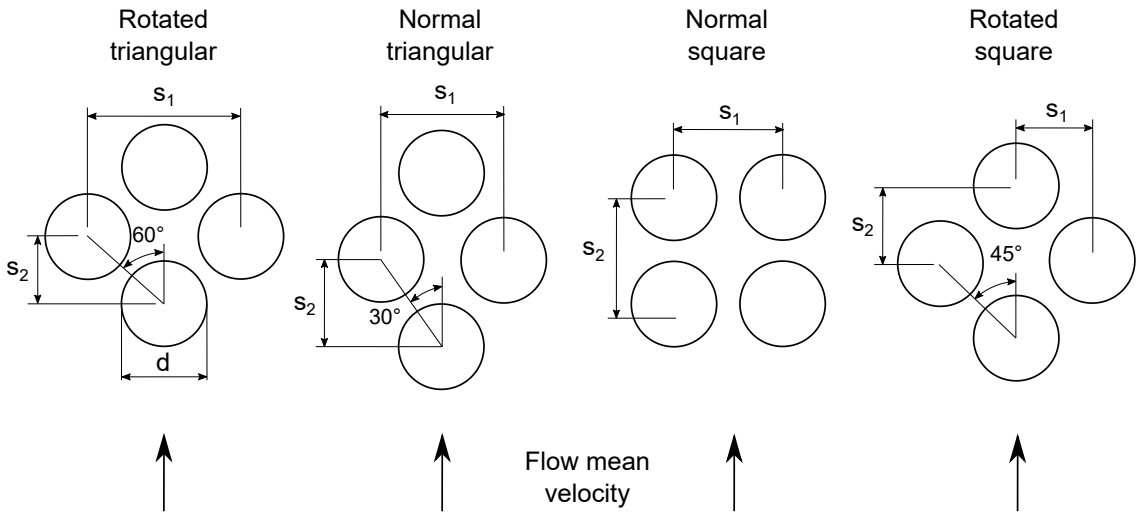

longitudinal pitches and the tube diameter, as follows:

$$\tau = \frac{s_1}{d}, \tag{2.1}$$

$$\chi = \frac{s_2}{d}, \tag{2.2}$$

where d is the tube diameter.

Païdoussis et al. (2011) point out that the values of τ for most of heat exchangers in industry vary from 1.25 to 2, and the distance between baffles generally varies from 12 to 20 diameters.

In the case of tube banks with normal triangular and normal square configurations, the smallest section to flow passage corresponds to the region between tubes in the same row, whereas for rotated triangular and rotated square configurations the smallest section is that between the tubes of two adjacent rows (KANIZAWA, 2014).

2.2 Parameters of two-phase flows

Figure 2.4 depicts a multiphase flow passing through a duct. In this case, the flow is composed by two-phases: liquid and gas. The definitions in the present document for internal flow are also valid for the description of a crossflow in a tube bundle, since it can be assumed that the heat exchanger is a duct limited by its shell.

The mass flow rates is given by the sum of each phase flow rate:

$$\dot{m} = \dot{m}_g + \dot{m}_l, \tag{2.3}$$

where g and l sub-indexes define gas or liquid phase. In the case of liquid - vapor two-phase systems it can be admitted thermodynamic equilibrium between the phases, thus

Figure 2.4: *Scheme of a two-phase flow passing through a duct.*

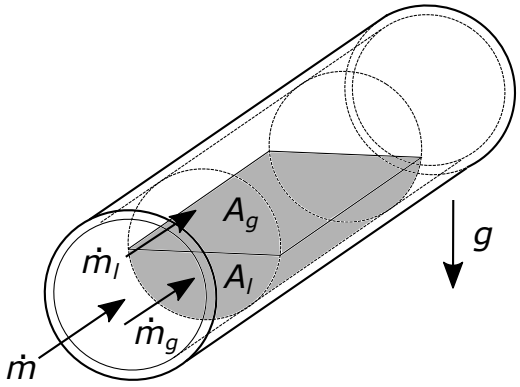

their mass flow rates can be expressed as functions of the mass quality, x, as follows:

$$\dot{m}_l = (1 - x)\dot{m}, \tag{2.4}$$

$$\dot{m}_g = x\dot{m}. \tag{2.5}$$

For a two-phase system in which liquid and gas phases are distinct substances, as in the experimental conditions in the present work, and assuming no mass transfer between these substances, the mass quality is constant along the test section.

The mass velocity, or mass flux, G, is the ratio between the mass flow rate and the area transverse to the flow velocity, A. Mass velocities for two-phase flow case are defined according the following expressions:

$$G = \frac{\dot{m}}{A} = G_g + G_l, \tag{2.6}$$

$$G_g = \frac{\dot{m}_g}{A} = x\frac{\dot{m}}{A}, \tag{2.7}$$

$$G_l = \frac{\dot{m}_l}{A} = (1 - x)\frac{\dot{m}}{A}. \tag{2.8}$$

In the case of a tube bank, mass flux and volumetric flux parameters are generally defined by using the smallest transverse area as reference.

Superficial velocity, or volumetric flux, is defined as the average velocity of each phase under the hypothesis that each phase flows through a duct of area equal to total duct area by which both phases are actually flowing. The superficial velocities for each phase are given by:

$$j_g = \frac{Q_g}{A} = \alpha u_g, \tag{2.9}$$

$$j_l = \frac{Q_l}{A} = (1 - \alpha)u_l, \tag{2.10}$$

where u is the flow velocity through the smallest section in the tube bundle where the

mixture is passing through, and Q_g and Q_l are the volumetric mass flux of gas and liquid, respectively. Liquid and gas velocities can be expressed as:

$$u_g = \frac{\dot{m}_g}{\rho_g A_g} = \frac{Gx}{\rho_g \alpha}, \tag{2.11}$$

$$u_l = \frac{\dot{m}_l}{\rho_l A_l} = \frac{G(1-x)}{\rho_l (1-\alpha)}, \tag{2.12}$$

where ρ is the density of the fluid and α is the superficial void fraction estimated regarding the smallest section in the tube bundle where the mixture is passing through.

The superficial void fraction is defined as the temporal mean of the ratio between the transverse section occupied by the gas phase and the total area of the section. In this way the superficial void fraction is given by:

$$\alpha = \langle \frac{A_g}{A} \rangle \tag{2.13}$$

Spatial and temporal mean values of void fraction will be equal only in especial circumstances, for example, in the case of stable and one-dimensional two-phase flow (COLLIER; THOME, 1994).

In addition to superficial void fraction, chordal void fraction, α_1, and volumetric void fraction, α_3, can be defined. They represent the temporal mean of the portion of a line and a volume, respectively, that is occupied by the gas phase. Furthermore, the local void fraction, α_0, can be defined as the time fraction that a point is occupied by the gas phase.

The phase mass velocities can be also expressed as

$$G_g = \rho_g j_g, \tag{2.14}$$

$$G_l = \rho_l j_l. \tag{2.15}$$

The superficial velocity of the mixture can be expressed as the sum of the superficial velocities of each phase

$$j = j_g + j_l. \tag{2.16}$$

Another important parameter for two-phase flow characterization is the volumetric quality defined as

$$\beta = \frac{Q_g}{Q_g + Q_l}. \tag{2.17}$$

Finally, by combining Eqs. 2.11 and 2.12, it can be obtained the slip ratio S, as the

ratio between the velocity of both phases

$$S = \frac{u_g}{u_l} = \left(\frac{x}{1-x}\right)\left(\frac{\rho_l}{\rho_g}\right)\left(\frac{1-\alpha}{\alpha}\right). \tag{2.18}$$

The concepts defined in this section are used throughout the present work in order to quantify the parameters of the two-phase flow and to serve as a reference to discuss the obtained results.

2.3 Flow patterns

The geometrical distribution of liquid and gas phases in the flow varies depending on parameters such as the velocity of each phase, void fraction and flow direction. Flows that present similar distributions characterize a flow pattern. Moreover, flow patterns are reviewed in the present study since they influence significantly the flow induced vibrations in tube bundles, not only through dynamic parameters, but also due to the different ways in which continuous and non-continuous flow patterns might excite the tubes (ÁLVAREZ-BRICEÑO et al., 2017). In this sense, methods capable of predicting the flow patterns that may take place in a tube bundle are required since early design stages of a heat exchanger.

Generally, the methods for flow pattern prediction have been developed based on experimental observations of flow topology in tube bundles, that is, flow patterns are subjectively identified. Further, the results of these studies are classified and presented as maps, in which the flow pattern transitions are demarcated.

Kanizawa (2014) presents a review on the basic definitions for the flow patterns reported in the literature (XU et al., 1998; GRANT; CHISHOLM, 1979). Moreover, Kanizawa (2014) presents a critical review on the flow pattern prediction methods proposed by Grant & Chisholm (1979), Pettigrew et al. (1989), Ulbrich & Mewes (1994), Xu et al. (1998), Taitel et al. (1980) and Venkasteswararao et al. (1982). Among these methods, only that proposed by Ulbrich & Mewes (1994) includes an objective identification technique, that is, it is based on the measurement of the variation of any two-phase flow parameter. Based on the comparison between these methods, Kanizawa (2014) concludes that, even if the methods tend to present qualitatively similar flow pattern transition criteria, there is no general method for two phase flow prediction since transition flow velocities found in literature present important differences from method to method. In this sense, the methods proposed in the mentioned bibliography are valid for experimental conditions and tube bundle configurations similar to those in which they were obtained.

Kanizawa & Ribatski (2016a) propose a method for flow pattern prediction based on the experimental results obtained in the same test section that will be used in the present

experimental study. Kanizawa & Ribatski (2016a) identified flow patterns subjectively by observing the two-phase flow across the tube bundle through lateral windows, technique that was also assisted by images and videos. Based on this approach, Kanizawa & Ribatski (2016a) define the following flow patterns:

- Bubbles: continuum liquid phase with gas bubbles smaller than tube spacing. This flow pattern was observed for reduced j_g and for the entire j_l range. There is no significant bubbles coalescence due to reduced gas flow rate, therefore the transition to intermittent flow pattern is absent. This flow pattern occurs due to the reduced gas injection rate, characterized by reduced j_g;

- Large bubbles: characterized by amorphous bubbles with dimensions larger than the tube spacing. This flow pattern was observed for reduced and intermediate j_l and for intermediate j_g. Due to the increment of j_g large bubbles are formed due to coalescence of small bubbles, and the limited turbulence intensity does not promote large bubbles disruption;

- Dispersed bubbles: characterized by high number of gas bubbles smaller than observed for bubble flow pattern. This flow pattern is only observed only for high j_l and intermediate j_g. With the increment of liquid velocity, the liquid turbulence disrupts large bubbles and inhibit coalescence. Therefore, there is no transition to large bubbles or non-continuous flow patterns even for intermediate gas velocities and void fractions;

- Churn: characterized by chaotic phases movement, with small portions of liquid moving up and down. This flow pattern is dominated by gravitational effects, and is verified for reduced and intermediate j_l, and for intermediate j_g. With the increment of bubbles size due to coalescence, the upper liquid portions do not present enough kinetic energy to maintain the upward movement and are not sustained by the gas bubble, therefore present downward movements during short periods. Then the fluids are propelled again by the flow in the upward direction;

- Intermittent: characterized by intermittent passage of liquid slugs and large gas portions, both at high velocity. It was observed for the entire j_l range and for high j_g; even though Kanizawa & Ribatski (2016a) highlighted that experiments for very high j_l and j_g were not performed due to these conditions induce excessive vibrations on the experimental facility and could lead to the test section damage. The high void fraction of the liquid phase precludes its flow as dispersed droplets or as liquid film along the tubes and shell wall, therefore it flows as pistons which are periodically propelled by the gas flow. This flow pattern is dominated by inertial effects;

- Annular: characterized by continuum liquid film over tube and shell walls, with gas flow in the core of the tube bundle. Entrained liquid droplets are also present. This flow is dominated by gas inertial effects and is observed for reduced j_l and high j_g.

Moreover, these flow patterns are depicted in Fig. 2.5.

Figure 2.5: *Schematics of two-phase flow patterns during upward flow across tube bundles (KANIZAWA; RIBATSKI, 2016a).*

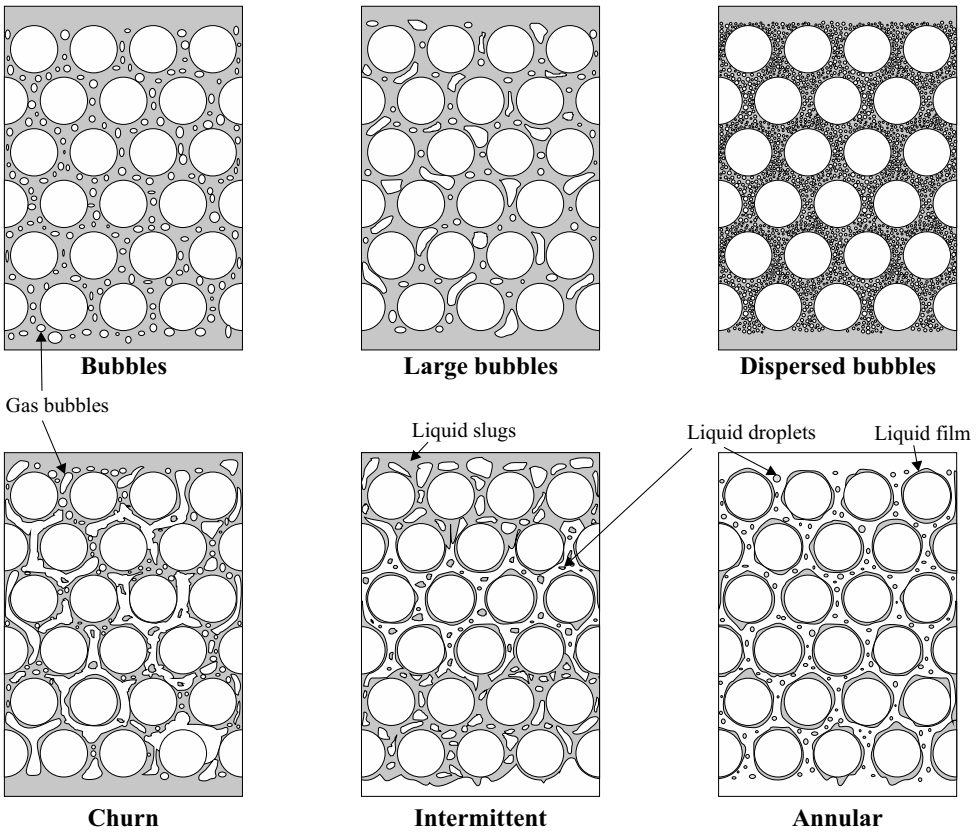

Furthermore, Kanizawa & Ribatski (2016a) performed an objective flow pattern identification based on the k-means clustering method, which is extensively described in Sempértegui-Tapia (2011) and MacQueen (1967). This method consists in clustering data so that the adopted characterization parameters present reduced deviation among the cluster elements. The clustering is done by using a reference point referred to as cluster centroid. Therefore, each data point corresponds to the closest centroid, in a Euclidian distance sense (KANIZAWA, 2014). This distance is defined based on the quantitative parameters used for the method application. In this manner, Kanizawa & Ribatski (2016a) used the signals from a fast response differential pressure transducer, which measures the pressure drop per tube row. Based on these signals, the quantitative parameters chosen for clustering the data were the mean, standard deviation, signal peak-to-valley amplitude and the kurtosis.

Since six distinct flow patterns were identified via subjective criteria, six distinct centroids were defined for objective approach and, therefore, six distinct data groups were obtained. Kanizawa & Ribatski (2016a) evaluated two different initial conditions for the six centroids, the first one assuming random initial values in the data base, and the second by using the previously classified data based on the subjective approach in order to define the centroids that correspond to each flow pattern. The data groups obtained for both sets of centroids initial values were similar. Therefore Kanizawa & Ribatski (2016a) concluded that the method is independent of the initial centroids.

Based on the data clustering generated in the objective approach, Kanizawa & Ribatski (2016a) define six flow patterns: Bubbles, Annular, Churn, Intermittent, Dispersed Bubbles and Harsh Intermittent. Further, Kanizawa & Ribatski (2016a) compared the results obtained via subjective and objective approaches by using a map with j_l and j_g input parameters as abscissa and ordinate coordinates, respectively. They realized that both Dispersed Bubbles and Churn flow patterns were identified in the same regions of the map, therefore it exists a mutual correlation between them.

Furthermore, Kanizawa & Ribatski (2016a) point out that no group was identified for conditions characteristic of Large Bubbles (defined according the subjective approach) through the objective approach, and this result can be attributed to the fact that this flow pattern corresponds to a transition between Bubbles and Churn. In addition, Kanizawa & Ribatski (2016a) note that Bubbles and Large Bubbles flow patterns present similar phases distributions and pressure drop signal, differing basically on the size of the bubbles. Furthermore, the objective approach divided the Intermittent pattern (subjectively identified) into Intermittent and Harsh Intermittent. According to Kanizawa (2014) the Harsh Intermittent pattern corresponds to a group of data whose differential pressure signals present higher amplitudes than in the Intermittent pattern case.

Finally, based on the results obtained by using subjective and objective approaches, and the flow pattern descriptions in literature, Kanizawa & Ribatski (2016a) defined a flow pattern predictive method. In this method, dispersed bubbles flow pattern was considered as bubble flow, and harsh intermittent was assumed as intermittent flow. The least square method was employed for determination of the transition criteria between flow patterns. Kanizawa & Ribatski (2016a) formulated the transition curves in terms of dimensionless parameters, that include fluids physical properties, and the geometrical characteristics of the tube bundle. The expressions each transition are detailed in the following paragraphs (ÁLVAREZ-BRICEÑO et al., 2018);

Transition to bubbles flow pattern For reduced liquid velocities, the transition from bubbles to churn flow patterns is dominated basically by the gas velocity, which can be represented in a non-dimensional form similar to the proposal presented by Wallis

(1969), as follows:

$$j_g^* = \frac{j_g}{\sqrt{gd\left(\rho_l - \rho_g\right)/\rho_g}}, \tag{2.19}$$

where g is the gravitational acceleration and d is the tube external diameter. This dimensionless parameter represents the ratio between liquid inertial and buoyancy forces.

With the increment of the liquid velocity, the flow turbulence promotes break up of large bubbles and inhibits the coalescence of small bubbles into large ones. In these conditions, the transition is dominated by liquid inertial effect, which is represented by the liquid Reynolds number given by:

$$Re_l = \frac{\rho_l j_l d}{\mu_l}, \tag{2.20}$$

where the liquid superficial velocity is also evaluated at the minimum cross section, and μ corresponds to the dynamic viscosity.

Both regions were combined according to Churchill (2000) method, and bubbles flow pattern is observed for gas velocities smaller than the estimative given by the following relationship:

$$j_g^* = \left\{\left[58\left(1-\tau\right)\right]^{-6} + \left[exp\left(Re_l/10000\right)/36\right]^6\right\}^{1/6}, \tag{2.21}$$

where τ is the transverse pitch-to-diameter ratio, $\tau = s_1/d$, and s_1 is the transverse pitch.

Transition to intermittent flow The churn flow pattern is dominated by gravitational and inertial effects, while the intermittent flow pattern is dominated mainly by inertial effects. In this context, the Froude number for the mixture is adopted to characterize the balance between inertial and gravitational effects, as follows:

$$Fr = \frac{G^2}{gd\left(\rho_l - \rho_g\right)^2}. \tag{2.22}$$

For reduced liquid velocities, the flow inertia is dominated by the gas flow, hence a transition is proposed based on the correlation of Fr and j_g^*. For higher liquid velocities, the liquid inertia starts to play a significant role, and a correlation is proposed based on the correlation of Fr, j_g^* and Re_l. By combining both transition criteria according to the Churchill's (CHURCHILL, 2000) approach, Kanizawa & Ribatski (2016a) obtained the following transition, according to which intermittent flow pattern is verified for gas superficial velocity higher than the value given as follows:

$$j_g^* = \left\{\left(\frac{Fr}{5460}\right)^{-1/2} + \left[\frac{54Fr}{\left(Re_l/1000\right)^{2.1}}\left(\frac{d}{d_0}\right)^{10/3}\right]^{-25.2}\right\}^{-1/6}, \tag{2.23}$$

where the reference diameter d_0 is 19.05 mm ($3/4$ inches).

Transition to annular flow The annular flow pattern is characterized by the flow dominated by the gas inertial effects. Therefore, the transition to annular flow pattern was correlated as follows:

$$j_g^* = \left[\frac{Re_l}{4466\,(\tau - 1)}\right]^{\frac{1}{5.4(\tau-1)}}, \tag{2.24}$$

and annular flow is observed for gas velocities higher than the velocity given by this equation.

Figure 2.6 depicts the flow patterns transitions according to the method proposed by Kanizawa & Ribatski (2016a). In this context, the flow pattern transition predictive method was compared with the results available in the open literature, including Ulbrich & Mewes (1994), Xu et al. (1998) and Noghrehkar et al. (1999), and showed good agreement, even considering significant differences in the tube bundle geometry and transition velocities.

Figure 2.6: *Flow pattern transitions according to Kanizawa & Ribatski (2016a) proposal.*

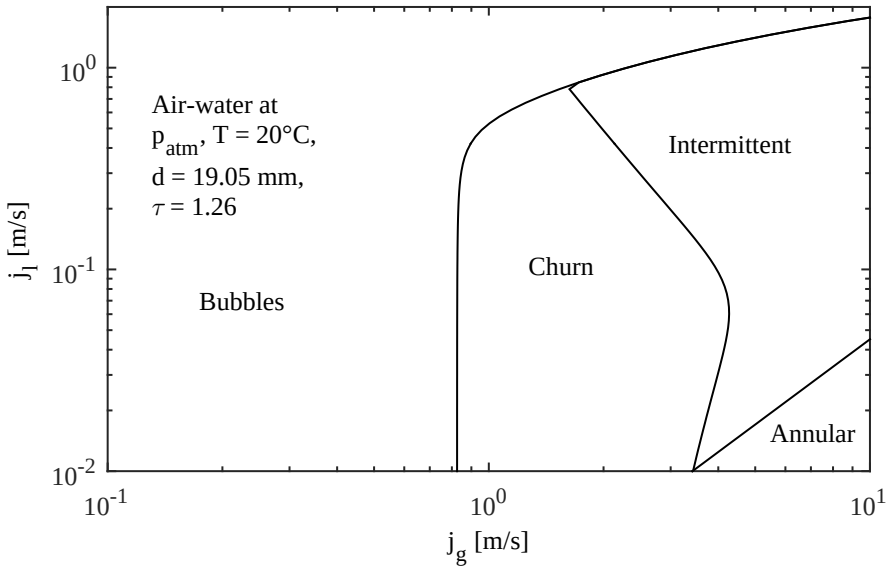

More recently, Mao & Hibiki (2017) proposed flow pattern transition criteria based on the drift flux model, which was introduced by Zuber & Findlay (1965). Mao and Hibiki proposed transitions for the following flow patterns: bubbly, cap bubbly, churn, finely dispersed bubbly and annular. That study will not be detailed since is beyond the scope of the present work, but it is recommended for those who would like an alternative approach for flow pattern characterization.

2.4 Two-phase flow modeling

The new mixture has properties, *e.g.* density, viscosity and velocity, certainly distinct from those of the phases that compose it. This fact makes that phenomena such as the FIV and pressure drop across the tube bundle do experiment variations if compared to phenomena in single-phase flow. Hence, prediction models for estimating these properties in two-phase flow have to reviewed in the present work.

As it can be noticed from equations defined in Section 2.2, it is necessary to previously define velocities and physical properties of the phases in order to define the two-phase flow parameters. In fact, by analyzing Eqs. 2.11 and 2.12, it can be seen that u_g and u_l depend on x and α, which in turn are interrelated. Moreover, the relationship between x and α is hard to be defined in a general manner. In this sense, there are some models in the literature to define this relationship, that, assuming a set of hypothesis, allow to solve the problem.

According to Collier & Thome (1994), the homogeneous model and the separated flow model are basic approaches that are widely used in the design of distinct engineering applications. The equipment that are designed via these approaches often operate under high pressure and temperature, which complicates the flow pattern identification and its variations across the tube bundle. In this sense, the equations of these models were developed so that mixture properties are independent of the flow patterns and, therefore, without the use of any flow pattern map as reference.

On the other hand, kinematic models can be theoretical or semi-empirical, allow to formulate the mixture properties and solve the problem of slip between phases without introducing any dynamic relationship. Kinematic models are important since they allow to formulate two-phase properties in a relative simple way thus avoiding to solve complex field equations.

There is another method to define the mixture properties; this is to use models, obtained experimentally, that relate x and α. The implementation of these models is complemented by the physical properties of the phases. In this manner, the two-phase flow velocity and pressure drop across the tube bundle can be estimated.

In the study of FIV under two-phase flow it is necessary to adopt a method capable of defining the flow properties so that the results from dynamic tests can be analyzed and discussed in terms of these properties. Based on the literature in the area, the homogeneous model is the most used. This is due to three main reasons: (i) parameters such as density and flow velocity are well defined in this model, (ii) its implementation is simpler and faster than other methods, and (iii) distinct from models in which relative velocity between phases is considered ($S \neq 1$), the homogeneous model has proved that its implementation leads to the best results on reducing and clustering dynamic parameters data. In fact, even being the two-phase flow that passes across tube bundles

in a heat exchanger hardly homogeneous, this is the model that presents the best results until now (TAYLOR; PETTIGREW, 2001).

Below, the formulation of the homogeneous model is introduced. Furthermore, the most important methods to estimate the void fraction (i.e. relationships between x and α) across a tube bank are presented. In this manner, the model that better represents the experimental data will be used for results discussion. It is important to mention that kinematic models such as that proposed by Bankoff and the slip model (ZUBER; FINDLAY, 1965; WALLIS, 1969; ISHII, 1975; ISHII, 1977) are not detailed in the present work since the interpretation of results based on these models did not lead to conclusions in literature. Moreover, only the necessary expressions for the formulation in void fraction models are presented.

2.4.1 Homogeneous model

It is the simplest model. Basically, this model proposes that the two-phase mixture behaves as a pseudo-fluid with average properties between the phases that compose it. This model is based on the following hypothesis: (i) phase velocities are equal and uniform in the duct section, (ii) the phases are in thermodynamic equilibrium [1] and (iii) the two-phase flow pressure drop is defined by using a friction factor model as in the case of single-phase flow. In this manner, the first hypothesis can be formulated as

$$u_g = u_l = \bar{u}, \tag{2.25}$$

where $\bar{u}$ denotes the velocity of the homogeneous flow. From Eq. 2.18, it can be seen that the homogeneous model is characterized by $S = 1$. Further, by replacing Eqs. 2.25, 2.11 and 2.12 in 2.17 it can be noticed that the volumetric quality is equal to the superficial void fraction ($\alpha = \beta$) in the homogeneous model even though this is not experimentally evidenced. In this way, the relationship between α and x can be obtained from Eq. 2.18 as follows

$$\alpha_H = \beta = \frac{1}{1 + \frac{\rho_g}{\rho_l}\frac{1-x}{x}}, \tag{2.26}$$

where the superficial void fraction that is estimated by assuming homogeneous model simplifications is denoted by α_H. According to Collier & Thome (1994), it is expected that the adopted simplifications allow estimate the two-phase flow parameters in a relative good manner, especially for bubbles and annular with dispersed bubbles flow patterns in ducts. However, engineers often use the homogeneous model indiscriminately in problems in which other flow patterns are expected.

In two-phase flow formulation, it is a common practice to represent the mixture

[1] A system is said to be in thermodynamic equilibrium if it maintains thermal, mechanical, phase and chemical equilibrium (CENGEL; BOLES, 2006).

density and viscosity as a function of each phase properties. Therefore, the mixture density, $\bar{\rho}$, is defined as

$$\bar{\rho} = \alpha\rho_g + (1-\alpha)\rho_l, \tag{2.27}$$

which also maintains the relationship with the mixture specific volume $\bar{v}$

$$\bar{v} = \frac{1}{\bar{\rho}}. \tag{2.28}$$

In some cases, the average velocity of the two-phase flow, u_{mb}, is used as reference, it is defined as

$$u_{mb} = \frac{G}{\bar{\rho}} = \frac{\rho_l u_l\,(1-\alpha) + \rho_g u_g \alpha}{\bar{\rho}}. \tag{2.29}$$

Regarding the mixture viscosity, there are some correlations that can be used to estimate this parameter, most of them result of experimental data. The type of relationship between $\bar{\mu}$ and x must be chosen so that it respects the limit values, that is:

$$x = 0, \bar{\mu} = \mu_l; \quad x = 1, \bar{\mu} = \mu_g. \tag{2.30}$$

In this manner, Collier & Thome (1994) collected the following expressions:

$$\frac{1}{\bar{\mu}} = \frac{x}{\mu_g} + \frac{(1-x)}{\mu_l}, \tag{2.31}$$

proposed by McAdams (1942),

$$\bar{\mu} = x\mu_g + (1-x)\mu_l, \tag{2.32}$$

proposed by Cicchitti et al. (1960), and

$$\bar{\mu} = \bar{\rho}\left[x v_g \mu_g + (1-x) v_l \mu_l\right] \tag{2.33}$$

defined by Dukler et al. (1964).

2.4.2 Drift flux model

The *Drift flux model* was developed and introduced by Zuber & Findlay (1965), Wallis (1969), Ishii (1975), Ishii (1977) and their collaborators. Its most important contribution is that it considers the slip between liquid and gas phases in the mixture. This model is completely developed in Wallis (1969), thus only their final expressions are presented in this document. By using the definitions for superficial velocity, Eqs. 2.9 and 2.10, the

relative velocity between the phases, u_{gl}, can be defined as:

$$u_{gl} = (u_g - u_l) = \frac{j_g}{\alpha} - \frac{j_l}{(1-\alpha)}, \tag{2.34}$$

and the slip flux, j_{gl}, is given by

$$j_{gl} = u_{gl}\alpha(1-\alpha) = j_g(1-\alpha) - j_l\alpha = j_g - \alpha j. \tag{2.35}$$

In a physical context, the slip flux represents the volumetric rate of gas phase that passes forwards (in upwards flow) or downwards (in downwards flow) through a cross section of the duct in which the mixture is flowing with superficial velocity j. In order to preserve the continuity law, a slip flux of liquid, j_{lg}, equal in magnitude and opposite in direction, must pass through the same cross section. Thus, reorganizing Eq. 2.35 it can be obtained

$$j_g = \alpha j + j_{gl}. \tag{2.36}$$

This relationship is valid for one-dimensional flow (i.e. any other point of the flow in the cross section of the duct). Therefore, the flow properties can be adopted equal to the spatial average in the cross section by using the symbol $\langle\rangle$. In this manner, Eq. 2.35 can be defined as:

$$\langle j_g \rangle = \langle \alpha j \rangle + \langle j_{gl} \rangle, \tag{2.37}$$

and dividing by $\langle \alpha \rangle$ it is obtained that

$$\frac{\langle j_g \rangle}{\langle \alpha \rangle} = \langle u_g \rangle = \frac{\langle \alpha j \rangle}{\langle \alpha \rangle} + \frac{\langle j_{gl} \rangle}{\langle \alpha \rangle}, \tag{2.38}$$

where the phases parameter distribution, C_0, can be defined as:

$$C_0 = \frac{\langle \alpha j \rangle}{\langle \alpha \rangle \langle j \rangle}. \tag{2.39}$$

Furthermore, the phases slip parameter, u_{gj}, that corresponds to the difference between the gas phase velocity and the superficial velocity of the mixture is given by

$$u_{gj} = \frac{\langle j_{gl} \rangle}{\langle \alpha \rangle}. \tag{2.40}$$

In this manner, by substituting Eqs. 2.39 and 2.40 in Eq. 2.38, and dividing the result by $\{j\}$ it is obtained

$$\frac{\langle u_g \rangle}{\langle j \rangle} = \frac{\beta}{\langle \alpha \rangle} = C_0 + \frac{u_{gj}}{\langle j \rangle}, \tag{2.41}$$

or

$$\alpha = \frac{\beta}{C_0 + \frac{u_{gj}}{\langle j \rangle}} = \frac{j_g}{C_0 j + u_{gj}}, \tag{2.42}$$

where, based on the void fraction definition adopted in section 2.2, $\langle \alpha \rangle = \alpha$.

As it can be noticed from Eq. 2.42, for cases in which both phases present equal velocity ($S = 1$; $u_{gj} = 0$), it can be obtained that $\alpha = \beta / C_0$. Moreover, in section 2.3.1 it was defined that, for a one-dimensional homogeneous flow $\alpha = \beta$. Therefore, it can be seen that C_0 represents an empirical parameter devoted to correct the velocity profiles and the gas phase concentration in the mixture, which are predicted as constant by the homogeneous model, however they certainly vary across the duct section.

According to Ishii (1977), the drift flux model can be implemented based on the identified flow patterns. In this case, the values of C_0 and j_{gl} are reported in bibliography in format of plots of j_g/α as function of j for each flow pattern. Based on Collier & Thome (1994), C_0 and j_{gl} can be well correlated without reference of any flow pattern map for water-steam mixtures (high pressure systems) by using the following expressions,

$$C_0 = 1.13, \quad u_{gj} = 1.41 \left[\frac{\sigma g (\rho_l - \rho_g)}{\rho_l^2} \right]^{1/4}. \tag{2.43}$$

The drift flux model plays an important role when the slip velocity is significant compared with total superficial velocity. Collier & Thome (1994) propose that the drift flux model must be used if $u_{gj} > 0.05 j$, which, according them, limits the model usage to bubbles, slug and churn flow patterns.

In the case of bubbles flow pattern, by assuming upwards one-dimensional flow with small entrained bubbles and low coalescence ($\alpha < 0.2$), Wallis (1969) propose the following expressions for parameters in Eq. 2.42:

$$C_0 = 1.0, \quad u_{gj} = 1.53 \left(1 - \alpha\right)^2 \left[\frac{\sigma g (\rho_l - \rho_g)}{\rho_l^2} \right]^{1/4}. \tag{2.44}$$

Alternative values for constant 1.53 in Eq. 2.44 are 1.18 (WALLIS, 1969) and 1.41 (ZUBER et al., 1967) *apud* (COLLIER; THOME, 1994).

For upwards flow in the transition region between bubbles and slug flow patterns (referred to as churn - turbulent by Zuber et al. (1967)), the recommended value for u_{gj} is given by

$$u_{gj} = 1.41 \left[\frac{\sigma g (\rho_l - \rho_g)}{\rho_l^2} \right]^{1/4}. \tag{2.45}$$

For slug flow patterns during upwards totally developed flow ($[j D \rho_l / \mu_l]$ >8000),

the following values can be used for parameters in Eq. 2.42 (COLLIER; THOME, 1994):

$$C_0 = 1.2, \quad u_{gj} = 0.35 \left[\frac{g(\rho_l - \rho_g)d}{\rho_l} \right]^{1/2}, \tag{2.46}$$

where the expression for u_{gj} represents the bubble rise velocity in a stagnant liquid in which case the inertial forces are dominant.

2.4.3 Methods for void fraction estimation

Kanizawa (2014) presents a thorough review on the methods for void fraction estimation in tube banks. Among them, the correlations based on results obtained under two-phase upwards crossflow are presented below.

Schrage et al. (1988)

Schrage et al. (1988) performed tests by using air - water mixture across a bank of 7.94 mm outside diameter tubes in normal square configuration with $\tau = 1.08$ and 1.4. The void fraction was obtained experimentally via quick-closing valve measurement technique. In this sense, the results correspond to the volumetric void fraction α_3. This method is based on the definition of a multiplier for the homogeneous void fraction given by

$$\frac{\alpha_3}{\alpha_H} = 1 + 0.123 Fr_{L0}^{-0.191} \ln x, \tag{2.47}$$

where the parameter Fr_{L0} is the Froude number that corresponds to the mixture flowing as a liquid, equal to $Fr_{L0} = G/\rho_l\sqrt{gd}$, in which G is based on the minor cross section relative to flow velocity and α_H is calculated by using Eq. 2.26. The authors verified that the minimum value of α_3/α_H ratio is equal to 0.1. Therefore, for conditions that Eq. 2.47 results in values lower than 0.1, it is adopted that α_3/α_H is equal to 0.1.

Dowlati et al. (1990)

Dowlati et al. (1990) performed analytic and experimental studies on an air - water upwards crossflow in a bank of 12.7 and 19 mm outside diameter tubes in normal square ($\tau = 1.3$) and ($\tau = 1.75$) normal triangular configurations. The superficial void fraction was measured by using gamma ray densitometry. Void fraction estimation is given by

$$\alpha = 1 - \frac{1}{\sqrt{1 + C_1 j_g^* + C_2 j_g^{*2}}}, \tag{2.48}$$

where the gas non-dimensional superficial velocity, j_g^*, is defined as the ratio between the momentum of gas phase and the buoyancy effect in the mixture according to Wallis

(1969):

$$j_g^* = \frac{Gx}{[d_h g \rho_g (\rho_l - \rho_g)]^{1/2}} \tag{2.49}$$

and the hydraulic diameter, d_h, is formulated as:

$$d_h = \frac{4s_1^2 - \pi d^2/4}{\pi d} \tag{2.50}$$

Dowlati et al. (1990) fitted the correlation parameters for the experimental data obtained in their test section, hence $C_1 = 35$ and $C_2 = 1$. For conditions in which j_g^* is greater or equal to 0.2, the authors recommend $C_2 = 30$.

Furthermore, Kanizawa (2014) points out that Eq. 2.48 predict void fractions less than unity for vapor quality equal to 1, i.e. gas single-phase flow, which indicates that the method is not appropriate for mixtures with high vapor quality.

Dowlati et al. (1992), Delenne et al. (1997)

The models proposed by Dowlati et al. (1992) and Delenne et al. (1997) are based on the *Drift Flux Model* introduced in section 2.4.2. Dowlati et al. (1992) adjusted values of C_0 and u_{gj} based on experimental results obtained via gamma densitometry in tube banks with normal square and normal triangular configurations. The obtained values for C_0 and u_{gj} are 1.1035 and 0.33 m/s, respectively. Different from that reported by Zuber & Findlay (1965), Dowlati et al. (1992) did not found flow pattern effects on phase distribution parameter and slip between phases.

On the other hand, Delenne et al. (1997) *apud* Feenstra et al. (2000) adjusted the parameter C_0 according to their own results, they propose $C_0 = 0.9$. Furthermore, the authors adopted a slip parameter given by the bubble rise velocity in stagnant liquid infinite medium. Therefore, the parameter u_{gj} is defined as in Zuber & Findlay (1965):

$$u_{gj} = 1.53 \left[\frac{\sigma g (\rho_l - \rho_g)}{\rho_l^2} \right]^{1/4} \tag{2.51}$$

Xu et al. (1998)

Xu et al. (1998) performed analytic and experimental studies on air - water crossflow in a bank of 9.79 mm outside diameter tubes in normal square configuration with $\tau = 1.25$. The void fraction was determined experimentally via quick-closing valve measurement technique by separating each flow pass in the shell-side of the heat exchanger mockup. Therefore, the experimental results correspond to measurements of the volumetric void fraction.

The method proposed by Xu et al. (1998) formulates the void fraction as a function

of the modified Lockhart - Martinelli parameter, given by

$$\alpha_3 = \left(1 + \frac{1}{C_1 Fr_{L0}^{C_2} X_{tt}^{-C_3}}\right)^{-1}, \tag{2.52}$$

where the Lockhart - Martinelli parameter, X_{tt}, is given by:

$$X_{tt} = \left(\frac{1-x}{x}\right)^{0.9} \left(\frac{\rho_g}{\rho_l}\right)^{0.5} \left(\frac{\mu_l}{\mu_g}\right)^{0.1} \tag{2.53}$$

Xu et al. (1998) fit the empirical constants in Eq. 2.52 based on their own experimental data and those reported by Schrage et al. (1988) and Dowlati et al. (1990) for upwards crossflow. This process resulted in the following values: $C_1 = 7.27$; $C_2 = 0.349$ and $C_3 = 0.948$.

Feenstra et al. (2000)

Feenstra et al. (2000) performed analytic and experimental studies on the estimation of superficial void fraction in halogen refrigerant flow across tube banks. They preferred halogen refrigerants rather than air - water mixture since there are two-phase phenomena that can be better observed in the former type of substances. According to Feenstra et al. (2000) and Khushnood et al. (2004), this is because the physical properties of two phases (liquid and vapor) of the same substance, in this case a refrigerant, present similar proportion to that found in the water - steam system. However, Kanizawa (2014) discuss this criterion showing that, even if the gas - liquid density ratio of water and refrigerants be in the same order, the gas - liquid ratios of other properties (viscosity, surface tension) disagree, thus this reasoning does not justify the choice of refrigerants.

Feenstra et al. (2000) carried out their experimental campaign in banks of 6.35 mm and 6.17 mm outside diameter tubes with τ equal to 1.44 and 1.48, respectively, for mass velocities up to 500 kg/m^{2}s and mass qualities up to 10% in upwards flow. Besides their own results, this superficial void fraction prediction method is also based on the results reported by Dowlati et al. (1990) and Dowlati et al. (1992) for air - water mixtures.

In this method, Feenstra et al. (2000) propose a correlation for the phases slip ratio. In this manner, S is formulated as

$$S = 1 + 25.7 \frac{\sqrt{Ri \cdot Cap}}{\tau}, \tag{2.54}$$

where Ri is the Richardson number that corresponds to the ratio between buoyancy and inertial effects,

$$Ri = \frac{(\rho_l - \rho_g)^2 g (s_1 - d)}{G^2}, \tag{2.55}$$

and Cap is the Capillary number that corresponds to ratio between viscous forces and

surface tension that acts across an interface between a liquid and a gas

$$Cap = \frac{\mu_l u_g}{\sigma}. \tag{2.56}$$

The superficial void fraction estimations through this method require of iterative solution of Eqs. 2.54, 2.55 and 2.18.

Kanizawa & Ribatski (2017)

Kanizawa & Ribatski (2017b) performed analytic and experimental studies in order to estimate the void fraction in the same test section that will be used in the present work, that is, air-water upwards crossflow in a bank of 19.05 mm outside diameter tubes mounted in normal triangular configuration with $\tau = 1.26$.

Based on the experimental results obtained via capacitive sensing of void fraction, Kanizawa & Ribatski (2017b) presented a formulation based on the minimum kinetic energy principle:

$$\alpha = \left[1 + \left(\frac{K_l}{K_g}\right)^{1/3} \left(\frac{\rho_g}{\rho_l}\right)^{1/3} \left(\frac{1-x}{x}\right)^{2/3}\right]^{-1} \tag{2.57}$$

The moment coefficient ratio, $(K_l/K_g)^{1/3}$, is proposed as a function of the transport phenomena and operational parameters as mass velocity, mass quality, viscosity, density and surface tension (KANIZAWA, 2014):

$$\left(\frac{K_l}{K_g}\right)^{1/3} = \left[\left(\frac{87.7}{We^{1.33}} \left(\frac{Re_l}{10000}\right)^{2.24} \frac{1}{1+(Re_l/6500)^4}\right)^n + \left(\frac{0.26}{Re_l^{0.75} x^{0.92}}\right)^n\right]^{1/n} \tag{2.58}$$

with $n = 2$, fitted to experimental data. The liquid Reynolds number, Re_l, based on the tube external diameter is given as follows:

$$Re_l = \frac{\rho_l j_l d}{\mu_l}, \tag{2.59}$$

and We is the Weber number of the mixture

$$We = \frac{G^2 d}{(\rho_l - \rho_g)\,\sigma}, \tag{2.60}$$

where σ is the surface tension.

Comparison between methods

In this section, the methods for void fraction prediction are compared. For this, the variation of void fraction with mass quality is analyzed for $G = 50$, 100 and 1000 kg/m^{2}s, in Figs. 2.7, 2.8 and 2.9, respectively. In general, it can be seen that all the methods

predict that void fraction increases with increasing mass quality, which is a behavior that has been verified in laboratory experiences. Moreover, it can be seen that void fraction variation with mass quality is more pronounced for higher mass velocities.

Figure 2.7: *Comparison between void fraction prediction methods for air-water mixtures, across bank of d =19 mm outside diameter tubes, s_1 =24 mm, p =95kPa, T =25C e G =50 kg/m^{2}s.*

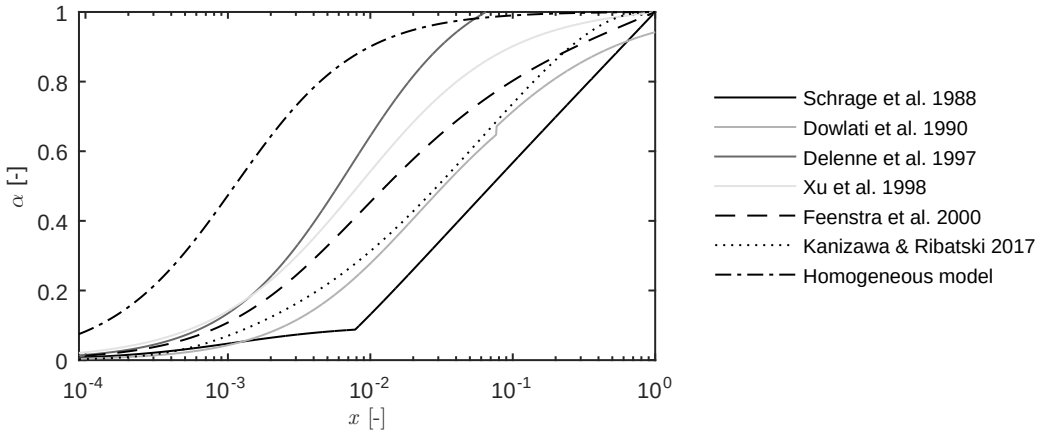

Figure 2.8: *Comparison between void fraction prediction methods for air-water mixtures, across bank of d =19 mm outside diameter tubes, s_1 =24 mm, p =95kPa, T =25C e G =100 kg/m^{2}s.*

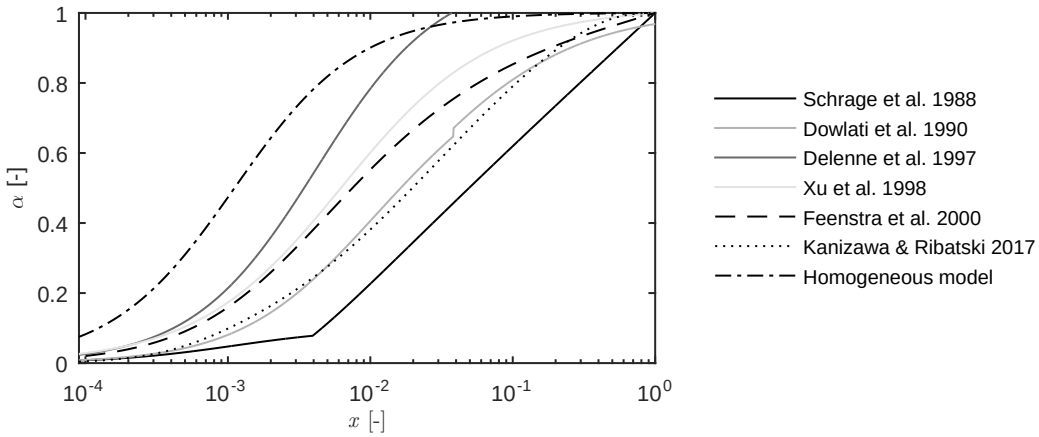

Although the compared models present the same tendency, it can be noticed that models differ for the same experimental condition. This can be related to the fact that these models were proposed based on experimental data obtained in distinct test sections. Furthermore, it is worth mentioning that models, such as those proposed by Schrage et al. (1988) and Xu et al. (1998), are based on volumetric void fraction rather than superficial void fraction as is the case of the other models. Anyway, the variation tendency of volumetric void fraction with mass quality is similar to that found for superficial void fraction.

Figure 2.9: *Comparison between void fraction prediction methods for air-water mixtures, across bank of d =19 mm outside diameter tubes, s_1 =24 mm, p =95kPa, T =25C e G =1000 kg/m^{2}s.*

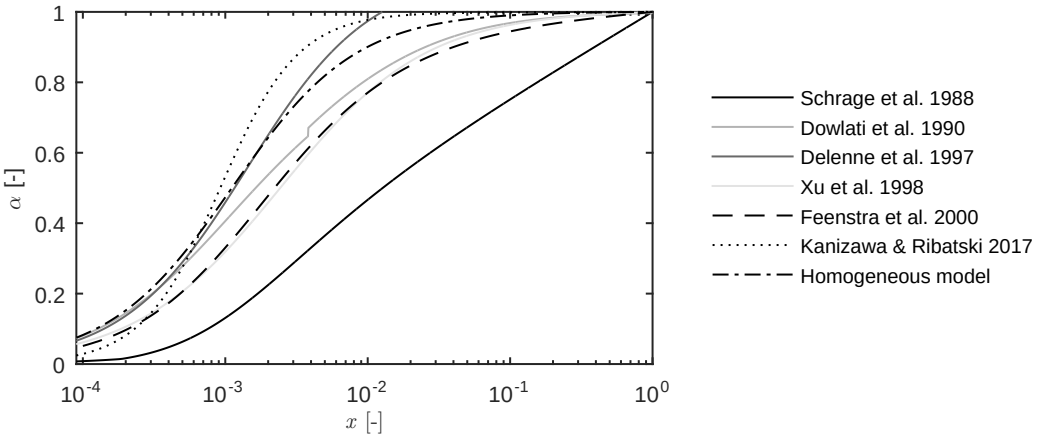

It can be noticed that the methods proposed by Dowlati et al. (1990) and Delenne et al. (1997), both of them based on the *Drift flux model*, fail to follow the condition of $\alpha = 1$ for single - phase gas flow. Therefore, it can be concluded that these methods are not appropriated for high mass quality. In addition, it can be seen that the model proposed by Dowlati et al. (1990) presents a discontinuity at $x = 4 \times 10^{-3}$, which is related to the characteristics of the function that recommends distinct correlation parameters depending on j_g^*.

The model presented by Schrage et al. (1988), if compared to all the other, predicts lower void fractions for the analyzed mass velocities. According to Kanizawa (2014), this is related to the fact that this method was developed from a database that include results with high mass quality values ($3 \times 10^{-4} < x < 0.64$). Following this reasoning, the void fraction predictions obtained from the model on Xu et al. (1998) ($3 \times 10^{-7} < x < 0.67$) should present the same characteristics, however as it can be seen from Figs. 2.7, 2.8 and 2.9, the differences are not so pronounced as those checked for the model proposed by Schrage et al. (1988).

In general, it can be seen that the homogeneous model overestimates void fraction for $G = 50$ and $G = 100$ kg/m^{2}s. This is due to homogeneous model neglect the slip between phases. However, for $G = 1000$ kg/m^{2}s under the experimental conditions detailed in Fig. 2.9, the model presented by Kanizawa & Ribatski (2017b) predicts void fractions even higher than those estimated through the homogeneous model. Further, it must be highlighted that the model of Kanizawa & Ribatski (2017b) is based on experimental data and it depends on mass velocity, while homogeneous model is completely theoretical and, as it can seen from Figs. 2.7 - 2.9, do not dependent on mass velocity.

Different from the model proposed by Kanizawa & Ribatski (2017b), the models

proposed by Schrage et al. (1988) and Xu et al. (1998) are relatively insensitive to mass velocity. Kanizawa (2014) discuss this behavior and explains that the methods based on database obtained from tube banks in normal square configuration present low influence of mass velocity if compared to the methods developed by Dowlati et al. (1990), Dowlati et al. (1992) and Feenstra et al. (2000), which were obtained from tube banks in triangular configuration. In this manner, Kanizawa (2014) concludes that, in general, higher mass velocity lead to a more pronounced void fraction increase for flow patterns across tube banks in triangular configuration if compared to tube banks in normal square configuration.

2.5 Concluding remarks on two-phase flow parameters

In this section, the main parameters that characterize a gas - liquid crossflow were introduced. These concepts will be used in further chapters. For example, geometrical parameters are key to formulate the confinement effect in tube bundles, which plays an important role in hydrodynamic mass and damping. Furthermore, the general parameters defined in Section 2.2 and the two-phase flow models in Section 2.4 are necessary to estimate the gap flow velocity and the local void fraction in the tube bundle, which seem to govern system's dynamic properties and vibration intensity. Although several methods for void fraction estimation were reviewed, not all of them will be used in the literature review and results analysis. For instance, the models proposed by Dowlati et al. (1990) and Delenne et al. (1997) are not considered in further discussions since they fail to follow the condition of $\alpha = 1$ for single - phase gas flow. Finally, it is worth mentioning that only the homogeneous model and the model proposed by Kanizawa & Ribatski (2017b) will be used to estimate the void fraction for results discussion in Chapter 6. This is because the homogeneous model is widely used in literature due to its simplicity and the model proposed by Kanizawa & Ribatski (2017b) was developed based on data obtained in the present test section.

Chapter 3

Flow-induced vibration in two-phase crossflow in tube bundles

In this chapter, the concepts regarding the tube vibration due to two-phase upwards crossflow are reviewed. In order to do that, the definitions about the dynamic parameters of the system, which comprises the tube and the surrounding flow, are introduced. The models used in the literature to estimate these dynamic parameters are reviewed. Further, the main characteristics of the most important vibration mechanisms in heat exchanger tube banks due to crossflow are defined. Among these mechanisms, the turbulence buffeting is analyzed in detail, since it corresponds to the condition that will be reproduced in the present test section. This chapter is mainly based on work published by the author at the Encyclopedia of Two-Phase Heat Transfer and Flow III (ÁLVAREZ-BRICEÑO et al., 2018).

3.1 Dynamic parameters

The dynamic response of any mechanical system, including a vibrating tube in a heat exchanger, depends on its inertia, stiffness and energy dissipation mechanisms (damping), which are referred to as the dynamic parameters and are depicted in a typical mechanical system scheme in Fig. 3.1. For instance, these parameters define the resonance frequency of the system, which is key to understand, estimate and formulate any crossflow induced vibration mechanism. The system's effective damping and inertia measured during two-phase flow are quite different from those measured in gas or liquid single-phase flows. Furthermore, these parameters are known to depend on fluid properties as well as on the component geometry and adjacent boundaries, whether rigid or elastic (KHUSHNOOD et al., 2012). In the sections below, the natural frequency of heat exchanger tubes, hydrodynamic mass and damping ratio are defined according to the literature. Also, the available methods to estimate these parameters are reviewed.

Figure 3.1: *One degree of freedom, viscously damped model, according to Blevins (2001).*

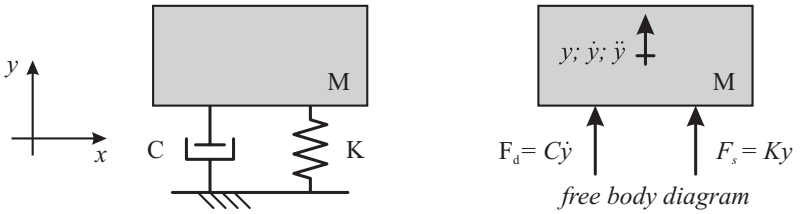

3.1.1 Natural frequency and vibration mode shape

In FIV design of heat exchanger tube bundles, resonant conditions can be avoided by ensuring separation of resonance frequencies of the tubes and exciting frequencies Shin & Wambsganss (1977). However, even at atmospheric conditions, this is a complex task, since most heat exchangers have multiple baffle supports, non-uniform unsupported spans and U-bend sections. Additionally, the number of the individual spans and the shell side crossflow velocities varies from one device to another. Nowadays, most of the heat exchanger manufacturers estimate natural frequencies by using software in which the finite element method has already been implemented. In case of lack of this kind of software, the natural frequencies can be obtained from formulas which has been developed based on the Euler - Bernoulli beam theory. Generally, these formulas are tabulated in manufacturer's references (TEMA Standards, 1999), encyclopedias (ÁLVAREZ-BRICEÑO et al., 2018) or books (LEE, 1971; SINGH; SOLER, 1984) for further details. The input data for these tables are the boundary conditions of the tube, if it is simply supported (on a baffle) or clamped (in a stationary tubesheet), if it comprises several spans (multispan) or a single span, etc.

On the other hand, for tubes mounted in sections for research purposes, the natural frequency may be easier to be obtained. For instance, it can be extracted from measured frequency response functions or simulation via finite element method. If these options are not available, one can use the tables mentioned above.

3.1.2 Hydrodynamic mass

For a submerged vibrating structure, hydrodynamic mass (sometimes called as added mass or virtual mass) is defined as the equivalent mass of external fluid (shell-side flow) vibrating with the structure (PETTIGREW; TAYLOR, 1994), in this case, a tube. This effect can be checked experimentally since it increases the apparent inertia of the vibrating tube, but the stiffness remains the same, hence modifying the resonance frequency of the tube and its dynamic behavior.

Based on experimental results obtained from tests performed for an only tube subjected to axial two-phase flow, Carlucci & Brown (1983) deduced experimentally the hydrodynamic mass per unit length of the cylinders in terms of the resonance frequency

of the cylinder within the two-phase mixture, f, as follows:

$$m_h = m_t \left[\left(\frac{f_g}{f} \right)^2 - 1 \right], \tag{3.1}$$

where m_h is the hydrodynamic mass per unit length, m_t is the mass of the tube alone per unit length and f_g is the resonance frequency of the tube in air. Since m_t and f_g are constant, one can understand the variation of m_h in terms of the variation of f, depending on the flow characteristics.

On the other hand, the hydrodynamic mass per unit length of a tube vibrating in a tube bundle and subjected to a fluid flow can be predicted by using the theoretical model presented by Rogers et al. (1984), as follows:

$$m_h = \left(\frac{\rho \pi d^2}{4} \right) \left[\frac{(D_e/d)^2 + 1}{(D_e/d)^2 - 1} \right], \tag{3.2}$$

where d is the tube outside diameter and ρ is the fluid density. The term (D_e/d) represents the effect of confinement, which is formulated by,

$$\frac{D_e}{d} = \left(0.96 + 0.5 \frac{s_1}{d} \right) \frac{s_1}{d}, \tag{3.3}$$

for a tube inside a triangular tube bundle Rogers et al. (1984). Similarly, for a square tube bundle, Pettigrew & Taylor (1994) found that,

$$\frac{D_e}{d} = \left(1.07 + 0.56 \frac{s_1}{d} \right) \frac{s_1}{d}, \tag{3.4}$$

is a reasonable approximation. In Eqs. 3.3 and 3.4, the available space between the tubes in the tube bundle is quantified by the transverse pitch-to-diameter ratio τ given by Eq. 2.1. Thus, larger values of τ indicate larger space to flow passage.

The Rogers' model (Eq. 3.2) for m_h can be extrapolated for the two-phase flow case by using the average density of the mixture given by Eq. 2.27, which is a function of void fraction. In this manner, it can be expected that hydrodynamic mass presents a decreasing tendency with increasing void fraction. In fact, hydrodynamic mass presents a linear decreasing behavior with increasing void fraction when estimated according the homogeneous model. Moreover, it is worth mentioning that, according to the open literature (CARLUCCI; BROWN, 1983; PETTIGREW et al., 1989), the homogeneous model is probably the most widely used in practical applications since its implementation is easier and faster than other methods. This is because of the premises in which the homogeneous model is based, which are described in section 2.4.1. Besides homogeneous

model, hydrodynamic mass can be estimated by implementing other void fraction models with the mixture average density in Eq. 2.27. Figure 3.2 shows hydrodynamic mass predictions based on distinct void fraction models and compared to that obtained through homogeneous model. The models proposed by Dowlati et al. (1990) and Delenne et al. (1997) were not considered since, as detailed in section 2.4.3, these methods fail to predict $\alpha = 100\%$ for single-phase gas flow.

Figure 3.2: *Hydrodynamic mass predicted for air - water crossflow ($P = 95$ kPa, $T = 25°C$, for distinct G [kg/m^{2}s]) across a normal triangular tube bundle ($\tau = 1.26$, $d = 19$ mm) by using distinct void fraction models: m_h1 - Schrage et al. (1988), m_h2 - Xu et al. (1998), m_h3 - Feenstra et al. (2000) and m_h4 - Kanizawa & Ribatski (2017b).*

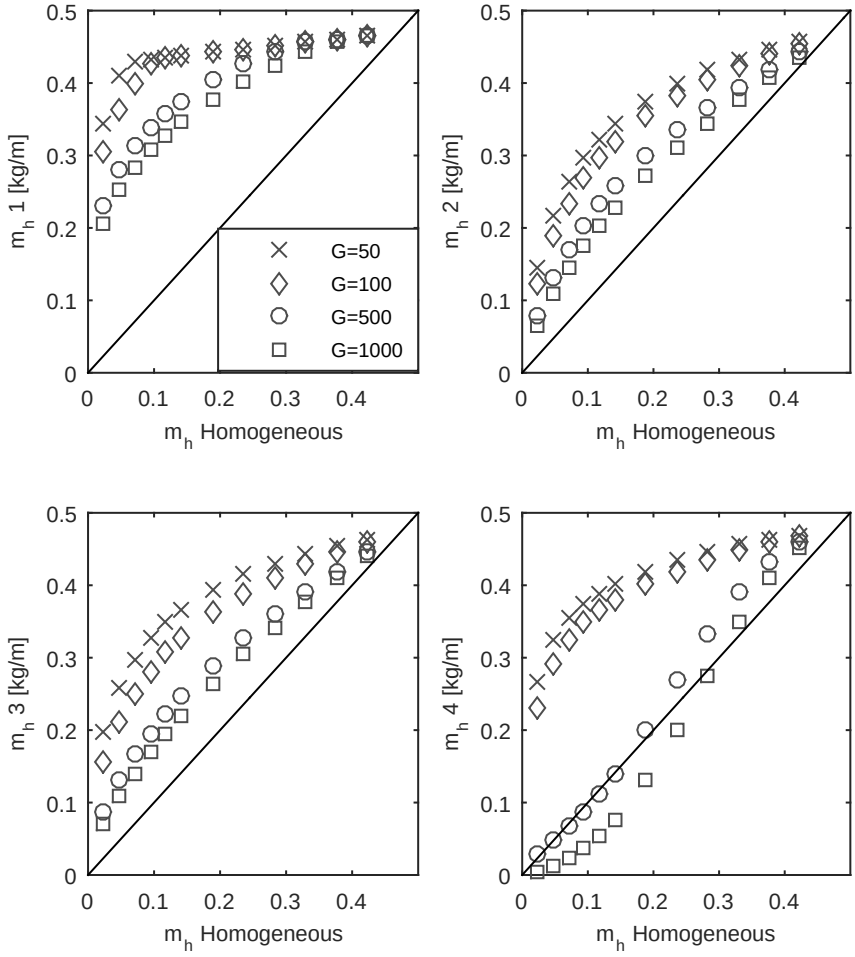

As it can be seen, in general, all the implemented models predict m_h values higher than those predicted by homogeneous model. This is because the homogeneous model overpredict the actual void fraction, which is inversely related to hydrodynamic mass. Furthermore, it can be noticed that the predicted hydrodynamic mass varies with increasing mass velocity, it tends to be lower with increasing mass velocity. This is directly related to the fact that, as a general behavior, the void fraction increases with

increasing mass quality and mass velocity, except the homogeneous model, according to which the void fraction is independent of the mass velocity (KANIZAWA; RIBATSKI, 2017b).

A new discussion of hydrodynamic mass behavior can be proposed based on the analysis of the basic dynamic model of a structure subjected to crossflow. According to Païdoussis et al. (2011), the flow forcing terms (initially modeled as terms that depend on tube displacement, velocity or acceleration) can be rendered as factors that modify the dynamic parameters of the system. Based on this argument, Païdoussis et al. (2011) suggest that parallel and transverse forces impinged on the tube may disturb added mass measurements. Based on literature for a single cylinder in liquid crossflow (CHEN, 1987), as well as in gas crossflow (BABAN et al., 1989), it is known that transverse forces are higher than parallel forces. Furthermore, according to experimental results on tube response reported in Pettigrew et al. (1989) and Axisa et al. (1990), unsteady transverse forces are higher than parallel forces also in tube bundles. However, despite one can speculate a direct relationship between unsteady transverse/parallel forces and hydrodynamic mass, the results presented in Pettigrew et al. (1989) show very similar values for hydrodynamic mass in both directions. Therefore, this fact hinders the understanding of hydrodynamic mass behavior in terms of transverse/parallel forces. Unfortunately, the number of experimental investigations that present force and corresponding hydrodynamic mass data for tube bundles in two-phase crossflow is limited.

3.1.3 Damping

Damping is the general term used to define the ability of a system to dissipate vibratory energy (SINGH; SOLER, 1984). Most vibrating systems have different mechanisms for dissipating energy. In general, the dissipative process is a result of the combination of all those mechanisms and, unless there is a single dominant behavior, it can be difficult to identify and model it accurately (MAIA; SILVA, 1998).

According to Singh & Soler (1984) and Blevins (2001), damping of structures in viscous fluids is generated by three distinct phenomena described below:

Structural damping related to friction, impact, scraping and motion of trapped fluid ("gas pumping" or "squeeze film" damping) within a joint. Furthermore, for the particular case of heat exchanger tubes, Singh & Soler (1984) indicate that structural damping is strongly related to the number and thickness of tube supports, the size of the baffle hole clearance, the surface adhesion between tube and baffle materials, etc.

Internal material damping due to yielding, heating, electromagnetic currents, internal energy dissipation of materials. Singh & Soler (1984) note this mechanism is not

significant at small vibration. However, Lowery & Moretti (1975) report that the location of the longitudinal weld seam with respect to the plane of tube vibration has an effect on the measured damping.

Fluid damping due to fluid drag, viscous dissipation, and radiation to the surrounding fluid. Some difficulties underlie fluid damping, particularly when tubes are subjected to two-phase flow because new parameters such void fraction and flow patterns do affect the dynamic response of the tube.

As it can be seen, several parameters do affect the actual damping that a tube experiences in a heat exchanger, which hinders the development of an all-purpose expression to represent the phenomenon. In the following subsections, definitions on damping representation and quantification are presented. Further, a thorough analysis on structural damping, internal material damping and fluid damping is proposed. When available, models and design guidelines that represent these effects are presented.

Damping ratio: general definitions

The most widely used and practically useful model for representing damping forces on structures is the ideal linear viscous damper, as shown in Fig. 3.1. This damper opposes structural motion with a force, F_d, which is proportional to velocity and can be formulated as

$$F_d = c\frac{dy}{dt} = c\dot{y}, \tag{3.5}$$

or

$$F_d = 2m\zeta\omega_n\dot{y}, \tag{3.6}$$

where $y(t)$ is the displacement of the structure, c is a proportionality constant with units of force per unit length and velocity, m is the mass of the structure and ω_n is the natural frequency of the system expressed in units of circular frequency. As it can be seen from Eq. 3.6, c has been replaced with another expression that is proportional to the dimensionless damping ratio ζ.

The damping ratio of the system is a non-dimensional value given by the ratio between the damping coefficient of the system and its critical damping coefficient (NICOLETTI, 2015):

$$\zeta = \frac{c}{c_c} = \frac{c}{2m\omega_n} = \frac{c}{2\sqrt{km}}, \tag{3.7}$$

where k is the stiffness coefficient of the spring and c_c is the critical coefficient damping of the system.

According to Blevins (2001), most structures that are subject of vibration study are lightly damped and have damping factors of the order of 0.05 or less. For free vibration of these structures, viscous damping induces negligible shifts in natural frequency and damping factor can be related to the dynamic response amplification factor, Q, the logarithmic decrement, δ, and the loss factor, η, as follows:

$$\zeta = \frac{1}{2Q} = \frac{\delta}{2\pi} = \frac{\eta}{2}. \tag{3.8}$$

The equivalences between the parameters shown in Eq. 3.8 are useful for measuring structural damping from experimental data.

The energy expended by damping is the integral of the product of the damping force and the displacement over which the force is applied (BLEVINS, 2001),

$$\text{Dissipated energy} = \int_{\text{one cycle}} F_d dy = \int_t^{t+T} F_d \frac{dy}{dt} dt, \tag{3.9}$$

where T is the period of vibration. Assuming that vibration is harmonic, given by $y(t) = A_y \cos(\omega t)$, then the energy dissipated in one cycle of vibration by the viscous damper can be calculated as (BLEVINS, 2001):

$$\text{Dissipated energy} = 2\pi m \omega_n \omega \zeta A_y^2, \tag{3.10}$$

where ω is the circular frequency in rad/s. The total energy of the elastic structure shown in Fig. 3.1 is equal to the maximum kinetic (or potential) energy that can be achieved during a cycle. For this case, the stored energy is given by Blevins (2001)

$$\text{Stored energy} = \frac{1}{2} m \dot{y}_{max}^2 = \frac{1}{2} m \omega^2 A_y^2. \tag{3.11}$$

The ratio of the energy expended per cycle due to viscous damping to total energy of the structure is proportional to the damping factor (BLEVINS, 2001):

$$\frac{\text{Dissipated energy}}{\text{Stored energy}} = 4\pi\zeta \frac{\omega_n}{\omega} \approx 4\pi\zeta. \tag{3.12}$$

This approximation is valid if the structure vibrates at its natural frequency, as is ordinarily the case in flow-induced vibration of structures in elastic deformation (non-

Table 3.1: *Equivalent viscous damping (BLEVINS, 2001).*

Damper	Damping force	Energy dissipation per cycle	Equivalent viscous damping factor, ζ_{equil}
Viscous	$c\dot{y}$	$c\pi\omega A_y^2$	$c/(2m\omega)$
Coulomb	$F_f \text{sgn}(\dot{y})$	$4F_f A_y$	$2F_f/(\pi m\omega^2 A_y)$
Quadratic	$c_2(\dot{y})^2\text{sgn}(\dot{y})$	$(8/3)c_2\omega^2 A_y^3$	$4c_2 A_y/(3\pi m)$
n*th*	$c_n\lvert\dot{y}\rvert^n\text{sgn}(\dot{y})$	$\pi c_n\gamma_n\omega^n A_y^{n+1}$	$c_n\gamma_n\omega^{n-2}A_y^{n-1}/(2m)$
Hysteretic	$c_h\dot{y}/\omega$	$\pi c_h A_y^2$	$c_h/(2m\omega^2)$

plastic deformation).

Often the damping force will not follow the ideal model of the viscous damper. It is possible to define an equivalent viscous damping that corresponds to the same energy per cycle as the actual damping force (BLEVINS, 2001). Based on this idea, the equivalent damping factors for Coulomb (friction) damping, hysteretic (displacement dependent) damping, and velocity power-law damping are given in Tab. 3.1[1].

It is worth mentioning that there are two approaches to introduce damping in a mathematical model representing a dynamic system:

- First, the structure can be modeled by considering the damping forces acting on the structure motion. In order to do so, a damping model must be selected (*e.g.* viscous, friction, hysteretic, etc) and introduce the corresponding damping force into the differential equation of motion through the physical model. The complication that arises with this option is that unless the damping model is proportional to the mass or stiffness matrices (or a linear combination of both), the modal equations will not decouple through the solution of the eigenproblem (MAIA; SILVA, 1998). In this manner, alternative methods of integration must be implemented, usually demanding more computational resources.

- The second alternative consists in applying damping in the form of Eq. 3.5 to the individual modes after the modal analysis on the structure has been completed. This approach is based on the fact that the eigenproblem given by the differential equation system results in the same eigenvalues (squared undamped natural frequencies) and eigenvectors (undamped mode vectors) in both cases, for undamped systems and for proportionally viscous damped systems (MAIA; SILVA, 1998). Thus, mathematical and computational complications can be avoided.

[1] ω =vibration frequency, rad/s; sgn()=sign(); $\gamma_n = (4/\pi)\int_0^{\pi/2}\cos^{n+1}u\,du$

Structural damping

As mentioned before, structural damping depends directly on supports and mounting configuration of tubes. Further, Pettigrew et al. (1986) indicate that there are two principal types of tube motion at the support, rocking motion and lateral motion, as shown in Fig. 3.3. Actually, the type of motion at a given support may be a combination of rocking motion and lateral motion. Damping due to rocking motion may be more relevant in practice since it is predominant in the lower vibration modes.

Figure 3.3: *Type of tube motion at support location, according to Pettigrew et al. (1986).*

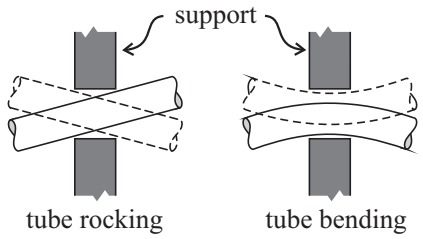

The tube motion at the support generates a dynamic interaction between these components, which may be categorized in three main types, namely: sliding, impacting and scuffing which is impacting at an angle followed by sliding as depicted in Fig. 3.4. The energy dissipated by sliding is due to friction and is related to the product of contact force and displacement. The energy dissipated by impact is in the form of local deformation of the support followed by stress wave propagation in the support and local deformation of the tube followed by high frequency traveling waves in the tube (PETTIGREW et al., 1986). In practice, the dynamic interaction between tube and tube-support may be a combination of the three mechanisms above.

Figure 3.4: *Type of dynamic interaction between tube and tube-support, according to Pettigrew et al. (1986).*

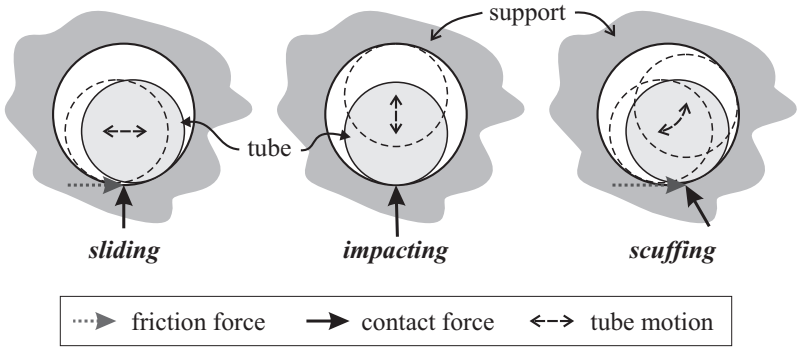

From a constructive point of view, the effective structural damping ratio for heat exchanger tubes is the result of the combination of effects produced by constructive parameters such as: number of supports, tube-to-tube-support clearances, etc. These values may vary from one heat exchanger to another. Thus, damping ratio for distinct cases may be difficult to compare. Pettigrew et al. (1986) suggest that structural

damping ratio can be normalized by these constructive parameters in order to analyze data properly. Based on experimental data and the described mechanisms of tube displacements at supports, Pettigrew et al. (1986) suggest that the following effects can be considered:

Effect of number of supports: Assuming that the span length and all other tube parameters are kept constant, the total vibration energy in a tube is proportional to the number of spans. The energy dissipated by friction at the support is obviously related to the number of supports. For instance, in a two-span heat exchanger tube with one support, there is the vibration energy of two spans but only one support to dissipate energy. Thus damping should be less than for a tube with a large number of spans and a large number of supports. According to Pettigrew et al. (1986), this trend was registered in the available damping data. In this manner, Pettigrew et al. (1986) suggest normalize damping data such that:

$$\zeta_{nNS} = \frac{\zeta N}{(N-1)}, \tag{3.13}$$

where ζ_{nNS} is the damping ratio normalized by the number of spans, N.

Effect of frequency: Based on experimental evidences compiled in Pettigrew et al. (1986), it is not possible to establish a trend with frequency.

Effect of vibration amplitude: There is no conclusive trend of damping as a function of vibration amplitude. Some researchers indicate that damping decreases with vibration amplitude. For sliding type damping, this would make sense since friction does not increase with vibration amplitude as would be expected from linear damping. Thus, it would be reasonable to expect damping to decrease with vibration amplitude (PETTIGREW et al., 1986). Conversely, other researchers have found damping to increase with amplitude. Pettigrew et al. (1986) explain this argument based on the type of contact between tube and supports at distinct vibration amplitudes. At low amplitude, the tube is in contact with the support and sliding type friction dominated. At higher amplitude, the tube may start rattling within the tube support. According to Pettigrew et al. (1986), this would cause impact type damping and non-linearities which would tend to increase damping. In practice, both sliding and impacting mechanisms are possible and, therefore, a definite trend of damping as a function of amplitude has not been established.

Effect of diameter or mass: Large and massive tubes in contact with a surface should experience large friction forces, hence the energy dissipated also should be large. How-

ever, the potential energy in the tube would also be proportionally higher in more massive tubes. In this manner, the damping ratio, which is related to the ratio of energy dissipated per cycle to the potential energy in the tube should be independent of tube size or mass (PETTIGREW et al., 1986). In fact, Pettigrew et al. (1986) checked this trend over the range of diameters from 13 to 25 mm, although damping was not specifically studied in any of the publications reviewed.

Effect of side loads: In real heat exchangers, side loads are possible due to misalignment of the tube-supports or due to fluid drag forces. These forces may increase or reduce damping. Small side loads may prevent impacting and thus, reduce damping, whereas large side loads may increase friction (PETTIGREW et al., 1986). Goyder (1982) *apud* (PETTIGREW et al., 1986) measured damping ratios in two conditions: with a carefully aligned tube with a single support and other when the support was misaligned. The former condition showed damping ratios as low as 0.2%, which is lower than the latter condition, which showed a damping ratio equal to 0.8%. Anyway, both in real heat exchangers as in test sections, misalignment and side load are not a controlled parameter. Therefore, the designer hardly may take advantage of this parameter to increase damping.

Effect of higher modes: Damping appears to decrease with increasing mode order when this mode order is higher than the number of spans. This is not surprising since these higher order modes involve relatively less interaction between tube and tube-support (PETTIGREW et al., 1986). Actually, higher order modes are rarely considered in FIV analysis.

Effect of support thickness: According to the data reviewed in Pettigrew et al. (1986), there is a clear evidence indicating that support thickness is a dominant parameter. Furthermore, Blevins (1975) and Hartlen (1974) show that damping is roughly proportional to support thickness up to about 15 mm. Beyond 15 mm, it is not clear that thicker supports increase damping (PETTIGREW et al., 1986). Further, Blevins (1975) found little increase in damping beyond 19 mm thickness. Aiming to take support into consideration, Pettigrew et al. (1986) correct the damping data linearly for support width less than 12.7 mm such that:

$$\zeta_{nSW} = \zeta_{nNS}\left(\frac{12.7}{t_s}\right), \tag{3.14}$$

where t_s is the support thickness in mm and ζ_{nSW} is the corrected normalized damping ratio.

Pettigrew et al. (1986) explain the damping dependence on support thickness. The energy dissipated by friction is proportional to the product of contact force and displacement. The contact force should be independent of support thickness. However, the displacement should be proportional to support thickness for rocking type motion with sliding interaction with the tube-support, as shown in Fig. 3.5. This kind of interaction between tube and tube-support are expected for lower vibration amplitudes that are the conditions of interest in practice.

Figure 3.5: *Sliding interaction: effect of support thickness based on Pettigrew et al. (1986).*

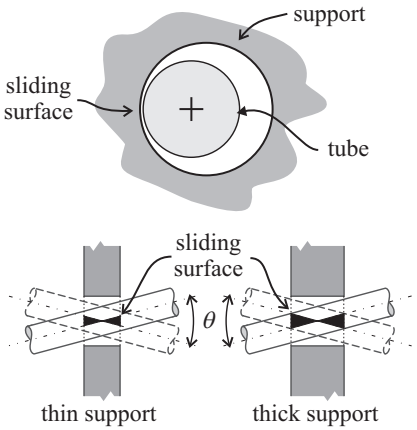

Damping due to rocking type motion with impact interaction should also increase with support thickness. In fact, the impact forces are expected to increase with support thickness, as depicted in Fig. 3.6. Damping due to lateral type motion, however, should not be affected by support thickness (PETTIGREW et al., 1986).

Figure 3.6: *Impact interaction: effect of support thickness, according to (PETTIGREW et al., 1986).*

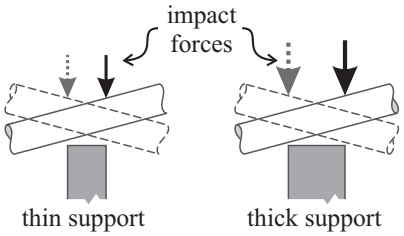

Effect of clearance According to the discussion presented in Pettigrew et al. (1986), damping should not be much affected by clearance since for the normal range of tube-to-tube-support diametral clearances (*i.e.*, 0.40 to 0.80 mm) there is no conclusive trend in the reviewed data. For very small clearances, in the order of 0.20 mm, damping appears to be larger (HARTLEN, 1974). This behavior may be related to the fact that a heat exchanger tube would normally touch most supports on one side or the other. Thus, the dynamic interaction between tube and support is taking place near one side and is not much affected by the proximity of the opposite side which depends on the

diametral clearance. This criterion is true in most cases, except when the vibration amplitude is very large or the clearance is very small, so that the tube is permanently hitting the support. In this manner, damping should not be much affected by clearance. Furthermore, it is possible that side forces in the support be larger for very small clearances thus explaining the somewhat higher damping (PETTIGREW et al., 1986).

Following the above discussions, Khushnood et al. (2012) compiled the design guidelines proposed by Pettigrew et al. (1986) and Pettigrew et al. (1991), which are devoted to evaluate damping ratio due to friction, squeeze film at supports and due to the supports.

Design guideline for friction damping: Pettigrew et al. (1986) derived expressions to evaluate friction damping ratio in a multi-span tube in liquid and in gas. For liquid, it is given by

$$\zeta_F = 0.5 \left(\frac{N-1}{N}\right) \left(\frac{t_s}{l_m}\right)^{1/2}, \tag{3.15}$$

while for gas,

$$\zeta_F = 5.0 \left(\frac{N-1}{N}\right) \left(\frac{t_s}{l_m}\right)^{1/2}, \tag{3.16}$$

where N is the number of tube spans, t_s is the support thickness and l_m is the characteristic span length usually taken as the average of three longest spans (PETTIGREW et al., 1991).

Design guideline for squeeze film damping ratio: Khushnood et al. (2012) present an expression for squeeze-film damping ratio for multi-span tube given by

$$\zeta_{SF} = \left(\frac{N-1}{N}\right) \left(\frac{1460}{f}\right) \left(\frac{\rho d^2}{m}\right) \left(\frac{t_s}{l_m}\right)^{0.6}, \tag{3.17}$$

where ρ is the density of the shell-side flow, f is the tube natural frequency, d is the tube outside diameter and m is the total mass per unit length including the hydrodynamic mass.

Design guideline for overall support damping: Pettigrew et al. (1991) compiled most of the available data on damping of multispan heat exchanger tubes in liquids available at that time. These data were used to deduce values of support damping by subtracting calculated viscous damping due to fluid from the total damping data. Subsequently,

the resulting support damping values were analyzed to find trends. Pettigrew et al. (1991) found that support damping is dominant. Roughly, 75% of the damping energy is dissipated at the support; it is attributed mostly to squeeze-film damping which is related to support thickness and is inversely proportional to tube frequency f. Thus, with the help of Mulcahy's theory (MULCAHY, 1980), Pettigrew et al. (1991) developed a semi-empirical expression to formulate support overall damping, ζ_{SU}, given by

$$\zeta_{SU} = \left(\frac{N-1}{N}\right)\left(\frac{2200}{f}\right)\left(\frac{\rho d^2}{m}\right)\left(\frac{t_s}{l_m}\right)^{0.6}. \tag{3.18}$$

Pettigrew et al. (1991) indicate that Eq. 3.18 is a reasonable formulation for the minimum support damping values, therefore, appropriate for design purposes.

Fluid damping

The vibration of a submerged structure is damped by the surrounding fluid. In this sense, two cases can be identified: damping within a quiescent fluid and damping within a fluid flow.

Damping within a quiescent fluid is the result of viscous shearing of the fluid at the surface of the structure and flow separation (BLEVINS, 2001). The drag force, F_D, per unit length on the structure depicted in Fig. 3.7 can be expressed as:

Figure 3.7: *Structure under drag force based on (BLEVINS, 2001).*

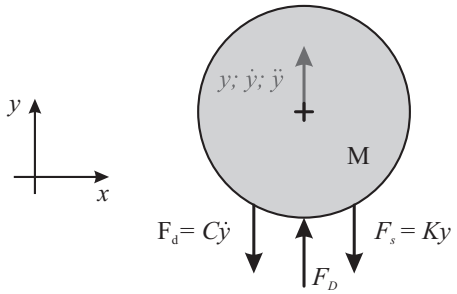

$$F_y = F_D = \frac{1}{2}\rho|U_{rel}|U_{rel}dC_D, \tag{3.19}$$

where ρ is the fluid density, C_D is the drag coefficient and U_{rel} is the fluid relative velocity with respect to the structure. Assuming quiescent fluid, it is accepted that:

$$U_{rel} = -\dot{y}. \tag{3.20}$$

Thus, the equation of motion for the structure can be obtained through Newton's second

law,

$$m\ddot{y} + 2m\zeta_S\omega_n\dot{y} + ky = F_y = -\frac{1}{2}\rho|\dot{y}|\dot{y}dC_D, \tag{3.21}$$

where the mass per unit length m includes the effect of added mass and ζ_S is the damping of the structure if fluid were absent, i.e. structural damping. This is a non-linear equation that can be rearranged in order to undercover the effect of fluid on effective damping.

If the structural motion is harmonic with amplitude A_y, i.e. $y(t) = A_y \sin\omega t$, then the forcing term in Eq. 3.21 can be expanded in a Fourier series Blevins (2001) given by:

$$|\dot{y}|\dot{y} = A_y^2\omega^2|\cos\omega t|\cos\omega t \approx \frac{8}{3\pi}A_y^2\omega^2\cos\omega t = \frac{8}{3\pi}\omega A_y\dot{y}, \tag{3.22}$$

where the factor $8/(3\pi)$ comes from the first term of the Fourier series expansion. Substituting this result back in Eq. 3.21 and rearranging gives:

$$m\ddot{y} + 2m\omega_n\left[\zeta_S + \frac{2\rho dC_D A_y\omega}{3\pi m\omega_n}\right]\dot{y} + ky = 0, \tag{3.23}$$

which implies that the effective damping is given by the structural component plus the contribution of quiescent fluid given by (BLEVINS, 2001)

$$\zeta_{SF} = \frac{2}{3\pi}\frac{\rho d^2}{m}\frac{A_y}{d}\frac{\omega}{\omega_n}C_D. \tag{3.24}$$

As it can be noticed from Eq. 3.24, C_D has to be previously known in order to estimate ζ_{SF}. According to Blevins (2001), for small-amplitude vibration in a viscous fluid, the fluid does not separate and the drag coefficient for a circular cylinder of diameter d at low Reynolds number can be approximated as

$$C_D = \left(\frac{fD}{V}\right)\left(\frac{3\pi^3}{2}\right)\left[\frac{\nu}{\pi f d^2}\right]^{1/2}, \tag{3.25}$$

where ν is the kinematic viscosity of the fluid and V is the amplitude of the velocity oscillation of the structure given by

$$V = \omega A_y. \tag{3.26}$$

Setting the oscillation frequency to the natural frequency, that is, $f = f_n = \omega_n/(2\pi)$ gives the damping of a cylinder in a viscous and quiescent fluid (BLEVINS, 2001):

$$\zeta_{SFcyl} = \frac{\pi}{2}\frac{\rho d^2}{m}\left(\frac{\nu}{\pi f d^2}\right)^{1/2}. \tag{3.27}$$

Furthermore, Rogers et al. (1984) developed a formula to estimate viscous damping, valid for Stokes numbers up to 3000 and $d/D_e < 0.5$ (d/D_e defined according Eqs. 3.3 and 3.4), which covers most heat exchangers. Thus, viscous damping for tubes in heat exchangers due to still fluid is given by (PETTIGREW et al., 1986):

$$\zeta_V = \frac{\pi}{2}\frac{\rho d^2}{m}\left(\frac{\nu}{\pi f d^2}\right)^{1/2}\left[\frac{[1+(d/D_e)^3]}{[1-(d/D_e)^2]^2}\right]. \tag{3.28}$$

On the other hand, when a circular cylinder is submerged in a uniform crossflow, the fluid exerts a drag force on the surface as a result of viscous effect. The resultant frictional force in the drag direction is usually called the skin friction drag. But when the fluid flows close to a surface that is not parallel to the main stream, there is an additional drag force resulting from differences of pressure over the surface. This force is called the pressure drag, or form drag. Thus, the skin friction drag is the resultant of forces tangential to the surface drag and the pressure drag is the resultant of the forces normal to the surface. In a flow around a circular cylinder, since the flow is separated over much of the cylinder surface in practical applications, the wake is large and the pressure drag is much greater than the skin friction. Therefore, the total drag can be expressed in terms of a dimensionless drag coefficient C_D as the total drag force per unit length divided by $(1/2)\rho U^2 d$. Moreover, it is worth to mention that the steady lift force generated due to uniform crossflow is generally null (CHEN, 1987).

Blevins (2001) presents the formulation for damping generated by fluid crossflow. Consider the elastically supported vibrating structure depicted in Fig. 3.8, which is exposed to a high Reynolds number cross flow. As the structure vibrates, a relative component of flow velocity is induced, which is given by

$$U_{rel}^2 = \dot{y}^2 + (U-\dot{x})^2 \approx U^2 - 2U\dot{x}, \tag{3.29}$$

where $\dot{x}$ and $\dot{y}$ are the horizontal and vertical components of structural velocity, respectively, that are assumed to be small relative to the mean horizontal flow velocity U. The angle of the relative velocity U_{rel} with respect to x axis is represented by γ, calculated as:

$$\gamma = \tan\left(\frac{\dot{y}}{U}\right) \approx \frac{\dot{y}}{U}. \tag{3.30}$$

Figure 3.8: *Section in a flow based on (BLEVINS, 2001).*

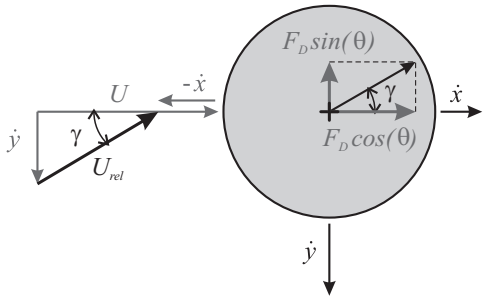

Using these linearizing approximations gives the following net horizontal and vertical forces induced by the relative drag (BLEVINS, 2001):

$$F_{x,drag} = F_D \cos\gamma = \frac{1}{2}\rho U_{rel}^2 dC_D \cos\gamma \approx \frac{1}{2}\rho U^2 C_D d\left(1 - \frac{2\dot{x}}{U}\right), \tag{3.31}$$

$$F_{y,drag} = F_D \sin\gamma = \frac{1}{2}\rho U_{rel}^2 dC_D \sin\gamma \approx \frac{1}{2}\rho U^2 C_D d\frac{\dot{y}}{U}. \tag{3.32}$$

If equations of motion in the form of Eq. 3.21 can be defined separately for x and y directions, then Eqs. 3.31 and 3.32 can be used as forcing terms. In this manner, the drag-induced damping due to cross flow can be obtained with (BLEVINS, 2001):

$$\zeta_{x,drag} = \frac{1}{4\pi}\frac{U}{f_n d}\frac{\rho d^2}{m}C_D, \tag{3.33}$$

$$\zeta_{y,drag} = \frac{1}{8\pi}\frac{U}{f_n d}\frac{\rho d^2}{m}C_D, \tag{3.34}$$

where m is the mass per unit length, including added mass.

As it can be noticed from Eqs. 3.33 and 3.34, the drag-induced damping for a circular cylinder in cross flow is proportional to flow velocity and inversely proportional to tube natural frequency, which, according to Blevins (2001), is in rough agreement with experimental data for cylinder subjected to small flow velocities. However, Blevins (2001) indicates that Eqs. 3.33 and 3.34 can overpredict damping. Actually, this was checked experimentally by Weaver & El-Kashlan (1981), as it is shown in Fig. 3.9. Furthermore, Blevins (2001) point out that the phenomena related with vortex shedding and instabilities obscures the study of fluid damping.

Figure 3.9: *Experimental data of Weaver & El-Kashlan (1981) for transverse dynamic damping of a tube in a rotated triangular array with pitch-to-diameter ratio equal to 1.375, $f = 20$ Hz, $d = 0.025m$, $(m/\rho d^2) = 200$, $C_D = 0.8$, in comparison with theory (Eq. 3.34).*

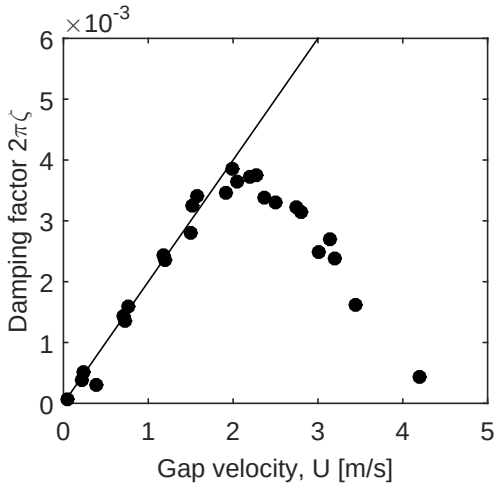

Damping in two-phase flow

According to Pettigrew & Taylor (2004), the study of damping is much more difficult in two-phase than in single-phase flow for several reasons. First, damping in two-phase flow depends on void fraction, which is an additional parameter when compared to single-phase flow. Second, damping measurements are difficult to obtain since it is impossible to maintain a stagnant two-phase mixture. This implies that damping measurements must be taken under some flow, which adds the mass velocity as a parameter to the problem. In addition, care must be exercised to avoid mass velocities near fluidelastic instability (FEI) because of coupling between hydrodynamic forces and tube motion may affect substantially the overall damping estimates. Thirdly, damping in two-phase flow depends on the flow pattern; the damping behavior is quite different in continuous-type flow patterns such as bubbly, froth and annular than for intermittent-type flows as churn or intermittent.

Distinct than that observed for single-phase flow, where damping is basically represented by a viscous component, damping during two-phase flow seems to have other mechanisms involved. In fact, total damping under these circumstances is generally larger than that of viscous damping alone based on homogeneous two-phase parameters (PETTIGREW; TAYLOR, 2004). Therefore, as first suggested by Carlucci (1980), fluid damping for structures exposed to two-phase flow is modeled as a sum of two components: viscous damping based on homogeneous two-phase parameters, $\zeta_{V,TP}$, and the two-phase damping component, ζ_{TP}.

The viscous component of damping in two-phase mixtures is taken to be analogous to viscous damping in single-phase fluids, as introduced by Pettigrew et al. (1986) (see Eq. 3.28):

$$\zeta_{V,TP} = \frac{\pi}{\sqrt{8}} \left(\frac{\bar{\rho} d^2}{m} \right) \left(\frac{2\nu_{TP}}{\pi f d^2} \right)^{0.5} \left\{ \frac{[1 + (d/D_e)^3]}{[1 - (d/D_e)^2]^2} \right\}, \tag{3.35}$$

where $\zeta_{V,TP}$ is the viscous damping ratio, m is the tube mass per unit length including the hydrodynamic mass and ν_{TP} is the kinematic two-phase viscosity evaluated according the McAdams model (COLLIER; THOME, 1994) given by Eq. 2.31 that also can be expressed as:

$$\nu_{TP} = \frac{\nu_l}{1 + \alpha \left(\frac{\nu_l}{\nu_g} - 1 \right)}, \tag{3.36}$$

where ν_l and ν_g are the kinematic viscosities of the liquid phase and gas phase, respectively. The homogeneous model is generally adopted to estimate the void fraction that is needed Eq. 3.36 as well as for the calculation of the density of the mixture, $\bar{\rho}$, according to Eq. 2.27.

Regarding to the two-phase damping component determination, it is perhaps the most complex parameter to be estimated in this analysis. Conversely, the industry presented the strong need to develop some guidelines for heat exchangers design. In this manner, several studies have been performed in order to improve the understanding on damping behavior in two-phase flow since this parcel seems to be more important than the viscous parcel (PETTIGREW et al., 1989).

Several experimental studies on the influence of mass velocity and void fraction on two-phase damping have been reported in the literature. For instance, Carlucci & Brown (1983) studied the effect of mass velocity on two-phase damping for an aluminum cylinder clamped at both ends which is subjected to parallel flow with mass velocities from 1000 to 2500 kg/m^{2}s. The results are presented in Fig. 3.10. Carlucci & Brown (1983) found that the two-phase damping factor present a peak behavior when analyzed in terms of void fraction, which is true for distinct mass velocities. Furthermore, the authors pointed out that the peak region is wider for higher mass velocities and that higher mass velocities present peaks at higher void fractions. However, for these results, the mass velocity cannot be pointed as the only parameter influencing damping since gradual transition of flow patterns was reported by the authors. In conclusion, the results reported by Carlucci & Brown (1983) show that the effect of mass velocity is distinct for different void fractions and, therefore, it is complex to establish a straightforward and direct correlation without consider the flow pattern transitions.

Pettigrew et al. (1989) studied the behavior of damping in some tube banks in two-phase flow. Figure 3.11 present results on the average (calculated between parallel and transverse directions) total damping plotted against mass velocity.

Based on Fig. 3.11, Pettigrew et al. (1989) concluded that damping is not too depen-

Figure 3.10: *Effect of mass flux on two-phase damping ratio: fixed-fixed aluminum cylinder, 40 mm I.D. flow tube Carlucci & Brown (1983).*

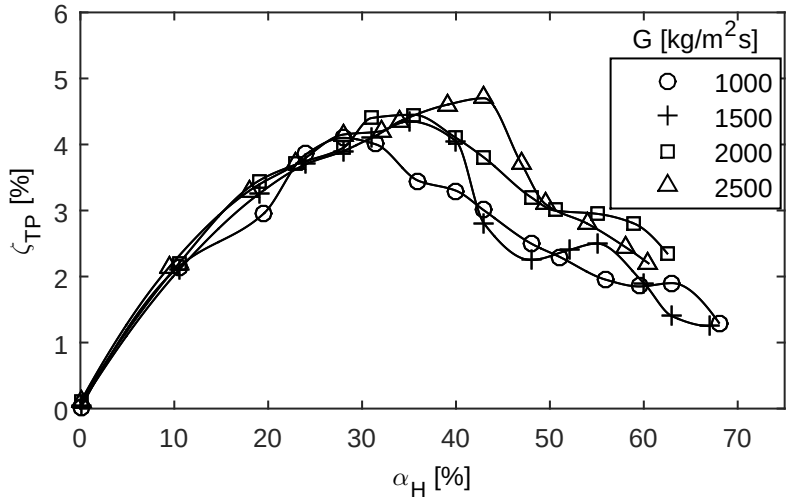

dent on mass velocity between one-third and two-thirds of the mass velocity for void fractions up to $\alpha_H = 90\%$. It is worth mentioning that Pettigrew et al. (1989) discussed their results based on the flow pattern map first introduced by Grant (1975). According to this map, most of the tested conditions from $\alpha_H = 25\%$ to $\alpha_H = 75\%$ correspond to the bubbly flow pattern. For $\alpha_H = 90\%$, the condition tested at critical velocity is in the transition between bubble and intermittent flow pattern, while the condition tested at half the critical velocity correspond to intermittent flow pattern. Despite the flow pattern transition that occurs in the conditions tested for $\alpha_H = 90\%$, it cannot be pointed out any difference in damping behavior.

According to the data presented in Pettigrew et al. (1989), higher void fractions present a defined tendency as is the case of results for $\alpha_H = 96\%$, which is plotted against mass velocity in Fig. 3.12. It is important to mention that for $\alpha_H = 96\%$ the conditions tested at critical velocity and half the critical velocity correspond to intermittent flow pattern. In this sense, based on the results reported by Pettigrew et al. (1989), it can be noticed that the flow pattern map proposed by Grant (1975) do not provide information that can be related to damping behavior.

Based on the results found in the literature, it is hard to point out a general tendency of two-phase damping with mass velocity. Moreover, it is worth mentioning that the analysis of damping with increasing mass velocity may be accompanied of flow pattern changes. Thus, it is difficult to isolate mass velocity effects from those generated by flow patterns. Somehow, better conclusions can be obtained from results in the literature corresponding to high void fraction, where it can be seen that two-phase damping in transverse direction decreases with increasing mass velocity. Conversely, two-phase damping in parallel direction can be higher than that for transverse direction at higher void fractions.

Figure 3.11: *Effect of mass velocity on tube damping, normal square tube bundle $\tau = 1.47$ (PETTIGREW et al., 1989). Point, dash and solid lines represent the one-third of, the two-thirds and three-thirds of the critical mass velocity for FEI, respectively.*

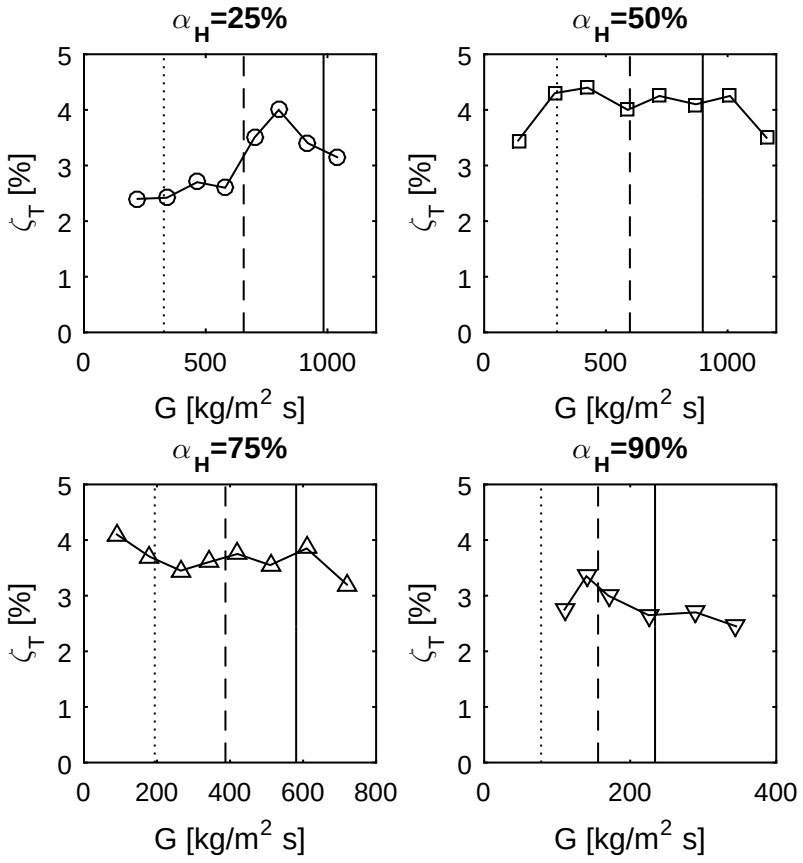

On the other hand, most damping studies in literature agree that two-phase damping greatly depends on void fraction. According to Taylor & Pettigrew (2001), two-phase damping is a direct function of void fraction. Figure 3.13 shows the typical behavior of ζ_T with increasing homogeneous void fraction. As it can be seen, ζ_T present a peaking behavior, damping reaches its maximum at intermediate void fractions. Subsequently, for higher void fractions, ζ_T decreases until it presents values similar to that obtained for single-phase gas conditions.

The behavior presented in Fig. 3.13 was found in several experimental studies (CARLUCCI; BROWN, 1983; PETTIGREW et al., 1989; LIAN et al., 1997; PETTIGREW et al., 2001), however this characteristic was only better understood after the research performed by (LIAN et al., 1997), whose results are presented in Fig. 3.14. They found that the RMS amplitude of local void fraction fluctuations increases until $\alpha_H \approx 40\%$ in bubbly flow pattern, after that it reaches a peak at $\alpha_H \approx 50\%$ and finally it decreases gradually with increasing α_H during intermittent and annular with droplets flow patterns.

According to Lian et al. (1997), the results presented in their work show that the RMS amplitude of local void fraction fluctuations are related to the energy dissipation

Figure 3.12: *Effect of mass velocity on tube damping in parallel and transverse directions for normal square tube bundle* $\tau = 1.47$ *and* $\alpha_H = 96\%$ *(PETTIGREW et al., 1989).*

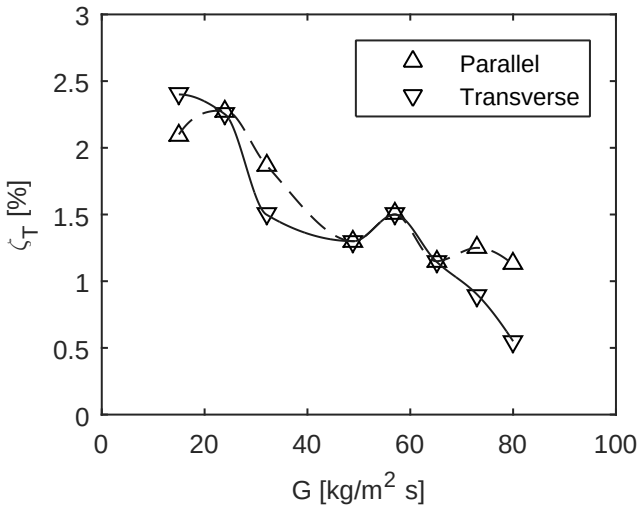

and, therefore, seems to play an important role in two-phase damping mechanism. This relationship between local void fraction fluctuations and damping ratio makes sense, since there are large temporal fluctuations in the fluid momentum whenever gas and liquid slugs alternately impinge on the vibrating tube in intermittent flow. This means that there is a fluid force associated with these rapid changes in fluid momentum and, if this force causes displacement of the tube, there will be energy transfer between the tube and the fluid (LIAN et al., 1997). In these cases, the fluid moment fluctuations can be higher, and as a result, the force impinged by the fluid, the energy transfer between the fluid and the tube and the damping ratio may reach its maximum. Following this idea, lower damping values can be expected for bubble flow patterns in low void fractions or during annular flow pattern with liquid droplets at higher void fractions because of the low energy transfer under these conditions.

Although the criterion proposed by Lian et al. (1997) about energy transfer is reasonable, care must be exercised when damping (and any other parameter) measurements are related to any flow pattern map since, as discussed in Noghrehkar et al. (1999), the flow pattern taking place next to the test section wall (next to the observation window) may be distinct from that occurring in the center of the tube bundle. For example, Noghrehkar et al. (1999) realized that visual observations (subjective criterion) of two-phase flow pattern through the window showed the passage of lots of bubbles, which could be interpreted as bubbles flow pattern, while the actual flow pattern occurring in the middle of the test section was intermittent, which was measured via objective criterion. In this manner, this situation may lead to wrong conclusions about the behavior of damping in terms of flow pattern map. Moreover, it is important to point out that the linking of damping results to a flow pattern depends on which flow pattern map or identifying technique is being used.

Figure 3.13: *Damping for tube bundle of $\tau = 1.47$, NT: Normal triangular, RT: Rotated triangular, NS: Normal square Pettigrew et al. (1989).*

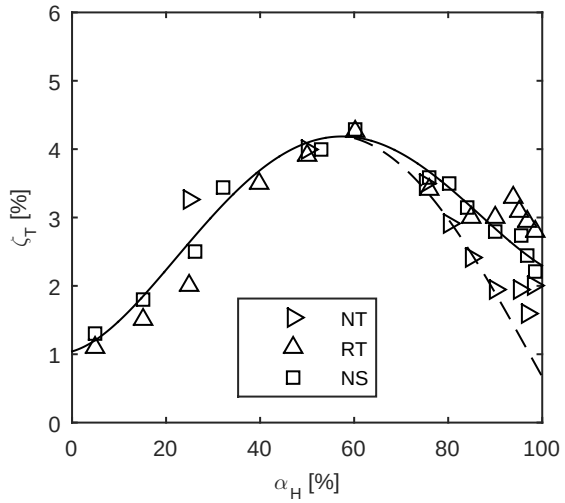

Figure 3.14: *Results presented by Lian et al. (1997).*

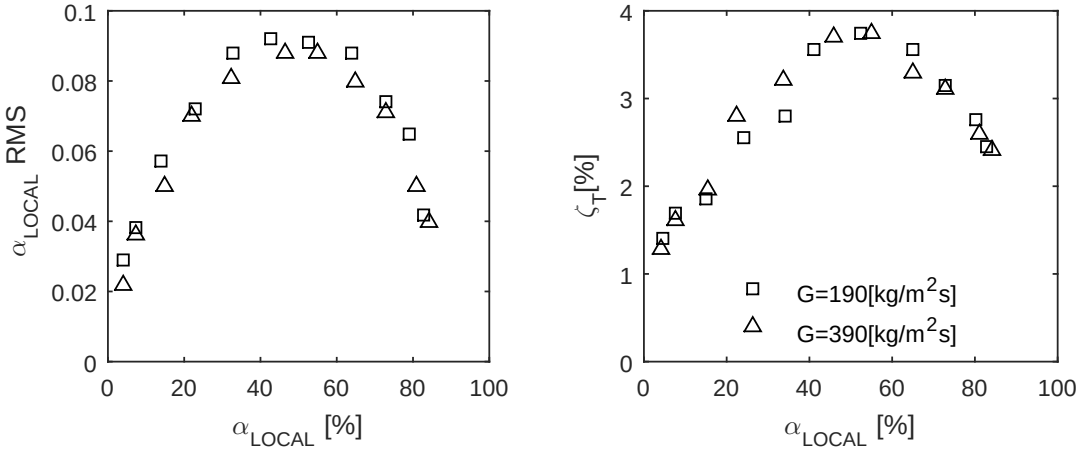

(a) *Variation of RMS amplitude of local void fraction fluctuations with void fraction.*

(b) *Variation of damping ratio with local void fraction.*

Carlucci & Brown (1983) suggest that the damping factor depends on the flow pattern and, therefore, depends on the spatial and temporal variation of the mixture density. Following this idea, a varying mixture density results in a time-varying effective mass component. Thus a true resonance condition does not exist. The peak in a measured response curve occurs when, as in the single-phase case, the steady component of the inertial force is balanced by the stiffness force. The external force required to maintain a given displacement will then be the vector sum of the opposing damping force and the time-varying component of the inertia force. Hence, the magnitude of the applied force is expected to be greater than for a constant mass system, resulting in an effective increase in damping (CARLUCCI; BROWN, 1983). However, it remains to know what is the flow pattern that in fact intensify this effect.

In this sense, it can be concluded that the variation of RMS amplitude of local void fraction fluctuations reported by Lian et al. (1997) must be related to the time-varying component of the inertia force pointed by Carlucci & Brown (1983), which results in an effective increase of damping giving place to the two-phase damping component.

Although it is important to have some knowledge in damping prediction under two-phase flow for tube bundles design, few authors have proposed methods to face this task. Hence two models to estimate two-phase damping are detailed in the next section.

Design guidelines for damping in two-phase flow

Regarding to the two-phase damping component determination, Pettigrew & Taylor (2004) presented a semi-empirical formulation based on the experimental database available until that year. Pettigrew & Taylor (2004) presented a thorough analysis of the factors that may affect damping to propose this model from which it can be summarized that two-phase damping is strongly dependent on void fraction and flow patterns, which in turn are somehow linked by mass velocity, even though it was found that mass velocity *per se* is not an important parameter in damping analysis. Furthermore, two-phase damping is directly related to confinement and to the mass ratio ($R = m/\rho_l d^2$), whose influence can be formulated and used to normalize two-phase damping ratio data. Moreover, ζ_{TP} is weakly related to the tube resonance frequency and tube bundle configuration.

Following these arguments, Pettigrew & Taylor (2004) approximated a lower-bound for two-phase damping as:

$$\zeta_{TP} = A \cdot \left(\frac{\rho_l d^2}{m}\right) \cdot \varphi(\alpha) \cdot C(D_e/d), \tag{3.37}$$

where A is an overall coefficient determined experimentally, which according to the authors is equal to 0.04. The effect of confinement is best formulated by the confinement function $C(D_e/d)$:

$$C(D_e/d) = \frac{\left[1 + (d/D_e)^3\right]}{\left[1 - (d/D_e)^2\right]^2}, \tag{3.38}$$

with d/D_e estimated by Eq. 3.3 or Eq. 3.4, depending on the tube bundle configuration. The function ($\rho_l d^2/m$) is the inverse of the mass ratio, calculated for the liquid density ρ_l, and $\varphi(\alpha_H)$ is a function of homogeneous void fraction, which was approximated aiming to present a similar shape to the collapsed available (at that time) experimental data:

$$\varphi(\alpha_H) = \begin{cases} \frac{\alpha_H}{40} & \text{for } \alpha_H < 40\% \\ 1 & \text{for } 40\% < \alpha_H < 70\% \\ 1 - \frac{\alpha_H - 70}{30} & \text{for } 70\% < \alpha_H \end{cases} \tag{3.39}$$

where α_H is in percent. In Fig. 3.15, the semi-empirical model given by Eq. 3.37 is compared with the experimental database of damping measured in normal triangular tube bundles (PETTIGREW; TAYLOR, 2004). Damping data was previously normalized by the mass ratio and confinement function in order to make the values comparable.

Figure 3.15: *Experimental data compiled by Pettigrew & Taylor (2004) for average (calculated between transverse and parallel directions) two-phase normalized damping in normal triangular tube bundles in comparison with semi-empirical model proposed by Pettigrew & Taylor (2004).*

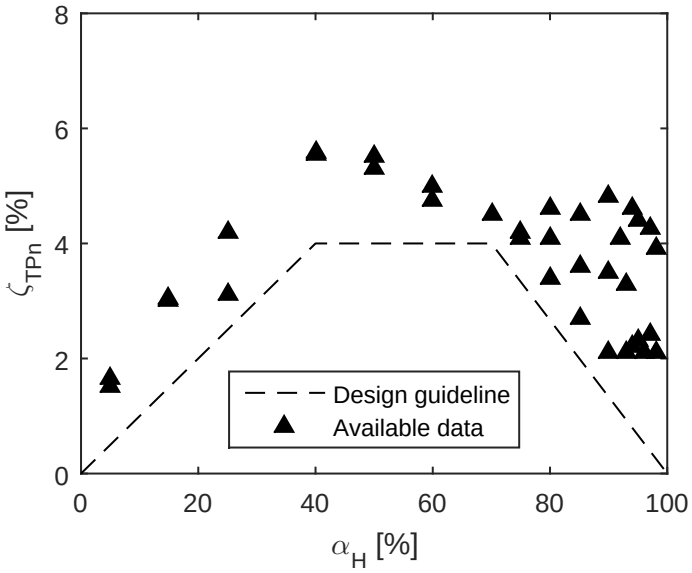

Recently, Sim (2007) developed a semi-analytical model for estimating the total damping ratio in the transverse (to the main flow velocity) direction. However, as reviewed from an extensive compilation of experimental data in Pettigrew & Taylor (2004), similar values can be inferred for parallel direction as long as the flow velocity is lower than fluidelastic instability threshold. Therefore, respecting this restriction, Sim's model can be used to estimate damping in the direction parallel to the flow.

Based on a scheme similar to that depicted in Fig. 3.8, Sim (2007) formulates total damping ratio in transverse direction as:

$$\zeta_y = K_{TP} \cdot Eu_{L0} \cdot \phi_{L0}^2 \cdot \frac{MF_{L0}}{8\pi f_n \bar{u} m}, \tag{3.40}$$

where f_n is the tube natural frequency and K_{TP} is the correlation factor adjusted for

experimental data, which is suggested to be equal to 1.5 for air-water systems. Moreover, a review of this model is presented in Sim & Mureithi (2014), in which the authors indicate $K_{TP} = 3$. The average velocity of two-phase flow, $\bar{u}$, is defined by:

$$\bar{u} = \frac{\rho_l u_l (1-\alpha) + \rho_g u_g \alpha}{\bar{\rho}} = \frac{G}{\bar{\rho}}, \tag{3.41}$$

where $\bar{\rho}$ is estimated according to Eq. 2.27 and α is calculated by using the void fraction model proposed by Feenstra et al. (2000). The velocities of liquid and gas phase, u_g and u_l, are given by Eqs. 2.11 and 2.12, respectively. It is worth mentioning that the mass velocity, G, for the estimation of u_g and u_l is based on the minimum cross sectional area.

According to Sim & Mureithi (2014), better damping estimations for two-phase air-water systems (low pressure systems) are calculated by using the two-phase friction multiplier, ϕ^2_{L0} (L0 stands for the two-phase mixture flowing as liquid), defined in Marchaterre (1961) *apud* (SIM; MUREITHI, 2014) as follows:

$$\phi^2_{L0} = \frac{(1-x)^2}{1-\alpha} + \frac{g(\rho_l - \rho_g)\rho_l d}{2 f_{L0} G^2}\alpha. \tag{3.42}$$

For steam - water systems (high pressure systems), ϕ^2_{L0} may be calculated by:

$$\phi^2_{L0} = \frac{(1-x)^{1.75}}{(1-\alpha)^2}, \tag{3.43}$$

and for a system assumed as homogeneous, it can be adopted the two-phase friction multiplier given by:

$$\phi^2_{L0} = \left[1 + x\frac{1/\rho_g - 1/\rho_l}{1/\rho_l}\right]\left[1 + x\frac{\mu_l - \mu_g}{\mu_g}\right]^{-1/4}. \tag{3.44}$$

The Darcy friction factor, f_{L0}, is given by Poiseulle relationship for laminar flow, and by Blasius for turbulent flow regime, as follows:

$$f_{L0} \approx \begin{cases} \frac{64}{Re_{L0}} & \text{Laminar flow} \\ \frac{0.316}{Re^{0.25}_{L0}} & \text{Turbulent flow} \end{cases} \tag{3.45}$$

with the Reynolds number given by $Re_{L0} = Gd/\mu_l$ and assuming that for fluid flows across tube bundles $Re_{L0} < 2 \times 10^5$ corresponds to laminar flow, while $Re_{L0} \geqslant 2 \times 10^5$ corresponds to turbulent flow (ŽUKAUSKAS, 1972). In Sim (2007), the Euler number,

Eu_{L0}, is given according to the following correlation proposed by Zukauskas (1988):

$$Eu_{L0} = 0.307 Re_{L0}^{-0.1} (\tau - 1)^{-0.36}, \tag{3.46}$$

where τ is the transverse pitch-to-diameter ratio. And the momentum flux in Eq. 3.40, MF_{L0}, is defined by:

$$MF_{L0} = \frac{G^2 d}{\rho_l}. \tag{3.47}$$

In this manner, the two-phase damping ratio variation with void fraction can be estimated as a function of flow parameters. Although this model was developed analytically, it can be seen from Eq. 3.40 that a constant to fit the model to experimental data remains necessary. This reveals that current models are unable to predict damping magnitude if tests were not carried out previously in that tube bundle. Figure 3.16 shows the variation of total damping with increasing void fraction, which in this case is denoted by α_F since it was estimated through the model developed by Feenstra et al. (2000).

Figure 3.16: *Damping predicted by the model proposed by Sim (2007), using $K_{TP} = 3$, for a normal triangular tube bundle, $\tau = 1.26$, under air-water upward flow $T = 25°C$, $P = 95kPa$ for distinct G [kg/m^{2}s].*

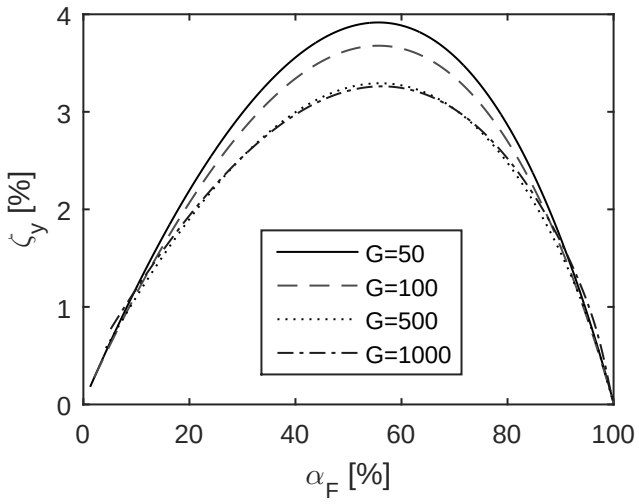

3.1.4 Concluding remarks about dynamic parameters

The expressions presented in this section are devoted to estimate dynamic parameters such as: hydrodynamic mass and damping of a tube in a shell-and-tubes heat exchanger.

It is worth to mention that, for the time being, the homogeneous void fraction is the model that has enabled us to draw better conclusions about the behavior of these parameters in two-phase flow. Therefore, as also recommended in TEMA Standards (1999), and in the absence of a better approach, the homogeneous model can be used as reference to estimate mixture properties and to formulate hydrodynamic mass and two-phase damping ratio (and logarithmic decrement).

The total damping for a tube subjected to two-phase flow is given by the sum of structural, viscous and two-phase damping components, that is:

$$\zeta_T = \zeta_S + \zeta_V + \zeta_{TP}. \tag{3.48}$$

It is important to emphasize that methods for damping prediction are generally valid for operational conditions in which the pitch velocity is considerably lower than fluidelastic instability threshold, say half the critical mass velocity. For mass velocities near fluidelastic instability, damping decreases considerably Pettigrew et al. (1989). In fact, to the best of our knowledge, there is not a reliable design guideline for dynamic parameters under fluidelastic instability conditions.

3.2 Vibration excitation mechanisms in tube bundles under crossflow

3.2.1 Introduction to flow-induced vibration mechanisms

Since critical failures in nuclear power plant equipment began to appear and engineers realized the lack of design guidelines to estimate and avoid FIV, considerable progress has been made in obtaining a better understanding of fluid-structure interaction in heat exchanger tube bundles and similar devices subjected to external crossflow. Researchers found that, under certain operational conditions, some common tube vibration patterns can be identified. These vibration patterns, referred to as FIV mechanisms, are characterized in a relatively good manner for single-phase crossflow, the most important are: (i) fluidelastic instability, (ii) turbulence-induced vibration, (iii) vortex-induced vibration and (iv) acoustic resonance. Moreover, the dynamical behavior of individual cylinders in an array subjected to single-phase crossflow may be summarized, at least in idealized form, as in Fig. 3.17 (PAïDOUSSIS, 1981). As it can be seen, cylinder vibration is present at all flow velocities. This is because cylinders are subject to turbulence-induced vibration and this "buffeting" is intrinsic to such fluid-structure interaction. The vibration amplitudes related to this mechanism are generally small, leading to long-term problems only,

e.g. impacting with supports promotes fretting wear or because of fatigue (PAïDOUSSIS et al., 2011).

Figure 3.17: *Idealized diagram of the response of a cylinder in an array subjected to cross flow, according to Païdoussis (1981).*

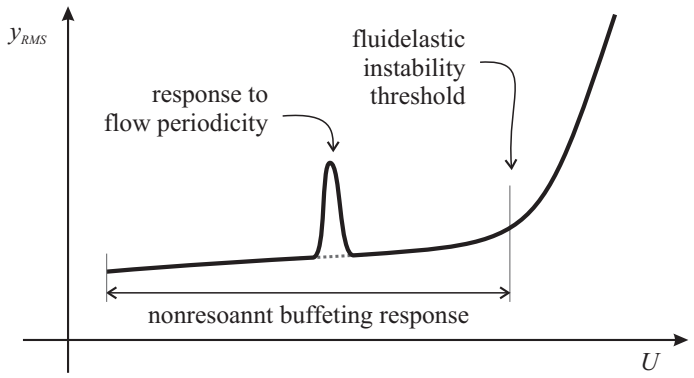

When a flow passes a bluff body, it generates a vortex street in the wake region referred to as von Karman vortex street. Periodic shedding of these vortices from the surface of the body induces periodic pressure variations on the structure (KANEKO et al., 2008). This mechanism may induce vibration in both coordinates, parallel and transverse to the flow. In the transverse direction, the excitation force has a dominant frequency called the von Karman vortex shedding frequency, while, in the drag direction, the dominant frequency is at twice the von Karman vortex shedding frequency (KANEKO et al., 2008). The vortex shedding frequency, f_w, is expressed in dimensionless form by the Strouhal number, St given by:

$$St = \frac{f_w d}{U}, \tag{3.49}$$

where d is diameter (characteristic length in the problem) and U the flow velocity. The problem arises when the dominant frequency of vortex shedding matches the tube resonance frequency, thus generating a high amplitude response of the tube, denoted as response to flow periodicity in Fig. 3.17. In fact, even if vortex shedding frequency is not exactly the same but very close to resonance frequency, the vortex shedding frequency synchronizes with the natural frequency of the structure, which is a phenomenon known as lock-in. According to Kaneko et al. (2008), such synchronization can occur both in transverse and parallel directions. Moreover, depending on conditions, synchronization in the parallel direction accompanied by symmetric vortex shedding may occur at lower flow velocities compared to transverse direction lock-in, as depicted in Fig. 3.18. In addition, Kaneko et al. (2008) indicate that the flow velocity that generates the symmetric synchronization may be suppressed in many cases when the fluid has low density (*e.g* gas flows).

Vortex may occur in tube arrays in a modified form of vortex shedding from a

Figure 3.18: *Vortex-induced synchronization, according to (KANEKO et al., 2008).*

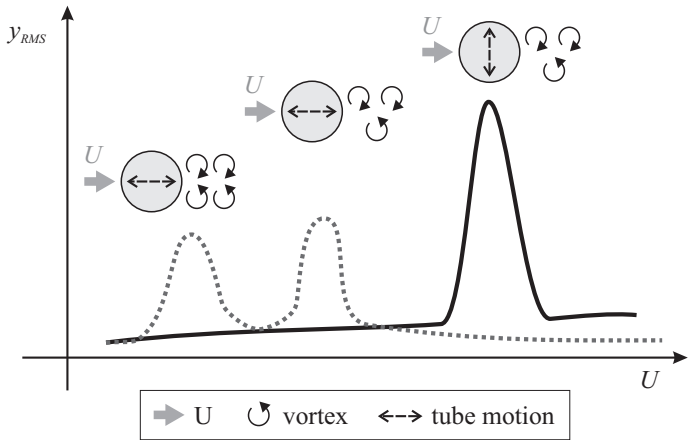

single cylinder (PAïDOUSSIS et al., 2011). The Strouhal number has been experimentally determined for tube arrays and is presented in Kaneko et al. (2008) in the format of maps, as shown in Fig. 3.19.

Figure 3.19: *Strouhal numbers for tube arrays related to pitch-to-diameter ratio (a) in-line array (b) staggered array, taken from (KANEKO et al., 2008).*

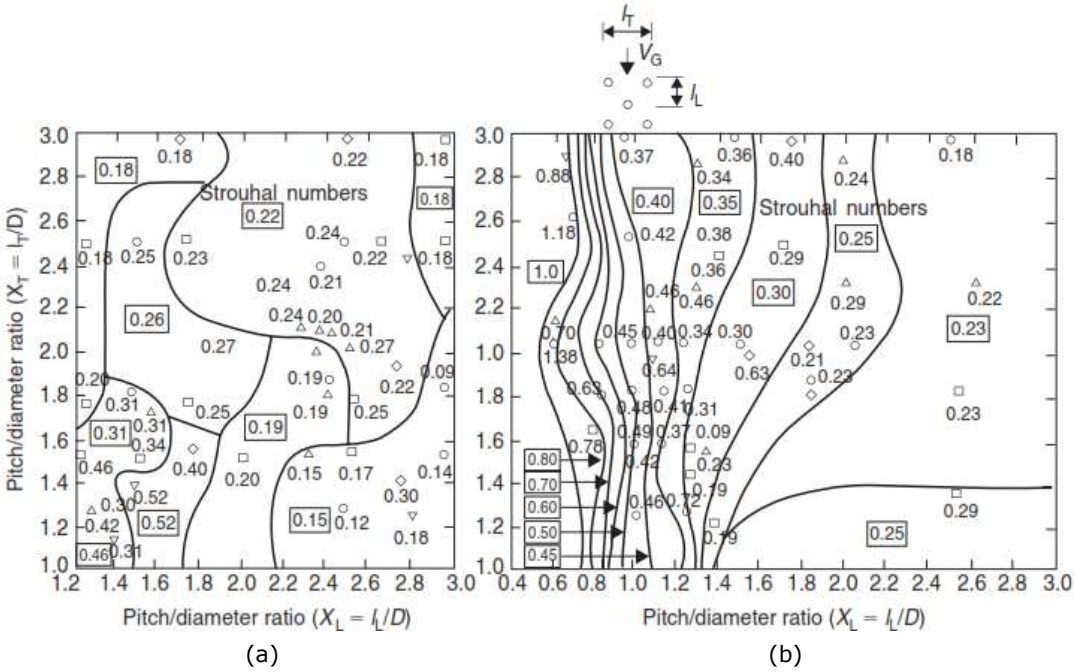

Undoubtedly, the most dangerous vibration mechanism is that referred to as fluidelastic instability, since once a critical cross flow velocity is exceeded, the vibration amplitude increases very rapidly with the flow velocity, as depicted in Fig. 3.17. For flow velocities higher than instability threshold, the tubes vibrate at or very near the tube natural frequency, in the natural modes of vibration, with amplitude that usually varies as U^4, compared with $U^{1.5}$ below the critical instability (BLEVINS, 2001).

Probably the most widely used model for predicting fluidelastic instability for

Table 3.2: *Values for fluidelastic instability constant K (BLEVINS, 2001).*

K	**Normal triangular**	**Rotated triangular**	**Rotated square**	**Normal square**	**All arrays**
K_{mean}	4.5	4.0	5.8	3.4	4.0
$K_{90\%}$	2.8	2.3	3.5	2.4	2.4

cylinder arrays subjected to crossflow is that attributed to Connors (1970), who derived a handy expression based on a quasi-static analysis given by:

$$\frac{U_{pc}}{f_n d} = K_C \left(\frac{m\delta}{\rho d^2} \right)^{1/2}, \tag{3.50}$$

where U_{pc} is the critical pitch flow velocity, δ is the logarithmic decrement, f_n is the tube natural frequency, and K_C is the Connor's constant, which is adjusted based on experimental database. Moreover, a identical expression for fluidelastic instability was deduced by Blevins (1974) by assuming that the fluid forces on a cylinder are purely due to the relative displacements with respect to its neighboring cylinders, which is not correct since Price & Païdoussis (1986) demonstrated that it is the motion of individual cylinders, rather than the relative motion between the cylinders, which is important. Anyway, the form of Eq. 3.50 is often referred to as Connors - Blevins model.

For example, Blevins (2001) suggests values for distinct array configurations. These are presented in Tab. 3.2, where K_{mean} is the mean-based fitted line and $K_{90\%}$ is a statistical lower bound for K so that 90% of the data points (experimentally registered instability threshold) will fall above the line described by Eq. 3.50. In addition, Pettigrew & Taylor (2003a) recommend a value of $K = 3.0$ for all tube bundle configurations in single-phase flow.

Another serious problem that may arise in tube arrays of heat exchangers with gaseous outer flow is that of acoustic resonance, involving very strong sound (160 - 176 dB in the heat exchanger, according to Blevins (2001) and only 20 - 40 dB less outside) (PAïDOUSSIS et al., 2011), which is a dangerous noise level for plant workers. Furthermore, sound discrete harmonic components may excite any structural element in the heat exchanger that present similar resonant frequency.

After that, due to the fact that phase change occurs in most of these heat exchangers, the attention came over two-phase flow. Khushnood et al. (2012) pointed out that the same vibration mechanisms of single-phase flow are present during two-phase flow, and that the occurrence of a specific vibration mechanism depends on the operational conditions. In fact, fluidelastic instability and turbulence-induced vibration during two-phase flow have been reported in the open literature. Moreover, parameters such

as void fraction and flow pattern hinder the study of these vibration mechanisms and the formulation of design guidelines aiming to predict the phenomena.

Regarding vortex shedding in two-phase flow, the information compiled in Kaneko et al. (2008) shows that periodic vortex shedding is observed in the low void fraction interval, below $\alpha_H = 15\%$, as in the case of single-phase flow. Furthermore, they indicate that no periodic vortex shedding has been observed at higher void fractions, however, the possibility of periodic vortex shedding in mist flow pattern should be considered. Kaneko et al. (2008) conclude that vortex shedding can be neglected in the homogeneous void fraction range of 15 - 95%, but its effect must be estimated otherwise, even in two-phase flow conditions, by using expressions capable of modeling two-phase flow velocity, *e.g.* homogeneous model, separated flow models (see, for instance, Collier & Thome (1994) Chapter 2).

Recently, another type of quasi-periodic forces have been reported in literature (ZHANG et al., 2007; PERROT et al., 2011), however only Zhang et al. (2007) make more precise observations about the results. Zhang et al. (2007) found quasi-periodic forces in both the parallel and transverse directions. These forces are significantly larger in the parallel direction. According to their results, the excitation force frequencies are relatively low (*i.e.*, 3 - 6 Hz) and not directly dependent on flow velocity in the parallel direction, which clearly differs from vortex-induced vibration mechanism. On the other hand, forces with quasi-periodic components at higher frequencies (up to 16 Hz) are present in transverse direction and they are directly related to flow velocity. According to Zhang et al. (2007), the quasi-periodic forces in parallel and transverse frequency are generated by different mechanisms that have not been observed so far. The quasi-periodic forces in parallel direction seem to be related to the moment flux fluctuation in the main flow path between the cylinders. On the other hand, the quasi-periodic forces in transverse direction are mostly correlated to oscillations in the wake of the cylinders of the tube bundle, that is, similar to vortex-induced vibration mechanism, even though periodic shedding was not believed to have occurred at such high void fraction (PETTIGREW et al., 1991; KANEKO et al., 2008; ZHANG et al., 2007). The feature that characterizes this mechanism is the fact that, in this mechanism, the Strouhal number seems to vary depending on pitch velocity. For instance, for $\alpha_H = 80\%$, Zhang et al. (2007) reported that periodic force frequency in the lift direction increases from about 5.75 to 16.75 Hz for a corresponding increase in pitch velocity of 1 to 10 m/s, which yields to Strouhal numbers variation from 0.22 to 0.07. Conversely, in the vortex shedding phenomenon in single-phase flow, the Strouhal number is a function of the geometrical parameters of the tube bundle (see Fig. 3.19). It is important to mention that Zhang et al. (2007) remark that further investigations are needed in order to be sure about the mechanisms that generate these forces.

In summary, there are some experimental conditions that favor one or another FIV

Table 3.3: *Vibration excitation mechanisms in two-phase crossflow (PETTIGREW et al., 1991).*

Flow situation	Fluidelastic instability	Periodic shedding	Turbulence excitation	Acoustic resonance
Liquid	•	+	+	o
Gas	•	o	+	•
Two-phase	•	o	•	o

•: Most important, +: Possible , o: Unlikely

mechanism. According to that proposed by Pettigrew et al. (1991) in Tab. 3.3, fluidelastic instability and turbulence-induced vibration are the most important mechanisms in tube bundles during two-phase crossflow, while vortex-induced vibration and acoustic resonance are unlikely to occur. However, recent experimental evidence suggests the existence of more vibration mechanisms, one of them in transverse direction, with some characteristics similar to vortex-induced vibration mechanism. Furthermore, these mechanisms related to quasi-periodic forces are currently been studied and information about its causes is scarce. Anyway, it is worth pointing out that Zhang et al. (2007) and Perrot et al. (2011) found these mechanisms with quasi-periodic forces by analyzing the buffeting vibration induced by two-phase flow.

The present study is focused on the buffeting vibration induced by turbulent flow, therefore this phenomenon is described below. Furthermore, design guidelines to predict this vibration mechanisms are presented.

3.2.2 Buffeting vibration induced by turbulent flow

The presence of turbulent flow is unavoidable and nearly universal in heat exchanger bundles (SINGH; SOLER, 1984). Although turbulence may sound as a difficulty, it is not entirely bad since it favors the heat transfer when compared with laminar flow. Thus, turbulence is also desirable to improve heat exchanger performance.

A turbulent flow field is characterized by a mean flow velocity on which a band of velocities associated with eddies and vortices are superposed. The turbulence, at the point of analysis, is the result of the combination of the turbulence level of the incoming flow and the turbulence generated by the passage across the upstream rows. A tube in the path of such a flow experiences a steady drag force and a series of periodic forces associated with the eddies. Thus, the fluid force acting on the tube may be described as an aggregate of a band of pulsating forces (SINGH; SOLER, 1984). This type of excitation, referred to as turbulence-induced vibration mechanism, is responsible by the tube vibration response below the threshold velocity for fluid elastic instability (PETTIGREW et al., 2001).

Turbulence-induced vibration mechanism will not lead to catastrophic failure; how-

ever there is a practical need for the designer of heat exchangers to be aware of the magnitude of vibration levels so that fretting-wear and fatigue can be avoided throughout the required heat exchanger lifetime. In this context, researchers have been able to bound the problem by developing relations for "some average of tube deflection amplitude" assuming an idealized level of coherence in the forcing functions (SINGH; SOLER, 1984). Design guidelines devoted to estimate the vibration level of a tube subjected to crossflow are given in the following section.

Buffeting vibration induced by single-phase flow: design guidelines

Singh & Soler (1984) indicate three design guidelines for turbulence-induced vibration, which correspond to that proposed by: Pettigrew et al. (1978), Pettigrew & Gorman (1981), Gorman (1981), Blevins et al. (1981) and Owen (1965).

Pettigrew et al. (1978), Pettigrew & Gorman (1981), Gorman (1981) For a simply supported tube and under the assumptions that the excitation field is fully correlated spanwise and the the tube vibrates in its first vibration mode, Pettigrew et al. (1978) propose a practical formula to estimate the mid-span root-mean-square amplitude of vibration of the tube, y_{rms}, given by:

$$y_{rms} = \frac{S_p^{1/2}}{\left(4\pi^5 f^3 m_0^2 \zeta\right)^{1/2}}, \tag{3.51}$$

where S_p is the power spectral density of the excitation force per unit length. The fundamental tube frequency and total damping ratio are represented by f and $zeta$, respectively, and m_0 is the total mass of the tube per unit length, including the added mass. Furthermore, as explained in Singh & Soler (1984), S_p may be defined in terms of the "effective random excitation coefficient" C_R^*, as follows:

$$S_p^{1/2} = \frac{1}{2}\rho v^2 d C_R^*, \tag{3.52}$$

where v is the reference gap crossflow velocity, d is the tube outside diameter and C_R^* is plotted in Fig. 3.20 based on experimental data collected by Pettigrew & Gorman (1981).

These values of C_R^* were obtained from experiments performed in water. Furthermore, as it can be seen from Fig. 3.20, the response of the tubes facing the shell inlet nozzle is predicted to be stronger than the tubes in the interior of the bundle.

Blevins et al. (1981) indicate that the following expression can be used to estimate the mid-span rms deflection:

Figure 3.20: *Random excitation coefficient C_R^* for calculating buffeting response of a cylinder array in crossflow, according to Pettigrew et al. (1978).*

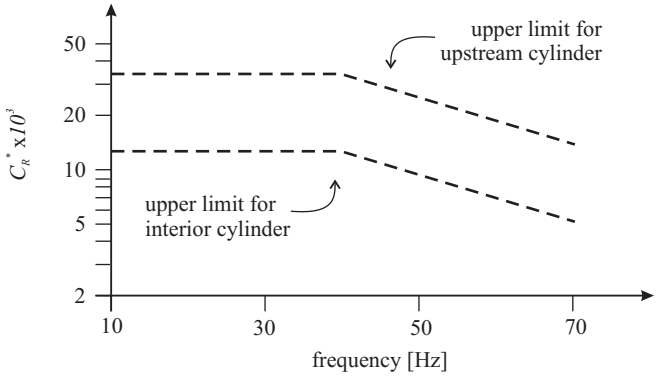

$$y_{rms} = \frac{S_F^{1/2} J \psi\,(l/2)}{\left(64\pi^3 f^3 m_0^2 \zeta\right)^{1/2}}, \tag{3.53}$$

where $\psi\,(l/2)$ is the mode shape deflection at mid-span, and J is the joint acceptance of the mode, which is a measure of the degree to which the distribution of force along the tube is compatible with the structural mode shape. J can be assumed to be equal to unity for a perfectly correlated force. For this expression, the power spectral density function, S_F, can be evaluated from Fig. 3.21, which is based on data obtained from tests performed in a wind tunnel by Blevins et al. (1981). Singh & Soler (1984) point out that,

Figure 3.21: *Lift coefficient C_L for buffeting response of a cylinder in crossflow, according to Pettigrew et al. (1978).*

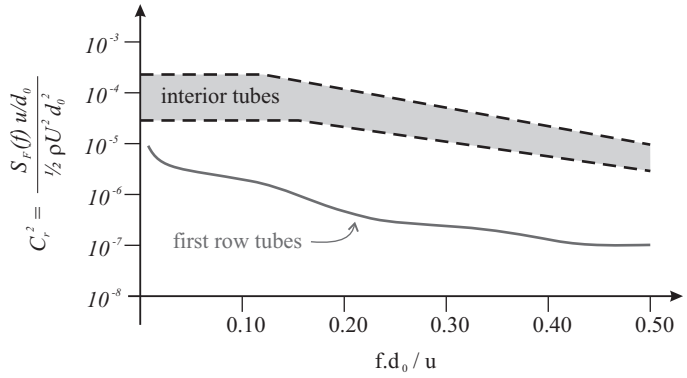

in contrast to data published by Pettigrew & Gorman (1981), the Blevins correlation seems to indicate that the interior tubes will experience greater deflection than the upstream tubes, which may be related to the differences in the upstream turbulence between the two sets of data.

Owen (1965) He noted that any turbulent flow contains a fluctuating pressure field, and reasoned that the tubes extract energy from the turbulent energy spectrum selectively in the manner of a narrow band filter (SINGH; SOLER, 1984). Following an heuristic

reasoning and buttressed with experimental data, Owen (1965) proposed an expression for the turbulent buffeting frequency, f_{tb}

$$f_{tb} = \frac{v}{d\tau\xi}\left[3.05\left(1-\frac{1}{x_t}\right)^2 + 0.28\right], \tag{3.54}$$

where τ and ξ are the transverse and parallel pitch-to-diameter ratio, respectively. Then, the proximity of f_{tb} to the natural frequency of the tube has to be checked in order to avoid any resonant response. Furthermore, Owen (1965) point out that this formula is not recommended when $\tau \to 1$. However, Weaver & Grover (1978) compared the frequency predicted by Eq. 3.54 with their experimental data and concluded that the estimated value of f_{tb} is quite reliable, even as $x_t \to 1$, as long as the minimum gap velocity, v_g, is used instead of the mean gap velocity, v (SINGH; SOLER, 1984).

Axisa et al. (1990) Pettigrew & Taylor (2003b) presented a review on vibration analysis procedures and recommended design guidelines for shell-and-tube heat exchangers. Regarding turbulence-induced excitation, the suggested method for defining an excitation upper bound is that presented by Axisa et al. (1990), which estimates an "equivalent power spectral density" (EPSD). First, the force power spectral density, $S_F(f)$, can be rendered dimensionless using a pressure scaling factor, p_0, and a frequency scaling factor, f_0, as follows:

$$\tilde{S}_F(f_R) = \frac{S_F(f)}{(p_0 d)^2} f_0, \tag{3.55}$$

where f_R is the reduced frequency, defined as f/f_0, and d is the tube diameter.

As explained by Axisa et al. (1990), a parameter referred to as correlation length, λ_c, which is used to formulate $S_F(f)$, is rarely known. Moreover, determinations of λ_c are very scarce, which hinders the calculation of $S_F(f)$. However, for practical applications, exact knowledge of λ_c is not required, at least provided that λ_c/L is much less than unity, where L is the tube length (AXISA et al., 1990). Thus, Axisa et al. (1990) present an EPSD, $\tilde{S}_F(f_R)_e$, defined as follows:

$$\tilde{S}_F(f_R)_e = \frac{\lambda_c}{L_e}\tilde{S}_F\left(f_R\right), \tag{3.56}$$

where L_e is the currently excited tube length. Using this definition, and based on the assumptions that the dynamic system presents a single dominant mode with a small damping ratio and that the modes are reasonably separated, Pettigrew & Taylor (2003b) present the EPSD for vibration mode 1 defined in terms of tube displacement, $y(x)$, as

Table 3.4: *Modal factor (a_1) and mode shape ($\phi_1^2(x_{max})$) (PETTIGREW; TAYLOR, 2003b).*

Configuration	Parameter	
	a_1	$\phi_1^2(x_{max})$
Rigid tube	2	1.0 (Translation)
Clamped - clamped	0.8	2.522
Clamped - pinned	0.9	2.578
Clamped - free	0.5	4.0
Pinned - pinned	1.1	2.0

follows:

$$\tilde{S}_F(f_R)_e = \frac{\overline{y^2(x)_1}64\pi^3 f_1^3 m^2 \zeta_1}{\phi_1^2 a_1} \frac{1}{(p_0 d)^2} f_0, \tag{3.57}$$

where $\phi_1(x)$ is the normalized mode shape for the first vibration mode, a_1 is the first dimensionless coefficient for the modal joint acceptance, f_1 is the first mode tube natural frequency, m is the total tube mass per unit length including hydrodynamic mass and ζ_1 is the damping ratio for the first vibration mode. Pettigrew & Taylor (2003b) present values for $\phi_1(x_{max})$ and a_1 for a variety of conditions, these are shown in Tab. 3.4.

To correctly compare spectra obtained using experimental rigs with varying geometries, it is necessary to define a reference EPSD, $\tilde{S}_F(f_R)_e^0$, based on a reference excited tube length, L_0:

$$\tilde{S}_F(f_R)_e^0 = \tilde{S}_F\left(f_R\right)_e \frac{L_e}{L_0} \tag{3.58}$$

It is important to note that the reference excited tube length stands for the length in which the design guideline upper bound is based. In this manner, the boundaries proposed by Pettigrew & Taylor (2003b) are defined for interior tubes as follows:

$$\tilde{S}_F(f_R)_e^0 = \begin{cases} 4 \times 10^{-4}(f/f_0)^{-0.5} & \text{if } 0.01 < f/f_0 < 0.5 \\ 5 \times 10^{-5}(f/f_0)^{-3.5} & \text{if } 0.5 < f/f_0 \end{cases} \tag{3.59}$$

and for inlet tubes:

$$\tilde{S}_F(f_R)_e^0 = \begin{cases} 1 \times 10^{-2}(f/f_0)^{-0.5} & \text{if } 0.01 < f/f_0 < 0.5 \\ 1.25 \times 10^{-3}(f/f_0)^{-3.5} & \text{if } 0.5 < f/f_0 \end{cases} \tag{3.60}$$

with a reference length of $L_0 = 1\text{m}$, $f_0 = U_p/d$ and $p_0 = \rho U_p^2/2$, where U_p is the pitch velocity.

Buffeting vibration in two-phase flow: design guidelines

In two-phase flow, various methods have been developed to analyze, collapse and normalize the available experimental data sets so that models can be proposed in order to define an upper bound envelope of two-phase flow-induced forces under certain operational conditions. There are few design guidelines available in literature, among them those proposed by Taylor et al. (1989), Papp & Chen (1994) and de Langre & Villard (1998), which will be detailed below.

Taylor et al. (1989) This design guideline is based on random vibration theory and relates the mean-square of a tube, $\bar{y^2}\,(x)$, to the excitation power spectral density, $S_F\,(f)$. Thus, for the fundamental vibration mode of a lightly-damped tube subjected to uniformly distributed and spatially correlated forces over its entire length, Mirza & Gorman (1973) propose that:

$$\bar{y^2}(x) = \frac{C_1 S_F(f)}{16\pi^3 f^3 \zeta M^2}, \tag{3.61}$$

where M is the tube mass per unit length including the hydrodynamic mass, ζ is the total damping ratio and f is the resonance frequency. The coefficient C_1 is adjusted for different boundary conditions and with the position x in the span L. For cantilever and fixed-pinned tubes, at their points of maximum displacement, the coefficients are 0.613 (at $x = L$) and 0.4213 (at $x = 0.581L$), respectively (TAYLOR et al., 1989). Among the considerations for Eq. 3.61 implementation, Taylor et al. (1989) indicate that it is valid only if there is a dominant peak at tube natural frequency. Furthermore, they remark that this is a conservative approximation since the random forces in multispan heat exchangers are not likely to be as well correlated as the forces acting on the idealized tube bundles used in test sections.

The excitation power spectral density, S_F, can be estimated from

$$NPSD = \frac{S_F(f)}{(Gd)^2}, \tag{3.62}$$

where G and d are the mass velocity and tube outside diameter, respectively, and the Normalized Power Spectral Density, $NPSD$, represents an upper bound that the force spectra induced by two-phase flow may reach. Based on experimental data, Taylor et al. (1989) fitted a function aiming to estimate $NPSD$ in terms of void fraction estimated according to the homogeneous model given by:

$$NPSD = 10^{(3\cdot\alpha - 5)}. \tag{3.63}$$

Taylor et al. (1989) analyzed the validity of the proposed design guideline and concluded that it should only be applied for homogeneous void fraction up to 90%. However, it is important to consider that homogeneous void fraction even lower than 90% may lead to intermittent-type flow patterns, which is an operational condition inducing high amplitude vibration and, therefore, it must be totally avoided in tube bundles.

Papp and Chen [1994] In this model, the authors proposed a correlation to estimate the RMS vibration displacement based on the hypothesis that energy related to the structure vibration corresponds to the dissipated energy from the fluid flow. The momentum transfer from the fluid to structure by means of mechanical vibration is mainly related to the mechanical energy of the flow, whose variation corresponds to the pressure drop. In this manner, when other flow parameters remain the same, Papp (1988) *apud* Papp & Chen (1994) proposed the following relationship for RMS tube displacement measured at tube free-end $\left(\bar{y^2}\right)^{0.5}$:

$$\left(\bar{y^2}\right)^{0.5} \sim \Delta P d, \tag{3.64}$$

where ΔP is the pressure drop across the tube row. From Eqs. 3.61 and 3.64, the following relation can be inferred for two-phase flows:

$$S_F(f) = C_I^2 \cdot \Delta P_{2\phi}^2 \cdot d^2, \tag{3.65}$$

where C_I is the coefficient of interaction. In this sense, Papp & Chen (1994) speculated that the relationship between tube response, its dynamic parameters and flow parameters can be studied by analyzing the behavior of C_I, which intends to capture and quantify the fluid-structure interaction under distinct flow conditions. Based on the fact that pressure drop occurs even for conditions without vibrating tubes, and it is related to viscous dissipation within the fluid, in the contact between fluid and solid walls and between the phases, it can be concluded that the highest parcel of the flow energy lost due to pressure drop is converted to heat. Therefore, it can be speculated that Papp & Chen (1994) adjusted a parameter to take into account only a parcel of the total energy, which is given by the coefficient of interaction.

The two-phase flow pressure drop, $\Delta P_{2\phi}$, as suggested by Papp & Chen (1994), can be obtained by combining the definition of two-phase friction multiplier, Φ_{l0}:

$$\phi_{l0}^2 = \frac{\Delta P_{2\phi}}{\Delta P_{l0}}, \tag{3.66}$$

and the correlation for pressure drop per tube row for liquid single-phase flow, ΔP_{l0},

proposed by Zukauskas & Ulinskas (1983):

$$\Delta P_{l0} = Eu_{l0}\frac{G^2}{2\rho_l}, \tag{3.67}$$

where Eu_{l0} is the Euler number related only to the pressure drop of liquid flow (total mass flux represented by liquid). Thus, $\Delta P_{2\phi}$ can be written as:

$$\Delta P_{2\phi} = \phi_{l0}^2 \cdot Eu_{l0} \cdot \frac{G^2}{2\rho_l}, \tag{3.68}$$

where, as suggested by Papp & Chen (1994), ϕ_{l0}^2 can be estimated as proposed by Grant & Chisholm (1979). Finally, the expression for the RMS vibration amplitude is obtained by substituting Eq.3.67 and Eq.3.68 in Eq.3.61, it results that:

$$\left(\bar{y^2}\right)^{0.5} = C_I \cdot \phi_{L0}^2 \cdot Eu_{L0}\left(\frac{C_1}{16\pi^3 f^3 m^2 \zeta}\right)^{0.5}\frac{G^2}{2\rho_l}d, \tag{3.69}$$

where $C_1 = 0.613$ for cantilevered tubes at maximum displacement point, as presented in Taylor et al. (1989). A remarkable feature of the model developed in Papp & Chen (1994) is that Eq.3.69 takes into account all the parameters of a coupled fluid-tube system; i.e.: (i) ϕ_{l0} is a function of two-phase flow parameters (α_H, G and P); (ii) Eu_{l0} depends on tube bundle geometry; and (iii) the group of parameters enclosed in parentheses contains information about the dynamic characteristics of the tube, as modeled in Mirza & Gorman (1973).

Once the flow parameters and dynamic characteristics of the tube can be estimated and $\left(\bar{y^2}\right)^{0.5}$ is measured, then Eq. 3.69 is used to calculate C_I. Papp & Chen (1994) reported values of C_I for two-phase flows based on experimental results reported by Taylor et al. (1989) across normal triangular, normal square and parallel triangular tube bundle configurations. The bundles consisted of cantilevered stainless steel tubes which are 600 mm in length, 13 mm in diameter, and have a wall thickness of 1.07 mm. The resulting natural frequency in air was a realistic value of approximately 33 Hz. Papp & Chen (1994) pointed out that, for each geometry, C_I values can be regarded as constant according to the following intervals of homogeneous void fraction; $\alpha_H \leqslant 50\%$ and $\alpha_H > 50\%$, as shown in Tab. 3.5.

Table 3.5: *Values of the coefficient of interaction C_I (PAPP; CHEN, 1994).*

α_H (Percent)	Normal triangular array $P/d = 1.47$	Normal triangular array $P/d = 1.32$	Normal square array $P/d = 1.47$	Parallel triangular array $P/d = 1.47$
$\leqslant 50\%$	0.0270	0.0171	0.0359	0.0312
$> 50\%$	0.0462	0.0326	0.0666	0.0641

De Langre and Villard [1998] Following the analysis of Axisa et al. (1990), de Langre & Villard (1998) found a scaling procedure capable of reducing the experimental force spectrum data and collapsing the results obtained during two-phase flow. Similarly to Taylor et al. (1989), de Langre & Villard (1998) proposed an upper bound for the dimensionless reference equivalent force spectrum, $\left[\bar{\Phi}_E^0\right]_U$, as:

$$\left[\bar{\Phi}_E^0\right]_U = 10 \cdot f_R^{-0.5} \quad \text{for} \quad 10^{-3} \leqslant f_R \leqslant 0.06, \tag{3.70}$$

$$\left[\bar{\Phi}_E^0\right]_U = 2 \cdot 10^{-3} f_R^{-3.5} \quad \text{for} \quad 0.06 \leqslant f_R \leqslant 1, \tag{3.71}$$

where f is the tube resonance frequency. The reduced frequency, f_R, is a dimensionless parameter given by:

$$f_R = \frac{f D_w}{U_p}, \tag{3.72}$$

where U_p is the average velocity of the two-phase homogeneous mixture calculated as:

$$U_p = G v_m = G \left(\frac{x}{\rho_g} + \frac{1-x}{\rho_l} \right), \tag{3.73}$$

where v_m is specific volume of the mixture assuming thermodynamic equilibrium. The parameter D_w is the length scale formulated as:

$$D_w = \frac{0.1d}{\sqrt{1-\alpha}}, \tag{3.74}$$

where, according to de Langre & Villard (1998), the void fraction is estimated according to the homogeneous model.

The practical use of the upper bound defined in Eqs.3.70, 3.71 and 3.74 is that, if the mechanical boundary conditions of the tube are linear, the RMS displacement contributed by the mode n can be formulated as:

$$\left[y_n^2(x)\right]^{0.5} = \left[\frac{\phi_n^2(x) L^2 a_n}{64\pi^3 f_n^3 M_n^2 \zeta_n} (\rho_l g D_w d)^2 \frac{D_w}{U_p} \left(\frac{L_0}{L} \right) \left(\frac{D}{D_0} \right) \left[\bar{\Phi}_E^0\right]_U \right]^{0.5}, \tag{3.75}$$

where L is the tube length, M_n is the tube total mass (including hydrodynamic mass), ζ_n is the total damping ratio and f_n is the resonance frequency. The modal shape, $\phi_n^2(x)$, and the modal correlation factor, a_n, for the first mode can be seen from Tab. 3.4. The

reference lengths are $L_0 = 1$ m and $D_0 = 0.02$ m, and g represents the gravitational acceleration.

Regarding the validity of this design guideline, the authors based on the data sets used to derive the model, indicate that the upper bound seems applicable for homogeneous void fractions from 10 to 95%, homogeneous velocities from 0.2 to 14 m/s.

Chapter 4

Virtual sensing

In recent years, virtual sensing has been proposed as a solution for determining forces when direct measurements are not feasible or present important technical challenges. In this context, virtual sensing has been proposed as a solution for problems in several areas in which forces are difficult to be modeled, for example, wind loads on turbines (BERG; Keith Miller, 2010), loads on mechatronic systems (CROES, 2017), dynamic forces on beams (LOURENS et al., 2012) and floating bridges (PETERSEN et al., 2018). In this sense, virtual sensing appears as a potential tool to study flow-induced vibrations in tube bundles.

According to the definition in Wilson (WILSON, 1997) *apud* Croes (CROES, 2017), virtual sensors, based on a previously modeled system, take readings from real physical sensors to calculate the desired outputs by using some process models. Moreover, these readings, say measurements, are used to get the system model continuously updated, thus model imperfections or non considered in-operating modifications are taken into account for every time instant. This feature enables the assessment of uncertain parameters or variabilities within the system (NAETS et al., 2015a), which, with the study of flow-induced vibration phenomena in mind, could mean tracking dynamic changes in the tube bundles promoted by the surrounding fluid and flow conditions.

Recently, the focus has shifted toward the development of combined deterministic - stochastic methods. These techniques differ from purely deterministic techniques since they model the noise as stochastic processes and assume that noise is present not only on the measurements, but also on the state variables. Furthermore, they differ from purely stochastic techniques because force values are still considered to be deterministic quantities (LOURENS et al., 2012). In this context, Kalman filtering (KF) (KALMAN, 1960; KALMAN; BUCY, 1961) based techniques have been introduced in the field of force estimation. This method provides a particularly practical and efficient state estimation algorithm for linear systems which leads to an optimal result with respect to the expected error covariance (NAETS et al., 2015b). In order to do that, the approach adopted by some authors (BERG; Keith Miller, 2010; LOURENS et al., 2012; NAETS et al., 2015a;

NAETS et al., 2015b) is to implement a coupled state - disturbance - parameter estimator based on a state-augmented Kalman filter (AKF). In other words, the regular states are augmented with the unknown forces in order to estimate them together (LOURENS et al., 2012). Such kind of estimator is needed in order to distinguish whether changes in time history result from inherent system dynamics or external excitation (CROES, 2017).

The AKF algorithm stability and methods to avoid estimates divergence are currently being discussed (LOURENS et al., 2012; NAETS et al., 2015b). Moreover, one of the most important questions to be clarified in this matter is what type of forces can be estimated reasonably via AKF. For instance, Berg and Keith Miller (BERG; Keith Miller, 2010) implemented the AKF algorithm to estimate random wind loads, while Lourens et al. (LOURENS et al., 2012) used the method to predict impulse and sine-sweep forces, showing acceptable results in both cases. Furthermore, Naets et al. (NAETS et al., 2015b) tested the AKF algorithm for the identification of impulsive forces showing good results. The main challenge in the present study resides in the fact that only accelerometers are used as sensors, which can lead to divergence in the estimated states (NAETS et al., 2015b). This issue is tackled here by augmenting the AKF algorithm with displacement dummy measurements (AKF-DM). In this manner, this modified AKF appears as a potential technique to study flow-induced forces in tube bundles based only on acceleration measurements, which is a clear advantage since these kind of sensors are versatile, can be easily installed, and their cost is reasonable.

In the following sections, the KF algorithm and the manipulation of its equations until obtain the AKF algorithm are introduced. Further, the inclusion of dummy measurements to correct drifts in AKF state estimations will be addressed. This chapter is mainly based on work submitted by the author at the Journal of Mechanical Systems and Signal Processing (ÁLVAREZ-BRICEÑO et al., 2018b).

4.1 Kalman filter and augmented Kalman filter algorithms

This section is devoted to define the formulation used in the implementation of the KF algorithm. Before that, it is necessary to define the equations that model a mechanical system. Since the present study will implement the KF algorithm on an existing physical structure, the system modeling equations are expressed in terms of the results provided by a typical Experimental Modal Analysis (EMA) procedure. Moreover, the discrete format of the state space model is introduced since the KF is a recursive algorithm that, for the present application, uses acceleration measurements (acceleration time histories) as reference in order to minimize estimates deviation.

4.1.1 State equations for the mechanical system

Mechanical systems can be modeled as a system of second-order differential equations:

$$\mathbf{M}\ddot{\xi} + \mathbf{C}\dot{\xi} + \mathbf{K}\xi = \mathbf{b}\mathbf{f} + \mathbf{b_d}\mathbf{f_d}, \tag{4.1}$$

where $\mathbf{M}$, $\mathbf{C}$ and $\mathbf{K}$ are the system's mass, damping and stiffness matrices, respectively, and ξ is the vector of physical generalized coordinates. The terms $\mathbf{f}$ and $\mathbf{f_d}$ represent the forces and unknown disturbances, which are applied on the system at positions described by the selection matrices $\mathbf{b}$ and $\mathbf{b_d}$, respectively.

The properties of the mechanical system represented by Eq. 4.1 can be extracted from either numerical or experimental techniques. A common approach in structural dynamics and control is to use a modal representation which often leads to compact and computationally efficient models (TRINDADE et al., 2015). In that way, after the tests are performed, and under the assumptions that the system is Linear Time - Invariant (LTI) with proportional viscous damping, related algorithms are used to obtain a $n \times n$ modal matrix $\mathbf{\Psi}$, n undamped natural frequencies ω_n, and n viscous damping ratios ζ_n, where n is the model size given by the n degrees of freedom (DOFs) used to represent the system. This set of data enables the derivation of a completely defined modal model, which is a decoupled representation of the system in Eq. 4.1 and it is given by:

$$\ddot{\eta} + 2\mathbf{\Lambda}\mathbf{\Omega}\dot{\eta} + \Omega^2\eta = \mathbf{\Psi}^T\mathbf{b}\mathbf{f} + \mathbf{\Psi}^T\mathbf{b_d}\mathbf{f_d}, \tag{4.2}$$

where η is the modal coordinate such that

$$\xi = \mathbf{\Psi}\eta, \tag{4.3}$$

and Λ and Ω are defined as

$$\mathbf{\Omega} = \begin{bmatrix} \ddots & & \\ & \omega_r & \\ & & \ddots \end{bmatrix}, \qquad \mathbf{\Lambda} = \begin{bmatrix} \ddots & & \\ & \zeta_r & \\ & & \ddots \end{bmatrix}. \tag{4.4}$$

The system of differential equations presented in Eq. 4.2 can be expressed as a system of first order differential equations referred to as state space model, which is more convenient from a computational point of view (de Oliveira et al., 2009). Thus, for a LTI system it can be defined by:

$$\dot{\mathbf{x_s}}(t) = \mathbf{A}\mathbf{x_s}(t) + \mathbf{B}\mathbf{u}(t) + \mathbf{B_1}\mathbf{w}(t), \tag{4.5}$$

with measurements

$$\mathbf{y}(t) = \mathbf{H}\mathbf{x_s}(t) + \mathbf{v}(t), \tag{4.6}$$

where $\mathbf{x_s}(t)$ is the state vector defined as $\{\eta, \dot{\eta}\}^T$, $\mathbf{u}(t)$ is the known control inputs vector, $\mathbf{y}(t)$ represent the sensor outputs vector, and $\mathbf{w}(t)$ and $\mathbf{v}(t)$ are the process and measurement noise, which are assumed as stochastic processes (LOURENS et al., 2012). The state matrix $\mathbf{A}$, the input matrix $\mathbf{B}$ and input disturbance matrix $\mathbf{B_1}$ are formulated as:

$$\mathbf{A} = \begin{bmatrix} 0 & \mathbf{I} \\ -\mathbf{\Omega}^2 & -\mathbf{2\Lambda\Omega} \end{bmatrix} \qquad \mathbf{B} = \begin{bmatrix} 0 \\ \mathbf{\Psi}^T\mathbf{b} \end{bmatrix} \qquad \mathbf{B_1} = \begin{bmatrix} 0 \\ \mathbf{\Psi}^T\mathbf{b_d} \end{bmatrix}. \tag{4.7}$$

Furthermore, $\mathbf{H}$ is the measurement matrix used to theoretically formulate the measurement as a linear combination of the states at a given time. The measurement matrix will be formulated further for the augmented-state case.

Equations 4.5 and 4.6 are derived in continuous time domain. However, the simulation analysis using KF algorithms is performed by sampling the system dynamics at regular time intervals, therefore it is convenient to define the system equations in the discrete time domain. In this manner, these differential equations can be expressed as recursive difference equations (FRANKLIN et al., 1998)

$$\mathbf{x_s}(k+1) = \mathbf{\Phi}\mathbf{x_s}(k) + \mathbf{\Gamma}\mathbf{u}(k) + \mathbf{\Gamma_1}\mathbf{w}(k), \tag{4.8}$$

with measurements

$$\mathbf{y}(k) = \mathbf{H}\mathbf{x_s}(k) + \mathbf{v}(k), \tag{4.9}$$

where $\mathbf{\Phi}$, $\mathbf{\Gamma}$ and $\mathbf{\Gamma_1}$ are the discrete versions of matrices $\mathbf{A}$, $\mathbf{B}$ and $\mathbf{B_1}$, respectively. There are some methods to convert continuous system matrices into their discrete - time versions that have already been implemented in MATLAB ®. In the present study, the zero-order hold (ZOH) method is adopted.

Regarding the properties of process and measurement noise, $\mathbf{w}(k)$ and $\mathbf{v}(k)$, respectively, it can be assumed that they are random stationary sequences, mutually uncorrelated, with zero mean, that is:

$$\mathbf{E}\{\mathbf{w}(k)\} = \mathbf{E}\{\mathbf{v}(k)\} = 0,$$

have no time correlation or are "white" noise, that is:

$$\mathbf{E}\left\{\mathbf{w}(i)\mathbf{w}^T(j)\right\} = \mathbf{E}\left\{\mathbf{v}(i)\mathbf{v}^T(j)\right\} = 0 \qquad \text{if} \quad i \neq j,$$

and their covariances or mean square "noise levels" are defined by

$$\mathbf{E}\left\{\mathbf{w}(k)\mathbf{w}^T(k)\right\} = \mathbf{R_w}, \qquad \mathbf{E}\left\{\mathbf{v}(k)\mathbf{v}^T(k)\right\} = \mathbf{R_v}.$$

as detailed in (FRANKLIN et al., 1998) and accepted in references (BERG; Keith Miller, 2010; LOURENS et al., 2012; NAETS et al., 2015b).

4.1.2 Kalman filter equations

The Kalman filter (KALMAN, 1960; KALMAN; BUCY, 1961) can be defined as a recursive linear state estimator designed to be optimal in a minimum - variance unbiased sense (LOURENS et al., 2012).

The backbone of Kalman filtering is the propagation of the covariance of the state estimates, $\mathbf{P}$ (NAETS et al., 2015b). In this manner, the basic idea behind this algorithm is to calculate the best state estimate $\hat{\mathbf{x}}_\mathbf{s}(k)$, by combining a previous estimate $\bar{\mathbf{x}}_\mathbf{s}(k)$ with the current measurement $\bar{\mathbf{y}}(k)$, based on the relative accuracy of both, which is given in terms of the covariance of the prior estimate, $\mathbf{G}(k)$, and the covariance of the current measurement $\mathbf{R_v}$. Furthermore, the other key idea is to use the known dynamics of $\mathbf{x}_s$ to predict its behavior in order to estimate $\bar{\mathbf{x}}_\mathbf{s}(k)$ given $\hat{\mathbf{x}}_\mathbf{s}(k-1)$ (FRANKLIN et al., 1998).

The discrete KF algorithm can be organized in two-stages: measurement update and time update. Based on Franklin et al. (1998), a summary of the required relations is:

- At the measurement time (measurement update)

$$\hat{\mathbf{x}}_\mathbf{s}(k) = \bar{\mathbf{x}}_\mathbf{s}(k) + \mathbf{P}(k)\mathbf{H}^T\mathbf{R}_\mathbf{v}^{-1}\left(\mathbf{y}(k) - \mathbf{H}\bar{\mathbf{x}}_\mathbf{s}(k)\right), \tag{4.10}$$

  where

$$\mathbf{P}(k) = \mathbf{G}(k) - \mathbf{G}(k)\mathbf{H}^T\left(\mathbf{H}\mathbf{G}(k)\mathbf{H}^T + \mathbf{R_v}\right)^{-1}\mathbf{H}\mathbf{G}(k). \tag{4.11}$$

- Between measurements (time update)

$$\bar{\mathbf{x}}_\mathbf{s}(k+1) = \mathbf{\Phi}\hat{\mathbf{x}}_\mathbf{s}(k) + \mathbf{\Gamma}\mathbf{u}(k), \tag{4.12}$$

  and

$$\mathbf{G}(k+1) = \mathbf{\Phi}\mathbf{P}(k)\mathbf{\Phi}^T + \mathbf{\Gamma_1}\mathbf{R_w}{\mathbf{\Gamma_1}}^T, \tag{4.13}$$

  where the initial conditions for $\bar{\mathbf{x}}(0)$ and $\mathbf{G}(0)$ must be assumed to be some value for initialization.

4.1.3 Augmented Kalman filter for input estimation

The discrete Kalman filter algorithm can be redesigned in order to allow the coupled state - disturbance estimation. In order to do that, the input vector is included in the state vector. However, as noted by Naets et al. (2015b) and Berg & Keith Miller (2010), the dynamics relating $\dot{\mathbf{u}}$ to the new state vector, now composed by η, $\dot{\eta}$ and $\mathbf{u}$, are likely

unknown. This lack of knowledge can be modeled setting:

$$\dot{\mathbf{u}}(t) = 0 + \mathbf{z}(t), \tag{4.14}$$

where $\mathbf{z}$ is a random vector, thus making $\mathbf{u}$ constant except for model uncertainty. In this manner, Eq. 4.8 can be rearranged as (BERG; Keith Miller, 2010):

$$\begin{gathered}\begin{bmatrix}\mathbf{x_s}(k+1)\\ \mathbf{u}(k+1)\end{bmatrix} = \begin{bmatrix}\mathbf{\Phi} & \mathbf{\Gamma}\\ 0 & \mathbf{I}\end{bmatrix}\begin{bmatrix}\mathbf{x_s}(k)\\ \mathbf{u}(k)\end{bmatrix} + \begin{bmatrix}\mathbf{\Gamma_1} & 0\\ 0 & \Delta t\mathbf{I}\end{bmatrix}\begin{bmatrix}\mathbf{w}(k)\\ \mathbf{z}(k)\end{bmatrix},\\ \begin{bmatrix}\mathbf{w}(k)\\ \mathbf{z}(k)\end{bmatrix} \sim N\left(0, \begin{bmatrix}\mathbf{R_w} & 0\\ 0 & \mathbf{R_z}\end{bmatrix}\right)\end{gathered} \tag{4.15}$$

where Δt is the time step. Furthermore, in the case of acceleration measurement on each DOF, the measurements equation is given by

$$\mathbf{y}(k) = \begin{bmatrix}\mathbf{-\Psi\Omega^2} & \mathbf{-2\Psi\Lambda\Omega} & \mathbf{\Psi\Psi}^T\mathbf{b}\end{bmatrix}\begin{bmatrix}\mathbf{x_s}(k)\\ \mathbf{u}(k)\end{bmatrix} + \mathbf{v}(k), \quad \mathbf{v}(k) \sim N\left(0, \mathbf{R_v}\right) \tag{4.16}$$

Therefore, the AKF for coupled state - disturbance excitation can be implemented by substituting the non-starred matrices by the starred ones in Eqs. 4.10 - 4.13:

$$\begin{gathered}\mathbf{\Phi}^\star = \begin{bmatrix}\mathbf{\Phi} & \mathbf{\Gamma}\\ 0 & \mathbf{I}\end{bmatrix}, \quad \mathbf{\Gamma}^\star = 0, \quad \mathbf{\Gamma_1^\star} = \begin{bmatrix}\mathbf{\Gamma_1} & 0\\ 0 & \Delta t\mathbf{I}\end{bmatrix},\\ \mathbf{R_w^\star} = \begin{bmatrix}\mathbf{R_w} & 0\\ 0 & \mathbf{R_z}\end{bmatrix}, \quad \mathbf{H}^\star = \begin{bmatrix}\mathbf{-\Psi\Omega^2} & \mathbf{-2\Psi\Lambda\Omega} & \mathbf{\Psi\Psi}^T\mathbf{b}\end{bmatrix}.\end{gathered} \tag{4.17}$$

4.2 Dummy measurements implementation in augmented Kalman filter

Naets et al. (NAETS et al., 2015b) point out that the stability of AKF estimation algorithms is mainly dependent on the choice of measurements since, in general, the system is given. Thus, based on previous work by Lourens et al. (LOURENS et al., 2012) and using the Popov-Belevitch-Hautus (PBH) criterion (HAUTUS, 1970), Naets et al. (NAETS et al., 2015b) proposed a detectability evaluation, so that long-term stability is guaranteed. This detectability analysis showed that the typical case where forces are reconstructed via AKF methods, based only on acceleration measurements on a structure, will inevitably lead to divergence issues. In fact, the estimator stability can only be guaranteed in the case of a full position measurement on the system under consideration, which is impractical (NAETS et al., 2015b).

Aiming stable simulations, Naets et al. (NAETS et al., 2015b) propose to add dis-

placement dummy measurements for the positions in which the acceleration response is measured. In fact, they show via numerical and experimental validations that the inclusion of such dummy measurements to the AKF algorithm (AKF-DM) present stable and consistent results on force predictions, while force estimation through regular AKF diverges from the real force values over longer estimation periods. This is a solution similar to that initially proposed by Chatzi and Fuggini (CHATZI; FUGGINI, 2012) for civil structure monitoring purposes. This artifice is plausible since, in structural systems, the deformation of the structure is bounded and it can typically be estimated a priori via analytical models or finite element models. In this way, the estimated deformation can then be considered as the uncertainty on a dummy measurement with an actual zero value (NAETS et al., 2015b).

It is worth mentioning that Naets et al. (NAETS et al., 2015b) used dummy measurements on displacement, since their notation was formulated such that the state vector is composed by physical coordinates and its time derivatives, that is according to the present nomenclature, ξ and $\dot{\xi}$. On the other hand, since the present study is formulated in modal coordinates, the dummy measurements must be proposed on η. The dummy measurements have equations

$$\mathbf{H_{dm}}\mathbf{x_s} + \mathbf{v_{dm}} = 0, \tag{4.18}$$

with

$$\mathbf{H_{dm}} = \begin{bmatrix} \mathbf{I}_n & 0 & 0 \end{bmatrix}. \tag{4.19}$$

Equation 4.18 states that the value of that modal coordinate is zero with an uncertainty $\mathbf{v_{dm}}$ with covariance $\mathbf{R_{dm}}$. Moreover, the entries of $\mathbf{R_{dm}}$ can be used for the tuning of the KF. For instance, if the problem is formulated in physical coordinates, Naets et al. (NAETS et al., 2015b) suggest that values should be chosen an order of magnitude higher than the actual motion of the system. Furthermore, covariances smaller than the suggested will constrain the estimates too much and may lead to erroneous results. On the other hand, if too high covariances are set, the dummy measurement will not be able to properly restrict the drift on the estimates (NAETS et al., 2015b). In the case of systems modeled in modal coordinates, there are not suggestions in literature for values of dummy measurements on η, which is not surprising since this is the first work that uses AKF-DM in modal coordinates aiming input estimation.

In order to consider the dummy measurements in the AKF algorithm, some definitions must be updated. The measurement matrix has to include information about dummy measurements in Eq. 4.18,

$$\mathbf{H_T^\star} = \begin{bmatrix} \mathbf{H^\star} \\ \mathbf{H_{dm}} \end{bmatrix}, \tag{4.20}$$

the sensor outputs vector must contain the dummy measurements, $\mathbf{y_{dm}}$, which are null,

$$\mathbf{y_T} = \begin{Bmatrix} \mathbf{y} \\ \mathbf{y_{dm}} \end{Bmatrix} = \begin{Bmatrix} \mathbf{y} \\ 0 \end{Bmatrix}, \tag{4.21}$$

and the measurement covariance matrix must include the dummy measurements covariance, as follows,

$$\mathbf{R_T} = \begin{bmatrix} \mathbf{R_v} & 0 \\ 0 & \mathbf{R_{dm}} \end{bmatrix}. \tag{4.22}$$

Naets et al. (NAETS et al., 2015b) point out that, due to the relatively large uncertainty on these dummy measurements, they will not contribute considerably to the fast estimation, typically required in force estimation for control tasks. However, they will prevent the long term drift created by the force estimation based on only acceleration measurements. In fact, since the objective of the present work is to estimate a force rather than control a system, a fast estimation is not needed.

The dummy measurements proposed in this section are considered in the AKF algorithm by substituting $\mathbf{H}^\star$ by the new measurement matrix defined by Eq. 4.20, and the measurement vector $\mathbf{y}$ by that defined in Eq. 4.21.

Chapter 5

Experimental apparatus

This section describes the test bench used during the experimental campaign including its general configuration, systems for flow parameters measurements, as well as the instrumentation for tube response measurement. More detailed information on the test bench design and its validation can be found in Kanizawa & Ribatski (2016a).

5.1 Two-phase flow and measurement apparatus

The experimental facility used for flow pattern identification and FIV evaluation consists of a tube bundle that relies on injection and conditioning sections, a water loop and an air compression and conditioning system. The water loop comprises a reservoir, a 15 CV centrifugal pump, electromagnetic volumetric flow transducers, a heat exchanger to control water temperature, and a perforated tube injector. Air is compressed by a 40 HP rotary screw compressor, and passes sequentially by a heat exchanger, reservoir, regulating pressure valve, turbine volumetric flow meters, needle and globe valves and is injected by 7 membrane injectors. The water is injected in the bottom region of the test section, followed by the injection of air. The two-phase mixture passes by a static mixer just upstream the test section. Downstream the test section, the flow is directed to a cyclone type separator, from which the water is directed to the reservoir and the air to laboratory outside. The main features of the described experimental facility are shown in Fig. 5.1.

The test section consists of a triangular tube bundle, counting with 19 mm (3/4") OD, 381 mm long stainless steel tubes, with transverse pitch-to-diameter ratio τ equal to 1.26. The tubes are distributed in 20 rows, where even rows have 4 tubes and odd have 3 tubes plus two half tubes positioned in the section wall to avoid bypass flow, as it is shown in Fig. 5.2. Thus, the experiments can be performed for upward crossflow condition.

Regarding the tube bundle mounting, all tubes are rigidly installed, except the instrumented tube (detailed in Section 5.3), which is located at the center of the 13th

Figure 5.1: *Scheme for the experimental facility used in the present study.*

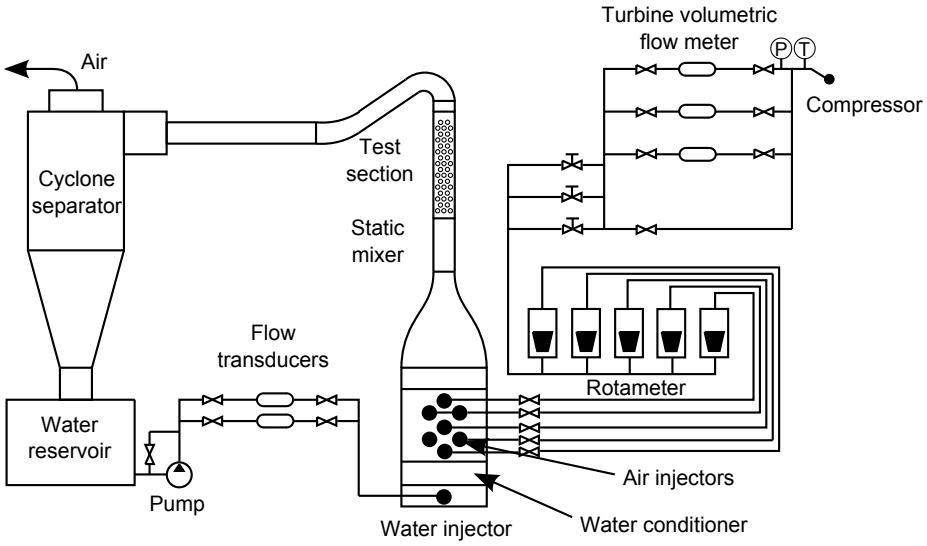

row. For the sake of experimental conditions repeatability, the tube has been installed at a zone where the two-phase flow is considered developed. Even though the flow characteristics continually change along the flow path due to variation of gas specific volume, the flow can be considered developed after the stabilization of flow pattern and negligible variation of flow parameters, such as pressure drop gradient. The required length, or number of rows in the case of external flow across tube bundles, for flow development depends on the inlet and operational conditions, as well as on the channel geometry. Hence, the tube bundle itself determines the phase distributions and mixing. In this context, Kanizawa & Ribatski (2016a) addressed criteria to characterize flow development during two-phase upward crossflow in tube bundles, which is based on the pressure gradient measurements; and for the present tube bundle geometry, the flow can be considered developed downstream the seventh tube row. Therefore, the instrumented tube is installed downstream the number of rows required for flow development. Moreover, this criterion is supported by the findings of Kondo & Nakajima (1980). They found that, under conditions of two-phase flow, reduced flow velocities and for $\tau = 1.28$, the flow is completely developed after the eleventh tube row. The authors also indicated that the number of tube rows required for the flow development increases with increasing τ. Nonetheless, Kondo & Nakajima (1980) performed experiments for very low flow velocities, typical of kettle reboilers.

5.2 Experimental conditions

The flow conditions set in the present study were defined according to the homogeneous void fraction model because of its ease of implementation. In this manner, distinct gas and liquid superficial velocities combinations are tested at void fractions α_H varying

Figure 5.2: *Scheme for the test section used in the present study.*

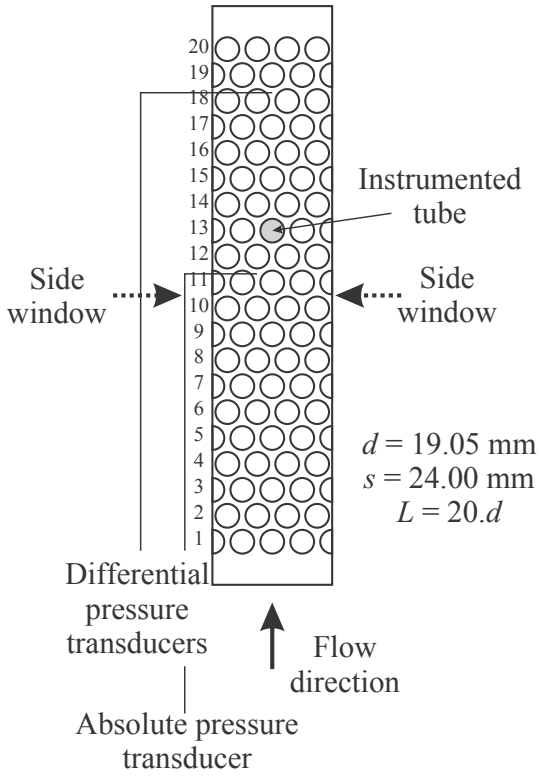

from 30% to 95%. These experimental conditions were represented in the flow pattern map proposed by Kanizawa & Ribatski (2016a), which is shown in Fig. 5.3. As it can be noticed, the selected experimental conditions are distributed in the bubbles, churn and intermittent flow patterns. Therefore, it is expected that the obtained results allow to notice distinct vibration response for each flow pattern.

5.3 Devices for vibration measurements

Flow-induced vibration studies are performed by analyzing the dynamic response of instrumented tubes, which are installed in a test section and subjected to the fluid flow. Álvarez-Briceño (2014) present a review on the distinct ways a tube has been mounted for FIV studies in the open literature. The installation method for the instrumented tubes may vary for each study. For example, the analyzed tube can be mounted in cantilever (clamped at one end), rigidly mounted or clamped at both ends, flexibly mounted by using devices with lower stiffness than the tube material or suspended by using tensioned wires as in Álvarez-Briceño et al. (2015).

Based on previous tests performed in the same test bench (ÁLVAREZ-BRICEÑO, 2014), the mounting configuration must be as simple as possible in order to minimize the number of uncertainties related to the tube installation. In this context, two types of configuration are feasible: cantilever and rigid mounting. In order to facilitate the tube

Figure 5.3: *Transition curves for air-water two-phase flow ($P = 95kPa$; $T = 25°C$) according to Kanizawa & Ribatski (2016a). Pentagram marks correspond to half the mass flux for fluidelastic instability threshold.*

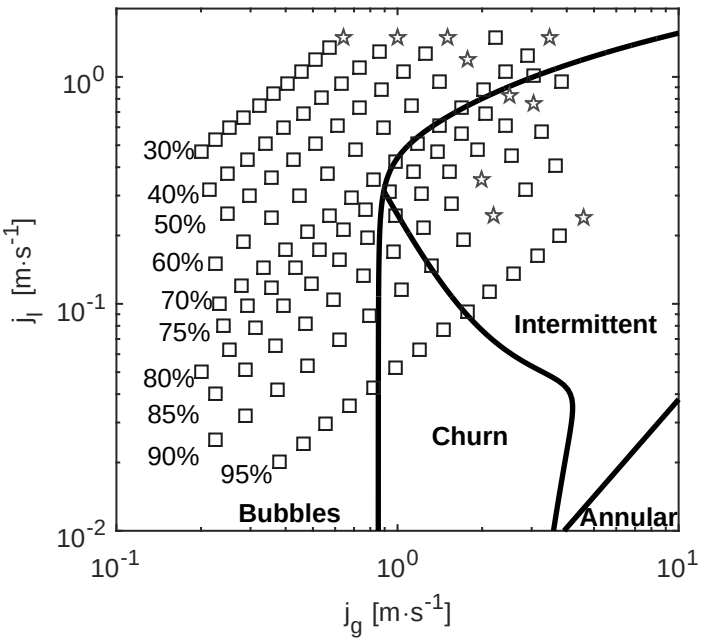

instrumentation, it was decided to use the cantilever configuration, which also allows the tube to present lower natural frequencies if compared to the rigid installation. It is important to point out that lower natural frequencies are considered as advantageous since typical resonance frequencies found in heat exchanger tubes are in the range of 30 Hz (PETTIGREW et al., 2001).

In the present study, two distinct cantilevered instrumented structures are used. At the first stage, the vibration of an instrumented tube is measured in order to analyze its dynamic response, check some turbulence - induced vibration guidelines and its dynamic parameters; *e.g.* damping and hydrodynamic mass. Some hardware limitations as tube length, tube diameter and instrumentation size hindered the installation of instruments at several positions along the tube. Therefore, the tube was instrumented as a 1 degree of freedom system along parallel and transverse (to the main flow velocity) directions. Subsequently, for the study of the crossflow induced forces, it was decided to use a structure whose response can be measured at more than one position. The main motivation behind this decision is to get more information about the structure response due to the crossflow induced force. In this sense, a cylinder was manufactured so that vibration can be measured at two positions. Thus, it can be modeled as a 2 degree of freedom system along transverse and parallel directions. These structures and their instrumentation are described in detail the following sections.

5.3.1 Instrumented tube

The dynamic response of the cantilevered tube is measured by piezoelectric uniaxial microaccelerometers model 352A24 with broadband resolution of 0.002 m/s^2 RMS (0.0002 g RMS), from PCB Piezotronics. The microaccelerometers were fixed in a support, which in turn is installed inside the tube at its free-end. The support was manufactured so that the accelerometers can be installed on its surfaces, with the sensing axes perpendicular to each other, allowing the measurement of transverse and parallel acceleration components. Furthermore, the support has the function of sealing the tube by means of o-rings, hence the leakage to the interior of the instrumented tube is avoided. Moreover, the condensation of air moisture tube is non-existent. This set-up is shown in Fig. 5.4.

Figure 5.4: *Tube instrumented with microaccelerometers*

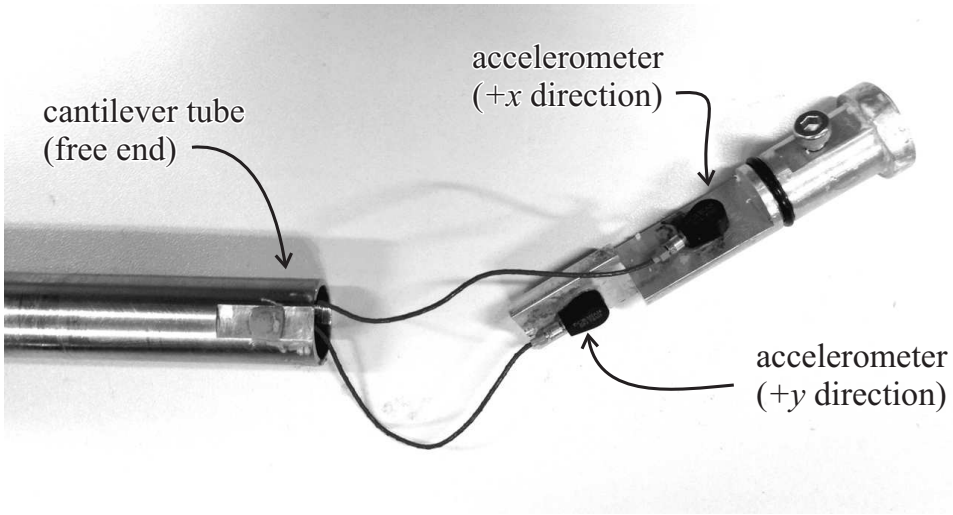

Data is acquired with a SCADAS Mobile system running Siemens Test.Lab. The authors have devised the methodology for data acquisition and signal processing based on the form that these results are typically presented in the recent literature as well as the qualitative evolution of the data during the initial runs. The dynamic behavior of the tube was identified. It was checked that the flow is not able to excite the tube at high frequencies. Moreover, a compromise was implemented considering the narrower time window, the better resolution as possible and an appropriate number of linear averages. In addition, the selected bandwidth must contain the first resonance peak since it is used to extract dynamic parameters such as hydrodynamic mass and damping. Based on these criteria, the acceleration was measured in periods of 8 s, with a sampling frequency of 2048 Hz and a resolution of 0.125 Hz. The analyzed PSDs are the result of 40 linear averages, which resulted in spans of 320 s for each flow condition, enough to ensure the present data quality as well as flow stability. The whole set-up used for dynamic measurements is depicted in Fig. 5.5.

Figure 5.5: *Set-up scheme for measuring tube response.*

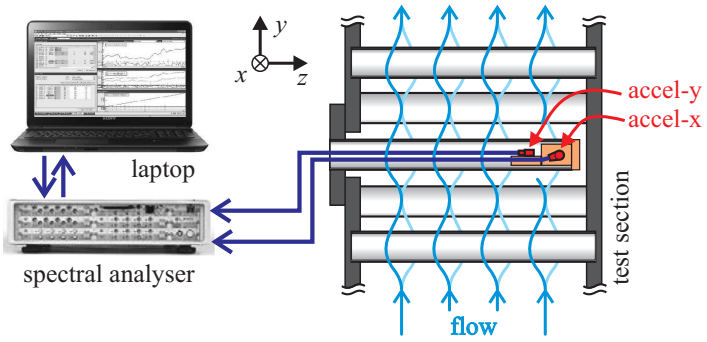

5.3.2 Two-degree of freedom cylinder

The stainless steel structure (386 mm length, 19 mm diameter), shown in Fig. 5.6, has been manufactured in order to allow the installation of the instruments that will sense the structure vibration due to crossflow induced forces. The structure is instrumented with four piezolectric uniaxial accelerometers model 352A24 with broadband resolution of 0.002 m/s^2 RMS (0.0002 g RMS), from PCB Piezotronics. They are installed at positions A1 (185 mm from fixed end) and A2 (345 mm) with sensing axes perpendicular to each other so that they can measure vibration in x and y coordinates.

Figure 5.6: *Instrumented cylinder.*

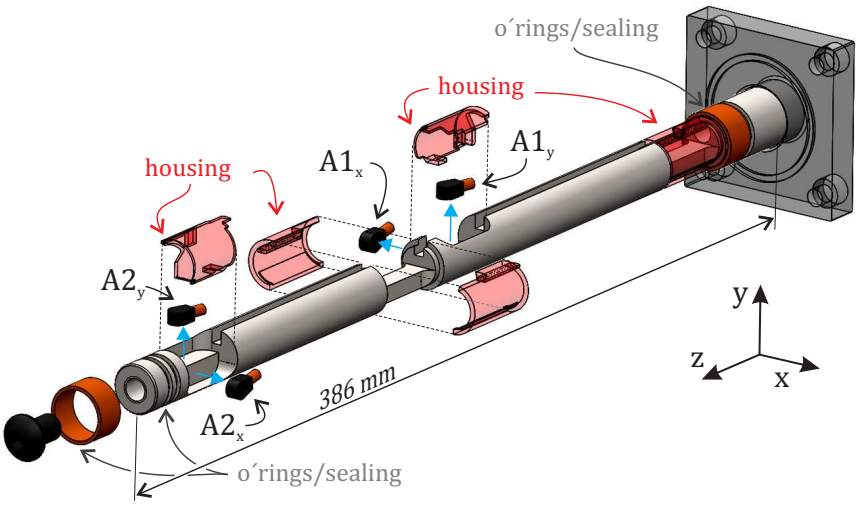

After the sensors are installed, four 3D printed housing components are mounted on the structure, as shown in Fig. 5.6, in order to provide a uniform cylindrical profile. Eventually, the structure is coated with a heat shrink tube in order to isolate the instruments from liquid when underwater test are performed. Two aluminum rings are used to compress the o-rings mounted at the end and close to the clamping edge, and a stainless steel bolt is used to compress the heat shrink tube against the structure tip,

adding some redundancy to the sealing of the instrumentation compartments.

As well as in the case of the instrumented tube, data is acquired with the same system described above. Furthermore, acquisition parameters were set following the same criteria described for the instrumented tube. Thus, the cylinder response was measured in periods of 4 s, with a sampling frequency of 2048 Hz and a resolution of 0.25 Hz. Moreover, the obtained FRFs are the result of 30 linear averages.

Based on the acceleration measurements of the instrumented cylinder, KF techniques (described in Chapter 4) will be used to estimate the flow-induced forces on the structure. Moreover, KF algorithms require an approximated model of the system in order to predict the system states. In the present work, EMA techniques such as Least Squares Complex Exponential (LSCE) and Least Squares Frequency Domain (LSFD) are used for system identification. In order to do that, tests have to be performed before the cylinder is installed in the test section otherwise the instrumentation devoted to excite the structure can hardly be mounted. For this purpose, the structure is mounted in cantilever on a section-model that represents an actual heat exchanger, whose dimensions (381 mm long and 95 mm width) and its lateral walls have been manufactured identical to the original test section. In this manner, the mounting and boundary conditions are as close as possible to those found in the actual tube bundle; the only difference being the absence of the remainder tubes that would prevent the shaker installation. Furthermore, this configuration facilitates tests with force aligned to y coordinate, however tests with force applied in x coordinate require the tube to be rotated 90° and reinstalled to allow the positioning of the shaker. In order to simulate in-fluid conditions, the section-model is filled with water until its level is 30 mm over the tube. The structure is excited with an electrodynamic shaker model K2007E01 from Modal Shop, which is mounted at point A2 in order to allow collocated measurements since, as reported by Lourens et al. (LOURENS et al., 2012), more accurate results can be obtained with the AKF algorithm. Force is measured with a force transducer model Y208C01 from PCB Piezotronics, it is set next to the shaker (rather than the structure) in order to avoid contact with water during tests. The described set-up is shown in Fig. 5.7.

The experimental data for system identification via EMA techniques were measured in periods of 2 s, with a sampling frequency of 4096 Hz and a resolution of 0.5 Hz. Moreover, the obtained FRFs are the result of 30 linear averages.

Figure 5.7: *Experimental set-up for tests in water with electrodynamic shaker mounted at point A2.*

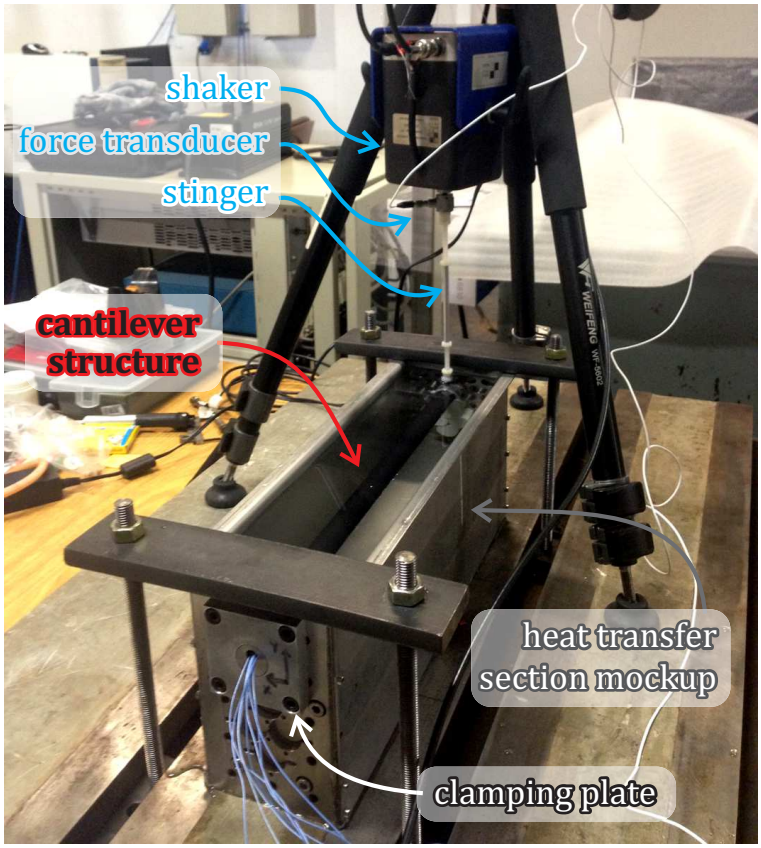

Chapter 6

Results

The results obtained during the experimental study of two-phase flow-induced vibration phenomena in a normal triangular tube bundle are presented in this chapter.

In a first stage, and using the instrumented tube described in Section 5.3.1, updated results in dynamic parameters such as hydrodynamic mass and damping estimations under two-phase crossflow are presented. In general terms, hydrodynamic mass and damping ratio results are similar to those found in literature. Besides the typical analysis of dynamic parameters in terms of homogeneous void fraction, further analysis using other void fraction models are present in this study. For instance, the model used for hydrodynamic mass prediction seems to capture the *hold-up* phenomena when implemented with void fraction models sensible to mass velocity. Regarding two-phase damping ratio, it is shown that the homogeneous void fraction model is still being the best alternative to collapse data and express the design guidelines. Furthermore, the turbulence induced vibration design guidelines available in open literature are validated with the same response data used for the study of dynamic parameters. One of these design guidelines was reformulated in order to define a fluid-structure interaction coefficient in terms of void fraction and Reynolds number, thus obtaining better results. This part of the chapter is mainly based on work published by the author at Álvarez-Briceño et al. (2017) and Álvarez-Briceño et al. (2018a).

In a second stage and using the two-degree of freedom cylinder described in Section 5.3.2, flow-induced equivalent forces are identified via Kalman filtering and dummy measurements. These equivalent forces are analyzed in frequency domain and in terms of their RMS amplitudes. Equivalent forces with peak at a quasi-constant frequency are found, which in part agrees with information in literature. Further, these forces are validated indirectly by comparing acceleration measurements with the simulated acceleration response that the force can generate on a synthesized system. It is found that RMS values of accelerations generated by equivalent forces agree with RMS values of acceleration measurements for void fractions, mostly in y coordinate and for void fractions up to 80%. RMS acceleration values generated by equivalent forces obtained

at higher void fractions and intermittent-type flow patterns disagree with RMS values of measured acceleration, mostly those in x coordinate.

6.1 Hydrodynamic mass

In order to evaluate this parameter, the first resonance frequency of the instrumented tube was measured at void fractions evaluated according to the homogeneous model, varying from 30% to 95%, then the hydrodynamic mass is calculated by using Eq. 3.1. The resonance frequencies are measured at mass velocities roughly half the velocity for FEI. This constraint in mass velocity was imposed since Pettigrew et al. (1989) noted that the tube resonance frequency must be measured at mass fluxes sufficiently below FEI threshold, otherwise significant shifts in its value can be observed and conclusions are hard to be drawn. In this way, the Connors - Blevins criterion to estimate the critical velocity for FEI was used as reference (Eq. 3.50) with $K_C = 2.8$. Moreover, this procedure was adopted in order to facilitate the comparison of present results to those reported in literature.

6.1.1 Influence of void fraction

The results on hydrodynamic mass are presented in Fig. 6.1. These results are normalized by the hydrodynamic liquid mass, m_l, which is the mass of only liquid that would be vibrating with the structure if the tube were immersed in single-phase flow. That mass can be calculated with Eq. 3.2 by using the density of liquid, in this case, the density of water.

As it can be seen, the experimental results present reasonable agreement with those predicted by Eq. 3.2, decreasing linearly with increasing homogeneous void fraction. Furthermore, for homogeneous void fractions up to 75%, hydrodynamic mass ratios in transverse direction are higher than those measured in parallel direction. This difference between parallel and transverse directions must be related to the distinct orientation and distance of neighboring tubes; while in the transverse direction there is one tube immediately adjacent at both sides, in parallel direction there is a gap between adjacent tubes in the upper and lower rows. In this sense, it is important to notice that Eq. 3.2 do consider the confinement effect, but it does not differentiate between transverse and parallel directions. For $\alpha_H \geqslant 80\%$, the difference between parallel and transverse directions decreases if compared with the differences found for low homogeneous void fractions, however, hydrodynamic mass ratios become higher than expected. According to Pettigrew et al. (1989), the measured hydrodynamic mass is close to that calculated using the average density of the two-phase mixture for the majority of tube bundles configurations for $\alpha_H \leqslant 80\%$. This may be attributed to the fact that a significant parcel

of experiments for these conditions ($\alpha_H > 80\%$) corresponds to intermittent flow pattern, in which liquid and gas phases flow somehow separately and the idealization of well mixed two-phase flow (gas entrained in liquid) differs from the actual flow topology. This effect is also represented by the higher slip between the phases at this condition, which would lead to higher liquid *hold-up*. This means that the tube is immersed in liquid for longer time periods, whereas gas slugs flow upwards faster, which implies on higher added mass in tube vibration. Furthermore, it is worth mentioning that homogeneous void fraction model assumes no slip between the phases, thus it is no surprising that this model is not able to predict hydrodynamic mass at high void fractions.

Figure 6.1: *Hydrodynamic mass as a function of void fraction for mass velocities at roughly half the velocity for FEI:* $G_{30} = 1498$*;* $G_{40} = 1498.4$*;* $G_{50} = 1498.9$*;* $G_{60} = 1191.3$*;* $G_{70} = 1501.1$*;* $G_{75} = 835.9$*;* $G_{80} = 761.7$*;* $G_{85} = 353.5$*;* $G_{90} = 246.7$*;* $G_{95} = 246.2$ kg/m^2s.

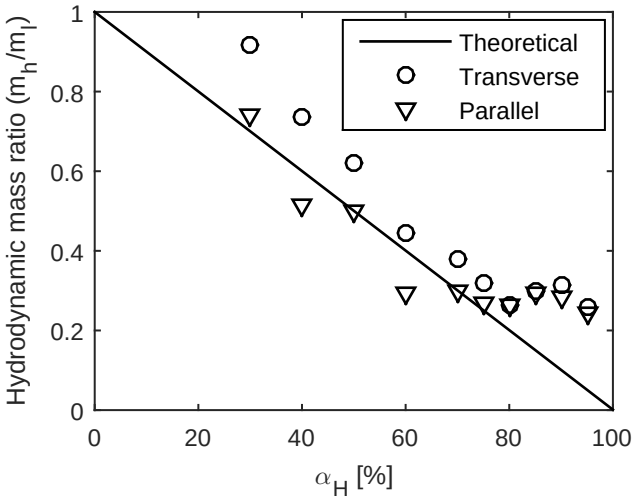

As mentioned in section 3.1.2, results on hydrodynamic mass are generally presented and analyzed in terms of the homogeneous void fraction. In fact, it is a common practice in literature to implement the homogeneous model to predict hydrodynamic mass through Rogers' model because of its simplicity. Although this is a marked trend, in the present study the Rogers' model was implemented with distinct void fraction models. The models selected for this new analysis are those proposed by Xu et al. (1998), Feenstra et al. (2000) and Kanizawa & Ribatski (2017b) since, according to Fig. 3.2, they generate hydrodynamic mass values similar to those obtained with the homogeneous model. The predicted and the present experimental values on hydrodynamic mass ratio are shown in Fig. 6.2. As it can be seen from Fig. 6.2, the implementation of void fraction models of Xu et al. (1998) and Feenstra et al. (2000) generate hydrodynamic mass values with a tendency similar to those predicted by the homogeneous model, even though those values are higher. The results obtained by implementing the void

fraction of Kanizawa & Ribatski (2017b) also present a decreasing tendency, however for $\alpha_H > 80\%$ the predicted values increase considerably. This is because of the influence of mass velocity on void fraction model proposed by Kanizawa & Ribatski (2017b), which is more pronounced than in models of Xu et al. (1998) or Feenstra et al. (2000). In this sense, the lower mass velocities are used, the lower void fractions are predicted and, therefore, the higher hydrodynamic masses are estimated. Moreover, it is worth noting that experimental values also present higher values than those predicted by Rogers' model implemented with the homogeneous model. Hence, results obtained via void fraction model proposed by Kanizawa & Ribatski (2017b) might be capturing the *hold up* effect better than other models.

Figure 6.2: *Hydrodynamic mass as a function of void fraction implemented for distinct void fraction models.*

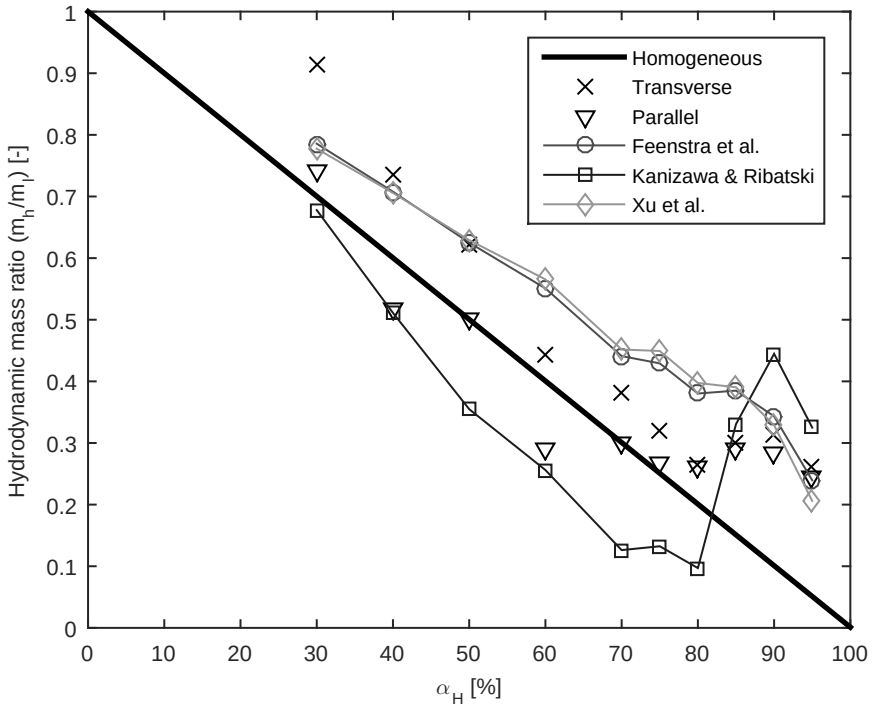

The results presented in this work somehow differ from those reported by Carlucci & Brown (1983), which indicate a reduction of hydrodynamic mass at higher rate than those predicted by Eq. 3.2 implemented with the homogeneous void fraction model. However, it must be emphasized that the results reported in Carlucci & Brown (1983) correspond to tests performed in axial flow. Therefore, the deviation is attributed to the non-uniform void distribution across the flow passage. For example, at void fractions of 60% to 80% the flow pattern is essentially annular and the central portion of the flow passage is occupied largely by the gas phase (CARLUCCI; BROWN, 1983). Thus, low hydrodynamic masses reported in Carlucci & Brown (1983) are likely to result more from dynamic decoupling, since the tube is submerged in the core of the annular flow.

In general, according to the open literature (PETTIGREW et al., 1989; PETTIGREW et al., 1995; PETTIGREW et al., 2002), as well as with the results of hydrodynamic mass found in the present work, the experimental hydrodynamic mass ratio during crossflow agrees with the model proposed in Rogers et al. (1984) expanded for two-phase flow.

6.2 Damping

Total damping ratios are calculated from tube response data via random vibration method. It is assumed that the turbulence excitation due to two-phase flow is essentially broadband random and constant near the tube natural frequency. Under these conditions, the vibration response spectrum is essentially the FRF (PETTIGREW et al., 1989). In order to avoid misunderstandings with terminology, it is important to emphasize that this technique will be used on acceleration PSD rather than acceleration response spectrum. This distinction is necessary since acceleration spectrum is properly scaled only for harmonic signals. Based on these considerations, the measured amplitude of PSD will appear similar to a FRF, and PSD amplitudes at resonance frequency (f) and half-power frequencies (f_1 and f_2) will have the same ratio as in a FRF (CHUNG; CHU, 2006). For a proper identification of the half-power frequencies, the PSDs were filtered by using a moving average with seven elements. Then, the total damping ratio is estimated by:

$$\zeta_T = \frac{f_2 - f_1}{2f}. \tag{6.1}$$

After that, depending on the analysis, the total damping ratio in transverse and parallel directions can be calculated.

In order to estimate the structural damping ratio, tests were performed during air single-phase flow since in this experimental condition the viscous damping can be considered as negligible and the two-phase damping parcel is zero. In this manner, a structural damping ratio equal to 4.89% was obtained for the transverse direction and 4.67% for the parallel direction. Even though these values are relatively high for structural damping, it must be considered that they include the effect of tube mounting tolerances and sealing components. Since structural damping is supposed to be constant for all the experimental campaign, it can be subtracted from total damping in order to focus on the effects of fluid flow on damping.

6.2.1 Influence of mass velocity

The influence of mass velocity on damping ratio was checked in the present study (excluding the structural component), and the experimental results are presented in Fig. 6.3. Mass velocities up to half the necessary for fluidelastic instability were used. As

Figure 6.3: *Effect of mass flux on tube damping in two-phase crossflow, (a) transverse direction and (b) parallel direction.*

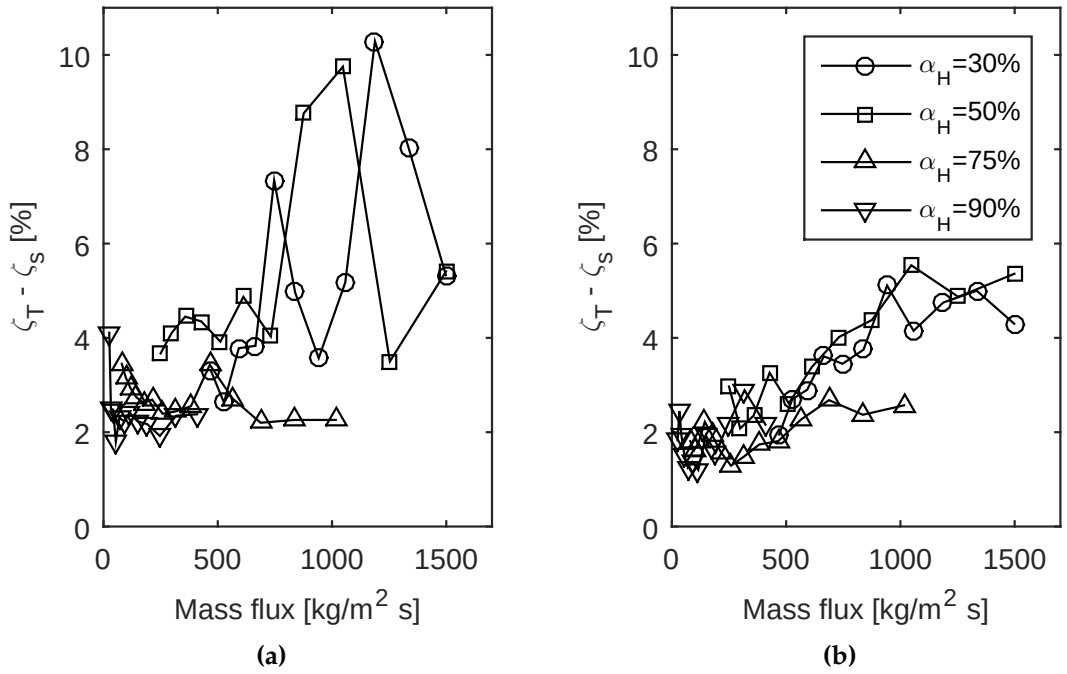

in the study of hydrodynamic mass, the Connors - Blevins criterion was adopted with $K_C = 2.8$.

As it can be noticed from Fig. 6.3, damping ratios in transverse and parallel directions present distinct behaviors with mass velocity. For lower mass velocities, say $G \leqslant 500$kg/m^{2}s, although data do not present a defined tendency, it can be seen that damping measurements in transverse direction are roughly higher than those in parallel direction. Actually, in this mass velocity range, it can be noticed that the measured damping ratios are visibly higher in transverse direction at $\alpha_H = 50\%$. For mass velocities higher than 500 kg/m^{2}s, it can be seen that damping ratio in the parallel direction presents a defined increasing tendency with increasing mass velocity, which is more noticeably for $\alpha_H = 30\%$, 50% and 75%. In counterpart, damping ratios measured in transverse direction at high mass velocities present an irregular behavior; their values at $\alpha_H = 30\%$ and 50% vary more than 100%, and its value at $\alpha_H = 75\%$ decreases and subsequently stabilizes. As it can be noticed, it is difficult to draw a general conclusion about damping ratio dependence on mass velocity. However, at least for results in parallel direction at $\alpha_H = 30\%$, 50% and 75%, it can be seen that damping increases with increasing mass velocity.

The dependence of damping measured in parallel direction on mass velocity agrees with the dynamic model that governs the fluid-structure interaction in crossflow (PAÏDOUSSIS et al., 2011), since it states that the effective damping of a cylinder in crossflow

increases with increasing flow velocity. Furthermore, also for a single cylinder in crossflow, Blevins (2001) formulates damping ratio as proportional to flow velocity and fluid density. Despite these analytical approaches for a single cylinder in crossflow, experimental studies on damping of tubes in tube bundles (CARLUCCI, 1980; CARLUCCI; BROWN, 1983; PETTIGREW et al., 1989) show that damping is not too dependent on mass velocity.

On the other hand, the irregular behavior of damping in transverse direction at $\alpha_H = 30\%$ and 50% depicted in Fig. 6.3 can be analyzed in terms of the tube response to unsteady parallel and transverse forces, which is shown in Fig. 6.4. As it can be noticed, RMS displacements in these conditions are very similar in both directions, then it is difficult to construct a direct relationship.

According to the results reported by Pettigrew et al. (1989) for $\alpha_H = 50\%$ (perhaps the same analysis is valid for all void fractions, this particular example was chosen since all the data necessary to draw conclusions is depicted in figures provided in that work), damping does not depend directly on tube displacement response. These authors showed that although RMS displacement in transverse direction is noticeable higher than in parallel direction, damping measured in parallel direction is higher than in transverse direction. Furthermore, this difference is small for low mass velocities, however, as mass velocity increases towards FEI threshold, damping in parallel direction increases while damping in transverse direction decreases, then the difference increases sharply with mass velocity.

6.2.2 Influence of void fraction

The influence of void fraction on damping has also been checked in the present study. With the aim of simplifying the analysis and making it comparable with results presented in the literature, the experiments were performed for velocities equal to half of fluidelastic instability threshold, similar to the conditions adopted for determination of hydrodynamic mass.

The obtained experimental results are depicted in Fig. 6.5, and according to this figure, two-phase damping ratio does vary significantly with homogeneous void fraction. Moreover, the results depicted in Fig. 6.5 show higher damping ratios in the transverse direction at intermediate void fractions with a maximum at $\alpha_H = 40\%$. Further, with subsequent increment of void fraction, the damping ratio decreases until the condition of gas single-phase flow. Conversely, the damping ratio in parallel direction does not present that strong tendency registered in transverse direction. In parallel direction, the maximum damping ratio was registered for $\alpha_H = 50\%$, however, the damping ratio at $\alpha_H = 40\%$ is lower than that measured at $\alpha_H = 30\%$ and similar to that measured at $\alpha_H = 60\%$ and 70%. If values of damping ratio in both directions are compared, one can

Figure 6.4: *RMS displacement in transverse (○) and parallel direction (▽). Filled markers correspond to mass velocities at roughly half the velocity for FEI.*

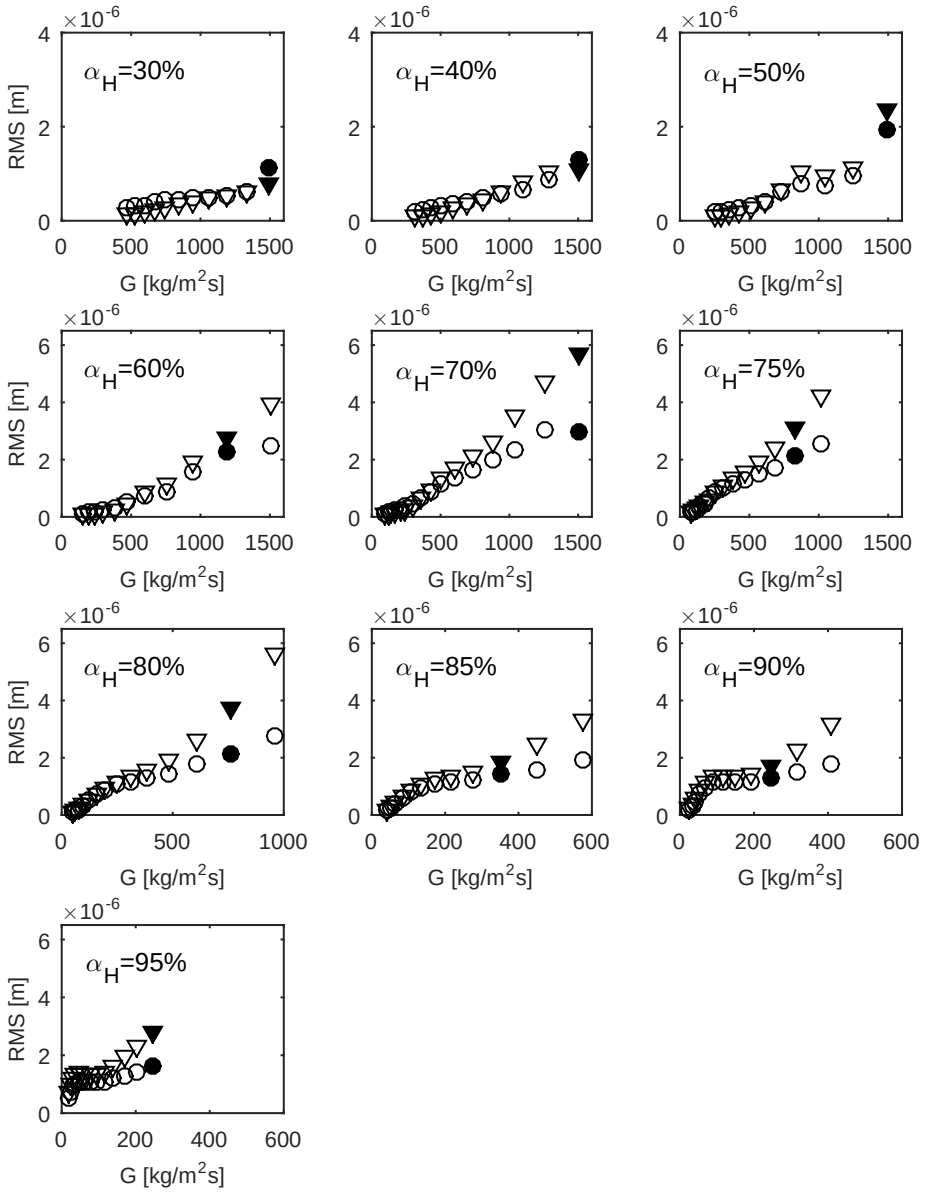

say that they are very similar, except for the values at $\alpha_H = 40\%$, where damping ratio in transverse direction is 91% greater than in parallel direction. Thus, excluding the results at $\alpha_H = 40\%$, the average damping ratio is a representative indicator of damping in both directions.

Figure 6.5: *Two-phase damping ratio measurements.*

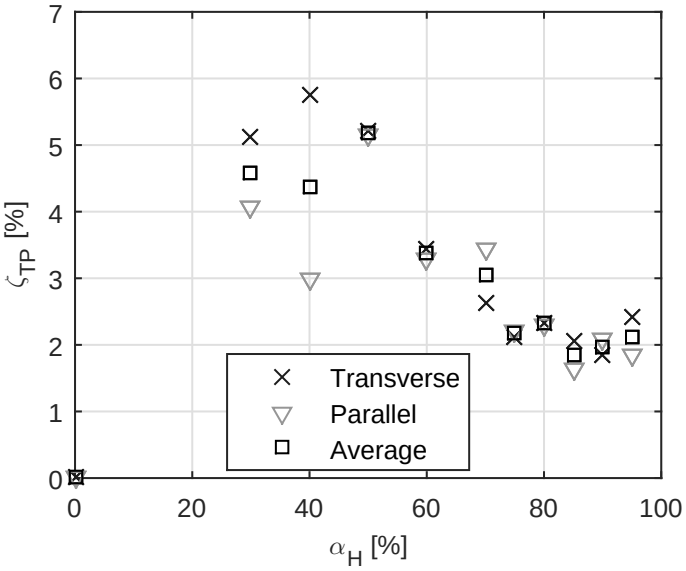

Even though experimental conditions for $\alpha_H < 30\%$ were unable to be set, one can notice that the two-phase damping ratio for $\alpha_H = 0\%$ is negligible if compared to that registered at intermediate void fractions. This behavior seems to agree, at least for the investigated void fractions, with the tendency of the data reported in the open literature (CARLUCCI; BROWN, 1983; LIAN et al., 1997; PETTIGREW et al., 1989; PETTIGREW et al., 2001), which mention a peaking behavior of damping ratio with homogeneous void fraction, with maximum damping at intermediate void fractions.

6.2.3 Effect of flow patterns

These results can also be analyzed in terms of the average two-phase damping ratio and the flow patterns by using the map provided in Fig. 2.6. At $\alpha_H = 30\%$, a bubbly flow pattern has been registered. Although this is a low void fraction, the measured total damping ratio is noticeably higher than that at liquid flow ($\alpha_H = 0\%$), where it is expected to be equal to viscous damping only. Further, dispersed bubbles flow pattern has been registered from 40% to 70% homogeneous void fraction, it can be noticed that the averaged data present a peak at α_H of approximately 50%. This result, also considering the results in transverse and parallel directions analyzed separately, is in agreement with Carlucci & Brown (1983); Lian et al. (1997) and Pettigrew & Taylor (2004), who indicate maximum damping between 40% and 80% homogeneous void

fraction. Moreover, contrary to the findings of Lian et al. (1997), which pointed out that maximum damping occurs during intermittent flow, in the present study the highest damping were observed during dispersed bubbles flow pattern. Thereafter, damping in transverse direction decreases from 50% until 70% homogeneous void fraction, while damping in parallel direction presents a slight variation under the same flow pattern.

Damping decreases slightly from $\alpha_H = 75\%$ to 90%, with the difference that 75% and 80% void fractions developed severe intermittent flow patterns, and churn flow was registered for $\alpha_H = 85\%$ and 90%. Finally, at $\alpha_H = 95\%$, a severe intermittent flow pattern is verified again. According to Fig. 6.5, for $\alpha_H \geqslant 85\%$, damping ratio does not present important variations, just a slight decrease can be noted if compared with results at $\alpha_H = 80\%$. About this behavior, Noghrehkar et al. (1999) associate these results to the decreasing RMS amplitude of local void fraction fluctuations at higher void fraction with intermittent-type flow patterns. Moreover, it is worth mentioning once again (it was commented in section 3.1.3) that it is difficult to draw conclusions about the behavior of damping with flow pattern from results in literature. This is because several flow pattern maps, criteria and definitions have been used in the experimental campaigns reported in literature, therefore damping data can hardly be clustered for general analysis.

6.2.4 Comparison to design guidelines

In order to compare the obtained results with a compilation of experimental data measured in distinct normal triangular tube bundles during air-water two-phase crossflow, the data must be normalized by the mass ratio and confinement factor. Such results can be found in Fig. 6.6. As it can be noticed, ζ_{TPn} becomes larger especially at low void fractions. Actually, normalized two-phase damping at $\alpha_H = 30\%$ is even larger than that at $\alpha_H = 50\%$, which is due to the large hydrodynamic mass measured at that void fraction. Despite of this, normalized two-phase damping until $\alpha_H = 50\%$ is noticeable higher than those at higher void fractions, which confirms the behavior discussed previously. Furthermore, ζ_{TPn} measured for $\alpha_H \geqslant 60\%$ agrees with the available data for two-phase air - water upward cross flow in normal triangular tube bundles.

Also, in Fig. 6.6a, average damping is compared with the design guideline formulated in Eq. 3.39. As it can be seen, most of the measured damping ratios are higher than the lower bound proposed by the model. An exception can be opened at $\alpha_H = 75\%$, which is slightly under the estimated value. As a conclusion, it can be suggested that care must be exercised when selecting the value of the correlation constant A (in Eq. 3.39) at design stage to avoid the possibility of estimating a larger damping than actual.

Figure 6.6: *(a) Comparison between the design guideline and available damping data collected (PETTIGREW; TAYLOR, 2004) with normalized damping ratio obtained in the present work, (b) Comparison between the design guideline and the results found in the present work.*

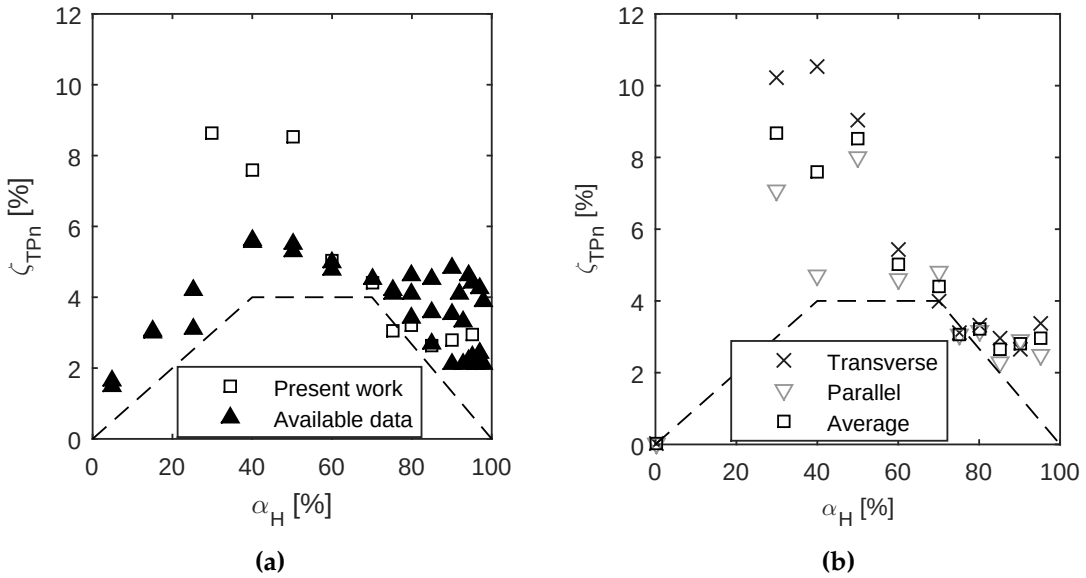

The two-phase damping ratios estimated by using Sim's model and those measured in the present work are depicted in Fig. 6.7. In order to perform a consistent comparison, it is necessary to bear in mind that the Sim's model was formulated with a void fraction model distinct from the homogeneous, while the present experimental conditions were given by the homogeneous void fraction model. For this reason, the damping ratios predicted by Sim's model must be taken at void fractions predicted by Feenstra et al. (2000) but equivalent to the present experimental conditions, which were defined by distinct combinations of j_l and j_g. Furthermore, it is important to note from Eq. 3.40 that this model uses a constant K_{TP} to fit results based on the experimental database. Thus, the values of K_{TP} that present the better results are used for curves plotted in Fig. 6.7. Although using distinct values of K_{TP} for distinct implementations of Sim's model may complicate the comparison of results in Fig. 6.7, data will be analyzed in terms of tendencies rather than absolute values.

For the comparison entitled as Sim & Mureithi (2014) in Fig. 6.7, the Sim's model is implemented with the void fraction model proposed by Feenstra et al. (2000) and it is set $K_{TP} = 3$, as originally proposed by Sim & Mureithi (2014). As it can be seen, the measured damping ratios at lower void fractions are higher than those predicted by Sim & Mureithi (2014). Moreover, the damping ratios predicted by Sim's model present a totally different tendency from that presented by the experimental results. In this context, it was analyzed what would be the reasons that make the Sim's model to differ from experimental results. One of the main causes may be the fact that some models

Figure 6.7: *Experimental two-phase damping ratio in terms of homogeneous void fraction compared to the transverse damping model as originally proposed by Sim & Mureithi (2014), implemented with the homogeneous two-phase multiplier, implemented with the void fraction predicted by Kanizawa & Ribatski (2017b), and implemented with the void fraction and two-phase multiplier proposed by Kanizawa & Ribatski (2017b).*

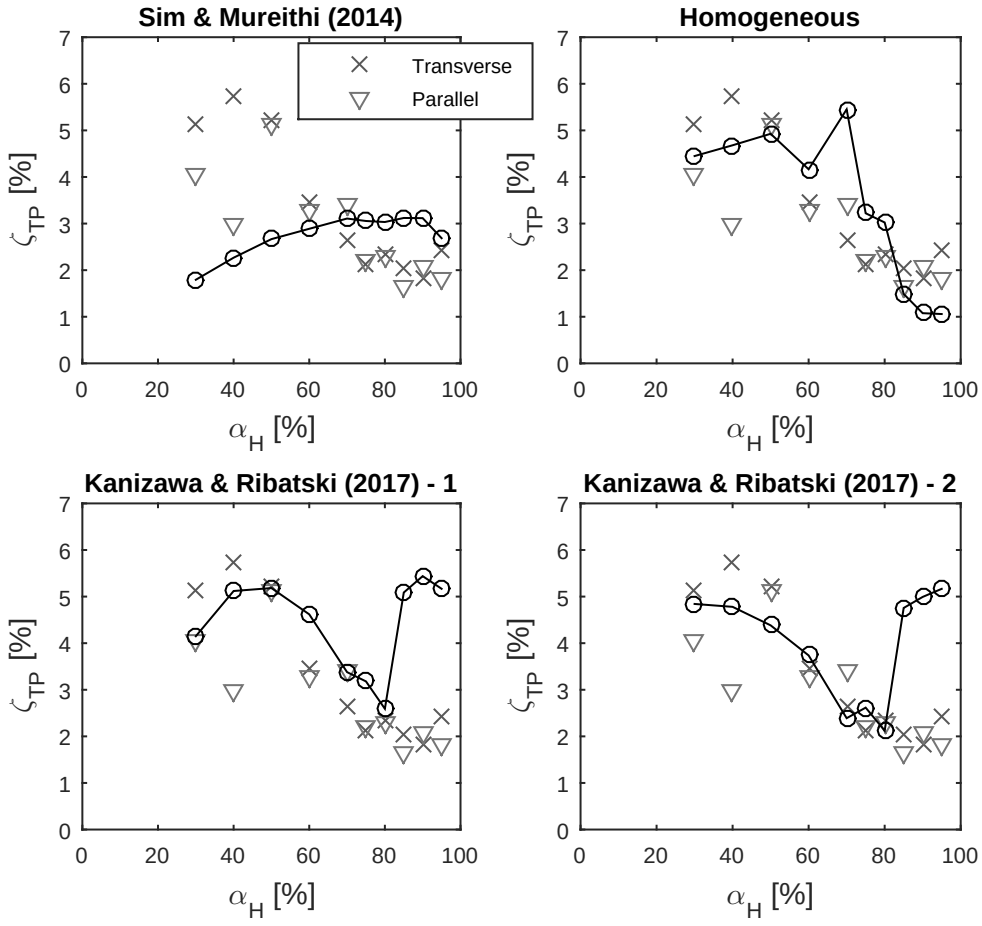

used for Sim's model implementation does not represent which is actually happening in the test section.

For instance, Sim & Mureithi (2014) suggest that ϕ_{l0}^2 in Eq. 3.40 can be calculated according to Marchaterre (1961) given by Eq. 3.42. However, as it can be noticed from Fig. 6.8, the Marchaterre's model predicts pressure drop satisfactorily only for $j_l = 1.500$ m/s, which in our experimental campaign correspond to the analyzed conditions for $\alpha_H = 30\%$, 40%, 50% and 70%. Despite this, the Sim's model is not able to predict damping in these void fractions. In this context, other models to predict void fraction and pressure drop can be combined to estimate the damping ratio. Moreover, it is preferable that these models do represent the phenomena occurring in the test section.

Based on Fig. 6.8, it can be said that two-phase pressure drop estimations based on the homogeneous model for ϕ_{l0}^2 are not satisfactory for $j_l = 0.02$, 0.183 and 0.553 m/s. However, it was decided to test its implementation with the Sim's model because of

Figure 6.8: *Comparison between experimental results obtained in Kanizawa & Ribatski (2017b) and the two-phase pressure drop $\Delta P_{2\phi}$ estimated according to Kanizawa & Ribatski (2017b), Marchaterre (1961) and the Homogeneous model.*

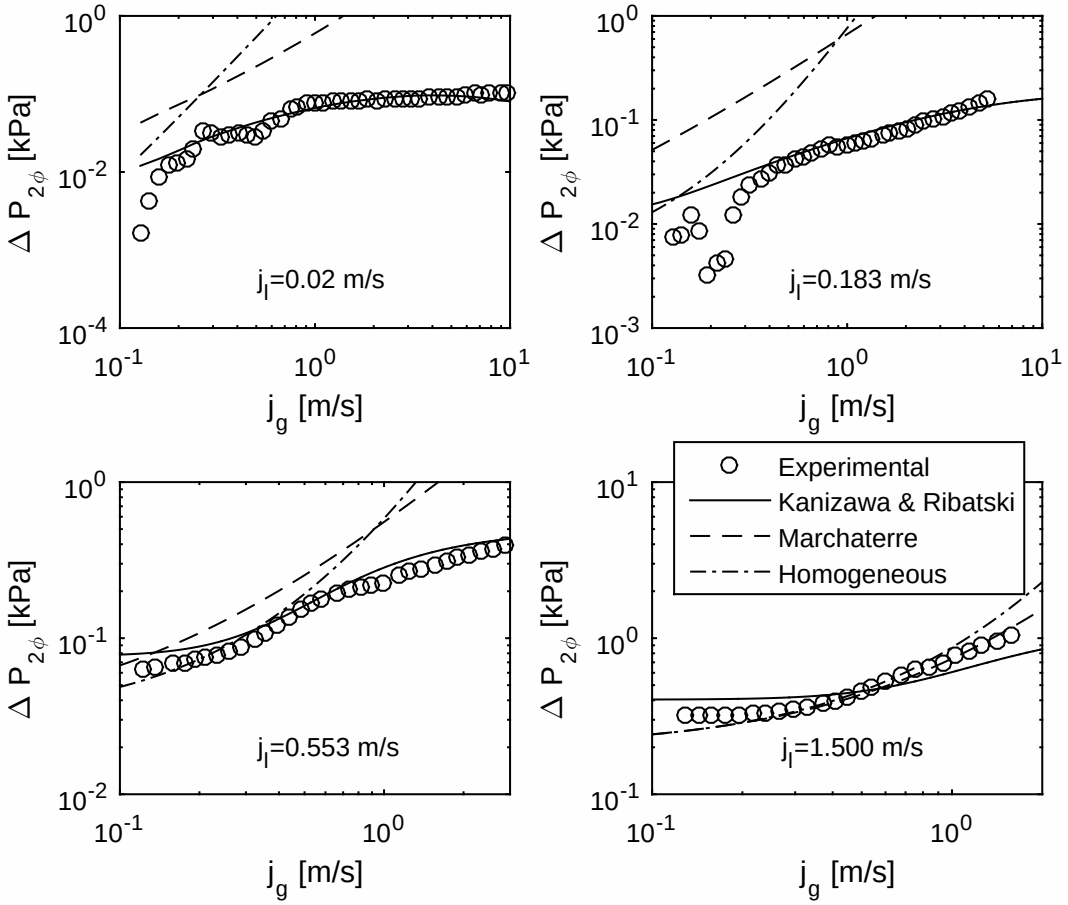

its simplicity. In this manner, the Sim's damping model was implemented with the homogeneous void fraction model, the homogeneous two-phase multiplier given by Eq. 3.44, and it is set $K_{TP} = 30$, and the results are entitled as Homogeneous in Fig. 6.7. As it can be seen, the tendency of the predicted damping values is similar to the experimental measurements. An exception can be opened for $\alpha_H = 70\%$ for which the Sim's model predicts the highest value, while experimental results present damping values lower than the values measured for $30\% < \alpha_H < 50\%$. Furthermore, the damping values predicted for higher void fractions ($\alpha_H \geqslant 85\%$) are lower than those experimentally obtained.

For the comparison entitled as Kanizawa & Ribatski (2017) - 1, the Sim's model is implemented with the void fraction model proposed by Kanizawa & Ribatski (2017b) (Eq. 2.57), the Marchaterre's model for the two-phase frictional multiplier and it is set $K_{TP} = 5$. As it can be seen, the predicted damping values agree with the tendency of experimental results for $30\% < \alpha_H < 80\%$. However, an exception can be opened

for damping at $\alpha_H = 40\%$ in parallel direction, where experimental damping ratio is noticeably lower than that predicted. Further, for $\alpha_H \geqslant 85\%$, predicted damping increases, thus predicted values are markedly different from those measured.

For the comparison entitled as Kanizawa & Ribatski (2017) - 2, the Sim's model is implemented with $K_{TP} = 20$, the void fraction model and the two-phase frictional multiplier, ϕ_l^2, proposed by Kanizawa & Ribatski (2017b). The latter is given as:

$$\phi_l^2 = 1 + \left[\left(98.9 \cdot \frac{\alpha_K^{1.75}}{We^{0.76}} \right)^2 + \left(7.76 \cdot 10^5 \frac{\alpha_K^{1.95}}{Re_l^{1.26}} \cdot \frac{1}{1 + (6500/Re_l)^2} \right)^2 \right]^{1/2}. \tag{6.2}$$

where α_K stands for the void fraction estimated according to Eq. 2.57.

In order to estimate the two-phase multiplier ϕ_{l0}^2 necessary for Eq. 3.40, it can be used the following expression:

$$\phi_{l0}^2 = \frac{\Delta P_{2\phi}}{\Delta P_{l0}}. \tag{6.3}$$

where $\Delta P_{2\phi}$ is the frictional pressure drop of the two-phase mixture and ΔP_{l0} is the frictional pressure drop of the mixture flowing as liquid. $\Delta P_{2\phi}$ can be calculated from the definition of ϕ_l^2 given as:

$$\Delta P_{2\phi} = \phi_l^2 \Delta P_l, \tag{6.4}$$

where ΔP_l is the frictional pressure drop per tube row considering only the liquid mass flow rate ($G_l = G(1-x)$), which can be evaluated by using the definition of Euler number definition reformulated as:

$$\Delta P_l = \frac{Eu_l \rho_l u_l^2}{2}. \tag{6.5}$$

The only liquid Euler number, Eu_l, can be calculated from relationships in Žukauskas (1972) considering the Reynolds number of liquid phase Re_l (Eq. 2.20). In the same way, the frictional pressure drop of the mixture flowing as liquid can be calculated as:

$$\Delta P_{l0} = \frac{Eu_{l0} \rho_l \bar{u}^2}{2}, \tag{6.6}$$

where the Euler number of the mixture flowing as liquid can be calculated from relationships in Žukauskas (1972) considering the Reynolds number Re_{l0} defined as:

$$Re_{l0} = \frac{Gd}{\mu_l}. \tag{6.7}$$

As it can be seen from results entitled as Kanizawa & Ribatski (2017) - 2, the predicted damping presents a decreasing tendency from $\alpha_H = 30\%$ to 80%, which somehow agrees with experimental results. However, as in comparison entitled as Kanizawa & Ribatski (2017) - 1, predicted values for $\alpha_H \geqslant 85$ increases, and these values are higher than

experimental values.

Based on the comparison of damping ratios plotted in Fig. 6.7, it can be said that results entitled as Homogeneous, Kanizawa & Ribatski - 1 and 2 present a features that differentiate them from results entitled as Sim & Mureithi, this is that they present a pronounced decreasing tendency for $\alpha_H \geqslant 50\%$, which agree with the present experimental results. Furthermore, it can be noticed that comparisons in Kanizawa & Ribatski - 1 and 2 present a strong increasing tendency with homogeneous void fraction for $\alpha_H \geqslant 85\%$. In order to analyze these features, the behavior of each one of the factors of Sim's model (Eq. 3.40) is analyzed in terms of homogeneous void fraction. Figures 6.9, 6.10, 6.11 and 6.12 show the behavior of Sim's model parameters for damping results in Fig. 6.7. It is worth mentioning that, for this comparison, it was set $K_{TP} = 1$ for the four cases, hence the analysis can be simplified. The term $gr.$ in Figs. 6.9, 6.10, 6.11 and 6.12 is given by $gr = MF_{L0}/8\pi f_n \bar{u} m$.

As it can be noticed from Figs. 6.9 and 6.10, the behavior of ϕ_{l0}^2 proposed by Marchaterre (1961) is distinct from the homogeneous model. On the other hand, the term $gr.$ seems to present a similar behavior in both cases, where as Eu_{l0} is the same. In this sense, it can be said that the resultant decreasing behavior of ζ_{TP} with α_H in the Homogeneous case in Fig. 6.7 is principally because of the lower values of ϕ_{l0}^2. Thus, the tendency of ζ_{TP} is governed by $gr.$

Figure 6.9: *Damping factors analysis for results entitled as Sim & Mureithi in Fig. 6.7.*

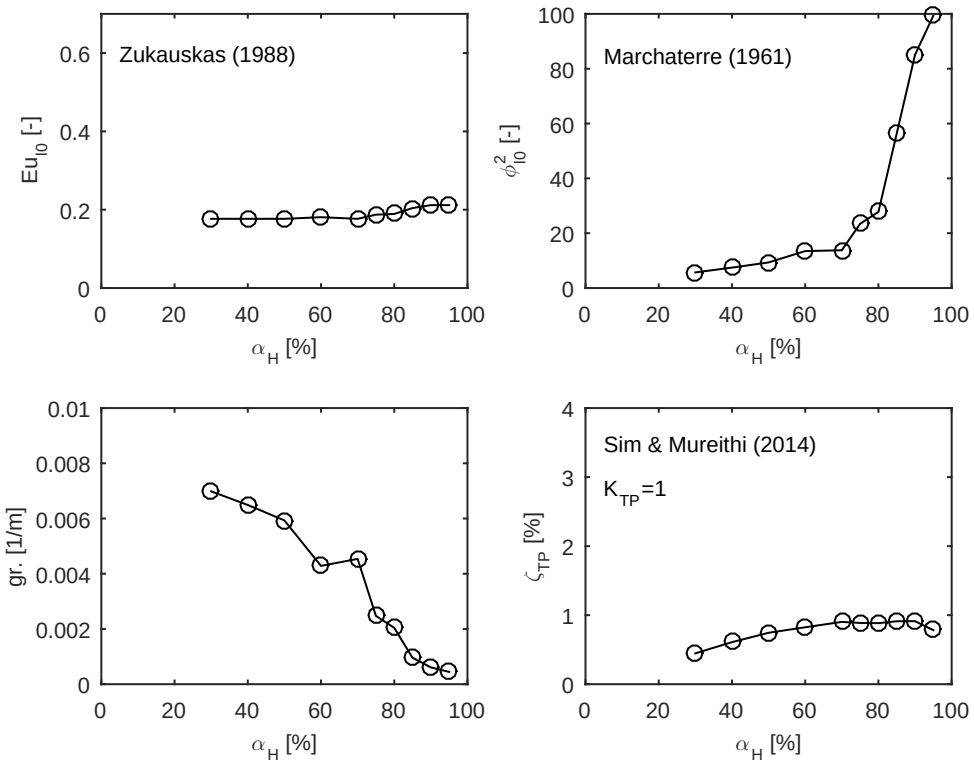

Figure 6.10: *Damping factors analysis for results entitled as Homogeneous in Fig. 6.7.*

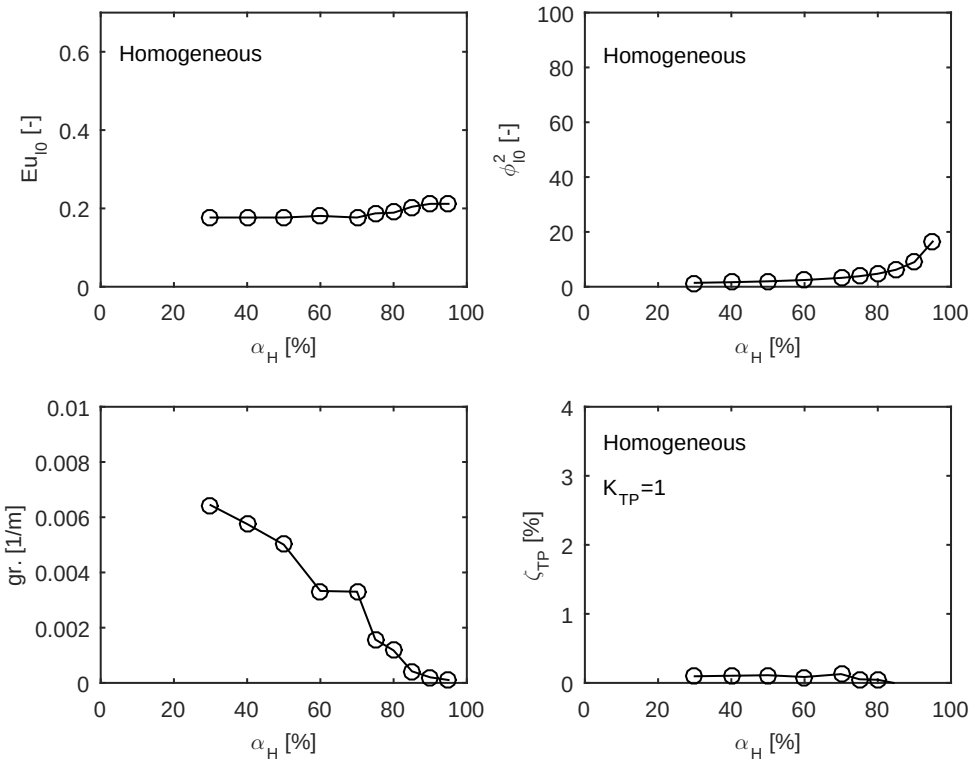

As it can be seen from Figs. 6.11 and 6.12, the two-phase frictional multiplier according to Zukauskas (1988) differs from that estimated indirectly, which is based on Eq. 6.2. Furthermore, it can be noticed that Eu_{l0} estimated through Žukauskas (1972) (Kanizawa & Ribatski - 2) is higher than that estimated through Zukauskas (1988) (Kanizawa & Ribatski - 1), especially for $\alpha_H \geqslant 85\%$. In this manner, the resultant decreasing tendency of ζ_{TP} for Kanizawa & Ribatski - 1 and 2 for $\alpha_H \leqslant 80\%$ seems to correspond to a void fraction range in which the behavior of $gr.$ governs. Further, for $\alpha_H \geqslant 85\%$, the values of ϕ_{l0}^2 are higher and govern the behavior of ζ_{TP} for Kanizawa & Ribatski - 1. On the other hand, higher damping predictions in Kanizawa & Ribatski - 2 seem to be the result of higher Eu_{l0}, whose effect is light but it can be compensated by using higher values of K_{TP} when adjusted to experimental data.

In summary, it can be said that the factors used in Sim's damping expression can be expressed according to distinct models. However, there is not a set of models that lead to acceptable results. The Sim's model results entitled as Kanizawa & Ribatski (2017) - 1 and Kanizawa & Ribatski (2017) - 2 in Fig. 6.7 show good agreement with experimental data up to $\alpha_H = 80\%$. Moreover, these damping estimates are subjected to the choice of K_{TP} value, which may vary in a wide range depending of the models used to calculate the factors of Sim's model.

Until now, only experimental results obtained in air - water mixtures have compared

Figure 6.11: *Damping factors analysis for results entitled as Kanizawa & Ribatski - 1 in Fig. 6.7.*

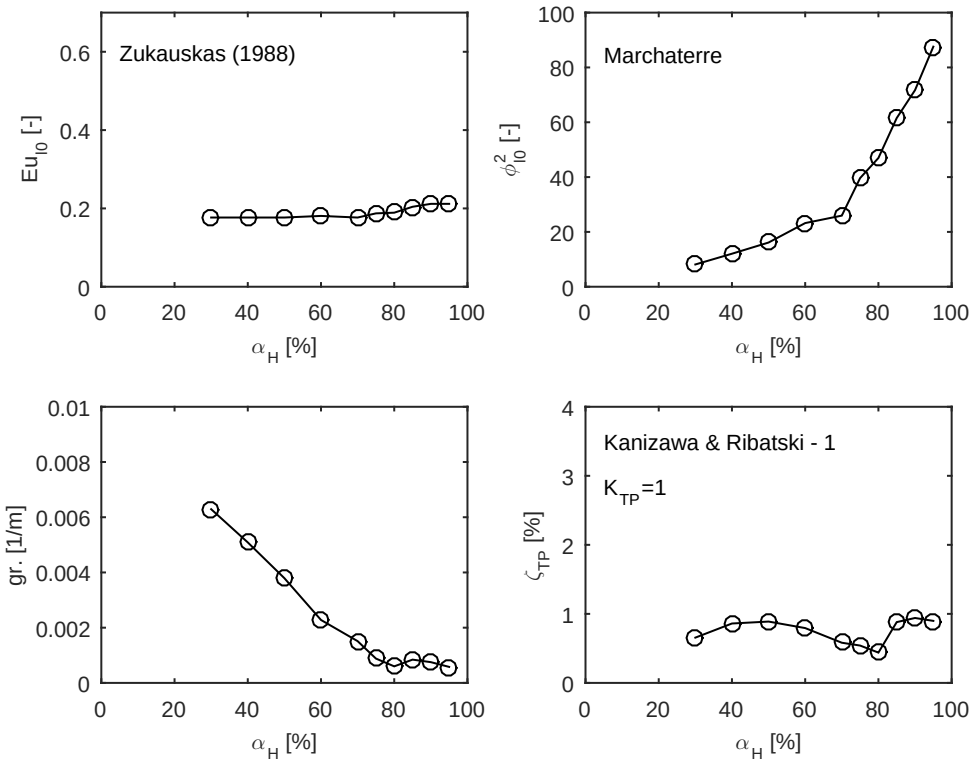

to the damping predicted by Sim's model. Although this mixture is widely used to study two-phase mixtures, it is important to check results for other fluids. In this sense, Figs. 6.13 and 6.14 show experimental results for damping measured in a tube bundle under Freon 22 and Freon 11 crossflows, respectively, which are compiled in Pettigrew & Taylor (2004). These results are compared with damping values predicted by Sim's model.

Two problems arise in Sim's model implementation: firstly, the value of the empirical constant K_{TP} varies in a wide range from one implementation to another, which would complicate the implementation of the Sim's model every time that new operational conditions have to be tested, which is a problem also found in air - water mixtures; secondly, the tendency of the predicted values fails to follow any of the experimental results plotted in Figs. 6.13 and 6.14. Based on these results, it can be said that the Sim's model presents some problems on damping prediction, further studies on the fluid type dependence of K_{TP} are necessary and thus it is not recommended to estimate damping values under experimental conditions for which a database is not available.

Figure 6.12: *Damping factors analysis for results entitled as Kanizawa & Ribatski - 2 in Fig. 6.7.*

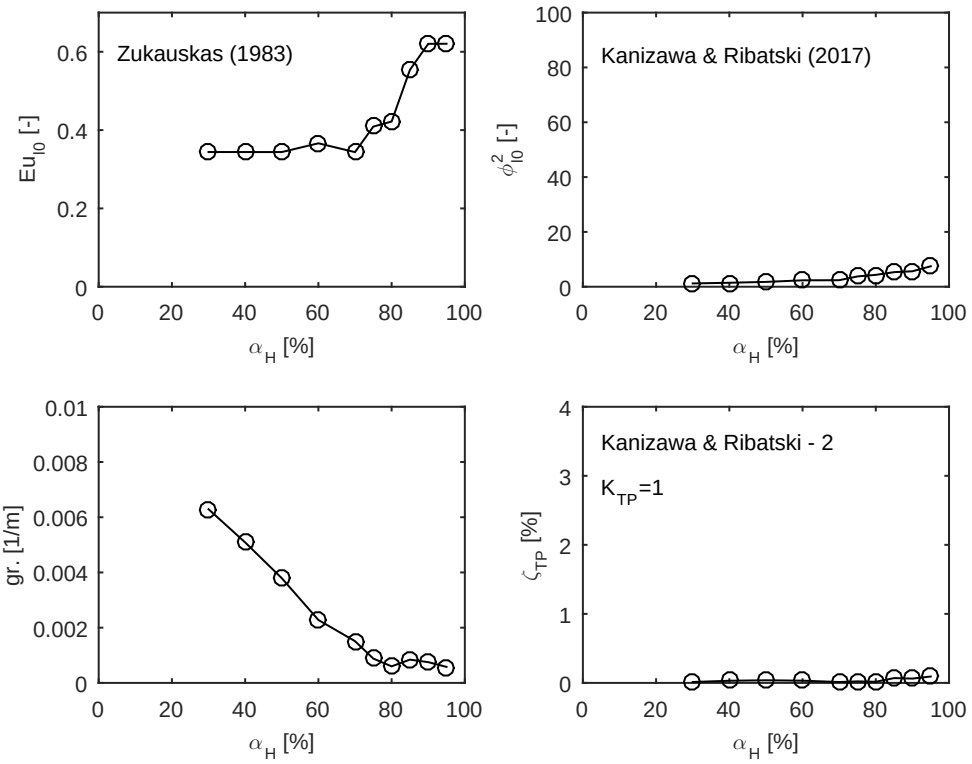

6.3 Buffeting vibration in two-phase flow

In this section, the characteristics of the buffeting vibration mechanism induced by air-water crossflow on the instrumented tube described in 5.3.1 are analyzed. For this, the acceleration spectra obtained for distinct mass velocities and void fractions are compared. Further, the RMS values of tube displacement are also analyzed in terms of void fraction and mass velocities. Three design guidelines (presented in Section 3.2) are implemented for the present experimental conditions and compared to the results obtained in the current experimental campaign.

6.3.1 General discussion on results

First, the influence of void fraction and mass velocity on turbulence-induced vibration is studied. The tests were performed for mass velocities up to roughly half the necessary to reach instability, thus any instability phenomenon is initially discarded. The Connors-Blevins criterion was adopted in order to define the instability mass velocities; this model was implemented with $K_C = 2.8$, as suggested by Blevins (2001).

Figures 6.15 and 6.16 show the PSDs of the acceleration responses measured at $\alpha_H = 30\%$ and 50%, which have been taken as examples. As it can be seen from these

Figure 6.13: *Experimental damping measurements compiled in Pettigrew & Taylor (2004) for Freon 22 ($T = 30°C$) compared to the transverse damping model proposed by Sim & Mureithi (2014) implemented with distinct void fraction and frictional two-phase multipliers models.*

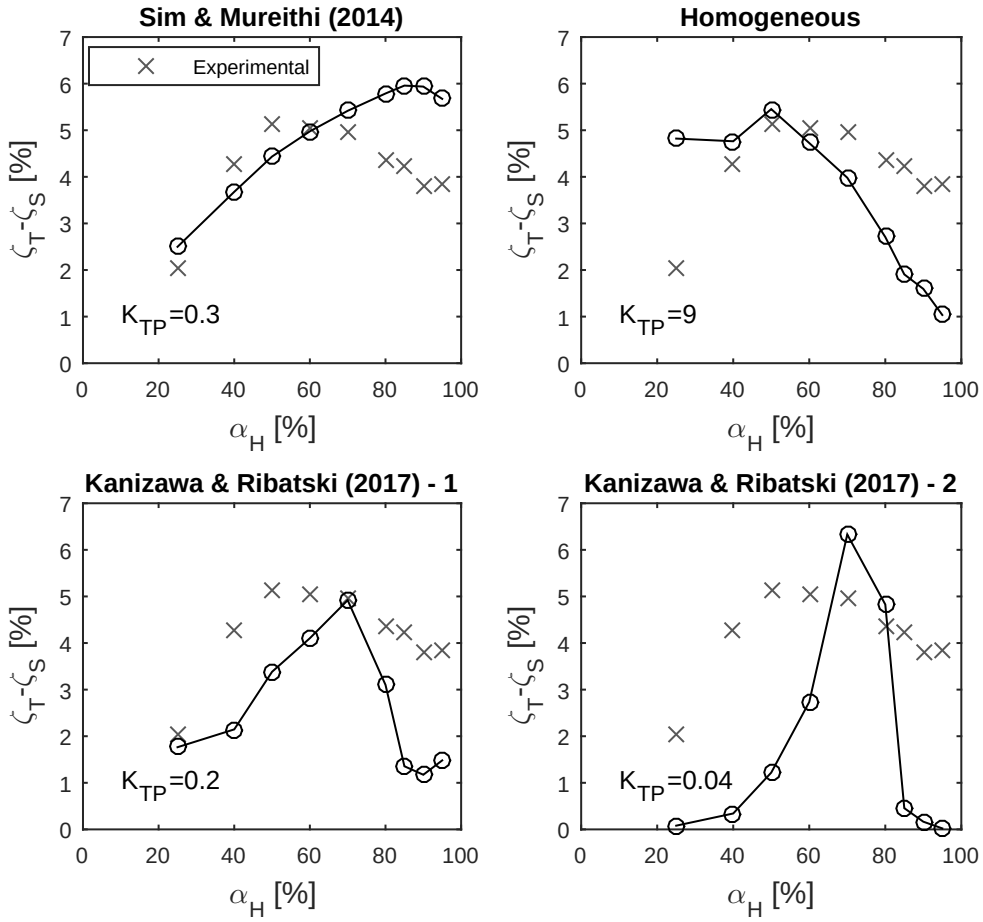

figures, the vibration response increases with increasing mass velocity. Furthermore, it can be noticed that different vibration levels occur in similar mass velocities and distinct void fractions, which must be related to differences in the local flow pattern. These results emphasize the importance of instantaneous evaluation of fluid momentum given not only by the mass velocity but also by flow pattern on buffeting vibration due to two-phase flow.

The findings in Taylor et al. (1989) about the direct proportionality between the RMS displacement amplitude and the mass velocity were also evaluated in the present study. For this purpose, the RMS value of tube displacement was computed in the 10-1024 Hz bandwidth to each experimental condition, after that, results were clustered for each void fraction. The components within the 0-10 Hz bandwidth were not considered, since in this band appears a resonant peak that corresponds to a vibration mode of the whole structure used for supporting the test bench. This vibration mode varies in this range due to changes in total mass of the experimental facility since liquid and gas

Figure 6.14: *Experimental damping measurements compiled in Pettigrew & Taylor (2004) for Freon 11 ($T = 36°C$) compared to the transverse damping model proposed by Sim & Mureithi (2014) implemented with distinct void fraction and frictional two-phase multipliers models.*

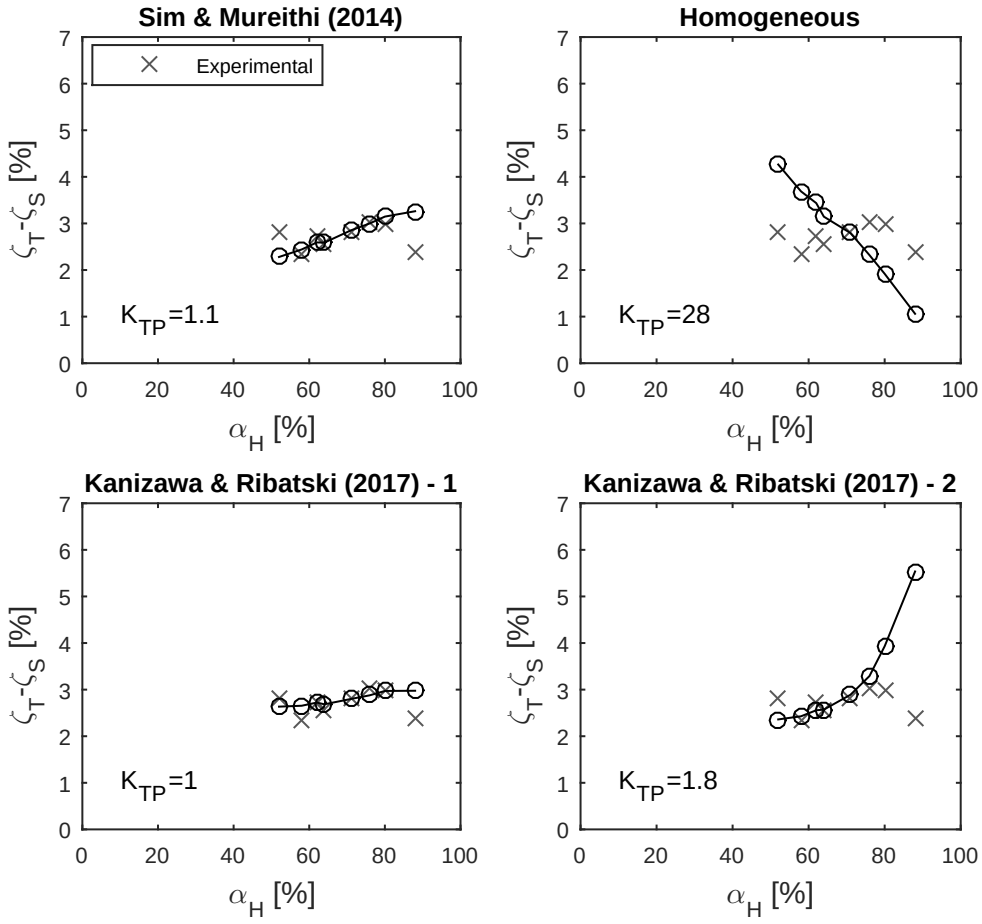

phases are mixed in distinct proportions during the tests. This dynamic behavior is not related to the instrumented tube response, jeopardizing the analysis of FIV.

The regression analysis is performed between the RMS of the resultant displacements (vector component addition since transverse and parallel components were measured) and mass velocities, the results are depicted in Fig. 6.17. Polynomials of first and second degrees were used to fit the experimental data. As it can be seen for $\alpha_H \leqslant 40\%$, the linear curve seems to represent most of the experimental data. However, for higher mass velocities tested at those void fractions, the RMS displacement and mass velocity seems to lose its linear behavior as void fraction increases from 30% to 60%. Thus, a second order polynomial seems to be more appropriate to fit these data.

For void fractions of 70% and 75%, it can be said that the results can roughly be represented by a first degree polynomial. Nonetheless, it must be pointed out that the second degree polynomial represents better the behavior of the RMS displacement for $\alpha_H = 70\%$ at low mass velocities. Furthermore, for $\alpha_H \geqslant 80\%$, it can be noticed

Figure 6.15: *Acceleration PSDs during $\alpha_H = 30\%$ for (a) transverse direction and (b) parallel direction.*

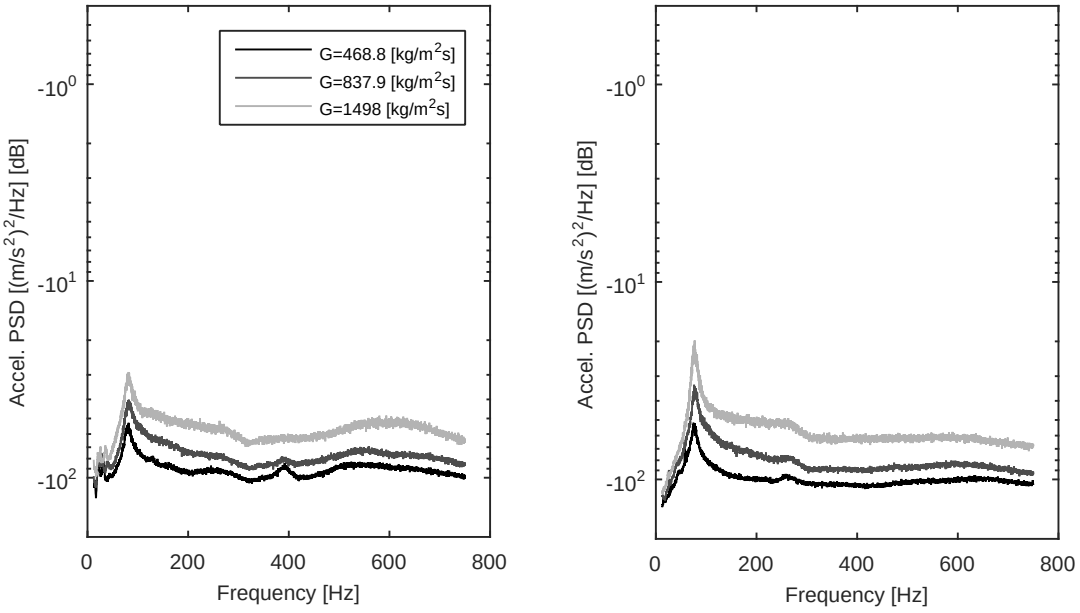

(a) **(b)**

Figure 6.16: *Acceleration PSDs during $\alpha_H = 50\%$ for (a) transverse direction and (b) parallel direction.*

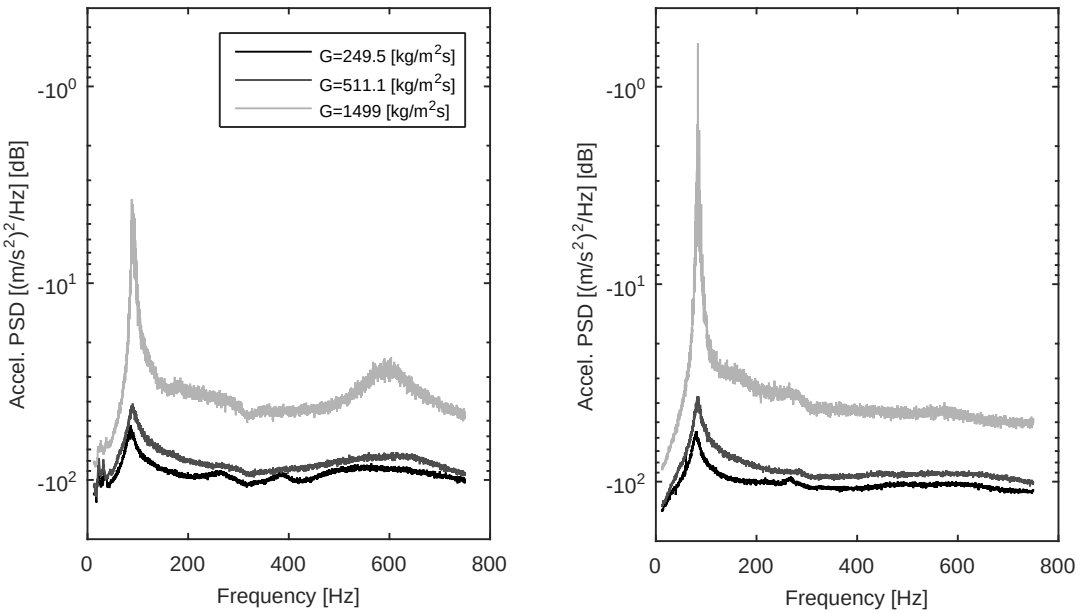

(a) **(b)**

that neither the first nor the second degree polynomial achieve a good agreement with experimental data. Moreover, for intermediate mass velocities, it can be seen that the RMS displacement stabilizes; this effect is more noticeable as void fraction increases. After this transition region, the RMS displacement increases again with mass velocity, but with a lower slope if compared with the slope presented before the transition region.

The results depicted in Fig. 6.17 can also be analyzed in terms of the flow patterns occurring across the tube bundle. For this, the flow pattern map developed by Kanizawa & Ribatski (2016a) is adopted as reference. According to Fig. 5.3, the experimental data for $\alpha_H \leqslant 60\%$ correspond to the bubbles flow pattern. Under these conditions, majority of the data of RMS displacement shows a linear relationship with the mass velocity. Moreover, as void fraction is increased from 30% to 60%, the RMS displacement is characterized by a steeper variation with mass velocity. In this sense, it is speculated that this variation is related to the flow pattern across the tube bundle. In fact, as void fraction is getting closer to 60%, the experimental conditions are closer to intermittent and churn flow patterns for intermediate j_g values, as can be observed from Fig. 5.3. Moreover, it must be pointed out that those RMS displacements that outline from the linear tendency, at high mass velocities and $\alpha_H \leqslant 60\%$, were measured under dispersed bubbles flow pattern. This flow pattern is characterized by gas bubbles with reduced diameter dispersed in a continuum liquid phase. Dispersed bubbles flow is present under conditions of high liquid velocities and reduced to intermediate gas velocities. Therefore, it can be concluded that the liquid flow in combination with immersed bubbles lead to higher buffeting forces in bubbles flow pattern, thus generating higher amplitudes of vibration.

The linear behavior shown by RMS displacement at $\alpha_H = 70\%$ and 75% correspond to experimental results measured under conditions of bubbles and intermittent flow patterns, and the transition region between them. Furthermore, it can be seen that these RMS displacements are higher than those measured for void fractions up to 60% in the same mass velocities range. Further, for $\alpha_H \geqslant 80\%$, it can be seen that neither a first degree nor a second degree polynomial can be fitted because of the transition region characterized by the stabilization of RMS displacement registered at intermediate mass velocities. It is speculated that these results must be strongly influenced by the flow pattern transition that is occurring under these conditions, which can be inferred from the analysis of Fig. 5.3. Actually, the experimental conditions showing this behavior were highlighted in Fig. 6.18 and, as it can be noticed, they mostly correspond to churn flow pattern. Subsequently, the RMS displacement increases again with mass velocity but now during intermittent flow pattern. In this case, it must be pointed out that lower mass velocities ($200 \leqslant G \leqslant 300$ kg/m^{2}s) during intermittent flow generate higher vibration than the same mass velocities during bubbles flow pattern.

Based on the above discussion, it can be concluded that flow-induced vibration

Figure 6.17: *Vibration response to air-water forced excitation for distinct void fractions and mass fluxes, and polynomial regression with degree $n = 1$ (solid line) and $n = 2$ (dashed line).*

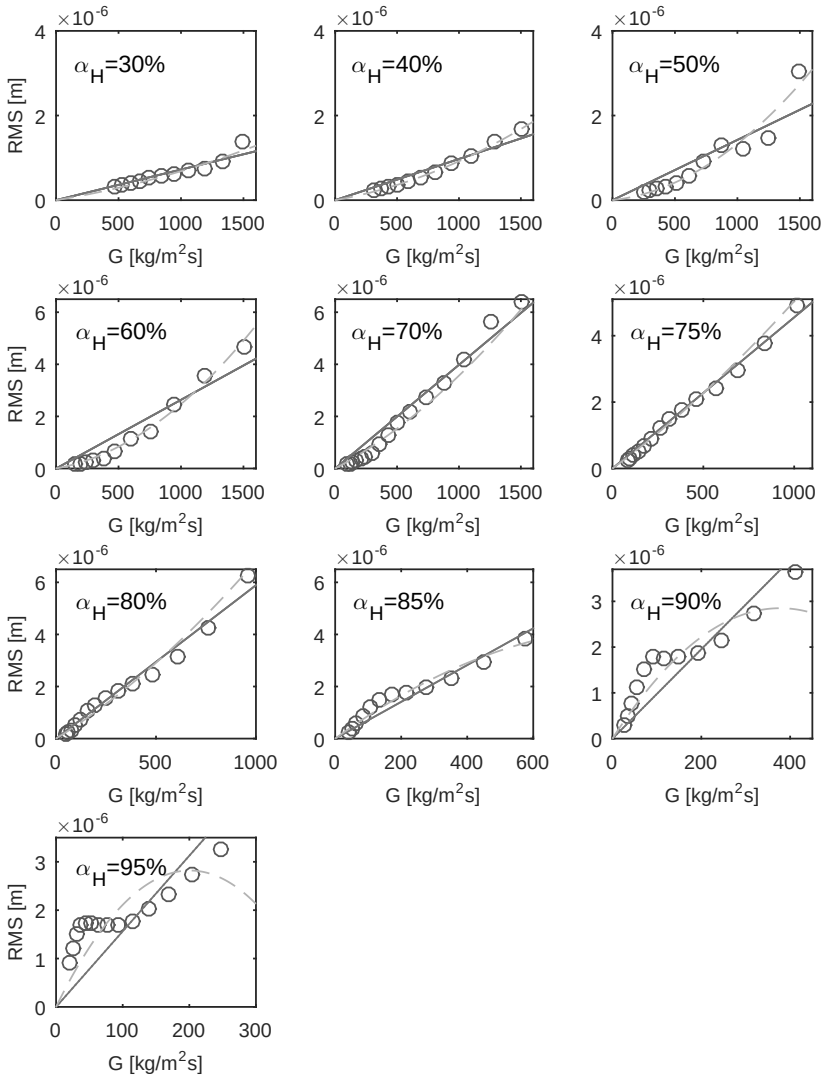

Figure 6.18: *Transition curves for air-water two-phase flow ($P = 95kPa$; $T = 25°C$) according to Kanizawa & Ribatski (2016a). Pentagram marks correspond to half the mass flux for fluidelastic instability threshold and circle filled marks correspond to transition zone.*

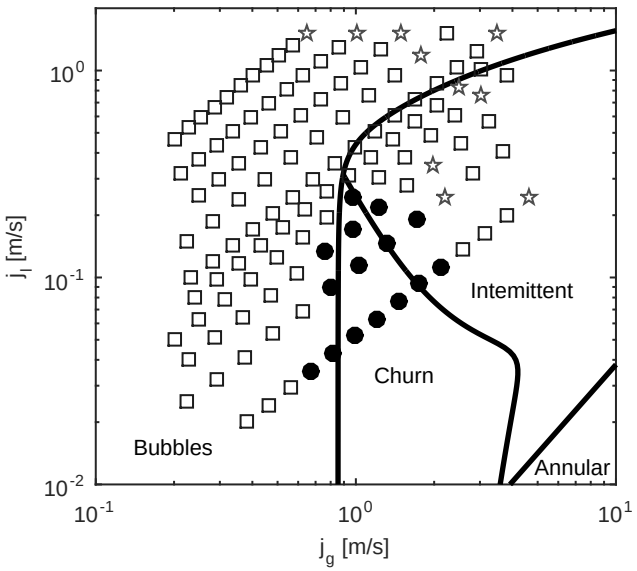

amplitude in tube bundles depends on the pair mass velocity/flow pattern. A first degree polynomial is a feasible approximation for the relationship between flow induced vibration amplitude and mass velocity, at least for homogeneous void fractions up to 75%. Though flow pattern plays an important role in tube vibration, modeling the fluid-structure interaction in terms of flow patterns is still a pending task. For the moment, these difficulties can be eluded by using models aiming to estimate the higher amplitudes that occur in buffeting vibration mechanism induced by turbulent flow, hence the design guidelines reviewed in section 3.2.2 are tested for the present experimental data.

6.3.2 Validation of design guideline proposed by Taylor et al. (1989)

The design guideline suggested by Taylor et al. (1989) was implemented for the present test section and flow parameters. This envelope and the results obtained for the experimental conditions covered by the present study are depicted in Fig. 6.19. As it can be seen from this figure, the design guideline proposed by Taylor et al. (1989) accomplishes its goal, that is to calculate an upper bound on $NPSD$ values within $25\% < \alpha_H < 90\%$. Also, it was verified that for $\alpha_H \geqslant 80\%$ the slope of experimental result increases. Actually, at $\alpha_H = 95\%$ the results are slightly higher than those predicted by Eq. 3.63, which is beyond the validity range of the method proposed in Taylor et al. (1989).

Figure 6.19: *Normalized power spectral density of random turbulence excitation for normal triangular tube bundle,* $\tau = 1.26$, $f = 105.2Hz$.

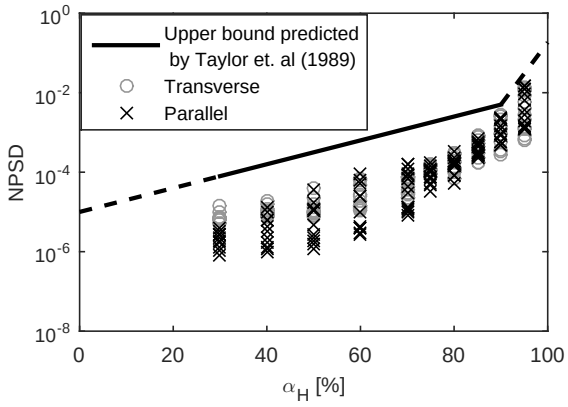

6.3.3 Validation of design guideline proposed by Papp and Chen (1994)

The coefficient of interaction, as proposed in Papp & Chen (1994), was calculated according to Eq. 3.69 for the experimental conditions tested in the present work. The results for transverse and parallel directions are depicted in Fig.6.20 against the homogeneous void fraction. In addition, the standard deviation of C_I data normalized by its mean value, σ/C_I, was calculated and shown in Fig.6.20.

As it can be seen from Fig. 6.20, the values of C_I in both directions are in the same order for void fractions up to 60%, however, from a strict point of view, the values obtained in the present study are one order of magnitude lower if compared with those proposed in Papp & Chen (1994). Some factors can be pointed out as decisive in these results, perhaps the most remarkable difference is that the tube response data used in Papp & Chen (1994) is two orders of magnitude higher than the response measured in the present work considering the same mass velocity range. This fact is directly related to the geometric differences between the instrumented tubes used in the present study and those used in Papp & Chen (1994). The instrumented tube used in the present study is shorter and its O.D. is greater than that used in Papp & Chen (1994), thus showing a higher bending modulus and, hence, a higher fundamental resonance frequency. Additionally, the pressure drop plays a fundamental role in the model proposed in Papp & Chen (1994). According to Papp & Chen (1994), higher pressure drop leads to higher tube RMS displacement, however, it is difficult to speculate that, regardless the tube bundle, the same amounts of mechanical energy, in form of pressure drop, are dissipated in form of tube vibration. Moreover, as it is analyzed later in this paper, the implementation of a distinct two-phase multiplier model affects the range of values of C_I.

Distinct behaviors can be pointed out for C_I mean values in each direction. While,

C_I mean values in the transverse direction are roughly constant for $\alpha_H \leqslant 60\%$, C_I mean values in parallel direction tend to increase with void fraction. Furthermore, as it can be seen from Fig.6.20, the standard deviation for $\alpha_H \leqslant 60\%$ in the transverse direction is lower than 24.4% of C_I mean value, and for parallel direction it is limited to 35.1%. Assuming that C_I presents a normal distribution, these results show that, for $\alpha_H \leqslant 60\%$, there is a probability of 68% that the actual C_I value is at least 24.4% and 35.1% higher than the C_I mean value in transverse and parallel directions, respectively. This result suggests that the adoption of maximum C_I as design criteria is more appropriate for $\alpha_H \leqslant 60\%$ than the C_I mean value.

Figure 6.20: *Coefficient of interaction for normal triangular tube bundle, $\tau = 1.26$, $f = 105.2Hz$, and C_I values proposed by Papp & Chen (1994) for normal triangular tube bundles with $\tau = 1.47$ and 1.32.*

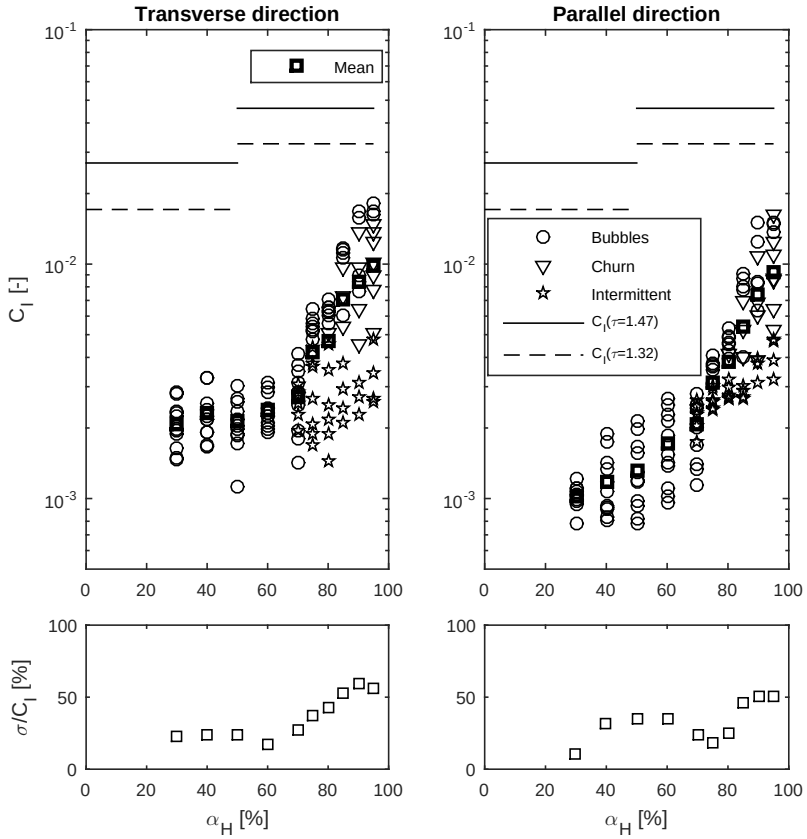

As it can be noticed from Fig. 6.20, C_I mean value increases with void fraction for $\alpha_H \geqslant 70\%$. Moreover, the standard deviation increases with void fraction for the same void fraction interval. In fact, the standard deviation reaches 60% and 50% of C_I mean value in the transverse and parallel directions, respectively. In this sense, based on the obtained results, it is difficult to point out a C_I mean value as a design guideline.

Regarding the behavior of C_I under distinct flow patterns, it can be said that bubbles flow pattern (occurring for all experimental conditions $\alpha_H \leqslant 60\%$) generates distinct

tendencies in transverse and parallel directions. Despite C_I mean value differences, it can be said that standard deviation seems to have a roughly constant value for each direction, except for $\alpha_H = 30\%$ in parallel direction. Furthermore, as it can be seen from Fig. 6.20, C_I mean values increase noticeably under bubbles flow pattern at high void fractions, while experimental conditions during intermittent flow pattern seem to generate lower and more similar C_I mean values, especially in parallel direction. The lower standard deviation values at $\alpha_H = 70\%$, 75% and 80% in parallel direction corroborate this behavior. In summary, it can be said that mass velocity and flow pattern hinder the characterization of a unique C_I mean value since the differences between the excitation impinged by different flow patterns, even at the same void fraction, contribute to the scatter in C_I data.

6.3.4 New results on the Coefficient of Interaction

The coefficient of interaction proposed in Papp & Chen (1994) also can be implemented by using different prediction methods for void fraction and pressure drop. It is of particular interest to use methods that were actually developed in the current test section. In this manner, the C_I values for all the tested conditions are calculated by using the void fraction (α_K) and pressure drop models proposed in Kanizawa & Ribatski (2017b), and the results are depicted in Fig. 6.21.

Figure 6.21: *Coefficient of interaction for normal triangular tube bundle, $\tau = 1.26$, $f = 105.2Hz$, implemented with void fraction and pressure drop models developed by Kanizawa & Ribatski (2016b), Kanizawa & Ribatski (2017b). Filled markers correspond to $G \leqslant 400kg/m^2s$ and empty markers correspond to $G > 400kg/m^2s$.*

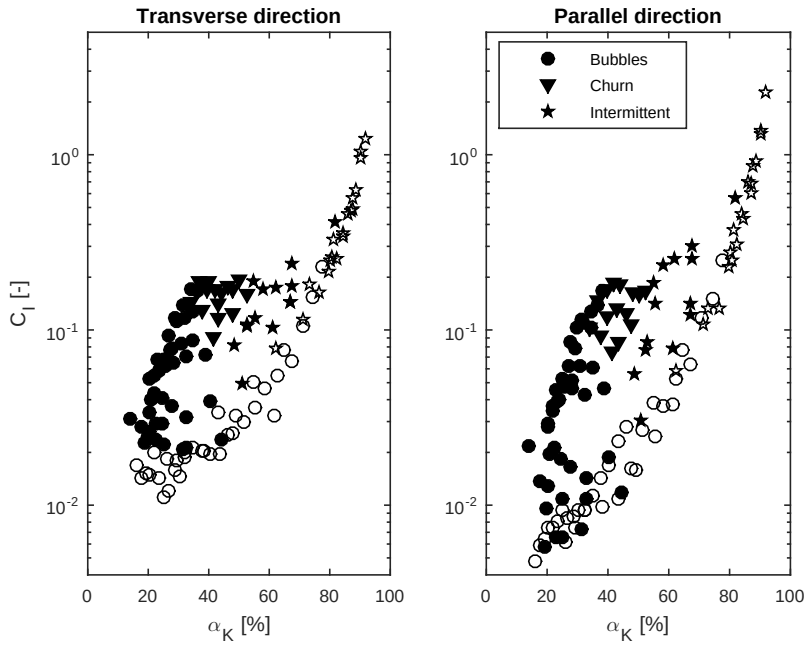

Based on a comparison of Figs. 6.20 and 6.21, it can be said that the implementation

of α_K allows to understand C_I values as a map, in which distinct flow patterns data tend to occupy defined regions. Furthermore, it can be said that the obtained C_I values are one order of magnitude higher than those estimated as proposed by Papp & Chen (1994). This divergence can be attributed to the difference in the estimated pressure drops, which were significantly smaller according to Kanizawa & Ribatski (2017a); hence, this aspect corroborates the discussion about the distinct excitation behaviors for each flow pattern. Moreover, according to Fig. 6.20, it can be observed that limiting the operational conditions for constant C_I might imply very low flow velocity, which deteriorates the heat exchanger performance. Therefore, in the present study a new predictive method that takes into account operational parameters, such as flow velocities, can be used to infer allowed safe operational conditions with higher heat transfer performance. Therefore, a predictive method is developed to estimate the coefficient of interaction as function of the flow velocity and void fraction. Since distinct trends were observed for each flow pattern, distinct correlations were proposed for bubbles, churn and intermittent flow pattern; unfortunately, experimental results for annular flow pattern were not obtained during the experimental campaign, hence a correlation for this flow pattern is not proposed. The correlations are function of non-dimensional parameters given by the only liquid Reynolds Re_l number (Eq. 2.59) and the void fraction α_K. In this manner, a correlation in the following form was proposed for each flow pattern:

$$C_I = a \cdot \alpha_K^b \cdot Re_l^c, \tag{6.8}$$

where the coefficient a and exponents b and c were obtained based on the Least Squares Methods. The flow patterns for each experimental condition were estimated according to Kanizawa & Ribatski (2016a), and the obtained constants are presented in Tab. 6.1 for the transverse and parallel directions.

Table 6.1: *Coefficient and exponents for C_I for each flow pattern and for each direction.*

Flow pattern	Direction	Parameters		
		a	b	c
Bubbles	Parallel	$3.66 \cdot 10^1$	1.76	-0.55
	Transverse	$1.67 \cdot 10^2$	2.50	-0.68
Churn	Parallel	$9.30 \cdot 10^0$	1.38	-0.40
	Transverse	$6.28 \cdot 10^1$	2.05	-0.60
Intermittent	Parallel	$2.84 \cdot 10^3$	7.33	-0.79
	Transverse	$4.45 \cdot 10^3$	7.47	-0.80

Figure 6.22 depicts the comparison between the estimated and experimental values of coefficient of interaction. According to this figure, it can be noticed that the proposed method presents good agreement with the experimental results for the transverse and parallel directions. However, some predicted values are slightly below the experimental

Figure 6.22: *Coefficient of interaction for normal triangular tube bundle, $\tau = 1.26$, $f = 105.2Hz$, estimated values according to Eq. 6.8 and Tab. 6.1 against experimental values.*

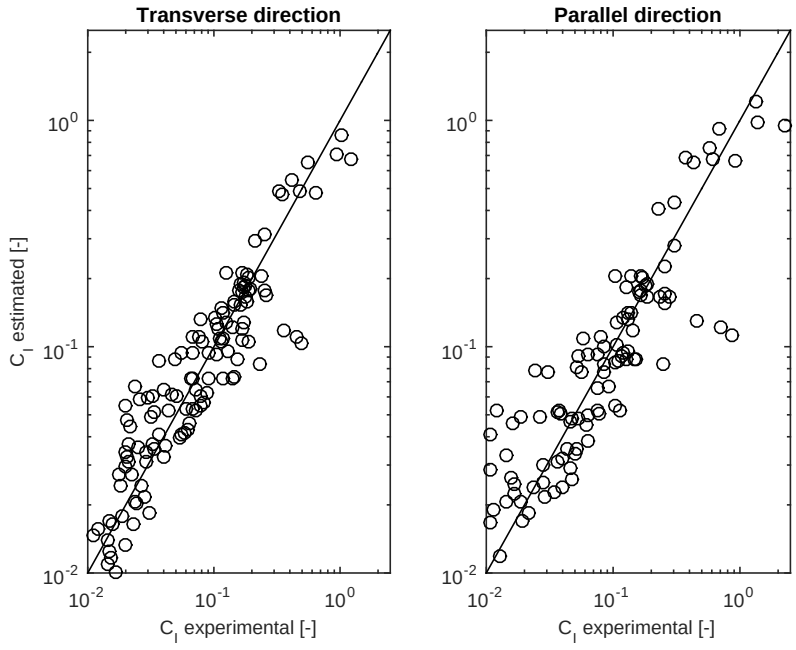

ones; hence, the adoption of a safety factor is recommended in order to avoid dangerous operating condition. Nonetheless, the predicted values would be well below those predicted according to Papp & Chen (1994) even for a safety factor of 2; hence, it is possible to define operating conditions with higher flow velocities, characterized by higher heat transfer coefficients. Based on the experimental results presented in Fig. 6.21, it is possible to infer that the variation of C_I with α_K presents distinct trends for different ranges of mass velocities. For higher mass velocities, characterized by $G > 400$ kg/m^{2}s, C_I seems to be directly related to α_K, while this relationship is unclear for lower mass velocities. Therefore, correlations for each mass velocity were also evaluated but they provide unsatisfactory predictions of the experimental data.

6.3.5 Validation of design guideline proposed by de Langre and Villard (1998)

The experimental data obtained in this work was also normalized and collapsed by using the method suggested by de Langre & Villard (1998), given by Eqs. 3.72 - 3.75, and the comparison with their design guideline, Eqs. 3.70 and 3.71, is shown in Fig. 6.23. As it can be noticed, the method developed by de Langre & Villard (1998) collapses the data measured in the present work, which is reasonable since it consists in a normalization of frequency and excitation level. Furthermore, the experimental data are below the upper bound defined by Eqs. 3.70 and 3.71. Thus, the results found in this work support the design guidelines proposed by de Langre & Villard (1998).

Figure 6.23: *Upper bound proposed in de Langre & Villard (1998) and experimental results obtained in the present work.*

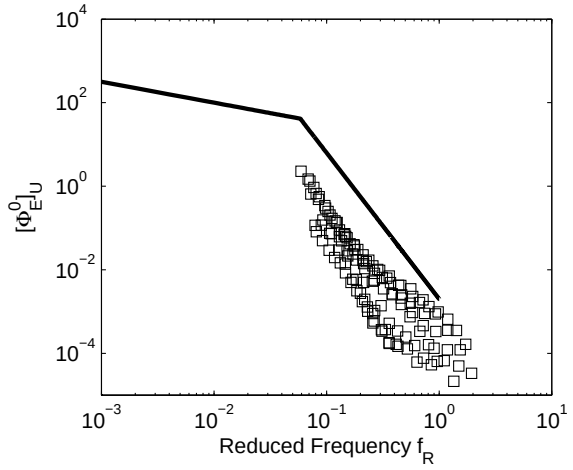

6.4 Implementation of AKF-DM algorithm

In order to estimate the flow-induced forces (and the other system states) via AKF-DM, it is necessary to have an approximation of the system model. Therefore, the first subsection below presents the identification of the system via EMA. After that, a series of pilot experiments are carried out aiming at checking the ability of the AKF-DM algorithm in the estimation of forces on multi-degree of freedom systems. Based on this analysis, some hypothesis are adopted in order to estimate the flow-induced forces on the cylinder in Section 6.5.

6.4.1 System identification

In the present study, EMA techniques are used to identify and represent the cantilevered cylinder described in Section 5.3.2. Since dynamic tests with known input would not be feasible in the actual test section, the identification procedure is performed by using the mock-up described in Section 5.3.2 and depicted in Fig. 5.7. After acquiring the FRFs, the data post-processing comprises two stages: (i) the poles and damping ratios are estimated via Least Squares Complex Exponential (LSCE) method, and (ii) residues and mode shapes coefficients are estimated via Least Squares Frequency Domain (LSFD) method (LMS, 2012). This procedure is performed in x and y coordinates, separately. Once the tube is mounted in the actual test section, these coordinates will correspond to the transverse (to the flow main velocity) and parallel directions, respectively (see Fig. 5.6). Moreover, the system is identified in air and submerged in quiescent water

The EMA procedure is performed in the 0 - 500 Hz frequency bandwidth, which presents the two expected resonance frequencies, as seen in Fig. 6.24. The undamped natural frequencies, damping ratios and modal vectors for tests in air and quiescent

Table 6.2: *EMA results in x and y coordinates, in air.*

Parameter		x coordinate		y coordinate	
		Mode 1	**Mode 2**	**Mode 1**	**Mode 2**
f [Hz]		38.4	258.4	34.7	227.1
ζ [%]		0.26	1.32	0.52	0.42
ψ	A1	9.81×10^{-1}	-2.61×10^{0}	9.96×10^{-1}	-2.78×10^{0}
	A2	2.67×10^{0}	1.68×10^{0}	2.50×10^{0}	1.60×10^{0}
MPC		1	1	1	1
MPD		$1 \times 10^{-14\circ}$	$3 \times 10^{-15\circ}$	$3 \times 10^{-15\circ}$	$3 \times 10^{-15\circ}$

water are shown in Tabs. 6.2 and 6.3. The modal vectors in these tables have been normalized according to the unity modal mass criterion available in LMS (2012). For the sake or brevity, and due to their similarity, only the vibration mode shapes for the x coordinate are shown in Fig. 6.25.

Figure 6.24: *Experimental and synthesized receptance FRFs in x and y coordinate, in quiescent water.*

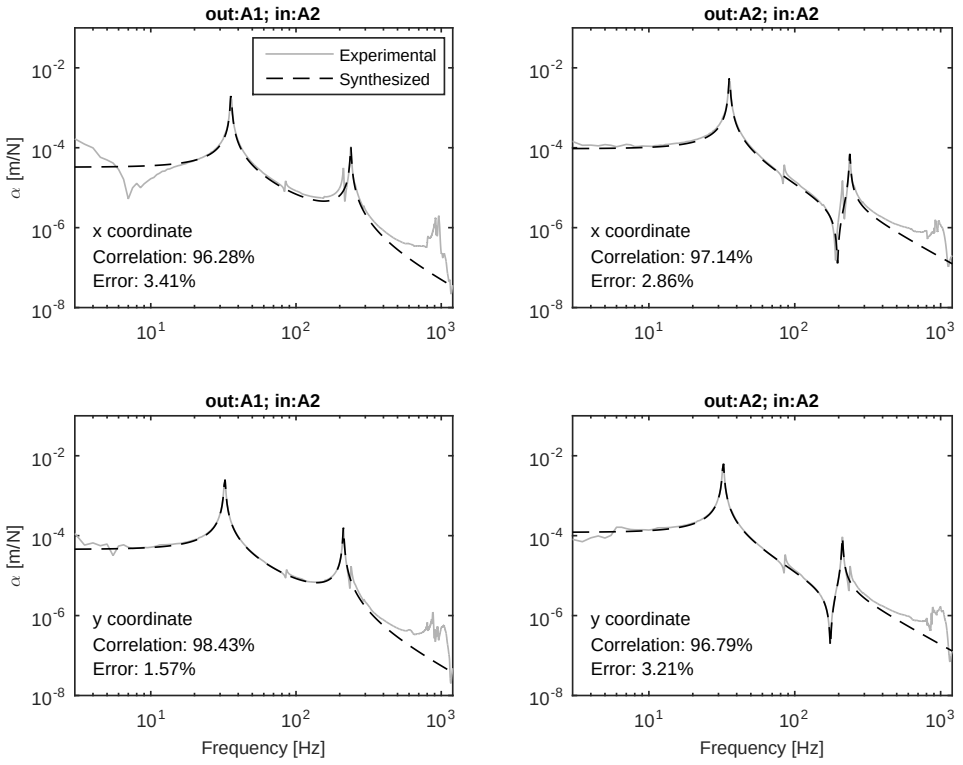

In order to check the hypothesis of proportionally damped structure, mode complexity indicators such as Modal Phase Collinearity (MPC) and Mean Phase Deviation (MPD) are included in Tabs. 6.2 and 6.3 for each calculated model. Considering that for real modes MPC approaches to unity and MPD scatter value should be zero, it can be said that calculated mode shapes are normal modes, thus proportional damping is a

Table 6.3: *EMA results in x and y coordinates, in quiescent water.*

Parameter		x coordinate		y coordinate	
		Mode 1	**Mode 2**	**Mode 1**	**Mode 2**
f [Hz]		35.6	238.3	32.3	212.0
ζ [%]		0.70	0.73	0.79	0.71
ψ	A1	7.93×10^{-1}	-2.30×10^{0}	8.85×10^{-1}	-2.58×10^{0}
	A2	2.17×10^{0}	1.51×10^{0}	2.22×10^{0}	1.53×10^{0}
MPC		1	1	1	1
MPD		$1 \times 10^{-14\circ}$	$3 \times 10^{-15\circ}$	$3 \times 10^{-15\circ}$	$3 \times 10^{-15\circ}$

Figure 6.25: *Mode shapes in x coordinate, in quiescent water.*

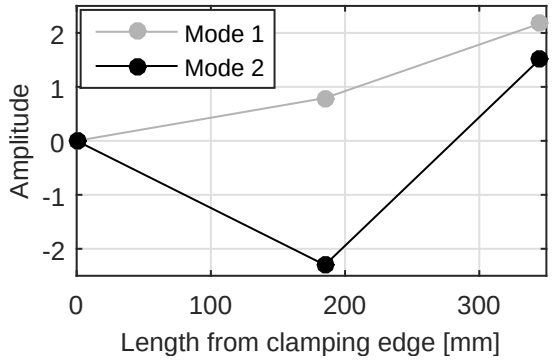

good approximation for the present study.

The synthesized and experimental receptance FRFs are compared in Fig. 6.24. As it can be seen from these FRFs, the models have been truncated to represent only the first two modes in each direction, since acceleration is measured only at two distinct points. Furthermore, as it can be noticed, there is some cross sensitivity, that is, the accelerometers in A1 and A2 in x coordinate are also sensing a portion of the tube vibration in y coordinate and vice versa. This must be related to manufacturing imperfections in the surfaces where the accelerometers are installed as well as on the fixturing of the sensors themselves. This effect is more accentuated in x than in y coordinate. Despite this, the identified system, represented by the synthesized FRFs, presents high correlation with experimental data within the frequency bandwidth in which the EMA algorithms are implemented [1].

6.4.2 Covariance matrices

Before the AKF-DM algorithm can be used, it is necessary to define the values of process, input and dummy measurements covariances, whereas measurement covariance, related to accelerometers, is obtained from calibration tests or provided by the instrument

[1] Correlation and error values are obtained from LMS Test.Lab - Modal Analysis module.

manufacturer.

The process noise covariance matrix, $\mathbf{R}_{\mathbf{w}}^{\star}$, as defined in Eq. 4.17, contains information about the uncertainty on the proposed model for the system and input force. Naets et al. (2015b) suggest to assume the model of the system as exact to eliminate these tuning variables and charge all the uncertainty to the unknown input force. This criterion agrees with that proposed by Berg & Keith Miller (2010), who used very low covariance for the system in comparison to the input force covariance. Although the modal model is truncated to considerate only the first two vibration modes, the system is known in a relatively good manner due to in situ identification detailed in Section 6.4.1. Therefore, very low covariance values in $\mathbf{R}_{\mathbf{w}}$ are assumed, given in the form:

$$\mathbf{R}_{\mathbf{w}} = \begin{bmatrix} R_{\dot{\eta}} & 0 \\ 0 & R_{\ddot{\eta}} \end{bmatrix}, \tag{6.9}$$

with

$$R_{\dot{\eta}} = 1(\mathrm{m/s})^2, \qquad R_{\ddot{\eta}} = 1(\mathrm{m/s^2})^2. \tag{6.10}$$

On the other hand, the input force is totally unknown. The input covariance matrix $\mathbf{R}_{\mathbf{z}}$ is defined as:

$$\mathbf{R}_{\mathbf{z}} = \begin{bmatrix} R_{\dot{u}1} & 0 \\ 0 & R_{\dot{u}2} \end{bmatrix}. \tag{6.11}$$

where, for tests in both directions, air and quiescent water $R_{\dot{u}1} = 0$ N^2 because no force was applied at point A1. Furthermore, $R_{\dot{u}2}$ is tuned and set equal to 2×10^3 N^2 for results in x and y coordinates in air, and 4×10^7 N for quiescent water.

The instruments covariance, $\mathbf{R}_{\mathbf{T}}$, given by Eq. 4.22, contains information about the uncertainty on the dummy measurements, whose matrix covariance is defined by

$$\mathbf{R}_{\mathbf{dm}} = \begin{bmatrix} R_{dm1} & 0 \\ 0 & R_{dm2} \end{bmatrix}, \tag{6.12}$$

where R_{dm1} and R_{dm2} are tuning variables chosen equal to the square of the order of magnitude of displacement, that is, $R_{dm1} = R_{dm2} = 1 \times 10^{-10}$ m^2. In this sense, estimates for displacement are obtained by using the model identified in section 3.2 and simulating its time response to the measured force applied on A2. Although these values will not be available in most of the real situations in which the AKF-DM algorithm can be applied, in the present study they are used to evaluate the ability of the method. Moreover, when dummy measurements are applied on displacement physical coordinates, Naets et al. suggest that the values of covariances may be chosen an order of magnitude higher than the actual motion of the system.

An alternative procedure to determine R_{dm} was tested before the values were set as

defined above. It was defined R_{dm} as inversely proportional to natural frequencies. The idea behind this is that low - frequency vibration modes are related to higher amplitude vibration, thus a higher covariance makes sense. Conversely, high - frequency modes that are related to lower amplitude vibration may have lower covariance. Although the main idea seems to be correct, acceptable results on simulation were not achieved.

Regarding the accelerometers covariance, $\mathbf{R_v}$, it is given by

$$\mathbf{R_v} = \begin{bmatrix} R_1 & 0 \\ 0 & R_2 \end{bmatrix}, \tag{6.13}$$

where R_1 and R_2 correspond to the covariance of accelerometers in A1 and A2, respectively, which were obtained via calibration and are detailed in Tab. 6.4.

Table 6.4: *Accelerometers covariance in (m/s^2)^2.*

Point	x **coordinate**	y **coordinate**
A1	40×10^{-4}	33×10^{-4}
A2	42×10^{-4}	22×10^{-4}

6.4.3 Initial tests on force estimation via AKF-DM algorithm

Previously to the estimation of flow-induced forces on the instrumented cylinder, it is necessary to make some tests on the performance of the AKF-DM algorithm. In order to do that under known conditions, a mock-up of the actual test section is used to mimic the boundary conditions of the cylinder installation. This set-up is described in section 5.3.2 and shown in Fig. 5.7. Further, discussions about the ability of the algorithm to predict forces in two-phase flow and the nature of them are proposed. Based on these discussions, some hypothesis for the force estimation via AKF-DM algorithm are summarized.

State estimation test

As it can be noticed from the literature review in Section 4.1, the only study in which random forces are identified via AKF is that proposed by Berg & Keith Miller (2010). In this sense, it is worth testing the ability of the AKF-DM on estimating an input force, which is random in time and concentrated on point A2. For this, the same force and acceleration data for system identification (section 6.4.1) is used. Since the force is predicted via a recursive type algorithm based on actual measurements for its updating, it is necessary to define the time step for its implementation. It is convenient to define the same sampling time used for data acquisition as the time step for system discretization, this is $\Delta t = 2.4414 \times 10^{-4}$ s.

For the sake of brevity, and due to their similarity, only the predicted forces obtained for x and y coordinates in quiescent water are shown in Figs. 6.26 and 6.27. The results are shown in a time window of 2 s and, for a more detailed view, results are presented in two distinct time lapses of 0.04 s, which are taken at the beginning and at the end of the complete window. As it can be noticed from these time lapses, the AKF-DM is able to predict the actual force in a relatively good manner based only on acceleration measurements and the introduced dummy measurements. An exception can be opened for the results in both directions at the beginning of the time window, where predicted values seem to be lower (x direction) or higher (y direction) than experimental results. Distinct combinations of covariances values were used to avoid this drift on the estimates, however the problem persisted.

Figure 6.26: *Measured and estimated force at DOF 2 in x coordinate shown for a complete time window and in detail for two distinct time lapses.*

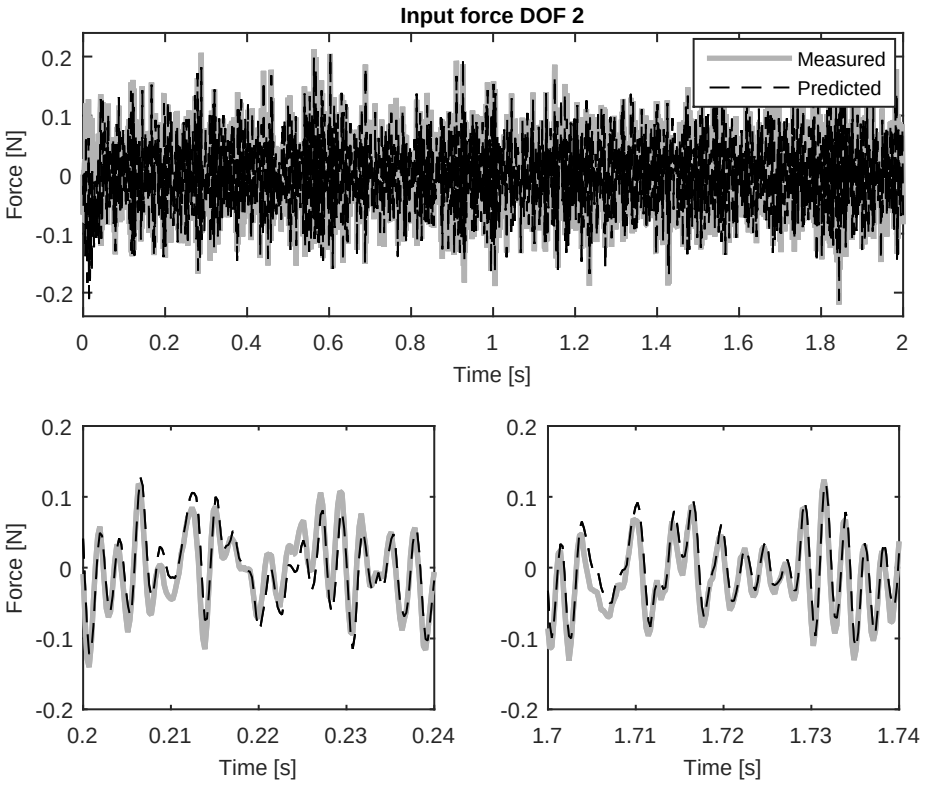

Since both measured and predicted forces are stochastic processes, basic statistical properties of importance for describing these signals are mean, Probability Density Functions (PDF), and Power Spectral Density (PSD) functions (BENDAT; PIERSOL, 2010). No prior differences were found by comparing the PSDs of measured and predicted forces for the present data. The probability distribution and the fitted PDF for forces in x and y coordinates are shown in Figs. 6.28 and 6.29. As it can be noticed , measured and predicted force in both coordinates present similar standard deviation, σ. On

Figure 6.27: *Measured and estimated force at DOF 2 in y coordinate shown for a complete time window and in detail for two distinct time lapses.*

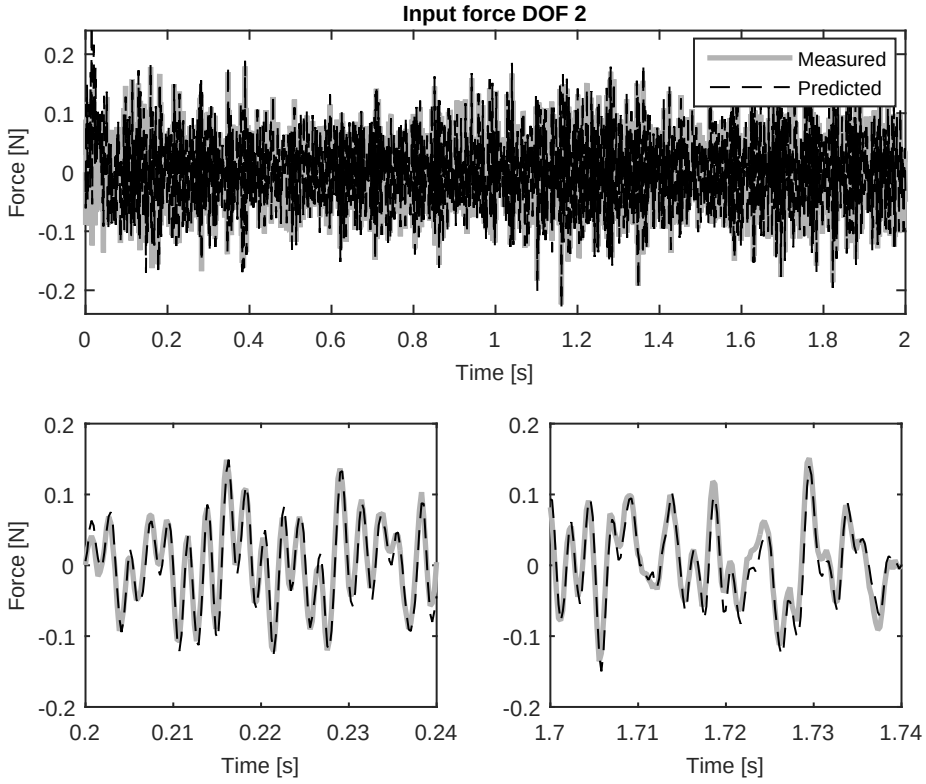

the other hand, it can be seen that the mean value of predicted force differ from that corresponding to measured data. This is directly related to the predicted values at the beginning of the time history that, as commented previously, present some deviation.

In general, it can be said that the AKF-DM algorithm allowed the prediction of concentrated, random in time forces, for a long time span. Furthermore, a relatively good prediction of the other state variables, that is η (modal coordinate defined in Chapter 4) and $\dot{\eta}$, is achieved.

States prediction when systems are identified in a distinct medium

Successful system state prediction for tests in air and quiescent water is the starting point for the present study on force estimation. Furthermore, it is expected that the same algorithm can be used to predict forces in two-phase flow, however, it is hard to perform a plant identification under these circumstances (two-phase flow) since a quiescent two-phase mixture cannot be maintained. In this sense, the plant initially identified, which is part of the input data for the AKF-DM algorithm, must be a close approximation of the actual plant in two-phase flow so that states prediction is feasible. In other words, the initial approximation of the plant has to be close enough to the actual plant in two-phase flow, so that the AKF-DM algorithm is capable of updating

Figure 6.28: *Probability distributions and density functions of measured and predicted forces in x coordinate.*

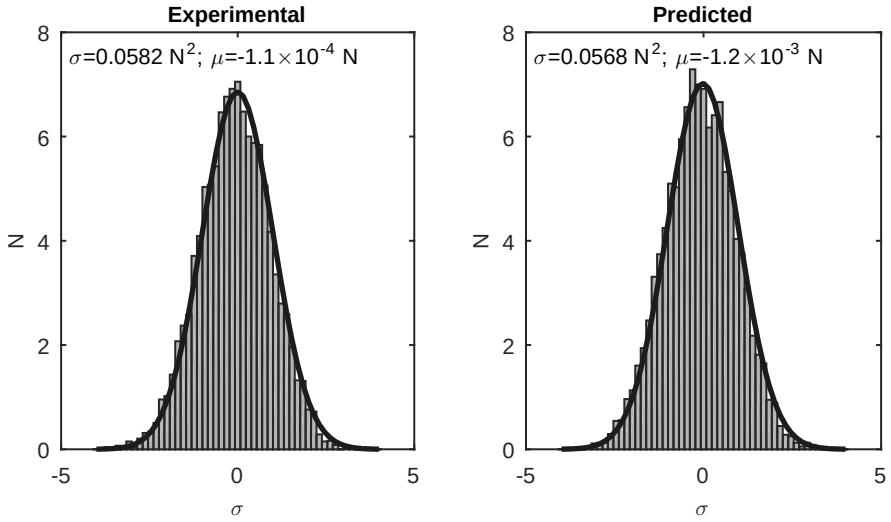

the plant characteristics based only on acceleration measurements.

In the present section, the experimental data obtained in tests performed in the mock-up in air and quiescent water are reused in order to check the algorithm versatility when the plant model differs from the actual conditions. In order to do that, the AKF-DM algorithm is used to predict the forces induced by the shaker when the cylinder is immersed in water, based on a plant previously identified in air and using acceleration data measured in quiescent water as reference. It was found that, despite the fact that the plant was identified in air, the algorithm tends to predict the states corresponding to tests in quiescent water, which is due to the fact that the reference accelerations are those measured in water. Moreover, it was found that the opposite case works well, that is, states corresponding to tests in air are successfully predicted when reference accelerations are those measured in air even if the initial plant for the recursive algorithm was previously identified in quiescent water. Besides the proof of the algorithm robustness, this result suggests that a plant successfully identified in liquid or gas can be used to predict system states in two-phase flow if acceleration measurements are used as reference for the AKF-DM algorithm. This is an interesting finding if one considers that system identification in two-phase flow poses an important experimental difficulty to face in tube response and flow-induced forces estimation. This should also hold true for other applications, in which plant identification is done in conditions that differ from the operational ones, such as: aerospace structures, systems subject to significant changes in temperature, inner pressure mass, systems with parameter dependent dynamics (robots and machine tools), etc.

Figure 6.29: *Probability distributions and density functions of measured and predicted forces in y coordinate.*

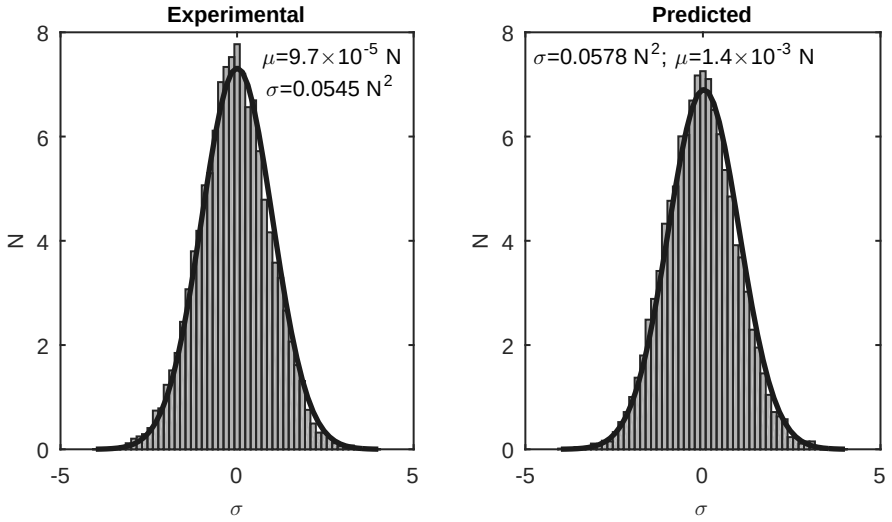

Nature of identified forces

As it can be noticed from Section 4.1.1 and Eq. 4.1, the system is modeled by using physical coordinates, which after some manipulation are expressed in modal coordinates in Eq. 4.2. According to this model, the forces can be applied on the present structure at positions A1 and/or A2. Therefore, the AKF-DM algorithm is able to predict the time history of forces at these positions. However, the closest representation of flow-induced fluctuating forces on tubes can be idealized as a distributed fluctuating load along the tube axis, in directions parallel and transverse to the flow main velocity. Furthermore, these forces could be assumed as uniform distributed along the tube if they are due to a continuous flow pattern (*e.g.* bubbles), that is, random forces with similar standard deviation.

The ideal instrumentation to identify each one of these forces, supposing that the AKF-DM is able to identify all these forces simultaneously, is the case of a full position measurement, which is impracticable. Therefore, it can be said that the present study is somehow bounded to represent the flow-induced fluctuating forces as a set of concentrated dynamic loads.

Ability of the AKF-DM algorithm on predicting a set of forces

In the discussion above, it was assumed that the AKF-DM algorithm is able to identify simultaneously as many as concentrated forces are acting on the structure. Given the fact that the instrumented cylinder that will be used in the present study can be modeled as a two degree of freedom system in each direction, separately, it is worth testing if the AKF-DM algorithm can predict and recognize two forces applied simultaneously on A1 and A2.

In order to carry out these tests, the response of the system identified in Section 6.4.1 is simulated by using command *lsim* of MATLAB ®. Subsequently, this response (acceleration) is the reference for the AKF-DM algorithm aiming to estimate the forces on the structure, which are known. Three distinct circumstances are tested. In all of them, random forces are applied. In order to generate the force time history, the command *randn* of MATLAB ® is used. This command returns an array of normally distributed random numbers. Moreover, this command is used to generate the forces since it is expected that, in the buffeting vibration induced by turbulent flow, the forces tend to be random in time. The following circumstances are simulated:

(I) One random force acting on the cylinder; AKF-DM algorithm configured for one input: Although an experimental validation on the identification of one force applied on the structure is detailed above (subsection *State estimation test*), this simulation is proposed because the force generated with command *randn* is distinct from the force applied by the electrodynamic shaker. The former is an approximation to a white Gaussian noise, whereas the latter present the effects of the shaker - structure interaction, that is, it is not a Gaussian but a colored noise. In this sense, the white Gaussian noise excites the structure homogeneously, while the colored noise has frequency bandwidths in which the excitation is more important. Based on these simulations shown in Fig. 6.30, it can be seen that the predicted force matches the actual force. However, the PSD of the predicted force presents peaks located at the first and second resonance frequencies of the system. These components should not be there.

(II) Two distinct random forces with the same standard deviation acting on the cylinder; AKF-DM algorithm configured for two inputs: By comparing the PSDs of actual and predicted forces in Fig. 6.31 it can be seen that the predicted forces present harmonic components at the system resonance frequencies that are not part of the actual force. Furthermore, it can be seen that the level of predicted forces is slightly lower than that of actual forces at low frequencies. In general terms, it can be said that, for frequencies higher than 10 Hz, the level of predicted force matches that of actual force, however, the presence of peaks at system resonance frequencies can be noticed.

(III) Two distinct random forces with the same standard deviation acting on the cylinder; AKF-DM algorithm configured for one input at the time: Since it was checked that a unique force can be predicted in a relatively good manner, it is proposed to predict the forces on A1 and A2, one at a time. For this, the AKF-DM algorithm can be reformulated to predict only one force but the acceleration response that is used as reference is the result of the action of both forces simultaneously. Following this procedure, it can be noticed that the force on A1 is overestimated, whereas, as it can be

Figure 6.30: *Comparison between actual and predicted force when one random force is applied on the cylinder. The AKF-DM algorithm is configured for one input.*

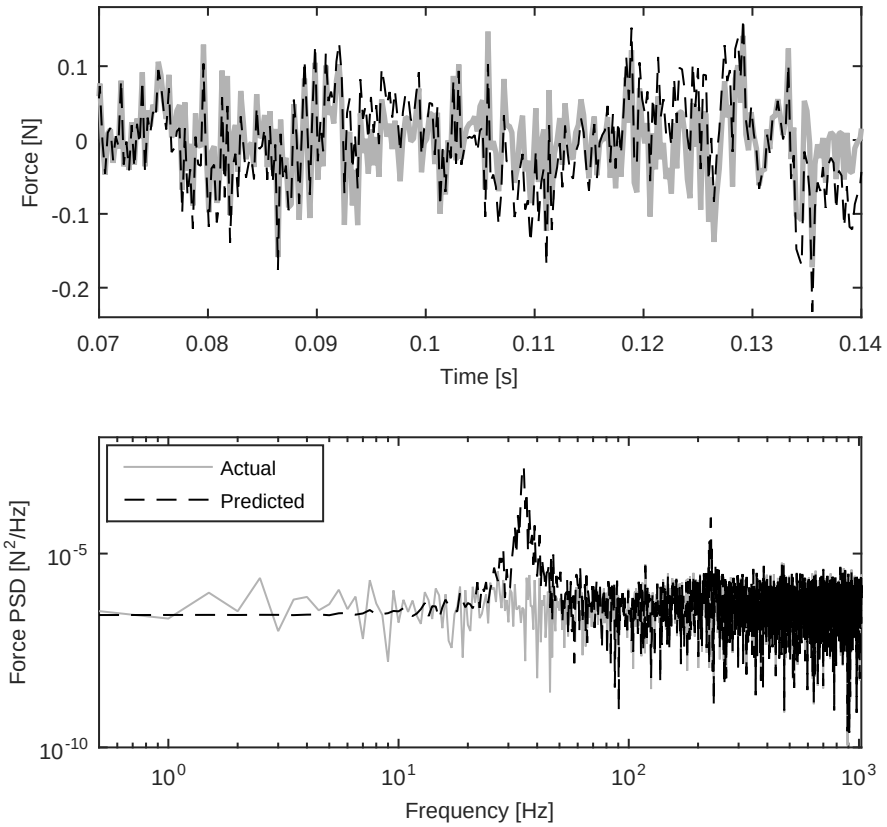

seen in Fig. 6.32, the force on A2 is relatively well predicted even though the peaks at the system resonance frequencies persisted.

Based on the simulations described above, it is possible to draw the following conclusions:

- The AKF-DM algorithm presents problems for predicting two forces acting simultaneously, these problems are: overestimation of forces and the inclusion of peaks at the system resonance frequencies. The analyzed cases show that forces at A1 are overestimated. Furthermore, predicted forces on A1 and A2 present peaks at system resonance frequencies as artifacts.

- It is difficult to predict the level of overestimation in the predicted force on A1, hence, it cannot be solved by using a known (or calculated) gain. Regarding the peaks, their influence can be attenuated by filtering, since their frequencies can be addressed from acceleration PSDs.

- To identify one force at the time do not solve the problem predicting the force applied on A1. On the other hand, the force on A2 is relatively well predicted, however the peaks at resonance frequencies persisted.

Figure 6.31: *Comparison between actual and predicted force PSDs when two random forces are applied on the cylinder. The AKF-DM algorithm is configured for two inputs.*

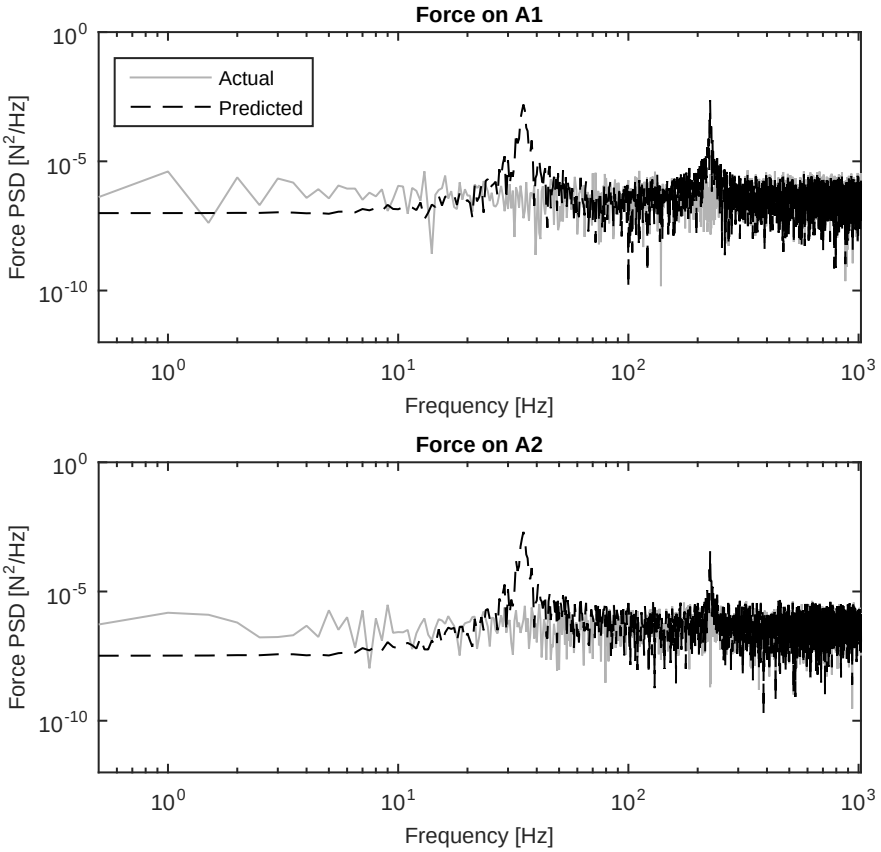

Based on these conclusions, it is proposed that, independently of the forces that may be acting on the structure, the acceleration responses of the structure to the forces applied simultaneously is used in the AKF-DM algorithm to predict just one *equivalent force*, that is, the force identified on A2. According to the simulations performed above, the equivalent force will be very similar to the actual force on A2, however, it cannot be referred to as force on A2 since the AKF-DM had to be modified in order to identify a single force based on the acceleration response that results from forcing the structure on A1 and A2.

Initially, the identified equivalent force will contain the peaks at system resonance frequencies, as discussed above. Further, these peaks can be filtered since, as discussed before, these peaks are assumed to be artifacts related to the implementation. The main idea is that the resulting equivalent force applied on the structure, at point A2, solely, is able to generate the same response as a set of random forces with similar standard deviation acting simultaneously, hence the claim of an equivalent force identification.

Figure 6.32: *Comparison between actual and predicted force when two random forces are applied on the cylinder but the AKF-DM algorithm is configured for one input.*

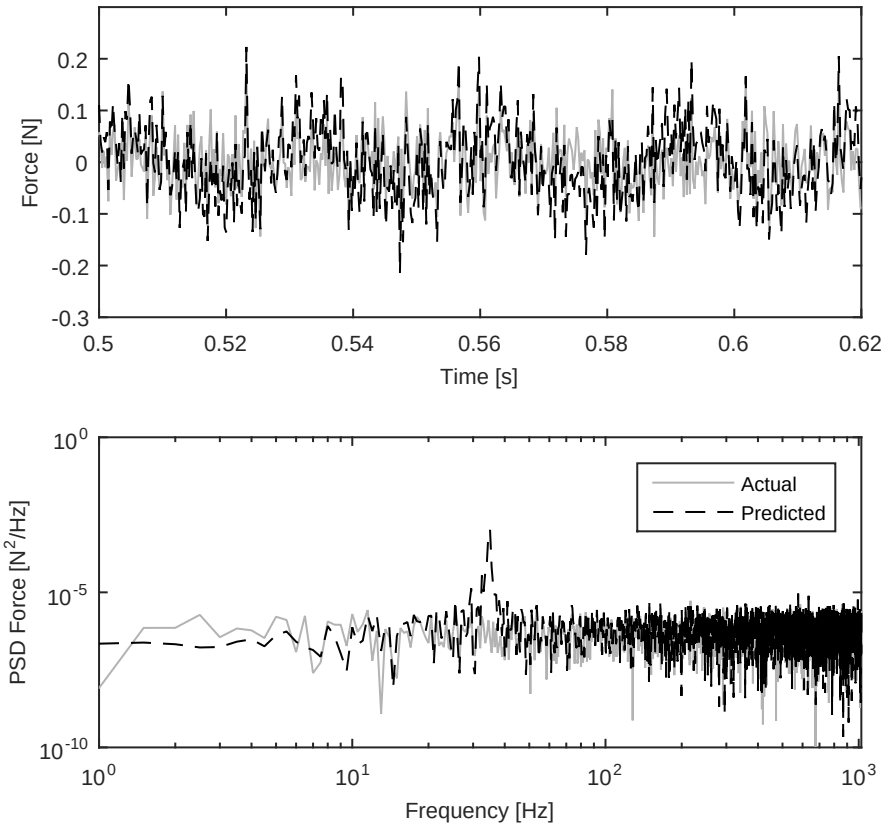

6.5 Forces induced by two-phase flow

In this section, the results of the equivalent flow-induced forces estimation via AKF-DM algorithm are analyzed. It is worth mentioning that these results are obtained by using the acceleration response data of the two-degree of freedom cylinder described in Section 5.3.2. This cylinder was subjected to the same experimental conditions used for the instrumented tube, whose results are detailed in sections 6.1, 6.2 and 6.3.

6.5.1 Conditioning of resultant force signals

Before the force results are analyzed, it is important to comment some conditioning procedures that are applied on the resultant predicted forces aiming to improve its quality for further discussion.

By analyzing the PSDs of the predicted forces, it was found that they present peaks at frequencies that should not be. For instance, predicted force signals present peaks at the resonance frequencies of the cylinder and the resonance frequencies of the whole test bench, however, there is no reason to believe that flow-induced forces do really have

these components. This circumstance may be justified if more tubes in the tube bundle had the same resonance frequency, however, this is not the case since the instrumented cylinder presents considerably lower natural frequencies. In order to avoid the effect of these peaks on the data analysis, the components at those frequencies are filtered in time domain by using a Butterworth type filter, executed by using command *filtfilt* in MATLAB ®. This command presents the feature of being a zero-phase digital filtering command. The filter is designed by using *buttord* command of MATLAB ®, which calculates the minimum order of the digital Butterworth filter required to meet a set of filter design specifications; *e.g.*, the passband ripple and the stopband attenuation.

Before the peaks can be filtered, it is necessary to address them in the spectra. Moreover, it has to be noted that the system resonance frequencies increase with increasing void fraction, that is, they vary from one experimental condition to another. Therefore, the values have to be tracked from the acceleration PSDs of each experimental condition.

Regarding the resonance frequency of the whole test bench, it must correspond to the first flexural vibration mode, which is justified due to the slender shape of the test section. In this sense, it vibrates along the direction of lower second moment of area, that is, along x direction (using the same coordinate system of the cylinder). The value of this resonance frequency depends on the quantity of mass in the test section, which depends on the void fraction. For this reason, this resonance frequency varies in the 5 - 15 Hz bandwidth. Furthermore, some effect of this vibration mode can be noted in y coordinate due to cross sensitivity.

6.5.2 Results on flow-induced forces

The PSDs of the equivalent forces for void fractions of 30%, 50%, 70% and 85% are presented in Figs. 6.33 - 6.36. The PSD of equivalent forces taken directly from the AKF-DM algorithm (non - filtered) and those post-processed according to the criteria described in section 6.5.1 (filtered) are plotted. As it can be seen, the filtered PSDs do not present peaks at the resonance frequencies of the system nor resonance frequencies of the whole test section. Moreover, any other peak not related to the system or test section resonances is maintained since it is expected that the calculated equivalent force is a fluctuating force, which, according to Perrot et al. (2011), is defined as a superposition of quasi-periodic and turbulence forces.

The results shown in Figs. 6.33 - 6.36 are chosen as example since they represent distinct experimental conditions. In each figure, the results obtained for distinct mass velocities are presented, lower mass velocities are presented in the upper subfigures. Furthermore, experimental results shown in Figs. 6.33 - 6.36 correspond to distinct flow patterns, which are defined according to the flow pattern map in Fig. 5.3. For instance, all the results presented in Figs. 6.33 and 6.34 correspond to bubbles flow

pattern. Moreover, the experimental conditions shown in Fig. 6.35 also correspond to the bubbles flow pattern, however, the PSDs in the middle and the bottom of the figure are conditions located in the transition boundaries between bubbles and churn - intermittent flow patterns, and bubbles and intermittent flow pattern, respectively. On the other hand, Fig. 6.36 present results for three distinct mass velocities at $\alpha_H = 85\%$, which correspond to three distinct flow patterns; bubbles (upper subfigure), churn (middle) and intermittent (bottom).

Figure 6.33: *Equivalent forces for* $\alpha = 30\%$.

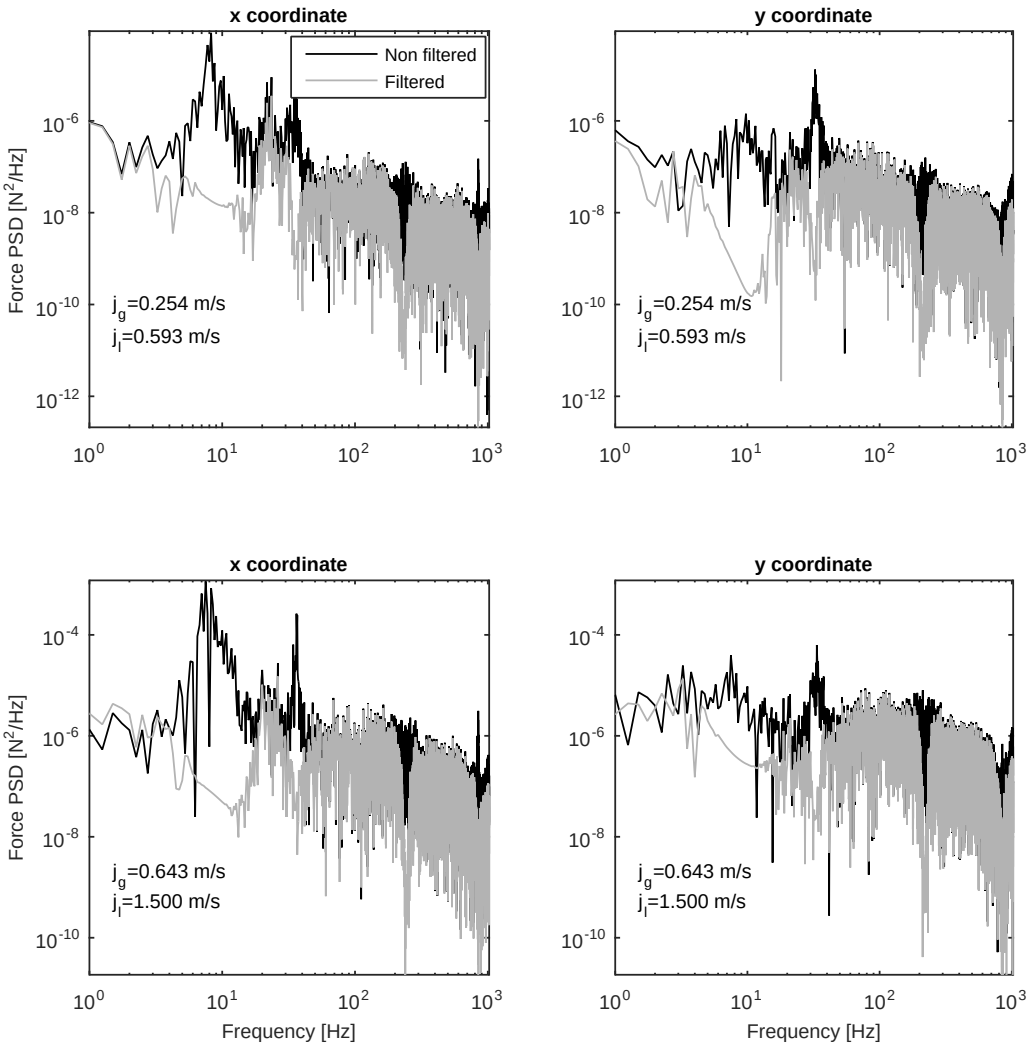

As it can be noticed from results in Figs. 6.33 - 6.36, buffeting is present in both coordinates and all the experimental conditions. It can be seen that, especially in y coordinate, the participation of turbulence is more notorious in the low frequency bandwidth, say 0 - 5 Hz, than in higher frequencies. In fact, intermittent-type flow patterns seem to accentuate this feature (see Fig. 6.36). Moreover, there are not peaks in

Figure 6.34: *Equivalent forces for* $\alpha = 50\%$.

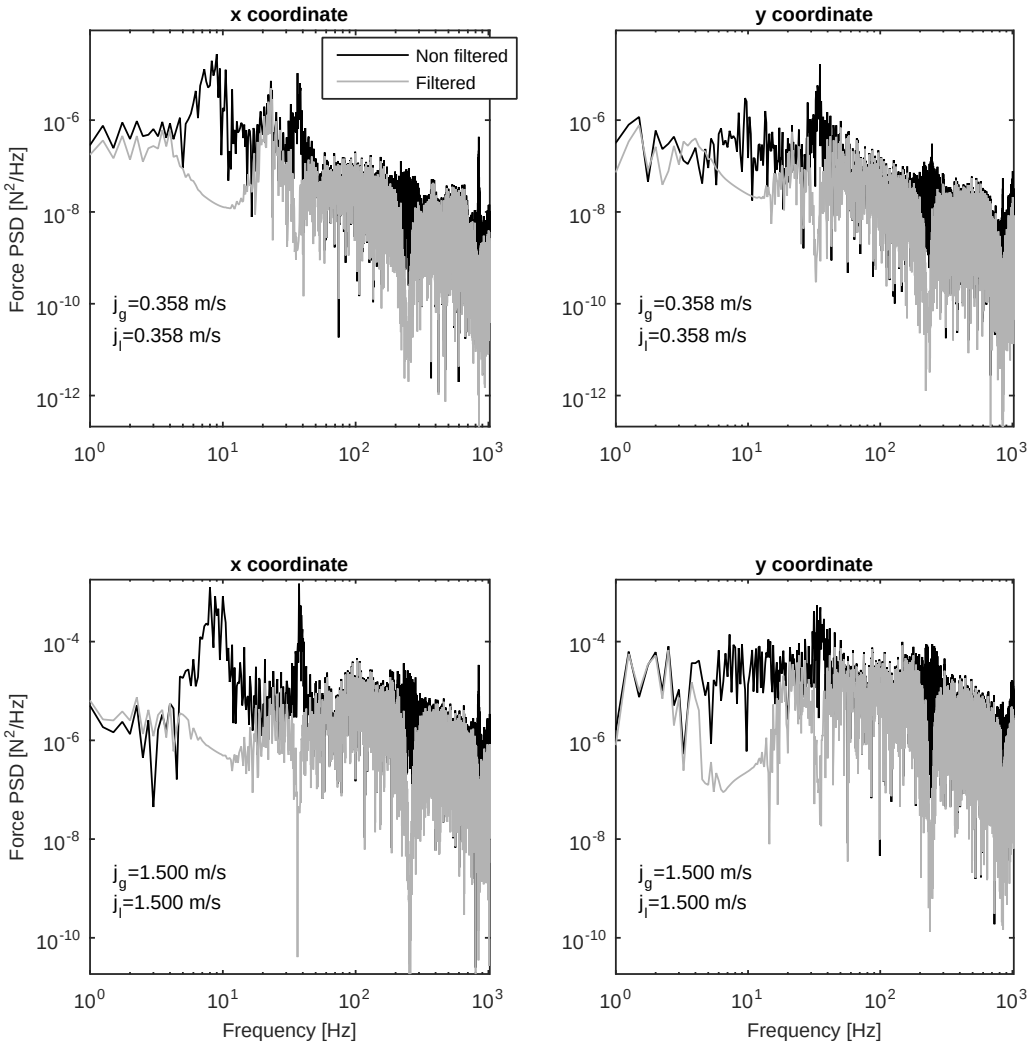

this low frequency bandwidth in x nor y coordinate.

As it can be seen from Figs. 6.33 - 6.35, results in the x coordinate present a peak at approximately 23 Hz. In fact, this peak is better defined for lower mass velocities and is more pronounced for void fractions up to $\alpha_H = 50\%$. The causes that lead to this peak are difficult to be explained since its frequency seems to be independent of mass velocity, namely quasi-constant frequency component. In this sense, this peak can hardly be related to vortex-induced vibration mechanism, which was described in Section 3.2.1, or quasi-periodic forces reported by Zhang et al. (2007) and Perrot et al. (2011). In fact, the results shown by Perrot et al. (2011) present a superposition of quasi-periodic forces with variable frequency and quasi-constant frequency components. According to their results, forces with a quasi-constant frequency component are present for $\alpha_H = 20\%$, at low pitch velocities (0.2 to 0.6 m/s), in both directions. Based on spectra and the type

Figure 6.35: *Equivalent forces for $\alpha = 70\%$.*

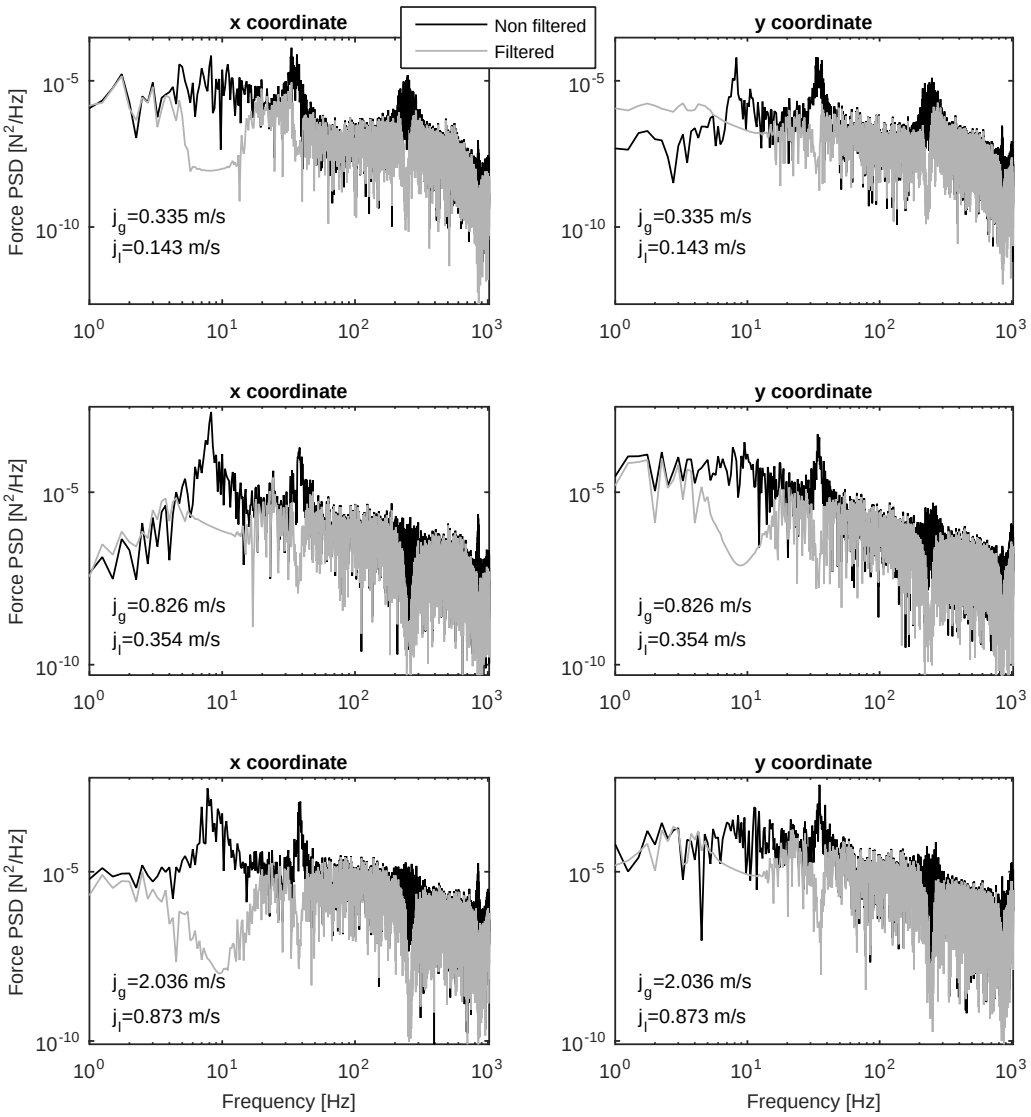

of data presented by Perrot et al. (2011), it is difficult to tell the exact frequency of this peak, however, one can conclude that it is located in the 0 - 10 Hz bandwidth. Therefore, the force component of quasi-constant frequency reported by Perrot et al. (2011) differs in frequency from that found in the present work.

According to Perrot et al. (2011), quasi-constant frequency forces for $\alpha_H = 50\%$ occur particularly in the parallel direction. Further, for $\alpha_H = 80\%$, forces present clearly defined periodicities with quasi-constant frequency components taking place in the pitch velocity range from 2 - 4 m/s. As it can be noticed, the behavior of these quasi-constant frequency components does not present a clear tendency. Moreover, Perrot et al. (2011) were not able to explain the mechanism behind the presence of this type of excitation neither.

Figure 6.36: *Equivalent forces for* $\alpha = 85\%$.

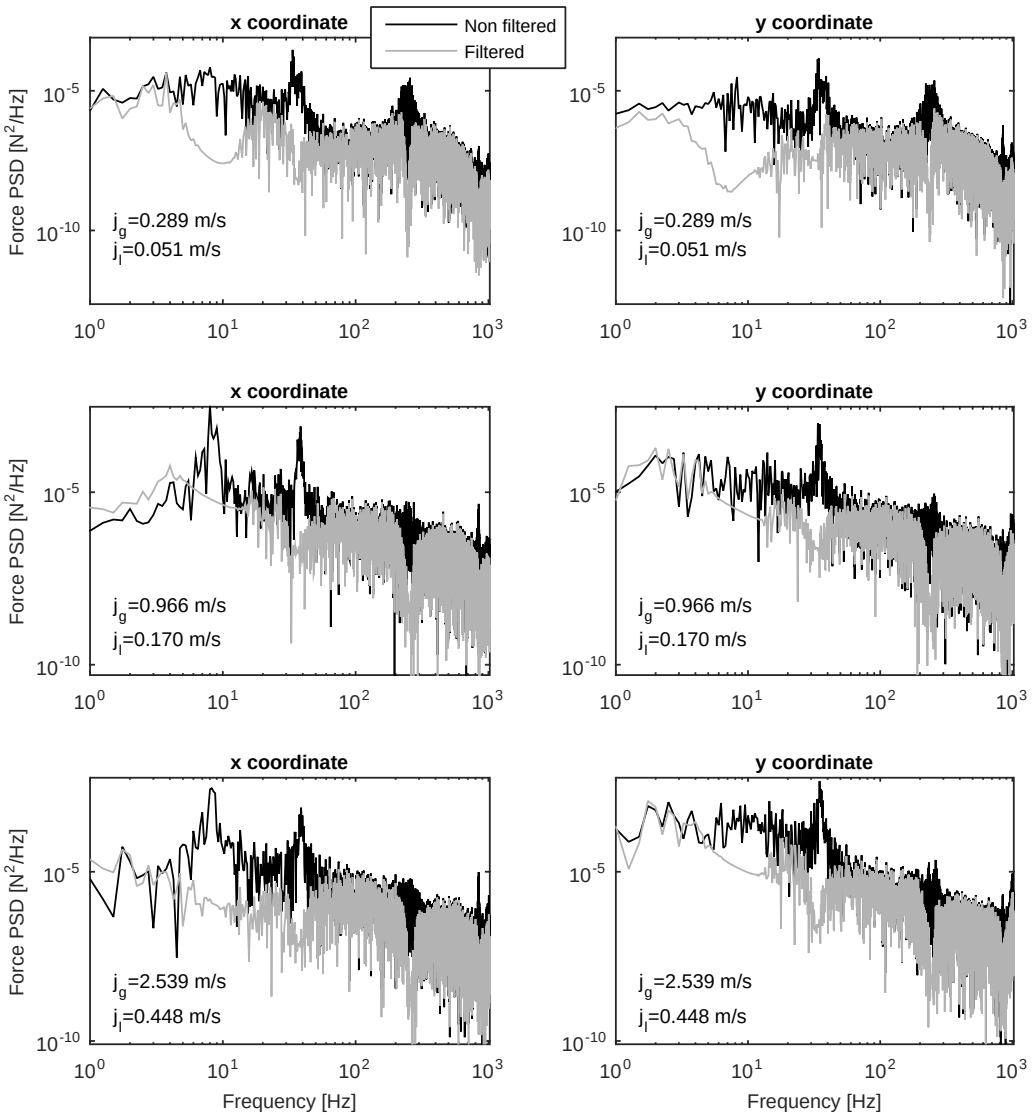

Based on the comparison between the present results and those found in literature (ZHANG et al., 2007; PERROT et al., 2011), it can be said that they differ on some points that, in fact, are not well defined in literature. For instance, the present results agrees with the results reported by Perrot et al. (2011) in the existence of forces with a peak at a quasi-constant frequency. However, as mentioned before, the frequencies found by Perrot et al. (2011) differ from the present results. In addition, Perrot et al. (2011) found this effect in both directions, while the results in the present work suggest forces with a quasi-constant frequency only in drag direction. For their part, Zhang et al. (2007) do not report any force with quasi-constant frequency.

Regarding quasi-periodic forces with frequency dependence on pitch velocity, they are reported by Zhang et al. (2007) and Perrot et al. (2011), however such phenomenon

is not found in the present work. In this context, there are two ways to understand this result: (i) the quasi-periodic forces with frequency dependence did not occur in the present test section, or (ii) the structure used in the present experimental campaign is insensitive to this phenomenon. By analyzing the first option, it must be pointed out that Zhang et al. (2007) report that the frequency of the periodic force in transverse direction varies linearly from 6 to 16 Hz, approximately, in the 1 to 10 m/s pitch velocity range, at $\alpha_H = 80\%$. In the present work, tests at $\alpha_H = 80\%$ with pitch velocities from 0.25 to 4.76 m/s are performed. In this sense, and by considering that both experimental campaigns use air-water mixtures, it can be proposed that the difference in the results between both works may be related to the tube bundle geometry. For instance, in the present work a normal triangular tube bundle with $\tau = 1.26$ is used, while Zhang et al. (2007) and Perrot et al. (2011) used rotated triangular and normal triangular tube bundles, respectively, in both cases with $\tau = 1.5$. In this context, one can think that the space between tubes in the tube bundle must play a role in the oscillations in the wake of cylinders and, therefore, in the vibration pattern in transverse direction. Regarding the vibration pattern in parallel direction, the differences between the results in the present work and those reported in Zhang et al. (2007) and Perrot et al. (2011) must be related to the distinct flow patterns that are taking place in each tube bundle (ZHANG et al., 2007). The occurrence of one flow pattern or another depends on the space between the tubes in the tube bundle as noted in some references (KONDO; NAKAJIMA, 1980). However, it is difficult to draw conclusions since the information provided by Zhang et al. (2007) and Perrot et al. (2011) about the flow patterns taking place in their test sections is scarce.

By analyzing the second option, the possibility that the structure is insensitive to the quasi-periodic components is related to the possibility that these components are undercovered by the dynamics of the structure and the test section. However, it is important to remark that these components vary with pitch velocity, therefore, they can hardly be hidden in all the experimental conditions. Furthermore, the presence of these components is checked in the non-filtered equivalent forces shown in Figs. 6.33 - 6.36; no additional peaks were found in these PSDs.

A straightforward manner to compare force intensity is to use the signal RMS amplitude as a parameter for discussion. The RMS values of forces obtained for experimental conditions at void fractions equal to 30%, 50%, 70% and 85% are shown in Figs. 6.37 - 6.40. In these figures, the RMS values of the post-processed (according filtering criteria discussed here) equivalent forces is presented in the upper subfigure. Furthermore, RMS values of non-filtered and filtered equivalent forces are compared in the bottom subfigures in order to check how filtering is influencing these tendencies.

As it can be seen from Figs. 6.37 and 6.38, the RMS values of the equivalent forces for $\alpha_H = 30\%$ and 50% increase with increasing pitch velocity. Moreover, for these void

Figure 6.37: *RMS values for equivalent forces for $\alpha = 30\%$.*

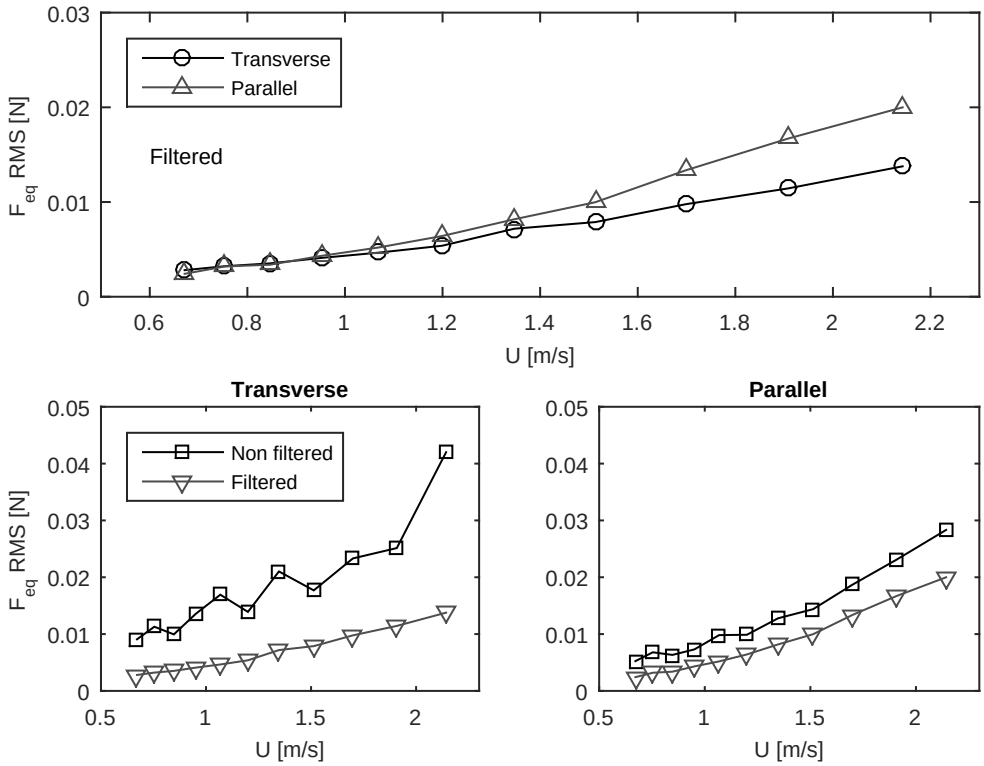

fractions, the RMS values of forces are similar in transverse and parallel directions for pitch velocities up to 1.3 and 1.4 m/s, respectively. Further, forces in parallel direction are higher than those in transverse direction for higher pitch velocities. These tendencies, increasing force RMS values with increasing pitch velocity, and force in parallel direction higher than in transverse direction after some pitch velocity, are also found for void fractions of 40% and 60%. Furthermore, it can be seen that non-filtered and filtered RMS values present similar tendencies in both directions, which implies that the filtering post-processing did not introduce any tendency to the RMS values analysis. From the point of view of flow patterns, all the conditions for $30\% \leqslant \alpha_H \leqslant 60\%$ correspond to bubbles flow pattern according to the map proposed by Kanizawa & Ribatski (2016a).

Although the analysis is in terms of RMS values of distributed fluctuating forces (given in units N/m), the results presented by Perrot et al. (2011) for a normal triangular array ($\tau = 1.5$) subjected to air-water mixtures with $\alpha_H = 20\%$ show tendencies similar to those found for $\alpha_H = 30\%$ in the present work; that is, the RMS value of fluctuating forces increases with pitch velocities when it is higher than 1 m/s, and parallel forces tend to be higher than transverse forces. For $\alpha_H = 50\%$, the RMS value of fluctuating distributed force in transverse direction tends to be quasi-constant for pitch velocities up to approximately 2.5 m/s. Conversely, the RMS values of fluctuating distributed force in parallel direction tend to increase with increasing pitch velocity and their values

Figure 6.38: *RMS values for equivalent forces for* $\alpha = 50\%$.

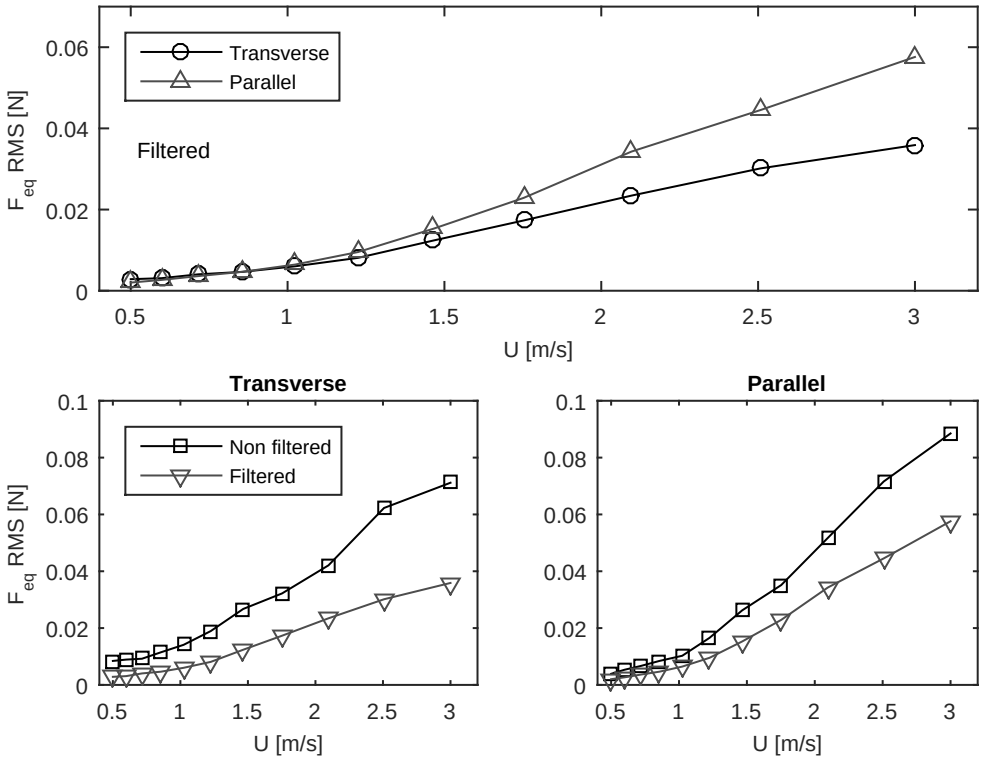

are higher than RMS values in transverse direction.

As it can be seen from Fig. 6.39, the RMS values of the equivalent force for conditions at $\alpha_H = 70\%$ maintain characteristics similar to results at $\alpha_H = 30\%$ and 50%. Moreover, all the conditions in Fig. 6.39 correspond to bubbles flow pattern according to the map in Fig. 5.3.

For higher void fractions, say $\alpha_H = 85\%$ in Fig. 6.40, it can be seen that the RMS values of equivalent forces in transverse direction are higher than the values in parallel direction for pitch velocities up to 0.9 m/s. Further, for higher pitch velocities, RMS force values in parallel direction are higher than RMS values in transverse direction. Additionally, based on the bottom subfigures in Fig. 6.40, it can be said that the behavior of the RMS value in transverse direction is not introduced by the post-processing filtering since non-filtered forces present the same tendency.

The same tendency identified for results at $\alpha_H = 85\%$ is observed for void fractions equal to 80%, 90% and 95%. Moreover, Fig. 6.41 presents force RMS values for $\alpha_H = 90\%$ and 95% and, as it can be noticed, the mentioned tendency becomes stronger as void fraction increases. According to the flow pattern map in Fig. 5.3 and the RMS values in Fig. 6.41, the local maximum force RMS amplitude in transverse direction is not generated by a specific flow pattern.

The characteristics of the equivalent forces obtained via AKF-DM algorithm have

Figure 6.39: *RMS values for equivalent forces for $\alpha = 70\%$.*

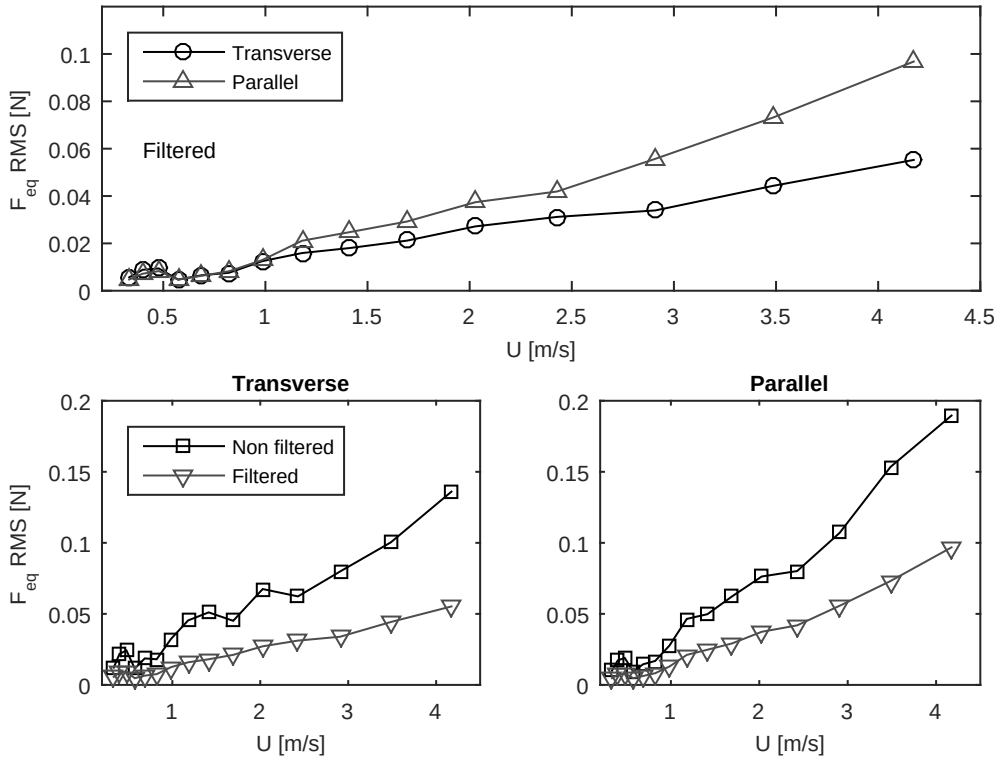

been described and discussed up to this point. Further, it is important to check how close are their values to the actual flow-induced forces on the tube. Unless the same structure has been used for tests reported in literature, the present results can hardly be compared to any database since these forces are a simplification that represents the actual set of forces. For the purpose of solving this lack of database for results validation, it is proposed to use an indirect method that compares the measured response to the response that would be generated by the estimated force.

In order to do that, a force time history based on the statistical parameters (*e.g.* mean and standard deviation) of the estimated force is generated in MATLAB. It is assumed that the flow-induced force can be represented as a normally distributed random vector, thus the MATLAB command *randn* can be used to generate the force vector. This force is applied on the system previously identified, which is described in Section 6.4.1. The acceleration response of the system is simulated by using the *lsim* command and the RMS values of the signals are calculated in MATLAB. Previously, the acceleration measurements have to be filtered in order to exclude components at frequencies that are not included in the synthesized model; *i.e.* the resonance peak of the whole test bench at approximately 8 Hz, cross-sensitivity peaks and any dynamic components at frequencies higher than 500 Hz, which was set as the upper frequency limit for system identification in EMA procedure. The comparison between simulations and measured

Figure 6.40: *RMS values for equivalent forces for* $\alpha = 85\%$.

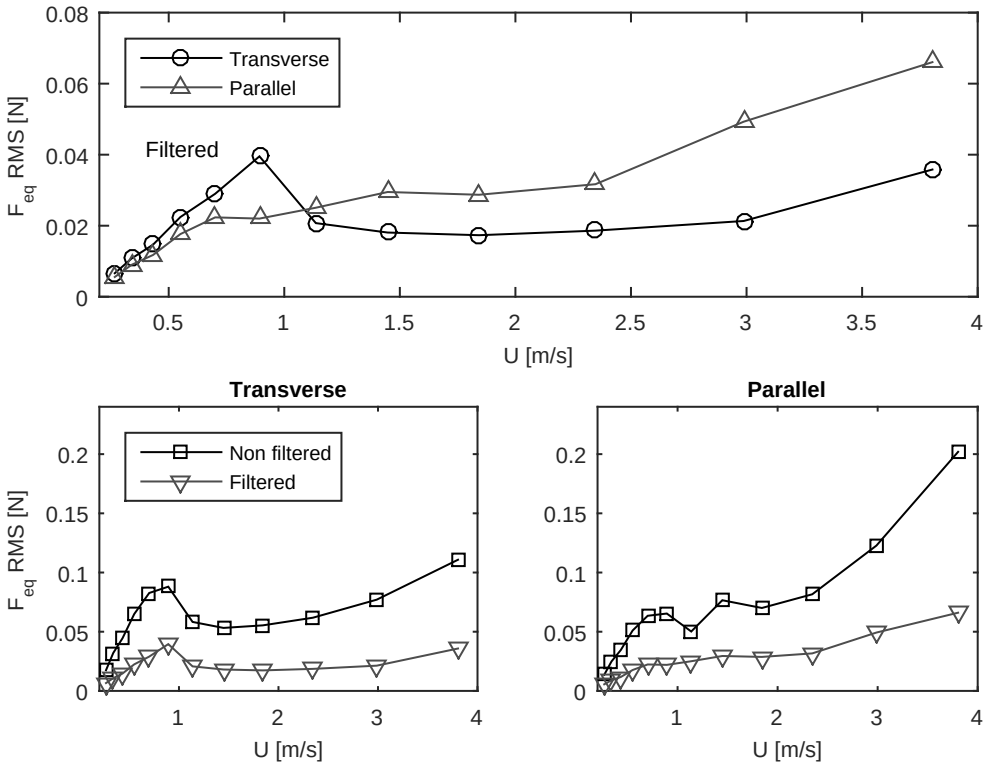

values for distinct void fractions are shown in Figs. 6.42 - 6.45.

The RMS values of measurements in Figs. 6.42 - 6.44 have something in common, they are relatively well organized. This is probably related to the fact that the experimental conditions (*e.g.* void fraction and flow pattern) behind these results generate a kind of response proportional to mass velocity. In this manner, the RMS values of acceleration appear as sorted following increasing amplitude criterion with increasing mass velocity. Moreover, it is worth mentioning that all experimental results in Figs. 6.42 - 6.44 correspond to bubbles flow pattern. Conversely, it can be noticed from Fig. 6.45 that data is somewhat unorganized, mostly in x coordinate. In fact, such kind of disorder in RMS amplitudes of acceleration measurements can be found for tested conditions with void fractions higher than 80%, where distinct flow patterns occur in the test section.

As it can be seen from Fig. 6.42, the simulated acceleration response at points A1 and A2 agree with the corresponding measurements, mainly in y coordinate. The difference between simulated and measured acceleration becomes more notorious as void fraction increases. For instance, Figs. 6.43 and 6.44 show that the simulated accelerations tend to underestimate the actual acceleration as mass velocity increases. Once again, Figs. 6.43 and 6.44 show that the RMS values of accelerations in y coordinate are better predicted than those in x coordinate.

Figure 6.41: *RMS values for filtered equivalent forces for $\alpha_H = 90\%$ and $\alpha_H = 95\%$. Filled and dotted lines correspond to transverse and parallel directions, respectively.*

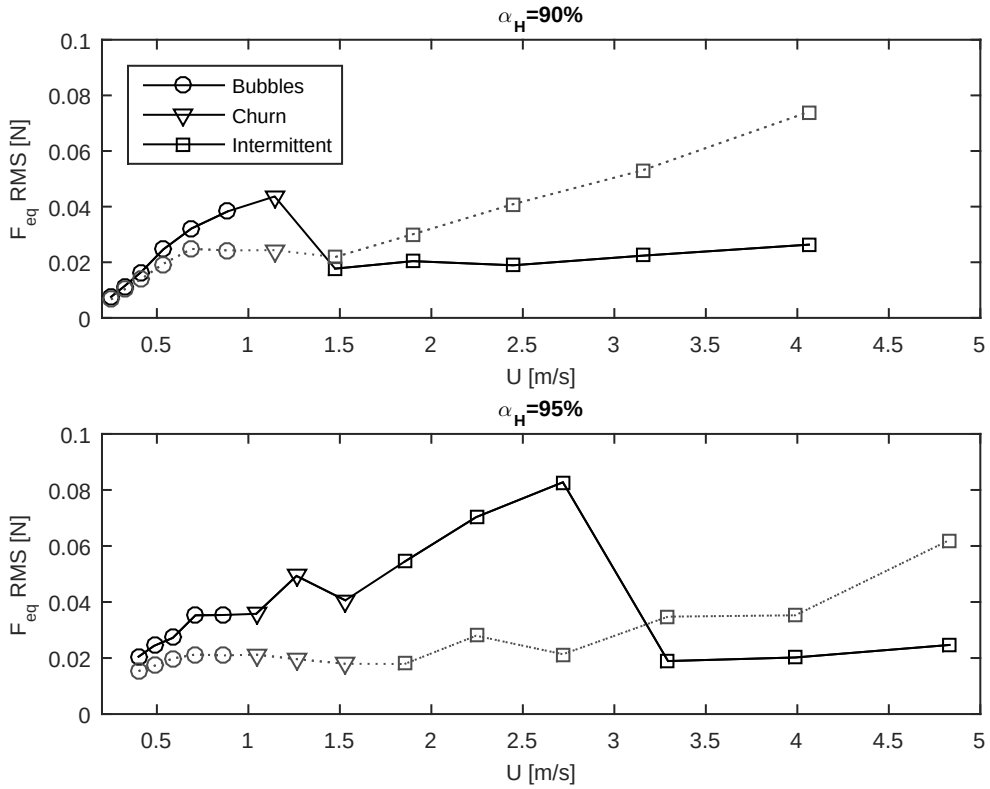

For void fractions higher than 80%, for example $\alpha_H = 85\%$ in Fig. 6.45, the simulated accelerations in x coordinate differ from measurements considerably. In these cases, simulated accelerations can be higher or lower than RMS values of measurements. Furthermore, it can be noticed that the RMS values of simulated accelerations are closer to actual values when bubbles flow pattern is taking place in the test section.

On the other hand, RMS values of simulated acceleration in y coordinate seem to present better coherence with RMS values of measurements. However, there are experimental conditions in intermittent flow pattern whose RMS values of acceleration are underestimated. Further, RMS values of simulated acceleration for $\alpha_H = 95\%$ totally fail in predicting RMS values of acceleration measurements in both coordinates.

Figure 6.42: *Comparison between measured and simulated accelerations for* $\alpha_H = 30\%$.

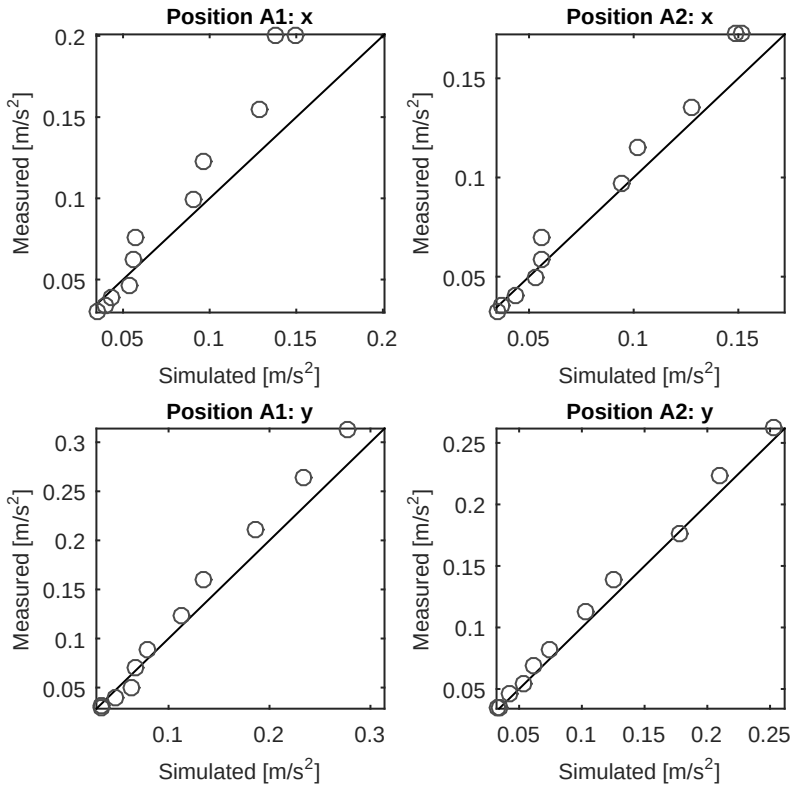

Figure 6.43: *Comparison between measured and simulated accelerations for* $\alpha_H = 50\%$.

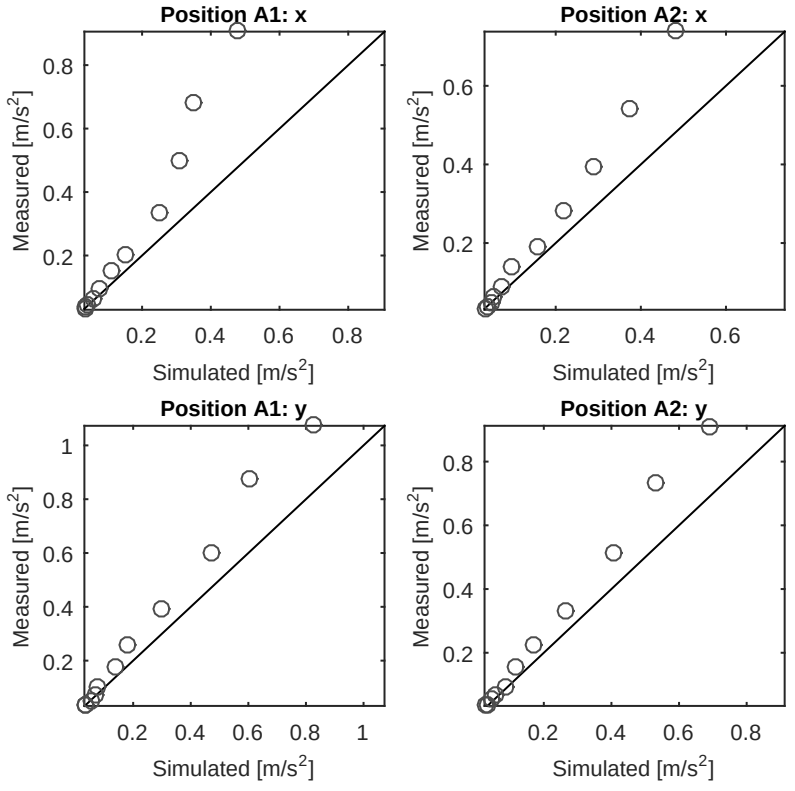

Figure 6.44: *Comparison between measured and simulated accelerations for* $\alpha_H = 70\%$.

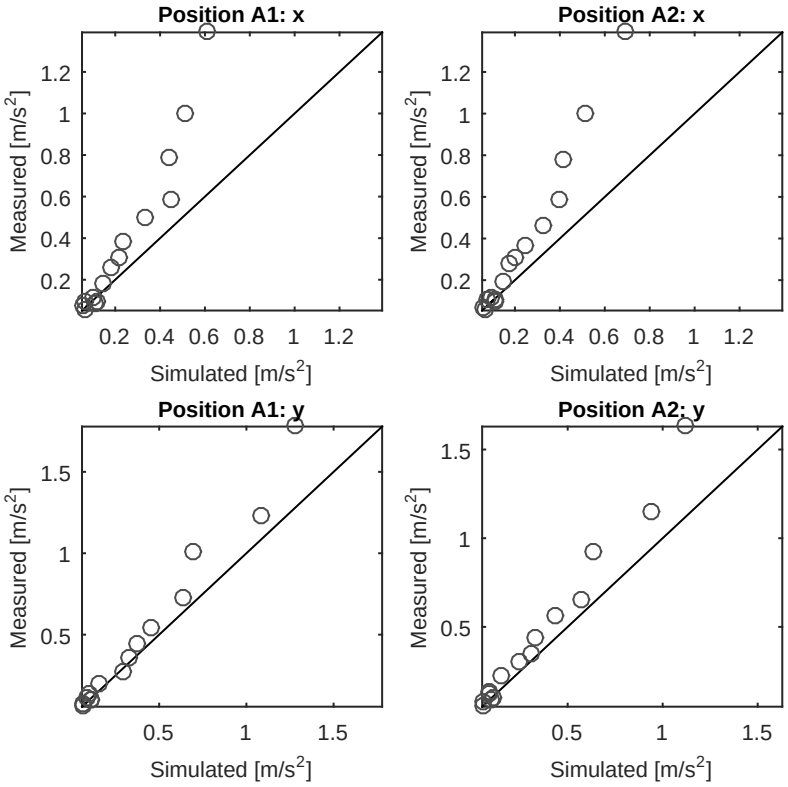

Figure 6.45: *Comparison between measured and simulated accelerations for* $\alpha_H = 85\%$.

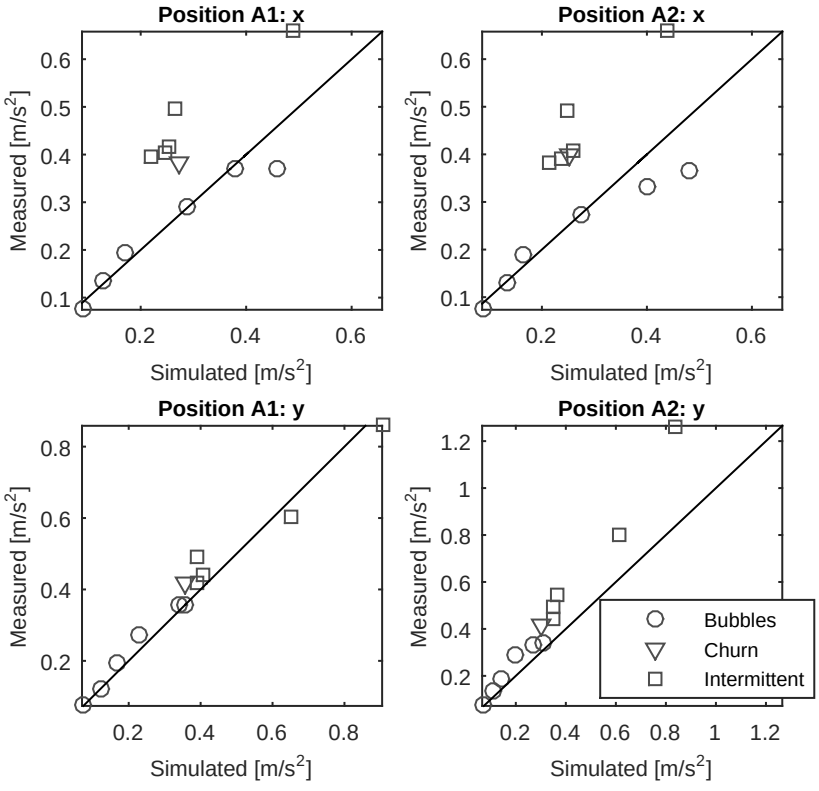

Chapter 7

Final remarks

This manuscript contains both bibliography review and experimental studies on flow-induced vibration phenomena in tube bundles. Particularly, the dynamic parameters of tube vibration in tube bundles and the buffeting vibration due to two-phase crossflow are studied.

Regarding the dynamic parameters, its definitions, experimental database and design guidelines on hydrodynamic mass and damping ratio are reviewed. This database is used to validate the experimental results obtained in the present work. Further, results are discussed based on the definitions in bibliography, mainly void fraction, flow patterns and mass velocity. A similar review is proposed for the buffeting vibration mechanism due to two-phase flow. In fact, three design guidelines are implemented based on the same experimental data used for the study of the dynamic parameters. One of these design guidelines is modified to consider the implementation of a more recent void fraction model. In addition, the forces induced by two-phase flow on a cantilever structure mounted in the tube bundle are estimated via AKF-DM algorithm. By using an indirect approach, equivalent forces are validated.

Based on this summary of activities, this chapter describes the conclusions that were obtained from this study, as well as the suggested future works.

7.1 Conclusions

Regarding to the dynamic parameters of the tube, the resonance frequency clearly depends on void fraction, which was expected due to hydrodynamic mass effect. The behavior of hydrodynamic mass measurements with increasing homogeneous void fraction agrees with that predicted by the analytical model. However, at high homogeneous void fractions ($\alpha_H > 80\%$), the measured values are higher than those predicted, which may be attributed to the effect generated by the intermittent type flow pattern, in which liquid and gas phases flow somehow separately and differs from the idealization of well-mixed homogeneous flow model. Such effect is also represented by the higher

slip between the phases, which would lead to a higher liquid *hold-up* phenomenon. This means that the tube is immersed in liquid for longer time periods, whereas gas slugs flow upwards faster implying higher added mass in tube vibration.

The presence of *hold-up* phenomenon in the present hydrodynamic suggest that, as indicated in the open literature, the homogeneous void fraction model is not appropriate for high void fractions. Based on the present experimental results, the void fraction models proposed by Xu et al. (1998), Feenstra et al. (2000) and Kanizawa & Ribatski (2017b) represent an important alternative to obtain better hydrodynamic mass predictions for higher void fractions.

The damping ratio is the sum of structural, viscous and two-phase components. Modeling two-phase damping ratio is a complex task since it strongly depends on void fraction and flow patterns, while it is slightly affected by mass velocity. Semi-empirical and a semi-analytical models found in the open literature were reviewed. The former aims to define a lower bound of damping values as a function of void fraction, while the latter formulates damping in the lift direction as a function of flow parameters. Despite of being developed only for lift direction, similar values can be inferred for drag direction as long as the flow velocity is considerably lower than fluidelastic instability threshold. It must be pointed out that there is still some difficulty in obtaining a robust model for the damping magnitude. For instance, the semi-empirical model depends on the approximation of a correlation constant that must be chosen carefully in order to avoid damping underestimation. In the case of the semi-analytical model, there are still some problems when it is used along with models that effectively represent the actual phenomena taking place in the test section (*e.g.* pressure drop, flow patterns and void fraction). Anyway, by the moment, the semi-empirical model proposed by Pettigrew & Taylor (2004) is preferable since it is easier to implement and is supported by all the available experimental results.

The behavior of damping values estimated in this work agrees with the reviewed data, that is a peaking behavior at intermediate void fractions. Moreover, in contrast to what has been reported in some works, which point out that maximum damping occurs during intermittent flow, in the present study the highest damping values were observed during dispersed bubbles flow pattern. However, it is worth mentioning that it is difficult to draw conclusions about the effect of flow pattern on damping since distinct flow pattern maps, criteria and definitions have been used in the experimental campaigns reported in literature.

In a second part, the buffeting vibration mechanism induced by two-phase flow was studied in the present work. Air–water mixtures with homogeneous void fractions from 30% to 95% and mass velocities up to half the critical velocity for fluidelastic instability were used. The comparison between vibration levels for distinct conditions showed that vibration amplitude is not only a function of mass velocity, but also depends on

void fraction. For instance, the vibration amplitude of a tube subjected to high mass velocity but low homogeneous void fraction can be lower than when subjected to low mass velocity but high homogeneous void fraction. This fact suggests that flow patterns play an important role in tube vibration.

Regarding the relationship between RMS amplitude of vibration and mass velocity, it was shown that it can be roughly represented by a linear function for homogeneous void fractions up to 75%, even though this approximation disagrees with the results for $\alpha_H = 60\%$, which would be better represented by a second order polynomial on mass velocity. Thereafter, for higher void fractions, this linear behavior is interrupted by a transition zone, which is characterized by a slight increase of RMS amplitude with mass velocity. The results for the transition zone correspond to churn flow pattern.

Three distinct design guidelines aiming to estimate the vibration severity in a tube bundle were implemented for the experimental conditions performed in the present study. It was found that the present experimental results are below the upper-bound given by two of the implemented guidelines. The remaining design guideline, based on the determination of a coefficient of fluid-structure interaction, overpredicted the vibration level. In this sense, this design guideline was reformulated as function of the latest void fraction model. This led to understand the behavior of the coefficient of interaction with void fraction as a map rather than a single value. Further, correlations in terms of void fraction and Reynolds number were defined to predict the coefficient of interaction.

Regarding the method for the study of flow-induced vibration based on output only, in a Virtual Sensing context, augmented-state Kalman Filter (AKF) based techniques have been introduced in the field of force estimation. In the present work, the formulation necessary to define the AKF algorithm has been presented in detail.

Based on a system identified in the 0 - 500 Hz frequency bandwidth via EMA procedures, the AKF-DM algorithm was implemented in order to estimate flow-induced forces. Previously, some pilot tests were performed aiming to address the difficulties that the algorithm may confront in flow-induced forces identification. Based on this study, the predicted forces are referred to as equivalent forces, which represent a set of fluctuating forces that is actually acting on the structure by using a only force applied on A2. Further, the equivalent force for each experimental condition is obtained via AKF-DM algorithm

Literature define the fluctuating forces as the superposition of quasi-periodic and buffeting forces. Equivalent forces obtained from AKF-DM algorithm show that buffeting due to turbulent flow is present in both coordinates and all the experimental conditions. This type of fluctuating load is more notorious, mostly in y coordinate, in the low frequency bandwidth, say 0 - 5 Hz, than in higher frequencies. Moreover, intermittent-type flow patterns seem to accentuate this effect. In addition, the present

results show equivalent forces with a quasi-constant frequency component at approximately 23 Hz, in x coordinate, and it is more pronounced for void fractions up to $\alpha_H = 50\%$. However, the causes that lead to this peak are difficult to be explained since its frequency seems to be independent of mass velocity. Such kind of periodic force has been reported by few references, not in the same frequency bandwidth, and the mechanism behind could not be justified. Differences in geometrical parameters in tube bundles are probably related to the distinct type of fluctuating forces found in literature.

Based on an analysis of RMS values of the equivalent forces, it can be said that for void fractions up to 60%, and under bubbles flow pattern, forces increase with pitch velocity. Furthermore, force RMS values in transverse and parallel directions are similar up to some velocity that varies with void fraction, thereafter force in parallel direction tends to be higher than that in transverse direction. For void fractions higher than 80%, the RMS values of force present a local maximum, which cannot be justified since any flow pattern transition occurs under these circumstances.

An indirect procedure is proposed in order to validate the obtained equivalent forces. According to this procedure, RMS values of measured accelerations are compared to the acceleration response that would be generated by the application of a normally distributed force (with mean and standard deviation equal to the equivalent force) on a synthesized system. Based on this comparison, it can be seen that simulated acceleration at points A1 and A2 agree with corresponding measurements for void fractions up to 80%, mainly in y coordinate. Despite this remarkable result, it is important to mention that predicted RMS acceleration amplitudes tend to overestimate actual values for higher mass velocities, mainly in x coordinate. For void fractions higher than 80%, simulated RMS acceleration amplitudes in x coordinate fail to predict the actual values, especially for intermittent-type flow patterns. This result emphasizes the difficulty introduced by this type of flow pattern. Moreover, there are two reasons why simulated accelerations differ from measured data, (i) the identified equivalent force is wrong and/or (ii) the synthesized system differs considerably from the system under intermittent-type flow patterns. Although both options seem to be feasible, it is worth mentioning that results in y coordinate at high void fractions are better than those in x coordinate. In these sense, it can be pointed out that there are some problems on force identification in x coordinate and intermittent-type flow patterns.

7.2 Recommendations and future works

Based on the literature review and experimental results presented in this work, the following future works can be outlined:

- The present results on flow-induced forces during turbulence-induced vibration

mechanism present a quasi-constant periodic component that cannot be explained with current measurements and/or knowledge. Further discussions can be proposed in terms of flow velocity profile in the tube bundle, which is currently been studied by the Heat Transfer Research Group at São Carlos School of Engineering. In this sense, the conclusions of both experimental studies can be compared, and look for the causes that generate this periodic component.

- Besides virtual sensing techniques, further methods that allow to estimate flow-induced forces based on *outputs only* can be tested. For example, Operational Modal Analysis (OMA) techniques and Dynamic Programming algorithms can be implemented with the obtained acceleration measurements. Regarding the former, some initial approaches have been made in a parallel work. The results showed that further studies are necessary to develop a method capable of normalize the modal matrices properly.

- Equivalent forces estimation via Kalman filtering techniques can be tested by using other kinds of sensors, for example, strain gauges.

- Also regarding virtual sensing and Kalman filtering techniques, there is still open room for studies regarding more complex equivalent force models, such as multiple forces and distributed loads, which are relevant for flow-induced phenomena.

Bibliography

ÁLVAREZ-BRICEÑO, R. **Projeto e análise de dispositivo dinâmico para o estudo das vibrações induzidas por escoamentos bifásicos**. Dissertação (Mestrado) — Escola de Engenharia de São Carlos, Universidade de São Paulo, São Carlos, 2014.

ÁLVAREZ-BRICEÑO, R.; de Oliveira, L. P. R.; KANIZAWA, F. T.; RIBATSKI, G. Two-phase flow induced vibrations in tube bundles under crossflow. In: THOME, J. R. (Ed.). **Encyclopedia of Two-Phase Heat Transfer and Flow III**. [S.l.]: World Scientific, 2018. v. 4.

ÁLVAREZ-BRICEÑO, R.; KANIZAWA, F. T.; RIBATSKI, G.; de Oliveira, L. P. R. An experimental analysis on the characteristics of a dynamic structure for the study of multiphase flow-induced vibrations in tube bundles. In: **In Proceedings of the XVII International Symposium on Dynamic Problems of Mechanics**. Natal, Brazil: [s.n.], 2015.

____. Updated results on hydrodynamic mass and damping estimations in tube bundles under two-phase crossflow. **International Journal of Multiphase Flow**, v. 89, p. 150–162, 2017.

____. Validation of turbulence induced vibration design guidelines in a normal triangular tube bundle during two-phase crossflow. **Journal of Fluids and Structures**, v. 76, p. 301–318, 2018.

ÁLVAREZ-BRICEÑO, R.; NAETS, F.; DESMET, W.; de Oliveira, L. P. R. Force identification via kalman filtering and dummy measurements on a cantilevered structure immersed in water. **Mechanical Systems and Signal Processing**, Under review, 2018.

AXISA, F.; ANTUNES, J.; VILLARD, B. Random excitation of heat exchanger tubes by cross-flows. **Journal of Fluids and Structures**, v. 4, p. 321–341, 1990.

BABAN, F.; SO, R. M. C.; ÖTÜGEN, M. V. Unsteady forces on circular cylinders in a cross-flow. **Experiments in Fluids**, v. 7, p. 293–302, 1989.

BENDAT, J.; PIERSOL, A. **Random Data: Analysis and Measurement Procedures**. New Jersey: Wiley, 2010.

BERG, J. C.; Keith Miller, A. Force estimation via kalman filtering for wind turbine blade control. In: **Proceedings of the IMAC - XXVIII**. Jacksonville, Florida, USA: [s.n.], 2010.

BLEVINS, R. D. Fluid elastic whirling of a tube row. **Journal of Pressure Vessel Technology**, American Society of Mechanical Engineers, v. 96, n. 4, p. 263–267, 1974.

____. Vibration of a loosely held tube. **Journal of Engineering for Industry**, American Society of Mechanical Engineers, v. 97, n. 4, p. 1301–1304, 1975.

____. **Flow-Induced Vibration**. 2nd edition. ed. Malabar, Florida: Krieger Publishing Company, 2001.

BLEVINS, R. D.; GIBERT, R. J.; VILLARD, B. **Experiments on vibration of heat-exchanger tube arrays in cross flow**. [S.l.], 1981.

CARLUCCI, L. N. Damping and hydrodynamic mass of a cylinder in simulated two-phase flow. **ASME Journal of Mechanical Design**, v. 102, p. 597–602, 1980.

CARLUCCI, L. N.; BROWN, J. D. Experimental studies of damping and hydrodynamic mass of a cylinder in confined two-phase flow. **Journal of Vibration, Acoustics, Stress and Reliability in Design**, v. 105, p. 83–89, 1983.

CENGEL, Y.; BOLES, M. **Thermodynamics: An Engineering Approach**. 5th edition. ed. Boston, MA: McGraw-Hill College, Boston, MA, 2006.

CHATZI, E. N.; FUGGINI, C. Structural identification of a super-tall tower by gps and accelerometer data fusion using a multi-rate kalman filter. In: **Life-Cycle and Sustainability of Civil Infrastructure Systems: Proceedings of the Third International Symposium on Life-Cycle Civil Engineering (IALCCE'12)**. Vienna, Austria: [s.n.], 2012.

CHEN, S. S. **Flow induced vibration of circular cylindrical structures**. Washington, DC: Hemisphere publishing corporation, 1987.

CHUNG, H. J.; CHU, I. Fluid-elastic instability of rotated square tube array in an air-water two-phase cross-flow. **Nuclear Engineering and Technology**, v. 38, p. 69–80, 2006.

CHURCHILL, S. W. The art of correlation. **Industrial & Engineering Chemistry Research**, ACS Publications, v. 39, n. 6, p. 1850–1877, 2000.

CICCHITTI, A.; LOMBARDI, C.; SILVESTRI, M.; SOLDAINI, G.; SAVATTARELLI, R. Two-phase cooling experiments - pressure drop, heat transfer and burnout measurements. **Energia Nucleare**, v. 7(6), p. 407–425, 1960.

COLLIER, J.; THOME, J. R. **Convective Boiling and Condensation**. 3rd edition. ed. Oxford: Oxford Science Publications, 1994.

CONNORS, H. J. Fluidelastic vibration of tube arrays excited by cross flow. In: **Symposium on Flow Induced Vibration in Heat Exchangers, ASME Winter Annual Meeting**. [S.l.: s.n.], 1970. p. 42 – 56.

CROES, J. **Virtual sensing in mechatronic systems. State estimation using system level models**. Tese (Doutorado) — Katholieke Universiteit Leuven, 2017.

de Langre, E.; VILLARD, B. An upper bound on random buffeting forces caused by two-phase flows across tubes. **Journal of Fluids and Structures**, v. 12, p. 1005–1023, 1998.

de Oliveira, L. P. R.; VAROTO, P. S.; SAS, P.; DESMET, W. A state-space modeling approach for active structural acoustic control. **Shock and Vibration**, Hindawi Publishing Corporation, v. 16, n. 6, p. 607–621, 2009.

DELENNE, B.; GAY, N.; CAMPISTRON, R.; BANNER, D. Experimental determination of motion-dependent fluid forces in two-phase water freon cross flow. In: **Proceeding of the ASME Int. Symposium on Fluid-Structure Interaction: Aerolasticity, Flow-Induced Vibration and Noise, Vol:II (ed. M.P. Páidoussis)**. New York, USA: [s.n.], 1997.

DOWLATI, R.; CHAN, A. M. C.; KAWAJI, M. Hydrodynamics of two-phase flow across horizontal in-line and staggered rod bundles. **Journal of Fluids Engineering - Transactions of the ASME**, v. 114, p. 450–456, 1992.

DOWLATI, R.; KAWAJI, M.; CHAN, A. M. C. Pitch-to-diameter effect on two-phase flow across an in-line tube bundle. **AIChE Journal**, v. 36, n. 5, p. 765–772, 1990.

DOWLATI, R.; KAWAJI, M.; CHISHOLM, D.; CHAN, A. M. C. Void fraction prediction in two-phase flow across a tube bundle. **AIChE Journal**, v. 38, n. 4, p. 619–622, 1992.

DUKLER, A. E.; WICKS, M.; CLEVELAND, R. G. Pressure drop and hold-up in two-phase flow part a - a comparison of existing correlations and part b - an approach through similarity analysis. **AIChE Journal**, v. 10, p. 38–51, 1964.

FEENSTRA, P. A.; WEAVER, D. S.; JUDD, R. L. An improved void fraction model for two-phase cross-flow in horizontal tube bundles. **International Journal of Multiphase Flow**, v. 26, p. 1851–1873, 2000.

FRANKLIN, G.; POWELL, J. D.; WORKMAN, M. **Digital control of dynamic systems**. [S.l.]: Ellis - Kagle Press, 1998.

GORMAN, D. J. Experimental study of the flow induced vibration of multi-span heat exchanger tube bundles in liquid cross-flow. In: **Structural mechanics in reactor technology. Vol. B**. [S.l.: s.n.], 1981.

GOYDER, H. G. D. Personal communication. 1982.

GRANT, I. D. R. Flow and pressure drop with single-phase and two-phase flow in the shell-side of segmentally baffled shell and tube heat exchangers. In: **NEL Report No. 590, National Engineering Laboratory**. Glasgow, Scotland: [s.n.], 1975.

GRANT, I. D. R.; CHISHOLM, D. Two-phase flow on the shell-side of a segmentally baffled shell-and-tube heat exchanger. **Journal of Heat Transfer**, v. 101(1), p. 38–42, 1979.

GREEN, S. J.; HETSRONI, G. Pwr steam generators. **International Journal of Multiphase Flow**, v. 21, p. 1–97, 1995.

HARTLEN, R. T. Effect of support-point details upon natural frequency and damping of heat exchanger tubes: Preliminary laboratory investigation. **Ontario Hydro Pesearcb Beport**, v. 74, 1974.

HAUTUS, M. L. J. Stabilization controllability and observability of linear autonomous systems. In: **Proceedings of Indagationes Mathematicae**. Eindhoven, Netherlands: [s.n.], 1970.

ISHII, M. **Thermo-fluid dynamic theory of two-phase flow. Chapters IX and X**. NY: Eyrolles, Paris, Scientific and Medical Publication of France, 1975.

____. **One dimensional drift-flux model and constitutive equations for relative motion between phases in various two-phase flow regimes**. [S.l.], 1977.

KALMAN, R. E. A new approach to linear filtering and prediction problems. **Journal of Basic Engineering**, v. 82 (1), p. 35–45, 1960.

KALMAN, R. E.; BUCY, R. S. New results in linear filtering and prediction theory. **Journal of Basic Engineering**, v. 83 (3), p. 95–108, 1961.

KANEKO, S.; NAKAMURA, T.; INADA, F.; KATO, M. **Flow- Induced Vibrations: Classifications and Lessons from Practical Experiences**. Primeira edição. Oxford, UK: Elsevier, 2008.

KANIZAWA, F. **Estudo teórico e experimental sobre padrões de escoamento, fração de vazio e perda de pressão durante escoamento bifásico água-ar cruzado ascendente externo a banco de tubos**. Tese (Doutorado) — Universidade de São Paulo, São Carlos, 2014.

KANIZAWA, F. T.; RIBATSKI, G. Two-phase flow patterns across triangular tube bundles for air-water upward flow. **International Journal of Multiphase Flow**, v. 80, p. 43–56, 2016.

____. Void fraction predictive method based on the minimum kinetic energy. **Journal of the Brazilian Society of Mechanical Sciences and Engineering**, v. 38, p. 209–225, 2016.

____. Void fraction and pressure drop during external upward two-phase crossflow in tube bundles - part i: Experimental investigation. **International Journal of Heat and Fluid Flow**, v. 65, p. 200–209, 2017.

____. Void fraction and pressure drop during external upward two-phase crossflow in tube bundles - part ii: Predictive methods. **International Journal of Multiphase Flow**, v. 65, p. 210–219, 2017.

KHUSHNOOD, S.; KHAN, Z. M.; MALIK, M. A.; KORESHI, Z. U.; KHAN, M. A. A review of heat exchanger tube bundle vibrations in two-phase cross-flow. **Nuclear Engineering and Design**, v. 230, p. 233–251, 2004.

KHUSHNOOD, S.; KHAN, Z. M.; MALIK, M. A.; KORESHI, Z.; JAVAID, M. A.; KHAN, M. A.; QURESHI, A. H.; NIZAM, L. A.; BASHIR, K. S.; HUSSAIN, S. Z. **Cross-Flow-Induced-Vibrations in Heat Exchanger Tube Bundles: A Review, Nuclear Power Plants**. 1st edition. ed. Riteja: InTech, 2012.

KONDO, M.; NAKAJIMA, K. I. Experimental investigation of air-water two phase upflow across horizontal tube bundles: Part 1, flow pattern and void fraction. **Bulletin of JSME**, v. 23(117), p. 385–393, 1980.

LEE, S. S. L. Vibration of u-bend segments of heat exchanger tubes. **Atomic Energy of Canada Limited, AECL**, v. 3735, 1971.

LIAN, H. Y.; NOGHREHKAR, G.; CHAN, A.; KAWAJI, M. Effect of void fraction on vibrational behavior of tubes in tube bundle under two-phase cross flow. **Journal of Vibration and Acoustics**, v. 119, p. 457–463, 1997.

LMS. **The LMS Test.Lab Modal Analysis manual**. Revision 13 a. [S.l.], 2012.

LOURENS, E.; REYNDERS, E.; De Roeck, G.; DEGRANDE, G.; LOMBAERT, G. An augmented kalman filter for force identification in structural dynamics. **Mechanical Systems and Signal Processing**, v. 27, p. 446–460, 2012.

LOWERY, R. L.; MORETTI, P. M. Natural frequencies and damping of tubes on multi-span supports. In: **15th National Heat Transfer Conference, AIChE, Paper**. [S.l.: s.n.], 1975.

MACQUEEN, J. Some methods for classification and analysis of multivariate observations. In: **Proceedings of the fifth Berkeley symposium on mathematical statistivs and probability**. Berkeley, California: [s.n.], 1967.

MAIA, N.; SILVA, J. **Theoretical and Experimental Modal Analysis**. 1st edition. ed. Hertfordshire: Research Studies Press LTD, 1998.

MAO, K.; HIBIKI, T. Flow regime transition criteria for upward two-phase cross-flow in horizontal tube bundles. **Applied Thermal Engineering**, Elsevier, v. 112, p. 1533–1546, 2017.

MARCHATERRE, J. F. Two-phase frictional pressure drop prediction from levy's momentum model. **Journal of Heat Transfer**, v. 83(4), p. 503–505, 1961.

MCADAMS, W. H. Vaporization inside horizontal tubes: Ii-benzene-oil mixtures. **Transactions of ASME**, v. 64, p. 193, 1942.

MIRZA, S.; GORMAN, D. J. Experimental and analytical correlation of local driving forces and tube response in liquid flow-induced vibration of heat exchangers. In: **Paper F615, 2nd Conference on Structural Mechanics in Reactor Technology**. Berlin, Germany: [s.n.], 1973.

MULCAHY, T. Fluid forces on rods vibrating in finite length annular regions. **Journal of Applied Mechanics**, American Society of Mechanical Engineers, v. 47, n. 2, p. 234–240, 1980.

NAETS, F.; CROES, J.; DESMET, W. An online coupled state/input/parameter estimation approach for structural dynamics. **Computer methods in applied mechanics and engineering**, v. 283, p. 1167–1188, 2015.

NAETS, F.; CUADRADO, J.; DESMET, W. Stable force identification in structural dynamics using kalman filtering and dummy - measurements. **Mechanical Systems and Signal Processing**, v. 50-51, p. 235–248, 2015.

NICOLETTI, R. **Basics of Mechanical Vibration**. 1st edition. ed. Saarbrücken, Germany: Lambert Academic Publishing, 2015.

NOGHREHKAR, G.; KAWAJI, M.; CHAN, A. Investigation of two-phase flow regimes in tube bundles under cross-flow conditions. **International Journal of Multiphase Flow**, v. 25, p. 857–874, 1999.

OWEN, P. R. Buffeting excitation of boiler tube vibration. **Journal of Mechanical Engineering Science**, SAGE Publications, v. 7, n. 4, p. 431–439, 1965.

PAïDOUSSIS, M. P. Fluidelastic vibration of cylinder arrays in axial and cross flow: state of the art. **Journal of Sound and Vibration**, Elsevier, v. 76, n. 3, p. 329–360, 1981.

PAïDOUSSIS, M. P.; PRICE, S. J.; de Langre, E. **Fluid-Structure Interactions - Cross-Flow-Induced Instabilities**. 1st edition. ed. New York: Cambridge University Press, 2011.

PAPP, L. Vibration of vver npp steam generator tubes. **,(in Czech) Jadera' Energie**, v. 34, No.7, p. 249–259, 1988.

PAPP, L.; CHEN, S. S. Turbulence-induced vibration of tube arrays in two-phase flow. **Journal of Pressure Vessel Technology**, v. 116, p. 312–316, 1994.

PERROT, E.; MUREITHI, N.; PETTIGREW, M.; RICCIARDI, G. Vibration excitation forces in a normal triangular tube bundle subjected to two-phase cross flow. In: **Proceedings of the ASME 2011 Pressure Vessels & Piping Division Conference**. Baltimore, USA: [s.n.], 2011.

PETERSEN, Ø. W.; ØISETH, O.; NORD, T. S.; LOURENS, E. Estimation of the full-field dynamic response of a floating bridge using kalman-type filtering algorithms. **Mechanical Systems and Signal Processing**, v. 107, p. 12–28, 2018.

PETTIGREW, M.; GORMAN, D. Vibration of heat exchanger tube bundles in liquid and two-phase cross-flow. **Flow-Induced Vibration Design Guidelines**, p. 89–110, 1981.

PETTIGREW, M. J.; CARLUCCI, L. N.; TAYLOR, C. E.; FISHER, N. Flow-induced vibration and related technologies in nuclear components. **Nuclear Engineering and Design**, v. 131, p. 81–100, 1991.

PETTIGREW, M. J.; ROGERS, R. J.; AXISA, F. Damping of multispan heat exchangers tubes - part2: In liquids. In: **ASME Pressure Vessels Symposium on Special Topics of Structural Vibration, and Piping Conference**. Chicago, USA: [s.n.], 1986.

PETTIGREW, M. J.; SYLVESTRE, Y.; CAMPAGNA, A. O. Vibration analysis of heat exchanger and steam generator designs. **Nuclear Engineering and Design**, Elsevier, v. 48, n. 1, p. 97–115, 1978.

PETTIGREW, M. J.; TAYLOR, C.; KIM, B. Vibration of tube bundles in two-phase cross-flow: Part 1 - hydrodynamic mass and damping. **Journal of Pressure Vessel Technology**, v. 111, p. 466–477, 1989.

PETTIGREW, M. J.; TAYLOR, C. E. Two-phase flow induced vibration: An overview. **Journal of Pressure Vessel Technology**, v. 116, p. 233–253, 1994.

____. Vibration analysis of shell and tube heat exchangers: an overview - part 1. flow damping, fluidelastic instability. **Journal of Fluids and Structures**, v. 18, p. 469–489, 2003.

____. Vibration analysis of shell and tube heat exchangers: an overview - part 2. vibration response, fretting-wear, guidelines. **Journal of Fluids and Structures**, v. 18, p. 485–500, 2003.

____. Damping of heat exchanger tubes in two-phase flow: Review and design guidelines. **Journal of Pressure Vessel Technology**, v. 126, p. 523–533, 2004.

PETTIGREW, M. J.; TAYLOR, C. E.; JANZEN, V. P.; WHAN, T. Vibration behavior of rotated triangular tube bundles in two-phase cross flows. **Journal of Pressure Vessel Technology**, v. 124, p. 144–153, 2002.

PETTIGREW, M. J.; TAYLOR, C. E.; JONG, J. H.; CURIE, I. G. Vibration of a tube bundle in two-phase freon cross flow. **Journal of Pressure Vessel Technology**, v. 117, p. 321–329, 1995.

PETTIGREW, M. J.; TAYLOR, C. E.; KIM, B. S. The effects of bundle geometry on heat exchanger tube vibration in two-phase cross flow. **Journal of Pressure Vessel Technology**, v. 123, p. 414–420, 2001.

PETTIGREW, M. J.; ZHANG, C.; MUREITHI, N. W.; PAMFIL, D. Detailed flow and force measurements in a rotated triangular tube bundle subjected to two-phase cross-flow. **Journal of Fluids and Structures**, v. 20, p. 567–575, 2005.

PRICE, S. J.; PAÏDOUSSIS, M. P. A constrained-mode analysis of the fluidelastic instability of a double row of flexible circular cylinders subject to cross-flow: A theoretical investigation of system parameters. **Journal of sound and Vibration**, Elsevier, v. 105, n. 1, p. 121–142, 1986.

ROGERS, R. G.; TAYLOR, C.; PETTIGREW, M. J. Fluid effects on multi span heat exchanger tube vibration. In: **Proceedings of the ASME PVP Conference**. San Antonio, EEUU: [s.n.], 1984.

SCHRAGE, D. S.; HSU, J. T.; JENSEN, M. K. Two-phase pressure drop in vertical crossflow across a horizontal tube bundle. **AIChE Journal**, v. 34, n. 1, p. 107–115, 1988.

SEMPéRTEGUI-TAPIA, D. F. **Estudo teórico - experimental dos padrões de escoamento durante a evaporação convectiva no interior de canais com diâmetro reduzido**. Dissertação (Mestrado) — Escola de Engenharia de São Carlos, Universidade de São Paulo, São Carlos, 2011.

SHIN, Y. S.; WAMBSGANSS, M. W. Flow-induced vibration in lmfbr steam generators: a state-of-the-art review. **Nuclear Engineering and Design**, Elsevier, v. 40, n. 2, p. 235–284, 1977.

SIM, W. G. An approximate damping model for two-phase cross-flow in horizontal tube bundles. In: **ASME Pressure Vessels and Piping Conference**. San Antonio, USA: [s.n.], 2007.

SIM, W. G.; MUREITHI, N. W. A two-phase damping model on tube bundles subjected totwo-phase cross-flow. **Journal of Mechanical Science and Technology**, v. 28(2), p. 553–563, 2014.

SINGH, K. P.; SOLER, A. I. **Mechanical design of heat exchangers and pressure vessel components**. [S.l.]: Springer Science & Business Media, 1984.

TAITEL, Y.; BARNEA, D.; DUKLER, A. E. Modelling flow pattern transitions for steady upward gas-liquid flow in vertical tubes. **AIChE Journal**, v. 26, n. 3, p. 345–354, 1980.

TAYLOR, C.; CURRIE, I.; PETTIGREW, M. J.; KIM, B. Vibration of tube bundles in two-phase cross-flow: Part 3 - turbulence-induced excitation. **Journal of Pressure Vessel Technology**, v. 111(4), p. 488–500, 1989.

TAYLOR, C.; PETTIGREW, M. J. Effect of flow regime and void fraction on tube bundle vibration. **Journal of Pressure Vessel Technology**, v. 123, p. 407–413, 2001.

TAYLOR, C. E.; PETTIGREW, M. J.; AXISA, F.; VILLARD, B. Experimental determination of single and two-phase cross flow. **Journal of Pressure Vessel Technology**, v. 110, p. 22–28, 1988.

TEMA Standards. **Standards of the Tubular Manufacturers Association**. [S.l.], 1999. v. 71.

TRINDADE, M. A.; PAGANI, C. C.; de Oliveira, L. P. R. Semi-modal active vibration control of plates using discrete piezoelectric modal filters. **Journal of Sound and Vibration**, Elsevier, v. 351, p. 17–28, 2015.

ULBRICH, R.; MEWES, D. Vertical, up-ward gas-liquid two-phase flow across a tube bundle. **International Journal of Multiphase Flow**, v. 20, p. 249–272, 1994.

VENKASTESWARARAO, P.; SEMIAT, R.; DUKLER, A. E. Flow pattern transition for gas-liquid flow in a vertical rod bundle. **International Journal of Multiphase Flow**, v. 8, n. 5, p. 509–524, 1982.

WALLIS, G. B. **One dimensional two-phase flow**. 1st edition. ed. Texas: McGraw-Hill, 1969.

WEAVER, D. S.; EL-KASHLAN, M. The effects of damping and mass ratio on the stability of a tube bank. **Journal of Sound and Vibration**, v. 76, p. 283–294, 1981.

WEAVER, D. S.; GROVER, L. K. Cross-flow induced vibrations in a tube bank—turbulent buffeting and fluid elastic instability. **Journal of Sound and Vibration**, Elsevier, v. 59, n. 2, p. 277–294, 1978.

WEAVER, D. S.; ZIADA, S.; AU-YANG, M. K.; CHEN, S. S.; PAIDOUSSIS, M. P.; PETTIGREW, M. J. Flow-induced vibrations in power and process plant components - progress and prospects. **Journal of Pressure Vessel Technology**, v. 122(3), p. 339–348, 2000.

WILSON, E. Virtual sensor technology for process optimization. In: **Proceedings of the Symposium on Computers and Controls in the Metals Industry in Iron and Steel Society**. Baltimore, Maryland, USA: [s.n.], 1997.

XU, G. P.; TSO, C. P.; TOU, K. W. Hydrodynamics of two-phase flow in vertical up and down-flow across a horizontal tube bundle. **International Journal of Multiphase Flow**, v. 24(8), p. 1317–1342, 1998.

ZHANG, C.; PETTIGREW, M. J.; MUREITHI, N. W. Vibration excitation force measurements in a rotated triangular tube bundle subjected to two-phase cross flow. **Journal of Pressure Vessel Technology**, v. 129, p. 21–27, 2007.

ZUBER, N.; FINDLAY, J. Average volumetric concentration in two-phase flow systems. **Trans. ASME Journal of Heat Transfer**, v. 87, p. 453, 1965.

ZUBER, N.; STAUB, F. W.; BIJWAARD, G.; KROEGER, P. G. **Steady state and transient void fraction in two-phase flow systems**. [S.l.], 1967.

ŽUKAUSKAS, A. Heat transfer from tubes in crossflow. **Advances in heat transfer**, Elsevier, v. 8, p. 93–160, 1972.

ZUKAUSKAS, A. **Heat transfer from tubes in crossflow**. 1st edition. ed. New York: Hemisphere Publishing Corporation, 1988.

ZUKAUSKAS, A.; ULINSKAS, R. **2.2.4 Banks of plain and finned tubes. In Heat Exchanger Design Handbook 2 - Fluid mechanics and heat transfer**. 1st edition. ed. United States of America: Hemisphere Publishing Corporation, 1983.